Dynamics of Metastable Magnetic Skyrmions

Max T. Birch

Supervised by Prof. Peter Hatton

The Skyrmion Project
Department of Physics
University of Durham

July 19th 2020

Metastable Dynamics of Magnetic Skyrmions

Max T. Birch

Skyrmions, vortex-like objects composed of magnetic moments, have seen a recent surge of research interest due to their unique transport and topological properties. With an ever-increasing demand for more efficient memory and computation, skyrmionic devices have been conceived as an ultra-low power, high density data storage solution. While they are found in a range of materials, in this thesis we will primarily be concerned with skyrmions found in bulk chiral magnets.

In such systems, skyrmions are typically only at equilibrium in a small range of temperature and applied magnetic field. However, they can exist in a metastable state over a much wider range of the magnetic phase diagram, formed by cooling the system under an applied magnetic field. Metastable skyrmions therefore have technological application by enabling the existence of skyrmions at room temperature and zero applied magnetic field. However, they also posses a finite, temperature-dependent lifetime, which places limitations on the stability of metastable skyrmions, and also restricts the population remaining after the cooling process. This lifetime is realised in nanoscopic mechanisms which are governed by topological defects, known as Bloch points. Due to the locality of these structures, the development of real-space imaging techniques are vital for gaining true understanding of skyrmion formation and annihilation.

In this thesis, the dynamics of metastable skyrmions are thoroughly investigated through the use of magnetometry, and a range of neutron and x-ray scattering techniques. The effect of chemical substitution, or doping, on the magnetic phase transitions in Zn-doped Cu_2OSeO_3 is explored, and found to introduce pinning effects which dramatically increases the lifetime of metastable skyrmions. Furthermore, by adapting x-ray imaging methods for cryogenic sample environments, the first real-space observation of the vertical, tube-like, structure of skyrmions is demonstrated. The results open the door to a variety of experiments capable of further investigation into the dynamics of the skyrmion spin texture.

Acknowledgements

The completion of this thesis would not have been possible without funding from EPSRC, Durham University and Diamond Light Source, and the help and assistance of colleagues and friends at a range of institutions.

My thanks to Paul Steadman, Raymond Fan and Mark Sussmuth at Diamond Light Source, for their tireless help with the I10 MPMS3 and RASOR; Bob Cubit and Marta Crisanti at ILL for our SANS measurements of skymoon and comical states; Horia Popescu and Nicolas Jaouen at Synchrotron SOLEIL and Feodor Ogrin at Exeter University for showing us the way with x-ray holography; Joachim Gräfe, Felix Groß, Nick Träger, Markus Weigand and Gisela Schütz at BESSY II and MPI Stuttgart for introducing me to the world of STXM; and Shinichiro Seki, Rina Takagi, Nguyen Khanh and Yoshinori Tokura for their warm welcome to Japan, and the vast experience I gained at RIKEN under their generous guidance.

I have the sincerest gratitude to all members of the UK Skyrmion Project, including James Loudon and Alison Harrison at Cambridge University, for teaching me to use the FIB, and collaborating with LTEM measurements; Tom Lancaster for his enlightening instructions on writing my first paper; Ales Štefančič, Sam Holt and Geetha Balakrishnan for their tireless efforts in meeting the groups' endless demands for samples; and David Cortés-Ortuño, whose simulations were vital to the success of our skyrmion tube project.

At my own institution Durham University, I am grateful to Luke Turnbull, Sam Moody and Murray Wilson, for their camaraderie on countless sleepless beamtimes, and their patient and helpful contributions when correcting and improving innumerable manuscripts and proposals.

I am indebted to my supervisor, Peter Hatton, for his encouragement of my crazy project ideas, and his valuable guidance during both my Masters and PhD projects – without whom I would not be on the path I am on today. Finally, I would thank my wife, Claire, and my parents, Rob and Julie, for enduring far too many physics-related dinner discussions, and for their endless interest in and support of my work on skyrmions.

Contents

Chapter 1

Introduction

1.1 What is a Skyrmion?

The concept of a skyrmion was originally proposed in 1962 by Tony Skyrme to describe nucleons in particle physics. He envisaged a nucleon as a topological soliton in a pion field, forming topologically invariant knot-like objects [1]. The model is able to account for some low-energy properties, but was eventually superseded by quantum chromodynamics [2]. Skyrme's original skyrmions can be visualised as a three dimensional wrapping of the vector field onto a unit sphere, giving them a three-dimensional hedgehog-like appearance, as shown in Fig. 1.1. The winding of the vector field around this sphere is a visual representation of its topological nature, forming a knot-like excitation, which endows the object with stability against unravelling into a topologically trivial state [3,4]. The discovery of the magnetic skyrmion, appearing as a two dimensional projection of Skyrme's original three dimensional skyrmions, as shown in Fig. 1.1, breathed new life into Skyrme's work [5, 6]. Originally, the concept of topology was thought to be exclusive to pure mathematics, with no applications to physics [7]. Now, the magnetic skyrmion is just one example of the recent discovery of topology in condensed matter physics, which has found further applicability in systems such as topological insulators [8,9], topological superconductors [10, 11] and topological semimetals [12, 13].

Skyrmions were theorised to exist in chiral magnetic systems in 2006 [5]. In this case, skyrmions appear as vortex-like arrangements of spins in the magnetisa-

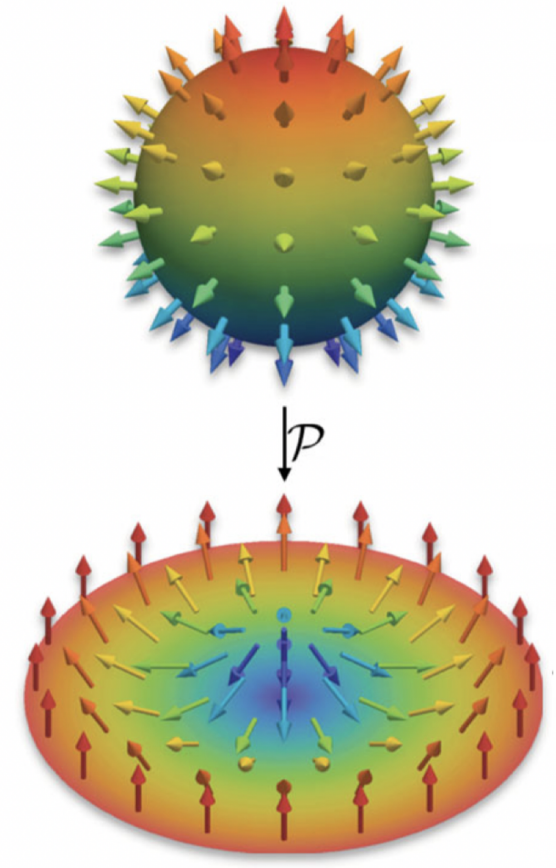

Figure 1.1: Visualisation of a three-dimensional skyrmion, as envisaged by Tony Skyrme, and its two-dimensional projection. Adapted from [4].

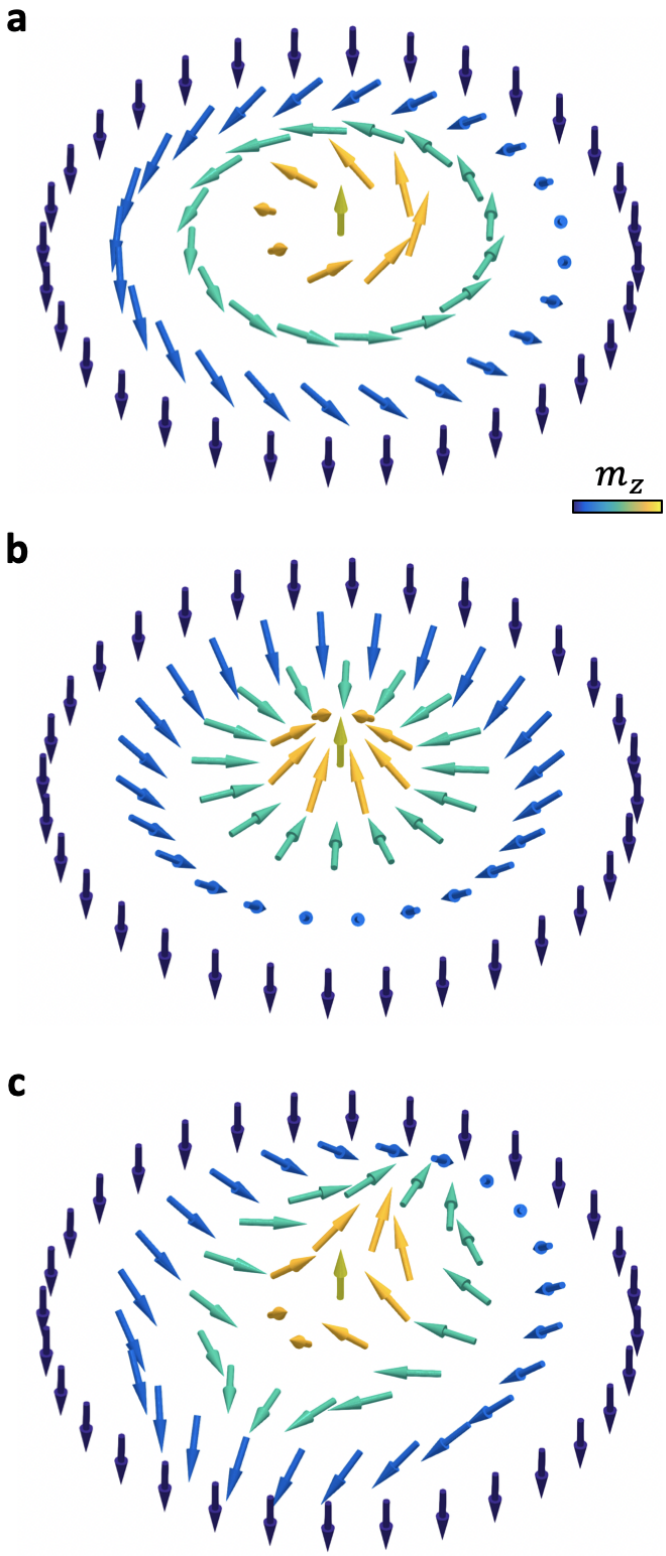

Figure 1.2: Schematics of a Bloch skyrmion (**a**), a Néel skyrmion (**b**) and an anti-skyrmion (**c**).

tion texture of the system. They are stabilised by the delicate balance of magnetic energies, including the crucial interplay between the exchange interaction, the anti-symmetric exchange, or Dzyaloshinskii-Moriya, interaction (DMI), and the Zeeman energy [14–16]. Shortly after, in 2009, they were discovered to exist in a bulk chiral magnet, MnSi, under the application of a magnetic field [6]. Since this original discovery, they have been observed in a wide variety of magnetic systems, stabilised by a range of magnetic interactions. Beyond magnetic materials, skyrmions have also been realised in other physical systems, including Bose-Einstein condensates [17,18], and nematic liquid crystals [19–21].

A range of skyrmion types have been observed, with an spin arrangement that reflects the delicate balance and relative magnitudes of the underlying magnetic energy terms [22]. Illustrations of a magnetic Bloch-type skyrmion and a Néel-type skyrmion are shown in Fig. 1.2**a** and **b**, so named as they respectively exhibit helical or cycloidal spin rotation across their diameter, similar to Bloch and Néel domain walls [23]. Antiskyrmions have also been discovered, characterised by both Bloch and Néel-type spin rotations [3], as shown in Fig. 1.2**c**. Beyond these basic skyrmion types, a range of other topological magnetic textures have been theorised and observed: skyrmionium, also known as a target skyrmion, which is composed of one skyrmion placed inside a skyrmion of opposite charge [24, 25]; biskyrmions, which are composed of a bound pair of two skyrmion with opposite chirality [26–28]; merons - half skyrmion spin textures which have been observed to form in a square lattice [29–33], and a range of further exotic topological objects [26, 34–39].

1.2 Applications of Magnetic Skyrmions

Shortly after the discovery of magnetic skyrmions, it was speculated that they could be utilised in spintronics applications, specifically as potential memory elements in data storage devices [40–43]. This application was primarily motivated by the transport properties of skyrmions: it was observed that skyrmions may be driven by electric current densities that are orders of magnitude lower than typical magnetisation textures in nanostructures [44–46]. However, despite the low threshold

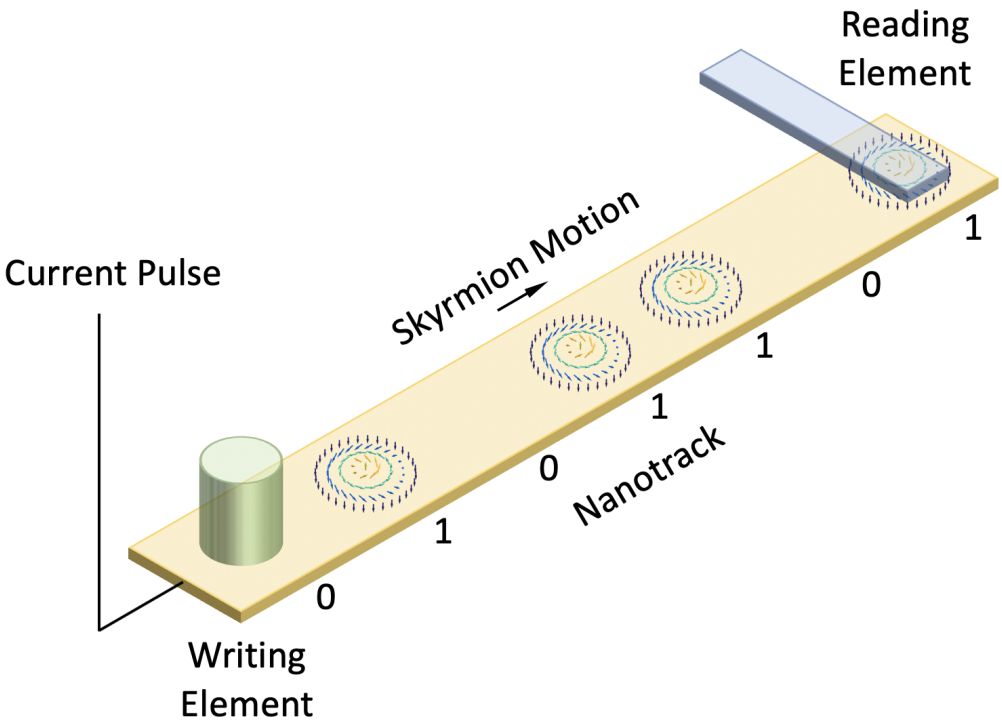

Figure 1.3: Schematic illustration of a skyrmion racetrack memory device.

current required to induce their motion, in this work they were displaced at a relatively low velocity, and as such higher current densities may be required for optimal device implementation. Since these initial studies, numerous works have investigated the ability to transport skyrmions with currents [47], drive the boundaries between skyrmions and other magnetic phases [48], or directly even create and destroy skyrmions [49].

Many suggested implementations involve the use of skyrmions in racetrack memory architectures. Racetrack memory was originally conceived as a method of storing of data in nanoscale magnetic domains [50]. These domains can be transported along a track by spin currents via the spin-momentum transfer mechanism [51]. The racetrack has the potential to be shaped or curved, allowing data to be stored in three dimensions. This would overcome the shortcoming of conventional, two-dimensional, data devices, allowing for far greater storage density [50]. One major problem encountered for domain wall racetrack memory is the propensity for the domain walls to be pinned by local disorder and defects in the underlying structure of the device, and the difficulty of controlling the exact distance travelled by each

domain wall [52, 53].

In a skyrmion racetrack memory device, the ferromagnetic domain walls are replaced by magnetic skyrmions [54,55]. A schematic illustration of a typical skyrmion racetrack device is shown in Fig. 1.3. Since the initial suggestion of skyrmion racetracks, studies of how skyrmions behave in a confined nanowire structure have been numerous [56–59]. Crucial to the successful development of such a device is realisation of efficient individual skyrmion formation, annihilation and detection, such that data may be efficiently written and read [60], as illustrated by the read and write heads in Fig. 1.3. Various methods for skyrmion writing have been proposed, such as by current injection [61–63], localised magnetic field application [64, 65], electric field application [66–68], laser exposure [69, 70], generation from magnetic stripes [71, 72], moving skyrmions through geometrical constrictions [73–75] or by otherwise exploiting the device geometry [76, 77]. Considering schemes for the electronic reading of skyrmions, it has been demonstrated that they can be detected by measurements of magnetoresistance using magnetic tunnel junctions [78, 79]. Many other proposed schemes for electronic skyrmion detection involve topological Hall resistivity measurements. The topological Hall effect (THE) arises from the Berry phase exhibited by a magnet with smoothly varying magnetisation. A skyrmion produces an emergent magnetic field, and thus electrons will have their motion deflected as they pass through a material hosting skyrmions [80–82], analogously to the well-known Hall effect. Therefore, the presence of a skyrmion can be electronically detected by a voltage measurement.

A further Hall effect, known as the skyrmion Hall effect, induces a translational Magnus force acting on a skyrmion experiencing current-induced motion [83], causing them to be deflected at the skyrmion Hall angle. This phenomenon presents a potential problem to skyrmion racetrack memory devices: skyrmions will move towards the edge of the track, potentially becoming stuck, or even annihilating, at the boundary [74, 84]. Measures have been suggested to mitigate his effect by ensuring that skyrmions are repelled from the racetrack boundary [84–86], or by utilising ferrimagnetic or antiferromagnetic skyrmions where the skyrmion Hall effect is minimised [87–89]. Alternatively, the skyrmion Hall effect might be turned

into an advantage by utilising curved or circular racetracks, which might then allow skyrmions to be driven with a magnetic field gradient [90].

Other ideas for skyrmion devices have been proposed, including the use of skyrmions confined in nano-discs as opposed to racetracks [91–98], or in skyrmion-driven logic gates or transistors [99–101]. More complex suggestions include the implementaion of skyrmions in synapse-like neuromorphic and probabilistic computing devices [102–104]. Beyond computing-inspired applications, the discovery of magnetic skyrmion resonances has led to the suggestions of skyrmion-based microwave detectors or nano-oscillator devices [105–108].

1.3 Skyrmion Materials

Since their discovery in MnSi, skyrmions have been found in a range of magnetic systems, from further bulk chiral magnets to thin films. The form and stability of skyrmions in each material is closely linked to the magnetic interactions governing each system. There have been distinctions made between skyrmions stabilised by the Dzyaloshinskii-Moriya interaction (DMI), or by long-range dipolar interactions. In the latter case, such objects have the same topology as a skyrmion, but have been called magnetic bubbles [109], which were investigated extensively in the 1970s with a view towards application in magnetic bubble memory [110]. While DMI skyrmions typically have a spatial size governed by the strength of the DMI and exchange interactions, skyrmion bubbles have a variable size, governed by the thickness of the material and the strength of the associated dipolar interactions [88, 111]. Furthermore, DMI skyrmions have a chirality fixed by the handedness of the underlying crystal lattice, while magnetic bubbles may form in one sample with either chirality [28]. For the rest of this section, we will explore the systems hosting skyrmions stabilised by DMI.

1.3.1 Thin Film Skyrmions

It was theoretically suggested [112], and later experimentally confirmed [73], that Néel-type skyrmions could be stabilised in sputter-grown magnetic heterostructures.

Typically, these multilayer thin films are composed of a trilayer of a heavy metal, a ferromagnetic material, and an insulator, such as Ta (5 nm)/CoFeB (1.1 nm)/TaO_x [73]. In these multilayer thin film systems, skyrmions are stabilised by interfacial DMI [113, 114]. Interfacial DMI arises due to the broken inversion symmetry at the interfaces of the ferromagnetic layer, induced by the presence of strong spin-orbit coupling provided by the heavy metal layer [62, 115]. These systems have the advantage of exhibiting skyrmions at room temperature [116]. Furthermore, due to being sputtered thin-films, from an application perspective, they can be manufactured using currently existing commercial film-growth equipment [111].

It was later demonstrated that performing multiple film growths to form a stack of such multilayers increased the strength of the DMI, leading to the formation of smaller skyrmions, as in, for example, $[\text{Pt (3 nm)/Co (0.9 nm)/Ta (4 nm)}]_{15}$ [62]. The magnetisation of the skyrmions extends through the entire multilayer stack [115], as was seen previously in coupled domain walls in similar stacked systems [117]. In this way, the properties of the skyrmions can be tuned by varying the materials used in the multilayers, the thickness of each layer, or the number of multilayer stacks in the film. For example, by utilising two different heavy metal layers which induce chiral interactions with opposite symmetry, the DMI induced by each interface is additive [115].

Another category of thin film skyrmion materials are those found in monolayer systems, such as a monolayer of Fe grown on an Ir(111) substrate. Skyrmions in these systems are on the scale of $\sim$1 nm, and thus require the use of a very high resolution imaging technique such as spin-polarised scanning tunnelling microscopy for real-space observations [118]. While the role of interfacial DMI is still vital for their formation, in these systems the driving force of skyrmion stabilisation are short range four-spin interactions [119]. Skyrmions in these systems have been found arranged in both a square lattice [119] and a hexagonal lattice [120].

1.3.2 Bulk Chiral Magnets

Shortly after their initial discovery in MnSi [6, 121, 122], skyrmions were found in a range of the B20 magnets: $Fe_{1-x}Co_xSi$ [123–125], FeGe [30, 126, 127], and MnGe

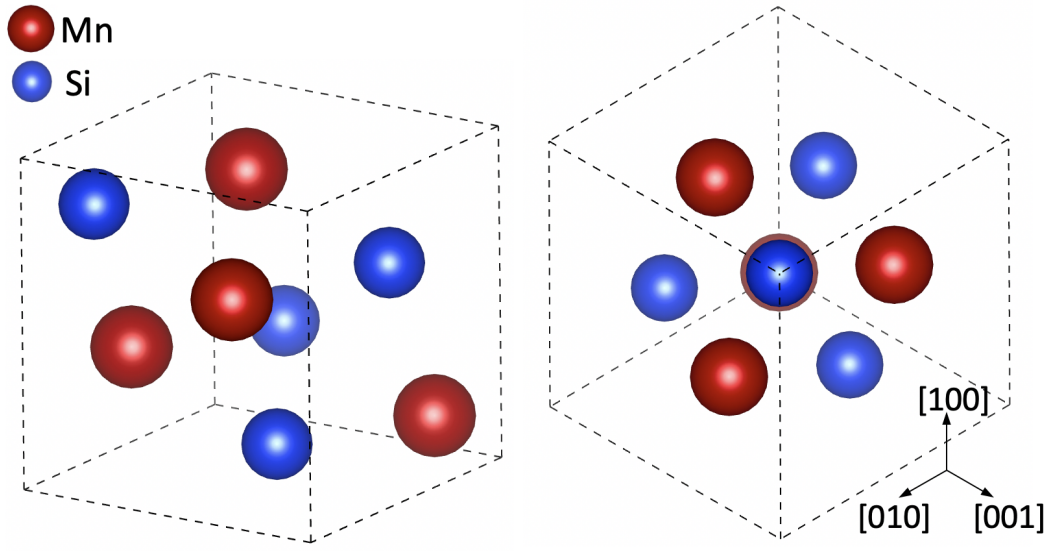

Figure 1.4: The non-centrosymmetric crystal structure of MnSi.

[128, 129]. In these materials, Bloch skyrmions are stabilised by the presence of bulk DMI, which arises due to the broken inversion symmetry of the underlying crystal structure. This lack of centrosymmtery is shown in the crystal structure of MnSi, shown in Fig. 1.4, which belongs to the space group $P2_13$. The broken inversion symmetry results in a weak spin orbit coupling, allowing the magnetic structure to decouple from the atomic lattice. Below the Curie temperature, T_C, the magnetisation forms a slowly varying, incommensurate helimagnetic structure [6]. While MnSi and $Fe_{1-x}Co_xSi$ both have a T_C below 50 K, the T_C of FeGe is ∼278 K - close to room temperature.

Later, in 2015, a new class of chiral magnetic hosting skyrmions was discovered in the Co-Zn-Mn alloy system [130]. Similar to the B20 materials, this system possess a non-centrosymmetric β-Mn-type crystal structure belonging to the $P4_132$, or $P4_432$ space groups, depending on its chirality. By substituting Mn atoms into the basic $Co_{10}Zn_{10}$ chemical composition, the T_C of this system can be tuned from 470 K to 100 K, allowing skyrmions to be stabilised at room temperature [131].

The majority of experiments investigating these chiral magnets have been performed with bulk crystal samples. There have been attempts to find skyrmions in thin films of MnSi [132–134] and FeGe [135] grown using sputtering and molecular beam epitaxy methods. However, while there have been reports of skyrmions

forming in the plane of the film sample [136], it appears that stabilisation of an out-of-plane skyrmion lattice is prevented by strain at the interface of the grown material and the substrate [137]. This causes the chiral modulations to be pinned to the out-of-plane direction to due the induced anisotropies, preventing the formation of a skyrmion lattice under an applied out-of-plane magnetic field [138]. Further research in this area is crucial if bulk skyrmion materials are to be adapted for application in the thin film dominated spintronics industry.

1.3.3 Cu_2OSeO_3

Among the metallic and semiconducting skyrmion-hosting bulk chiral magnets mentioned above, one insulating skyrmion material has been discovered: Cu_2OSeO_3 [139]. This material crystallises in the same $P2_13$ space group as MnSi, and exhibits a magnetic phase diagram that is very similar to the original B20 skyrmion materials. This demonstrates that the skyrmion formation is due to the competition of the same magnetic energy terms [122, 140, 141]. Beyond being an insulator, Cu_2OSeO_3 is also multiferroic [142], meaning that the electric polarisation of the system can be manipulated using a magnetic field, and its magnetisation can be influenced by an applied electric field [143, 144]. Therefore, Cu_2OSeO_3 offers the opportunity to control skyrmions using electric fields [145], for example by rotating the skyrmion lattice [146, 147].

The application of an electric field also changes the stability of the equilibrium skyrmion phase, increasing or decreasing its temperature extent depending on the direction of the applied field [148, 149], allowing for the switching of the skyrmion phase. This has led to the first measurement of the formation energy barrier of the skyrmion state [150]. The control of skyrmions with an electric field, as opposed to an electric current, is exciting from the perspective of applications, as there is no associated energy losses due to Joule heating effects [151].

Such magnetoelectric effects have been observed in the microwave excitation of skyrmions. Theoretical selection rules state that nonreciprocal directional dichroism (NDD) – that is, the effect that oppositely propagating spin waves exhibit different absorption – emerges depending on the alignment of the incoming spin wave with

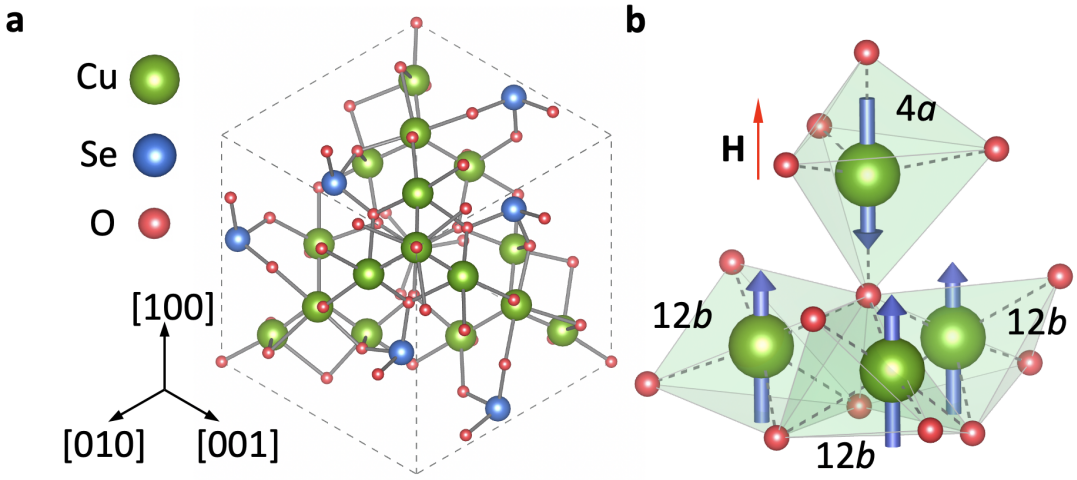

Figure 1.5: **a**, The unit cell crystal structure of Cu_2OSeO_3. **b**, One Cu_4 tetrahedra formed of four ferrimagnetically ordered Cu spins.

respect to the magnetisation $\mathbf{M}$ and electric polarisation $\mathbf{P}$ of the sample. Specifically, if the skyrmion phase in Cu_2OSeO_3 is magnetoelectric, then NDD will emerge if the incoming wavevector, $\mathbf{k}^{\omega}$, is orthogonal to $\mathbf{P} \times \mathbf{M}$, and this was experimentally verified [106].

The chiral crystal structure of Cu_2OSeO_3 is displayed in Fig. 1.5**a**. The underlying magnetic structure is composed of building blocks of Cu_4 tetrahedra formed of four ferrimagnetically ordered Cu spins [152], which act as a single spin triplet [153]. As shown in Fig. 1.5**b**, the three copper spins located on the $12b$ lattice sites, with a local square-pyramidal oxygen environment (termed Cu(II)), align parallel to the applied magnetic field. On the other hand, the single copper spin located on the $4a$ lattice sites (termed Cu(I)), with a local trigonal bipyramidal oxygen arrangement, couples antiferromagnetically [154]. In this thesis, the majority of measurements were performed with Cu_2OSeO_3 single crystal samples.

1.3.4 Further Bulk Skyrmion Materials

A range of more exotic bulk chiral magnets have been observed to host skyrmions beyond the original B20 materials. Recently, antiskyrmions were observed to exist in a Heusler alloy with D_{2d} crystal symmetry [155], stabilised by a negative bulk DMI coefficient. Néel-type skyrmions have been discovered in non-centrosymmetric polar

magnets such as GaV_4S_8 [156] and GaV_4Se_8 [157], which exhibit rhombohedral (C_{3v}) crystal symmetry at low temperatures. Similar to the B20 skyrmion materials, below T_C a spiral magnetisation is formed, but with a cycloidal, as opposed to a spiral, spin structure. Under an applied magnetic field, a hexagonal lattice of Néel-type skyrmions is formed. However, due to anisotropies enforced by the rhombohedral structure, the observed magnetic phase diagram has a strong dependence on the alignment of the magnetic field with respect to the crystalline axes [158, 159].

Recently, motivated by theoretical studies [160], frustrated magnetic system have also been shown to exhibit skyrmions, stabilised by the geometrical frustration of short range interactions on a triangular lattice. This has been observed in systems such as $Co_7Zn_7Mn_6$ [161], Gd_2PdSi_3 [162] and $Gd_3Ru_4Al_{12}$ [163], which all exhibit hexagonal skyrmion lattices at low temperatures. Recently, a square skyrmion lattice was observed in the frustrated magnet $GdRu_2Si_2$ [164], highlighting the rich variety of spin textures achievable in such frustrated systems. The discovery of new materials hosting skyrmions remains an active area of research.

1.4 Chiral Spin Textures

Bulk chiral magnets such as MnSi, FeGe and Cu_2OSeO_3 exhibit a range of chiral spin textures beyond skyrmions, induced by the presence of the bulk DMI energy term [165], see Sec. 2.1. Indeed, such materials were originally dubbed helimagnets due to the incommensurate spiral magnetisation structures they exhibit below T_C [166–169]. Above T_C, the system exhibits a paramagnetic state. However, below T_C, at zero applied magnetic field, the magnetisation consists of a continuous rotation of spins orthogonal to a propagation vector, known as the helical state [170, 171], as shown in Fig. 1.6**a**. Typically, the helical propagation vector aligns such that the spins lie in an easy-plane due to the present cubic anisotropy [172]. In MnSi, the helical vectors point along $\langle 111 \rangle$ crystal axes [173], in Cu_2OSeO_3 along $\langle 100 \rangle$ directions, and in FeGe the directions changes as a function of temperature [174]. Typically, this means that multiple, energetically-degenerate, helical domain orientations may be exhibited in one sample. Upon the application of an applied magnetic field, the spins

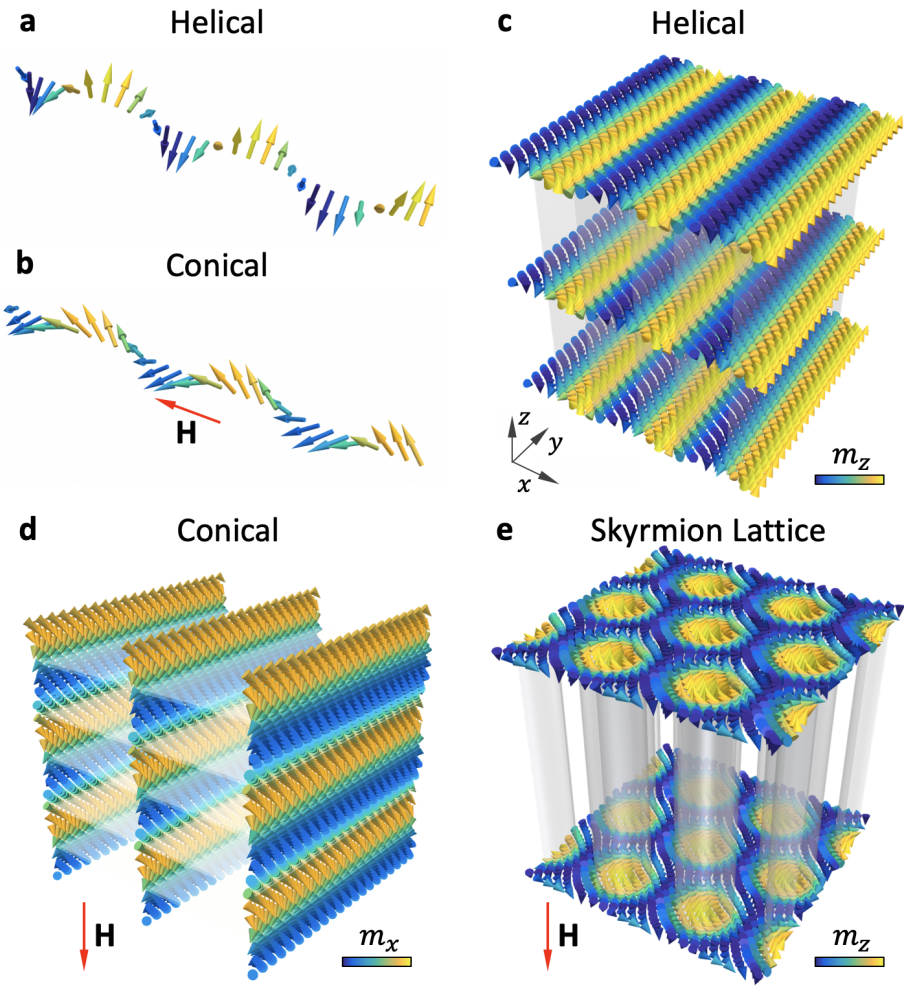

Figure 1.6: **a**,**b**, One dimensional representation of the helical and conical structures respectively. **c**,**d**, Three dimensional visualisation of the helical and conical spin textures. **e**, Three dimensional representation of a hexagonal skyrmion lattice, highlighting the extended vertical structure of the skyrmion tubes.

acquire a canted angle as they tilt to point partially along the applied field direction, as shown in 1.6**b**, forming a structure known as the conical state [175]. If the field is applied along an axis different to the propagation direction of a specific helical domain, the entire magnetic structure will rotate to lie along the field direction. Three dimensional visualisations of the helical and conical states are shown in 1.6**c** and 1.6**d**.

In a limited range of applied magnetic field and temperature just below T_C, bulk chiral magnets exhibit a hexagonal skyrmion lattice, as shown in Fig. 1.6**e** [176], sta-

bilised by thermal fluctuations [177]. This figure also illustrates the extended tube-like magnetic structure in the third dimension - in an idealised system, each layer of spins throughout the system is an exact copy of the two-dimensional skyrmion lattice [178]. In reality, the magnetisation of skyrmion tubes can vary along this vertical dimension. For example, it has been demonstrated that the magnetisation of the skyrmion may twist from Bloch-type to Néel-type as it approaches the surface of the sample [65]. Furthermore, skyrmion strings may form local topological defects where they break into shorter sections, or merge into neighbouring tubes [179, 180].

These local defects typically exhibit a magnetic singularity where the magnetisation direction rotates by 180 degrees over the distance of a single spin, known as a magnetic Bloch point [181]. Due to their divergent magnetisation texture, they have also been called emergent magnetic monopoles [182, 183]. The motion of these Bloch points is thought to be responsible for the formation and destruction of the skyrmion lattice [184], similar to the role it plays in magnetic vortex core reversal dynamics [185]. The Bloch points are thought to form at the break and merge points in skyrmion tubes, and subsequently travel along the length of the skyrmion, acting as a form of topological zipper [186]. Experiments have demonstrated that the unwinding of skyrmion tubes by Bloch point motion can be induced by an applied electric current [187]. Furthermore, stable chiral bobber states have been observed - consisting of short skyrmion tubes at the surface of a lamella of FeGe [188], which terminates at a Bloch point just below the sample boundary [181]. Skyrmion tubes where both ends terminate in Bloch points have been dubbed torons, and have been observed in both magnetic [184] and liquid crystal skyrmion systems [21]. The local nature of these structures necessitates real-space observations able to resolve their nanoscale dynamic behaviours. Current widely-utilised imaging techniques are often unsuitable for such experiments, and therefore there is a strong motivation to develop improved magnetic imaging techniques capable of imaging complex three dimensional spin textures.

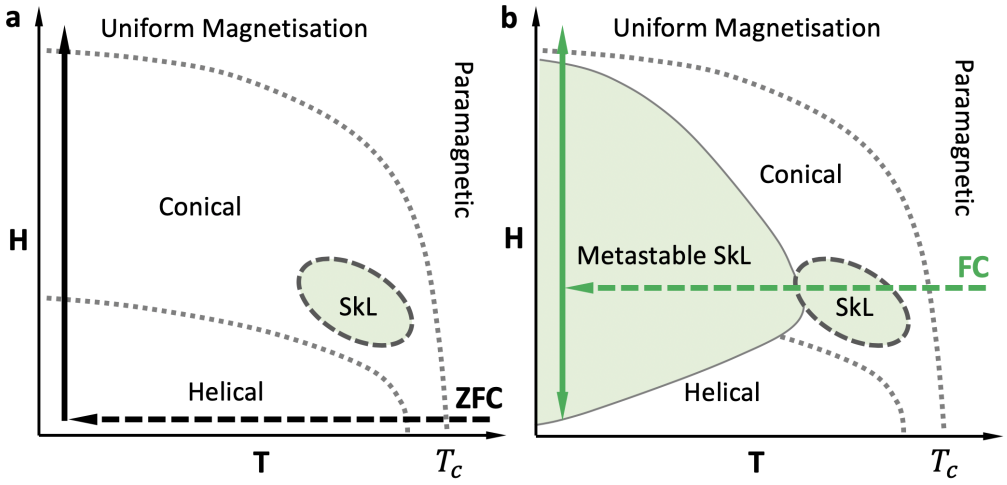

Figure 1.7: **a**, Generic magnetic phase diagrams of a bulk DMI skyrmion material, highlighting the typical equilibrium extent of the skyrmion lattice (SkL), helical and conical phases. **b**, Typical magnetic phase diagram observed when field cooling (FC) the system through the equilibrium skyrmion state, demonstrating the greater temperature and magnetic field extent of the metastable skyrmion phase.

1.5 Metastable Skyrmions

An example, generic skyrmion phase diagram is shown in Fig. 1.7**a**, which illustrates the general features of phase diagrams of MnSi, Cu_2OSeO_3, and other bulk DMI skyrmion materials [189]. The figure highlights the limited field and temperature range of the equilibrium skyrmion phase just below T_C. When considering skyrmion applications, skyrmions are required to exist at room temperature and zero applied magnetic field, ensuring the preservation of any stored data while the skyrmion device is unpowered. The limited extent of the equilibrium skyrmion phase in temperature and applied field therefore presents a significant obstacle which must be overcome.

The discovery of metastable skyrmions presents one avenue to overcoming this obstacle. Metastable skyrmions, which have now been seen in range of materials including MnSi [187, 190, 191], $Fe_{0.5}Co_{0.5}Si$ [179], the Co-Zn-Mn alloys [192–194], and Cu_2OSeO_3 [148, 195], have been observed to exist over a wide range of field and temperature. Typically, such skyrmions are formed by rapidly cooling the sample under an applied magnetic field, such that the system passes through the equilibrium

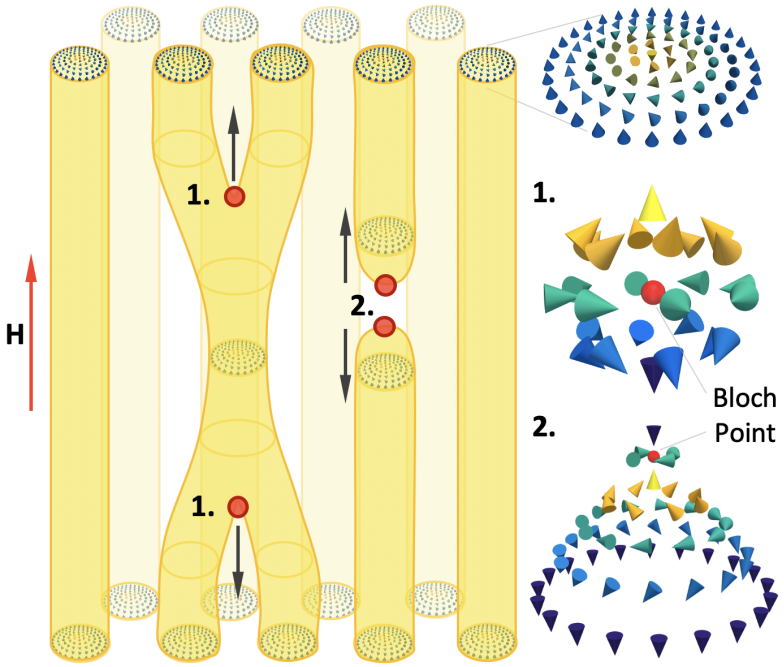

Figure 1.8: Illustration of the vertical, string-like structure of a hexagonal lattice of Bloch skyrmions. Two scenarios for the Bloch point unwinding mechanism are displayed for skyrmions decaying to the helical state (1) and to the conical state (2).

skyrmion phase [123], as shown in 1.7**b**. By field cooling (FC) at a sufficient cooling rate, a population of skyrmions will survive in a metastable state.

By definition, metastable states represent a local energy minimum in the system, separated from the ground state by some energy barrier ΔE [196]. Thermally activated processes can overcome this energy barrier, resulting in the system decaying from the metastable state to the ground state [197]. This gives rise to a finite, temperature dependent lifetime characterising the decay process. While this inherent instability may seem problematic when considering the applications of metastable systems, the lifetime of such states can be extremely long. For example, diamond is a metastable form of carbon, which will decay to graphite over time. However, the lifetime of diamond is so long under normal conditions, that the decay process has only recently been observed in real-time [198].

In a similar way, metastable skyrmions exhibit a finite, temperature dependent lifetime. At temperatures sufficiently low enough compared to T_{C}, the lifetime may be long enough to be useful for applications [190, 199, 200]. Therefore, in a material

with a high T_C such as $Co_9Zn_9Mn_2$, a metastable skyrmion lattice state may be formed at zero applied magnetic field, and at room temperature, with a lifetime over one thousand years [193]. Beyond the technological implications of metastable skyrmions, their formation also allows the fundamental behaviour of skyrmions to be studied over a wider range of experimental conditions. For example, one can investigate interactions between skyrmions and helical and conical states, and other skyrmions [201]. Such interactions between metastable skyrmions at low temperature can result in their deformation [194], or their reordering from a hexagonal to a square lattice arrangement [191, 192].

Metastable skyrmion decay dynamics are governed by the Bloch point decay mechanics mentioned in the previous section. When transitioning to the helical state, such Bloch points are thought to zip together neighbouring skyrmion tubes [179], as depicted by scenario 1 in Fig. 1.8. On the other hand, when transitioning to the conical state, it has been suggested that skyrmion tubes unwind via the motion of Bloch points formed at the end of each individual tube [187, 188], as illustrated by scenario 2 in Fig. 1.8. The motion of these Bloch points is expected to be strongly pinned by local defects and disorder in the underlying crystal lattice [179, 202]. This speculation is based on observation of a longer metastable skyrmion lifetime in the disordered $Co_9Zn_9Mn_2$ and $Fe_{0.5}Co_{0.5}Si$ when compared to the relatively ordered MnSi [191]. Therefore, there is a strong motivation for investigating skyrmion lifetimes in disordered materials, with the aim of engineering materials to optimise the metastable skyrmion lifetime for future applications.

1.6 Doping Skyrmion Materials

The properties of spin textures in bulk chiral magnets are governed by the interplay of a range of magnetic energy terms. One way to manipulate these energy terms, and therefore the properties of the resulting, is by varying the elemental composition of the underlying materials via chemical substitution or doping. Substitution effects have been studied in a range systems, such as $Fe_{1-x}Co_xSi$ [203–205], $Mn_{1-x}(Fe/Co)_xSi$ [206–209], $Mn_{1-x}Fe_xGe$ [210–213], $MnSi_{1-x}Ge_x$ [214],

$Co_{10-x}Zn_{10-y}Mn_{x+y}$ [130, 131, 193], $Co_{8-x}(Fe/Ni/Ru)_xZn_8Mn_4$ [215], the polar magnet $GaV_4(S_{8-x}Se_x)$ [158, 159], and the insulators $[Cu_{1-x}(Zn/Ni)_x]_2OSeO_3$ [150, 216–220] and $Cu_2OSe_{1-x}Te_xO_3$ [216, 221]. The properties altered include: variation of T_C, indicating a change in the exchange interaction strength; alteration of the magnitude and sign of the DMI, leading to changes in the helical and skyrmion lattice periodicity and chirality; switching of the magnetic easy-axes, and therefore the helical ground state domain orientation, by tuning of the cubic anisotropy constants; and modification of the spin wave propagation. In this work, we will specifically investigate the effects of zinc doping in $(Cu_{1-x}Zn_x)_2OSeO_3$, studying the resulting dynamics of metastable skyrmions, and the competing helical and conical states.

Chapter 2

Theory

2.1 Competing Magnetic Interactions

The magnetic moment exhibited by atoms and ions is the result of the angular momentum of their orbiting electrons. The angular momentum of the electron $\mathbf{l}$ (expressed here unitless) can be thought to generate a circular current as it orbits the nucleus, producing a magnetic dipole moment of $\mu_{\mathbf{l}} = \mu_{\mathrm{B}}\mathbf{l}$, where $\mu_{\mathrm{B}} = \hbar e/2m_{\mathrm{e}}$ is the Bohr magneton. Similarly, the spin of the electron $\mathbf{s}$ generates a magnetic dipole moment of $\mu_{\mathbf{s}} = -g\mu_{\mathrm{B}}\mathbf{s}$, where $g = 2.0023$ is the relativistic gyromagnetic ratio of the electron. These spin and orbital components are coupled by spin-orbit coupling.

The addition of quantum mechanical angular momentum for a free magnetic ion or atom is described [222],

$$\mathbf{J} = \mathbf{L} + \mathbf{S} = \sum_i \mathbf{l}_i + \sum_i \mathbf{s}_i, \tag{2.1.1}$$

where $\mathbf{J}$ is the total angular momentum, and all quantum numbers J, L and S can take integer or half-integer values. In full shells, all available states are filled, such that $J = S = L = 0$. Therefore only atoms or ions with partially filled shells can exhibit a non-zero J. Hund's rules empirically describe how the available states in a partially filled shell are occupied, taking into consideration the electrostatic repulsion, the Pauli exclusion principle and the spin-orbit coupling [222]: 1. Maximise

S. 2. Maximise L. 3. For shells less than half full, minimise J, and for shells more than half full, maximise J.

However, these rules are only general guidelines, and can be overcome by additional effects. For example, magnetic ions in a material cannot be considered free as they interact with neighbouring ions via electrostatic forces. These so-called crystal fields break the rotational symmetry of the atomic orbitals. In cases where this symmetry breaking lifts the degeneracy of the energy levels of these orbitals, this leads to quenching, such that the average contribution to the magnetic moment from $\mathbf{L}$ vanishes, and therefore $\mathbf{J} = \mathbf{S}$. This effect is seen for many of the transition metals with a partially filled $3d$ shell, and will be assumed for the following derivations.

The energy contributions of these interactions can be described by Hamiltonians. The interaction of the magnetic moments $\boldsymbol{\mu}$ with an external field $\mathbf{B}$, is described by the Zeeman Hamiltonian,

$$H_{\text{zee}} = -\boldsymbol{\mu} \cdot \mathbf{B} = -g\mu_{\text{B}} S_z B, \tag{2.1.2}$$

where S_z is defined as the spin component along the magnetic field direction.

The combination of electrostatic forces and the Pauli exclusion principle results in the exchange interaction. This effect can manifest in a number of ways, but there are two common examples. Direct exchange occurs when, due to the Pauli exclusion principle, the overlap of the electronic orbitals of the two ions ensures the separation of electrons with the same spin direction. The electrostatic energy is therefore lowered by parallel spins. Indirect exchange occurs when the two magnetic ions are linked by a neighbouring non-magnetic ion. If the electron spins are opposite, they are able to transfer between the two magnetic ions via the linking ion. This transfer lowers the kinetic energy due to the Heisenberg uncertainty principle. However, if the spins are parallel, the Pauli exclusion principle will prohibit the effect. Thus, this typically leads to antiparallel spin alignment being energetically favoured. Such interactions between two spins $\mathbf{S}_i, \mathbf{S}_j$ are described by the exchange Hamiltonian,

$$H_{\text{ex}} = J_{\text{ex}} \mathbf{S}_i \cdot \mathbf{S}_j, \tag{2.1.3}$$

where J_{ex} is the exchange constant. This interaction is short range, and therefore typically it is only necessary to consider nearest and next-nearest neighbouring spins.

2.2 Spin Textures

The chiral spin textures described in Sec. 1.4 arise from a complex energy landscape formed by the delicate balance of these magnetic energy terms. Incommensurate magnetic ordering such as the skyrmion, helical and conical states are stabilised by the interplay of the DMI with the exchange interactions, the Zeeman energy, and the magneto-crystalline anisotropies [111]. This energy balance can be effectively modelled using a classical continuum model [177],

$$H = \int d\mathbf{r} \left[\frac{J_{\text{ex}}}{2} [\nabla \mathbf{n}(\mathbf{r})]^2 + D\mathbf{n}(\mathbf{r}) \cdot [\nabla \times \mathbf{n}(\mathbf{r})] - \mathbf{B} \cdot \mathbf{n}(\mathbf{r}) + K_E \right]. \tag{2.2.4}$$

Here, instead of considering individual spins, $\mathbf{n}(\mathbf{r})$ represents the local spin texture. The first term, J_{ex}, is the exchange energy, which seeks to align neighbouring spins. The second term, D is the DMI strength, also known as the antisymmetric exchange interaction, is at a minimum when neighbouring spins align perpendicular to one another. Therefore, the competition and balance between these two terms induces the winding magnetic structure found in helimagnets, and as a result, determines the spin-helix length, $\lambda = 2\pi J_{\text{ex}}/D$ [3]. With increasing applied magnetic field, the third term, which represents the Zeeman term, seeks to align the spins with the applied magnetic field. Above a certain threshold field, it begins to dominate, causing the formation of the conical state, and at high enough fields, the uniformly magnetised state.

Finally, the anisotropy terms, K_{E} are responsible for the formation of hard and easy magnetic axes. This arises due to spin-orbit coupling: it is energetically favourable for the orbit of the electron to follow the spin orientation, but it is strongly coupled to the lattice. The anisotropy is simply the energy required to overcome this spin-orbit coupling [223]. Such spin-orbit coupling interactions are typically temperature dependent [224], becoming increasingly weak as the system approaches T_{C}. Additional contributions can be considered, such as shape anisotropy induced

by the demagnetising field formed as a result of the shape of the sample [225].

For cubic systems, such as the B20 skyrmion materials, the lowest order terms of the anisotropic energy density E/V take the form [223],

$$\frac{E}{V} = K_0 + K_1(\alpha^2\beta^2 + \beta^2\gamma^2 + \gamma^2\alpha^2) + K_2\alpha^2\beta^2\gamma^2 + \mathcal{O}^4, \tag{2.2.5}$$

where K_0, K_1 and K_2 are anisotropy parameters, α, β and γ are the directional cosines, and $\mathcal{O}^4$ denotes higher order terms. Due to time reversal symmetry, only even order terms are allowed. The relative magnitudes and signs of K_1 and K_2 are responsible to determining the easy axes of the magnetic system. When the second term can be neglected, the easy axes will be along $\langle 100 \rangle$ directions if $K_1 > 0$ or $\langle 111 \rangle$ directions if $K_1 < 0$. Inclusion of the second term allows the easy axes to lie along $\langle 110 \rangle$ directions [223]. Therefore, the balance of these anisotropy constants is responsible for the alignment of the helical ground state in B20 systems to specific crystalline axes, with the helical propagation direction lying along $\langle 111 \rangle$ in MnSi, and along $\langle 100 \rangle$ in Cu_2OSeO_3.

Recently, the role of cubic anisotropy in stabilising new spin textures has been highlighted in a number of studies. By utilising the wide temperature and applied field range of the metastable skyrmion phase, a transition from the typical hexagonal arrangement to a square skyrmion lattice has been observed in both MnSi [191], and $Co_8Zn_8Mn_4$ [192], induced by the increased effective anisotropy strength at low temperatures. Meanwhile, in Cu_2OSeO_3, the strong spin-orbit coupling results in a comparatively large, temperature-dependent cubic anisotropy [225]. At low temperatures, this anisotropy is of sufficient strength to rotate the conical state away from the applied magnetic field direction, forming the tilted conical state [226], and is further responsible for the stabilisation of the equilibrium low temperature skyrmion state over much of the temperature-field phase diagram [195, 227]. These observations can only be explained by considering the five fourth-order terms in the spin orbit coupling allowed in systems with $P2_13$ symmetry [226], denoted $\mathcal{O}^4$ in Eq. 2.2.5.

2.3 Topology of a Skyrmion

This subsection is largely adapted from the section on skyrmion topology in the excellent review article by N. Nagaosa and Y. Tokura [3]. The local spin texture $\mathbf{n}(\mathbf{r})$ of a single skyrmion can be visualised as winding around a unit sphere, pointing in all directions, as originally envisaged by Skyrme in his 3D skyrmions. The number of times $\mathbf{n}(\mathbf{r})$ winds around the sphere can be calculated by integrating over the solid angle,

$$N_{\mathrm{sk}} = \frac{1}{4\pi} \iint_S \mathbf{n} \cdot \left(\frac{\partial \mathbf{n}}{\partial x} \times \frac{\partial \mathbf{n}}{\partial x} \right) \mathrm{d}^2\mathbf{r}. \tag{2.3.6}$$

This topologically invariant quantity is known as the topological charge, topological index, or skyrmion number. By considering its circular symmetry, the local magnetisation $\mathbf{n}(\mathbf{r})$ of a skyrmion can be mapped with polar coordinates, $\mathbf{r} = (r\cos\psi, r\sin\psi)$,

$$\mathbf{n}(\mathbf{r}) = \begin{pmatrix} \cos\Theta(\psi)\sin\Phi(r) \\ \sin\Theta(\psi)\sin\Phi(r) \\ \cos\Phi(r) \end{pmatrix}. \tag{2.3.7}$$

Inserting this expression into Eq. 2.3.6, the skyrmion number can be evaluated,

$$N_{\mathrm{sk}} = \frac{1}{4\pi} \int_0^{\infty} \mathrm{d}r \int_0^{2\pi} \mathrm{d}\psi \frac{\partial\Theta(r)}{\partial r} \frac{\partial\Phi(\psi)}{\partial\psi} \sin\Theta(r), \tag{2.3.8}$$

$$N_{\mathrm{sk}} = [\cos\Theta(r)]_{r=0}^{r=\infty} [\Phi(\psi)]_{\psi=0}^{\psi=2\pi}. \tag{2.3.9}$$

Here, the topological number is determined by both the out-of-plane (Θ) and in-plane (Φ) magnetisation. Considering that far from the skyrmion, $r \to \infty$, the magnetisation points up, while at the centre of the skyrmion, at $r = 0$, it points down, then $[\cos\Theta(r)]_{r=0}^{r=\infty} = 2$. Evaluating $\Phi(\psi)$ requires the introduction of two important integers: the vorticity m and helicity γ of the skyrmion. The vorticity concerns the in-plane magnetisation component, $m = [\Phi(\psi)]_{\psi=0}^{\psi=2\pi}$. The helicity is the phase difference which appears in the expression for $\Phi(\psi)$, and essentially models

the chirality of the skyrmion spin texture.

$$\Phi(\psi) = m\psi + \gamma. \tag{2.3.10}$$

Chirality of skyrmions can be detected experimentally [228, 229]. Utilising these topological quantities, Eq. 2.3.7 can be rewritten in terms of m and γ,

$$\mathbf{n}(\mathbf{r}) = \begin{pmatrix} \sin(m\psi + \gamma)\cos\Phi(r) \\ \sin(m\psi + \gamma)\sin\Phi(r) \\ \cos\Phi(r) \end{pmatrix}. \tag{2.3.11}$$

Each combination of m and γ, and each value of the topological charge N_{sk} gives rise to a different skyrmion configuration, as shown in Figure 2.1, allowing representation of Néel and Bloch skyrmions, and antiskyrmions, with different chiralities.

In topology, structures of the same topological number can be continuously deformed into one another. However, structures with different topological indices require a discontinuity to facilitate the transition between the two states. A common analogy is to consider a coffee mug, with a handle, and a doughnut. These two objects can be shaped into one another with a continuous transformation, as they have the same topological index of 1: they each have a single hole. On the other hand, when trying to transform a solid sphere, which has an index of zero, into a doughnut, a discontinuous deformation must be made at the point where the hole is pierced.

Due to their knot-like arrangement, we have seen that magnetic skyrmions have a topological charge, or skyrmion number, of $N_{\mathrm{sk}} = 1$. For topologically trivial magnetic arrangements, such as uniform magnetisation, and even non-collinear spin textures such as the helical and conical structures, the skyrmion number is $N_{\mathrm{sk}} = 0$. The topological stability of the skyrmion lattice can therefore be explained analogously to the sphere and doughnut: there is a topological energy barrier separating the skyrmion spin texture from the competing helical and conical structures because of the discontinuous deformation required to unravel it.

In the case of two dimensional skyrmions, as they are formed in most magnetic systems, their topological charge is defined only in the x-y plane. The topological

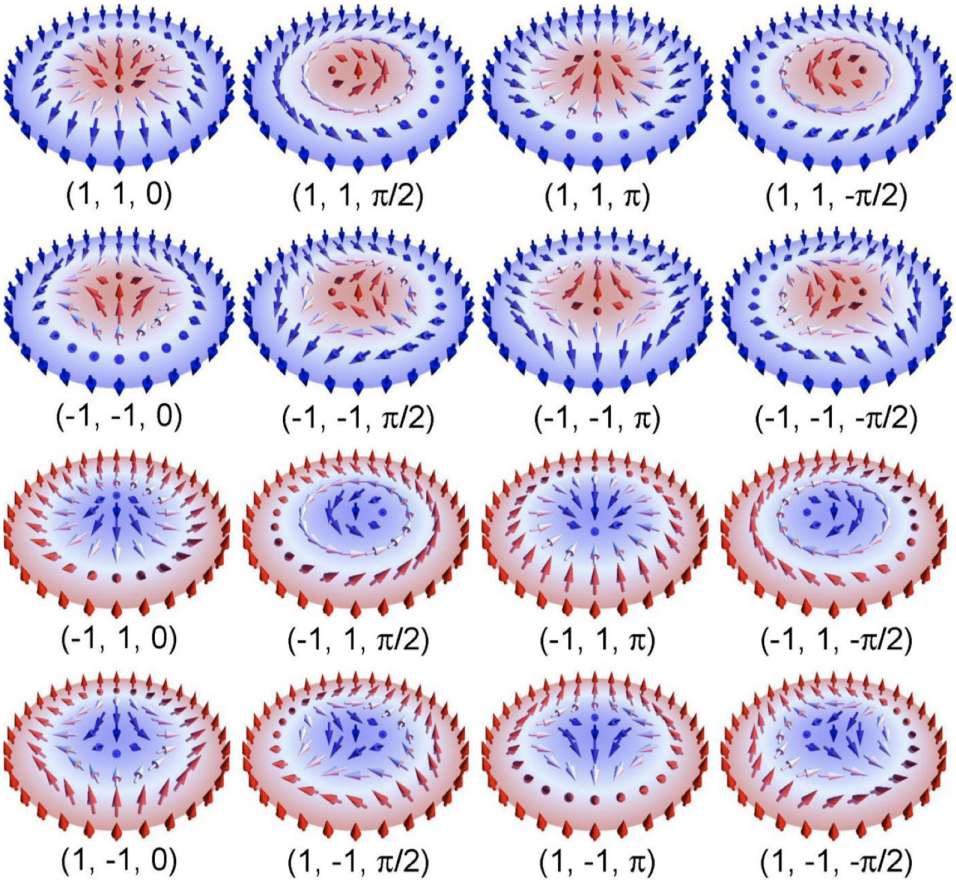

Figure 2.1: Visualisations of the skyrmion spin textures described by the topological charge, voticity number and helicity number: $(N_{\mathrm{sk}}, m, \gamma)$, as shown in Eg. 2.3.11. Adapted from [111].

protection may be broken in the presence of discontinuities in the magnetisation - for example, this allows skyrmions to be destroyed for little energy at the boundary of a magnetic sample. Furthermore, when considering a three dimensional skyrmion tube, each individual layer of skyrmions may have a high topological energy barrier. However, this topological protection is not afforded to the z direction of a skyrmion tube, which does not exhibit a topologically invariant winding [230]. In Sec. 1.5, topological defects known as Bloch points were introduced, which are thought to mediate the annihilation and formation of skyrmions along the vertical direction. In this way, the motion of such Bloch points is a form of magnetic zipper, acting as a source or sink of topological charge as it moves along this vertical axis of the skyrmion tube [179, 187].

2.4 Scattering Theory

Diffraction can be described by the formulation introduced by von Laue which considers the interference of scattered spherical waves, and yields an expression for the diffraction condition. Where $\mathbf{k}$ and $\mathbf{k}'$ are the wavevectors the incident and scattered waves, and $\mathbf{T}$ represents the set of lattice translations, the diffraction condition can be expressed as,

$$e^{2\pi i(\mathbf{k}-\mathbf{k}')\cdot\mathbf{T}} = 1. \tag{2.4.12}$$

Utilising this expression, one can explain the diffraction of both x-rays and neutrons from ordered atomic and spin structures. Intuitive understanding of this effect can be gleaned from Bragg's law, which describes the conditions required for waves with wavelength λ to constructively interfere at a scattering angle θ when scattered from lattice planes with spacing d: $n\lambda = 2d\sin(\theta)$. This results in the formation of Bragg peaks corresponding to each set of lattice planes, denoted by three Miller indices (h, k, l). However, this model does not account for the different intensities of the Bragg peaks - this requires description of diffraction using structure factors.

Assuming elastic scattering, for a unit cell with j atoms, the scattering amplitude at a scattering vector $A(\mathbf{q})$, where $\mathbf{q} = \mathbf{k} - \mathbf{k}'$ is the scattering vector, can be written as

$$A(\mathbf{q}) \propto \sum_j f(\mathbf{q}) e^{2\pi i \mathbf{q}\cdot\mathbf{r}_j} \sum_{\mathbf{T}} e^{2\pi i \mathbf{q}\cdot\mathbf{T}} = F(\mathbf{q})L(\mathbf{q}). \tag{2.4.13}$$

Here, $F(\mathbf{q})$ is known as the structure factor, which is dependent on the atomic species and their position within the unit cell, and $L(\mathbf{q})$ is the form factor, which considers only the form of the crystal lattice. The intensity of any Bragg peak is determined as the square of this scattering amplitude $I(\mathbf{q}) = |A(\mathbf{q})|^2$.

The scattering factor of each atom, f_j, found in this equation is an important quantity, and varies depending on the properties of the scattered particle and the atomic species. For example, in x-ray scattering f_j increases with atomic number, and resonant effects can enhance its value close to the electronic absorption

energies of the atom. On the other hand, in neutron scattering, the equivalent scattering length b_j, can be positive or negative, and does not show any relationship with atomic number. Furthermore, when considering scattering from magnetic structures, additional corrections to f_j are required, and the picture becomes more complicated [231]. In the following subsections, a brief description of magnetic x-ray and magnetic neutron scattering will be outlined.

2.4.1 X-Ray Scattering

This section is based upon a derivation by Hill and McMorrow [232]. X-rays scatter from the electrons surrounding each atomic nucleus. The total coherent elastic scattering amplitude for x-ray scattering from a magnetic ion can be written [233],

$$f = f_0 + f' + if'' + f_{\mathrm{m}}. \tag{2.4.14}$$

Here, f_0 is the Thomson charge scattering amplitude, and is given by the Fourier transform of the electron density $\rho(\mathbf{r})$,

$$f_0 = \int \rho(\mathbf{r}) \mathrm{e}^{2\pi i \mathbf{q}\cdot\mathbf{r}} dV. \tag{2.4.15}$$

The anomalous scattering coefficients f' and f'' contributions are wavelength dependent. Far from resonance, their contributions vary slowly with wavelength, and contribute terms proportional to the orbital and spin angular momentum [232]. However, close to the K and L absorption edges of the atom in question, where the energy of the x-ray is sufficient to excite an inner shell electron, they become significant, and account for the x-ray absorption observed close to a resonant edge [234]. This is known as resonant x-ray scattering. A theoretical treatment to explain their relativistic origin is given by Cromer and Liberman [235].

Similar to the charge scattering contributions outlined above, the magnetic scattering amplitude, f_{m} exhibits both non-resonant $f_{\mathrm{m}}^{\mathrm{NR}}$ and resonant $f_{\mathrm{m}}^{\mathrm{R}}$ contributions. In 1985, Blume theoretically calculated the non-resonant contribution of the magnetic scattering, and found it to be smaller than the charge component f_0 by a factor of $\hbar\omega/mc^2$ [236]. This results in a non-resonant magnetic scattering intensity

which is approximately 10^6 smaller than the charge scattering intensity [231]. Despite the small intensities, the advent of synchrotron x-ray sources allowed for initial investigations into such non-resonant magnetic scattering [237].

However, while $f_{\mathrm{m}}^{\mathrm{NR}}$ is typically small, it was found that at resonant absorption edges, $f_{\mathrm{m}}^{\mathrm{R}}$ can result in a significant intensity contribution. Such resonant enhancement of the magnetic scattering can be derived by considering an electric dipole transition at, for example, the L_3 absorption edge, which corresponds to a $2p_{3/2} \rightarrow 3d_{1/2}$ atomic transition. The formulation requires the introduction of the polarisation vectors of the incident and scattered x-ray beam, $\hat{\epsilon}$ and $\hat{\epsilon}'$ respectively, which point in the direction of the electric field component of the photon wave [238]. Considering the vector spherical harmonics, one can derive the expression,

$$f_{\mathrm{m}}^{\mathrm{R}} = (\hat{\epsilon}' \cdot \hat{\epsilon})F^{(0)} - i(\hat{\epsilon}' \times \hat{\epsilon} \cdot \hat{\mathbf{m}})F^{(1)} + (\hat{\epsilon}' \cdot \hat{\mathbf{m}})(\hat{\epsilon} \cdot \hat{\mathbf{m}})F^{(2)}. \tag{2.4.16}$$

Here, $\hat{\mathbf{m}}$ is the unit vector representing the direction of the moment of the magnetic ion. The factors $F^{(0)}$, $F^{(1)}$, $F^{(2)}$ are determined by the specific properties of the magnetic ion in question, governed by the overlap of the intergrals between the ground and excited state of the resonantly excited transition [239]. This effect gives rise to significant magnetic scattering, and allows for the observation of magnetic scattering from even small magnetic moments.

The first term of Eq. 2.4.16 does not depend on the magnetic moment, and therefore simply contributes to the charge Bragg peak. However, in incommensurate structures such as a helical domain or a skyrmion lattice, the second and third terms respectively give rise to the first- and second-order magnetic peaks which decorate each charge Bragg peak. In later experiments shown in Ch. 7, we make use of transmission small angle x-ray scattering to observe such magnetic satellites around the transmitted direct x-ray beam. An example figure illustrating this effect from a different published paper is shown in 2.2, which displays the energy dependent intensity of the transmitted direct beam and a magnetic satellite measured for such a scattering experiment with a lamella of Cu_2OSeO_3 [240]. It is clear that around the L_3 and L_2 Cu absorption edges, the transmitted intensity of the main beam

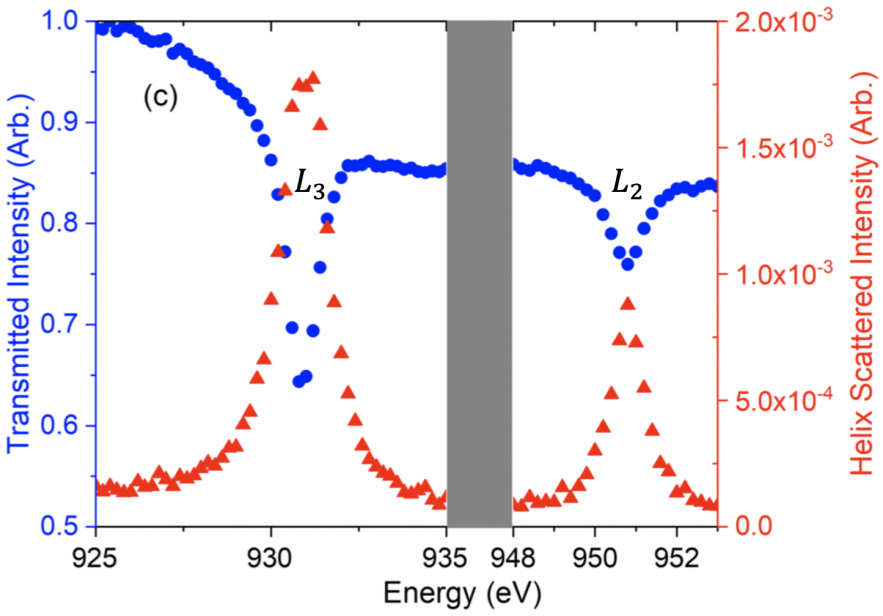

Figure 2.2: Energy scan of x-ray transmission (blue) and magnetic satellite intensity (red) for a 200-nm-thick Cu_2OSeO_3 lamella at 20 K and zero applied magnetic field. Adapted from [240].

(blue) decreases, highlighting the absorption effect at the resonant edges. However, around the same energy ranges, ∼931 and ∼951 eV, the measured intensity of the helical magnetic satellites is dramatically increased, demonstrating the clear resonant enhancement of the magnetic scattering contribution.

From this point, due to the introduction of the polarisation vectors, it is possible to derive the scattering contributions for different polarisation channels [241]. This effect can be experimentally measured using a linearly polarised incident x-ray beam, and measuring the intensity of the outgoing x-ray beam in different polarisation channels. For example, typically, the components of an x-ray beam with components polarised either parallel or perpendicular to the scattering vector are denoted as the π and σ channels. The first term in Eq. 2.4.16 only contributes terms where the polarisation is unchanged, often denoted $\pi \rightarrow \pi$ or $\sigma \rightarrow \sigma$ scattering. However, the second term allows $\sigma \rightarrow \pi$, $\pi \rightarrow \sigma$ and $\pi \rightarrow \pi$ scattering, but not $\sigma \rightarrow \sigma$ scattering [242]. Using this formulation, it is possible to probe and distinguish the in-plane and out-of-plane components of a magnetic spin texture by examining the intensity of a magnetic satellite in the different polarisation channels of the linearly

polarised light [232].

2.4.2 X-ray Magnetic Circular Dichroism

By generalisation of the electric dipole transition in Eq. 2.4.16, it is possible to derive similar equations considering circularly polarised light [243]. The detailed derivation is beyond the scope of this section (a relatively concise derivation of the relevant transition selection rules is given by Altarelli [244]), but the key result from such a treatment is the effect known as x-ray circular dichroism (XMCD) [245]. Specifically, the transmission of right and left circularly polarised light through a magnetised sample is found to exhibit different absorption close to the resonant edge of the magnetic atom, resulting from the broken time-reversal symmetry in the presence of a magnetic field [246].

The XMCD effect can be described simply as a two step process (following the comprehensive XMCD review by van der Laan and Figueroa [246]), using a $3d$ transition metal as an example. In such a system, the $2p$ core electron level is split into a $j = 3/2$ (corresponding to the L_3 edge) and $j = 1/2$ level (corresponding to the L_2 edge). In these two energy levels, the spin and orbital momentum are respectively coupled parallel and antiparallel. The emission of a photon with circular polarisation either parallel or antiparallel to the $2p$ orbital moment results in the preferential excitation of an electron to the $3d$ band with either spin up or spin down respectively. This excited electron must find a space in the unoccupied band. If there are less spin up holes available, the resulting XMCD contribution to the absorption spectrum will be positive at the L_3 edge, and negative at the L_2 edge. Such a technique is therefore sensitive to the component of the magnetisation which is parallel to the x-ray beam [247]. The XMCD contributions can be reversed by either changing the circular polarisation of the incoming x-ray beam, or by reversing the out-of-plane direction of the magnetisation.

An example XMCD spectrum measured on an FeGe lamella is shown in Fig. 2.3. A large magnetic field was applied to the sample to achieve a uniform out-of-plane magnetisation, and intensity of the transmitted x-ray beam was measured for right and left circularly polarised light. The subtraction of these two energy spectra

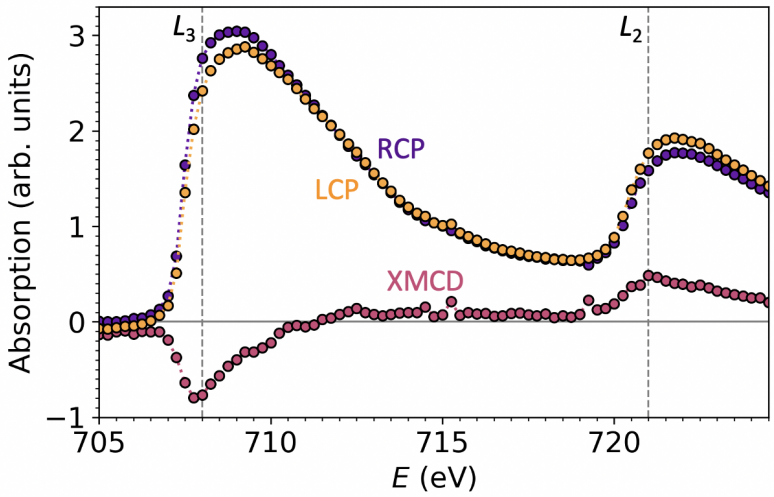

Figure 2.3: Absorption spectrum of the Fe L_3 and L_2 edges, measured for both left (LCP) and right (RCP) circularly polarised x-rays. The difference is the XMCD spectrum, displayed multiplied by two.

gives the XMCD spectra, demonstrating the contributions measured around the L_3 and L_2 absorption edges of Fe. Note that due to the large thickness of our lamella sample, the XMCD effect is not as pronounced as it would be in an ideal experiment. Detailed measurements of x-ray absorption spectra can allow for the orbital and spin contributions of magnetic moments to be determined [248], and has since found application in a range of systems, from biology to physics [246]. For our purposes, XMCD can be exploited to achieve real-space imaging with a resolution of ∼20 nm, in a technique known as scanning transmission x-ray microscopy. As will be explained in Sec. 3.5.4, by focusing the circularly polarised x-ray beam to a small point, the local out-of-plane component of the magnetisation can be measured, allowing a nanoscale image of a magnetic structure, such as a skyrmion lattice, to be acquired pixel by pixel.

2.4.3 Neutron Scattering

Unlike x-ray diffraction, where the x-rays interact with the electrons, in neutron diffraction the neutrons scatter elastically from the nucleus of each atom. Due to the fact that neutrons possess a magnetic moment, they also interact directly

with the magnetic field of unpaired electrons from the magnetic atoms. Neutron scattering intensity from magnetic materials is therefore a superposition of both the nuclear and magnetic scattering. The following derivations are largely based on the textbook by Marshall and Lovesey [249].

We can define a neutron flux Φ as the number of neutrons n passing through a surface area per second (typical units $n/\mathrm{cm}^2\mathrm{s}$). From here, the total neutron scattering cross section defines a system's ability to scatter neutrons, $\sigma_{\mathrm{tot}} = 1/\Phi$, and has units of area. However, such scattering will have an angular dependence, and therefore the differential scattering cross-section must be defined,

$$\frac{d\sigma}{d\Omega} = \frac{C}{\eta\Phi\Delta\Omega}, \tag{2.4.17}$$

where C is the count rate measured by a detector with an area $\Delta\Omega$, with an efficiency η. While this expression is suitable for elastic scattering, the double differential scattering cross-section is required for inelastic processes with final energy E_f,

$$\frac{d^2\sigma}{d\Omega dE_f} = \frac{C}{\eta\Phi\Delta\Omega\Delta E_f}. \tag{2.4.18}$$

The total cross-section is related to both differential cross-sections via integration,

$$\sigma_{\mathrm{tot}} = \int \frac{d\sigma}{d\Omega} d\Omega = \iint \frac{d^2\sigma}{d\Omega dE_f} d\Omega dE_f = \frac{C}{\eta\Phi}, \tag{2.4.19}$$

The scattering from nuclei can be described from the point of view of quantum mechanics, where $|\psi_i\rangle = Y^{-1/2}\mathrm{e}^{\mathrm{i}\mathbf{k}_i\cdot\mathbf{r}}$ and $|\psi_f\rangle = Y^{-1/2}\mathrm{e}^{\mathrm{i}\mathbf{k}_f\cdot\mathbf{r}}$ are the wavefunctions describing the initial incident and final scattered state of the neutron as complex plane-waves. The value Y can be thought of as the normalisation volume for the state, assumed to be a large cubic box with length L. Where the velocity of the incoming neutron with mass m_n is $v = \hbar k_0/m_n$, we can define the incoming neutron flux from the wavefunction,

$$\Phi = |\psi_0|^2 v = \frac{\hbar k_0}{Y m_n}. \tag{2.4.20}$$

The energy density of the final scattered states for neutrons scattered into $\Delta\Omega$ can be defined

$$\rho_1(E_f) = \frac{Y}{8\pi^3}\frac{m_n k_f}{\hbar^2}\Delta\Omega. \tag{2.4.21}$$

Considering the scattering as the interaction of a neutron with a potential described by an operator $\hat{V}$, the process can be described by Fermi's golden rule,

$$W_{i\to f} = \frac{2\pi}{\hbar}|\langle\psi_i|\hat{V}|\psi_f\rangle|^2\rho_1(E_f), \tag{2.4.22}$$

where $W_{i\to f}$ is the transition rate from the initial to final state. Using the expression for the density of states in Eq. 2.4.21, and considering neutrons scattered only into the area $\Delta\Omega$, we find

$$W_{i\to f,\Delta\Omega} = \frac{Y k_f m_n}{4\pi^2\hbar^3}|\langle\psi_i|\hat{V}|\psi_f\rangle|^2. \tag{2.4.23}$$

Utilising the expression for neutron flux in 2.4.20, an expression for the differential scattering cross-section can be found,

$$\frac{d\sigma}{d\Omega} = \frac{1}{\Phi}\frac{W_{i\to f,\Delta\Omega}}{\Delta\Omega}, \tag{2.4.24}$$

$$\frac{d\sigma}{d\Omega} = Y^2\frac{k_f}{k_i}\left(\frac{m_n}{2\pi\hbar}\right)^2|\langle\psi_i|\hat{V}|\psi_f\rangle|^2. \tag{2.4.25}$$

Because the renormalisation volume Y will vanish due to the factor Y^{-1} in $|\psi_i\rangle$ and $|\psi_f\rangle$, and because for inelastic scattering $k_i = k_f$, these terms can be neglected.

Due to the short range nuclear forces responsible for the interaction potential of an individual nucleus j, it can be described by a Dirac delta function,

$$\hat{V}_j(\mathbf{r}) = \frac{2\pi\hbar^2}{m_n}b_j\delta(\mathbf{r}-\mathbf{r}_j). \tag{2.4.26}$$

This potential is known as the Fermi psuedopotential, featuring the neutron scattering length b_j introduced in Sec. 2.4.

The scattering cross-section of the individual nucleus can now be calculated from the matrix element,

$$\langle\psi_i|\hat{V}|\psi_f\rangle = \frac{2\pi\hbar^2}{m_n}b_j\int \mathrm{e}^{\mathrm{i}\mathbf{k}_f\cdot\mathbf{r}}\delta(\mathbf{r}-\mathbf{r}_j)\mathrm{e}^{\mathrm{i}\mathbf{k}_i\cdot\mathbf{r}}d^3\mathbf{r}. \tag{2.4.27}$$

By utilising the definition of the scattering vector for inelastic scattering $\mathbf{q} = \mathbf{k}_i - \mathbf{k}_f$, we come to

$$\langle \psi_i | \hat{V} | \psi_f \rangle = \frac{2\pi\hbar^2}{m_n} b_j \mathrm{e}^{\mathrm{i}\mathbf{q}\cdot\mathbf{r}_j} \tag{2.4.28}$$

By inserting the expression for the matrix element in Eq. 2.4.28 into the expression for the differential scattering cross-section in Eq. 2.4.25, we find,

$$\frac{d\sigma}{d\Omega} = b_j^2. \tag{2.4.29}$$

Similar expressions can now be derived for two, or more nuclei, resulting in interference between the scattered waves. Furthermore, a similar expression may be obtained for inelastic scattering, by considering that the system from which the neutrons scatter also changes state from $|\lambda_i\rangle$ to $|\lambda_f\rangle$. Therefore, the double differential scattering cross-section is given,

$$\left(\frac{d^2\sigma}{d\Omega dE_f}\right)_{\lambda_i \to \lambda_f} = \frac{k_f}{k_i}\left(\frac{m_n}{2\pi\hbar}\right)^2 |\langle \lambda_i \psi_i | \hat{V} | \lambda_f \psi_f \rangle|^2 \delta(E_{\lambda_i} - E_{\lambda_f} + \hbar\omega), \tag{2.4.30}$$

where the Dirac delta function represents the conservation of energy.

The main contribution from the magnetic scattering of a neutron arises from its interaction with the magnetic moment of the unpaired electrons - all other contributions are far smaller and can be neglected [250]. Neutrons only interact with the thermally averaged value of the spin component perpendicular to the scattering vector: $\langle \mathbf{s}_\perp \rangle$ [251]. Following a similar derivation as above, and utilising the magnetic interaction potential operator, the analogous magnetic differential scattering cross section can be derived,

$$\frac{d\sigma}{d\Omega}_{\mathrm{mag}} = (\gamma r_0)^2 \left[\frac{g}{2} F_{\mathrm{m}}(\mathbf{q})\right] \mathrm{e}^{-2W} \left| \sum_j \mathrm{e}^{-\mathrm{i}\mathbf{q}\cdot\mathbf{r}_j} \langle \mathbf{s}_{j,\perp} \rangle \right|^2. \tag{2.4.31}$$

Here, $F_{\mathrm{m}}(\mathbf{q})$ is the magnetic structure factor, which depends on the specific magnetic structure being investigated.

Magnetic structures can be defined by a magnetic ordering vector $\mathbf{Q}$. When all magnetic ions are crystallographically equivalent, for example in a uniformly magne-

tised ferromagnetic state, the magnitude and direction of the moment at any lattice site $\mathbf{r}_j$ will be independent of j, and the system therefore has translational symmetry. Such a structure has a magnetic ordering vector of $\mathbf{Q} = \mathbf{0}$. For commensurate structures such as an antiferromagnet or ferrimagnet, typically $\mathbf{Q}$ takes an integer value $\mathbf{Q} = \pm n$. However, for incommensurate structures such as the helical, conical and skyrmion chiral spin textures, $\mathbf{Q}$ will take a non-integer value.

Similar to x-rays, magnetic neutron diffraction peaks will appear when the scattering vector $\mathbf{q}$ equals the magnetic ordering vector $\mathbf{Q}$. Thus, for incommensurate structures such as skyrmions, structural Bragg peaks, including the (000) main beam will be decorated by magnetic satellites with an intensity proportional to the square of the ordered moment [252]. However, unlike x-rays, the intensity of the magnetic scattering will be a similar order of magnitude to the nuclear scattering [253].

Chapter 3

Methods

3.1 Sample Preparation

The samples were synthesised by A. Štefančič, J. A. T. Verezhak, and G. Balakrishnan at the University of Warwick. In Sec. 3.1.1, the chemical vapour transport manufacturing method for the $(Cu_{1-x}Zn_x)_2OSeO_3$ single crystals is detailed, as laid out in [218]. The process was, in principle, identical to the growth of the FeGe crystals investigated in Ch. 7. From these single crystals, thin lamellae were created using a focused ion beam (FIB), as detailed in Sec. 3.1.2.

3.1.1 Crystal Growth

To create the initial precursor $(Cu_{1-x}Zn_x)_2OSeO_3$ polycrystalline samples, stoichiometric quantities of CuO (99.99%, metals basis, Alfa Aesar), Se_2 (99.999%, trace metal basis, Acros Organics) and ZnO (99.999%, Aldrich) were thoroughly ground together in an argon-filled glove box. A range of Zn-doped samples were prepared with nominal Zn-substitutions of $x = 0, 0.02, 0.05, 0.08, 0.10, 0.12, 0.15$. The resulting mixtures were transferred into silica tubes, and sealed under vacuum. The tubes were when heated to 920 K at a rate of 3.5 K/hr, and kept at this final temperature for 96 hours. This was followed by water quench cooling, resulting in polycrystalline $(Cu_{1-x}Zn_x)_2OSeO_3$ samples with a range of Zn-doping levels. The results for the characterisation of these powder samples are detailed in Ch. 4.

From these polycrystalline precursor samples, single crystal samples were pre-

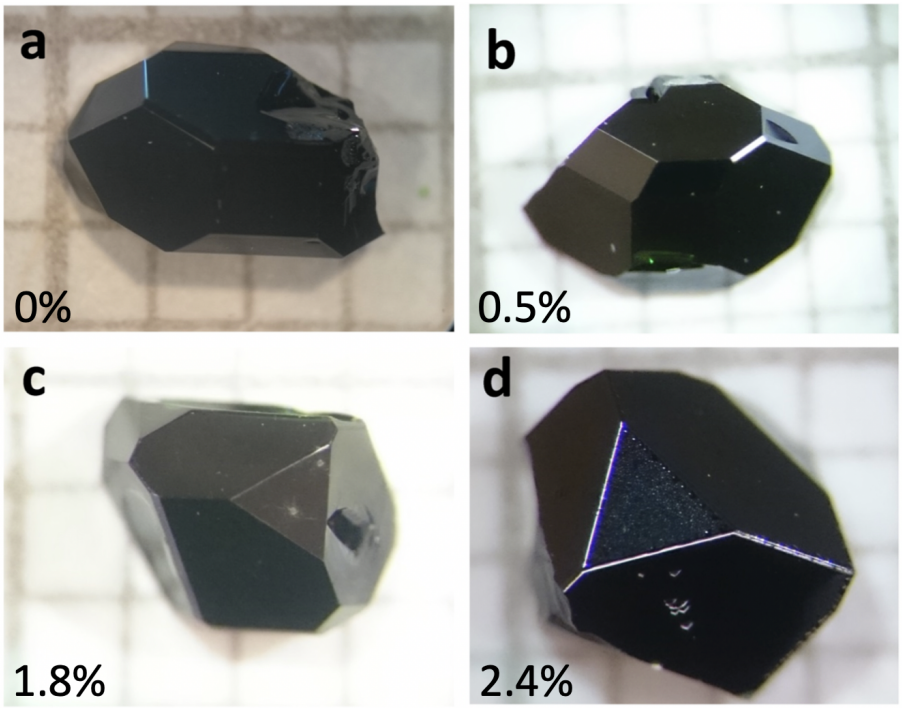

Figure 3.1: (**a-d**) Single crystals of $(Cu_{1-x}Zn_x)_2OSeO_3$ with measured Zn-substitutions as labelled. Pictures were taken on millimetre paper [218].

pared using the chemical vapour transport method [254]. 2.5 g of the powder samples with nominal Zn-substitution levels of $x = 0, 0.02, 0.05, 0.12$ was mixed with 1.5 to 2.0 mg/cm^3 of transport agent, $TeCl_4$, and the resulting mixture was sealed at one end of an evacuated silica tube. Each tube was then placed in a two-zone tube furnace. The source end of the tube was heated to 913 K, while the sink end was heated to 823 K, and then left for four weeks. The precursor powder is volatilised in the presence of the transport agent at the hotter end of the tube, and is then redeposited at the cooler, forming single crystals of $(Cu_{1-x}Zn_x)_2OSeO_3$, as shown in Fig. 3.1. The resultant crystals are characterised in Ch. 4. The FeGe single crystals were grown by a similar chemical vapour transport method, but with iodine as the transport agent.

3.1.2 Focused Ion Beams

For some of the techniques utilised in this thesis, it was necessary to investigate thin lamellae of the material with a thickness less than 300 nm. Such fabrication is

difficult to perform mechanically, and necessitates the use of the FIB manufacturing technique [255]. Operating similarly to a scanning electron microscope (SEM), a beam of ions can be used to image samples on the nanoscale. Due to the increased mass when using metal ions instead of electrons, this is a highly destructive imaging technique. However, this property can be turned into an advantage: ion milling, achieved via the sputtering process, can be exploited for nanofabrication [256]. To generate the beam, heated Ga^+ metal ions flow to the tip of a tungsten needle, where the opposing forces of surface tension and electrostatics cause ionisation and field emission. The resultant beam is then accelerated and focused using a series of electrostatic lenses to an energy of 1-50 keV.

In a SEM, imaging is achieved by detecting either the primary or secondary electron signal as the focused electron beam is rastered across the sample pixel by pixel [257]. Primary electrons, or backscattered electrons, result from the elastic scattering of the initial probe electrons from the surface of the sample. Secondary electrons originate from the atoms in the sample, excited by inelastic collisions with the accelerated primary electron beam, with enough energy to escape the sample surface. Similarly, ion beam imaging is achieved by detecting the secondary electrons produced by the collision of the accelerated ions with the sample.

Ion beams can also be used to perform ion-assisted chemical vapour deposition, with a nanometer precision [258]. A small quantity of a precursor gas, such as an organo-metallic compound, is injected close to the ion beam. The gas molecules are decomposed by the incident ions, resulting in the deposition of the non-volatile material, such a Pt, onto the surface of the sample, while the gaseous products are removed by the vacuum system. The inclusion of an in-situ nanomanipulator probe, typically operated via piezoelectric motors, allows for the manipulation and extraction of small quantities of the material.

3.1.3 Lamella Fabrication

In this work, a commercially-available FEI Helios Nanolab instrument was utilised for sample fabrication. This system features both Ga ion and a conventional SEM imaging column, positioned at a 52 degree tilt angle to one another, allowing for

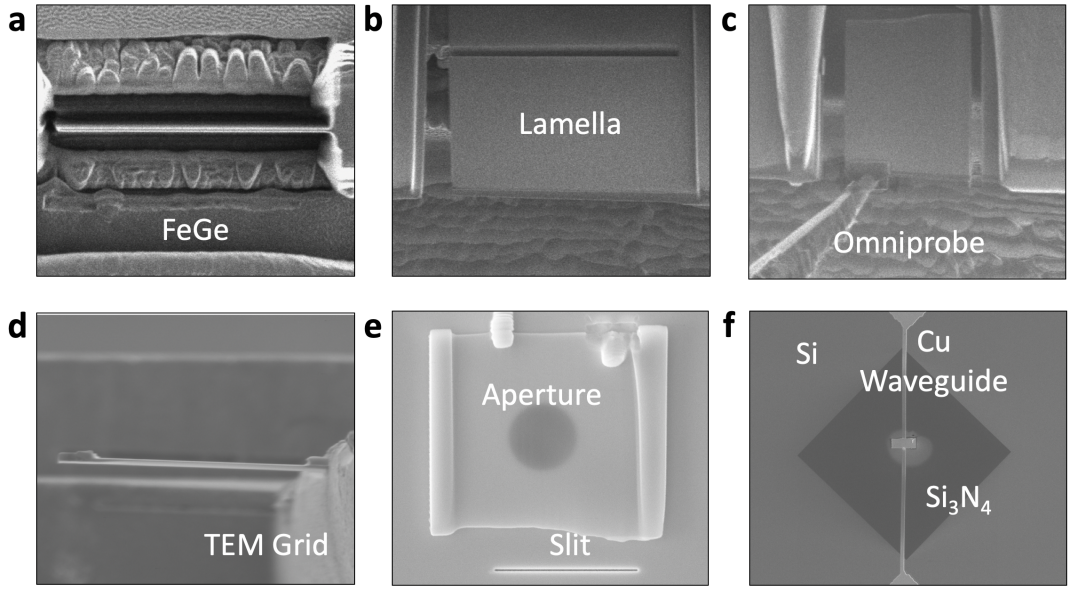

Figure 3.2: **a-f**, Scanning electron microscopy images of an example FeGe lamella fabrication process.

simultaneous ion nanofabrication and non-destructive electron imaging. The system also incorporated an in-situ Omniprobe micromanipulator for sample extraction. A typical step-by-step method for the production and extraction of a 200 nm thick lamella from the surface of a single crystal using this instrument is detailed below.

Single crystals of the target material were mounted on a metallic stub using conductive silver paint, and mounted inside the FIB instrument. Utilising the ion beam, a protective strip of Pt, was deposited by localised chemical vapour deposition, with lateral dimensions of 25×2 μm and a thickness of 2 μm. Two trenches, with dimensions 28×15 μm, and a depth of 10 μm, were then milled using a high current Ga ion beam either side of the Pt strip. This created a wall of sample material between the two trenches, capped by the protective Pt layer, which eventually became the lamella sample. Using successively lower ion currents, the wall of sample material was gradually thinned to a thickness of ∼1.5 μm, as shown in Fig. 3.2**a**. The sample stage was then rotated by 52 degrees to present the side of the wall between the trenches to the ion beam. Next, cuts around the edge of the lamella were milled, leaving one edge attached to the original material, as shown in Fig. 3.2**b**.

The in-situ Omniprobe was then carefully positioned on the top corner of the

lamella, and attached via a small deposited Pt weld. The final side of the lamella still attached to the main body of the crystal was then milled away, allowing the lamella to be extracted by the Omniprobe, as seen in Fig. 3.2**c**. The lamella was then attached to a standard copper transmission electron microscopy (TEM) grid, once again via Pt deposition, and the Omniprobe detached by ion milling, resulting in the configuration shown in Fig. 3.2**d**. From here, the lamella was then gradually thinned to ∼200 nm using progressively smaller ion beam currents.

At this point, with the lamella attached to a standard TEM grid, the sample is prepared for both TEM and x-ray microscopy measurements. However, for the small angle x-ray scattering (SAXS) and x-ray holography experiments, further fabrication was necessary to achieve more complex device structures, such those shown in Fig. 3.2**e** and 3.2**f**. For both experiments, silicon chips with dimensions $5 \times 5 \times 0.2$ mm, with four equally spaced 0.5×0.5 mm Si_3N_4 membrane windows, were sourced from Silson Ltd. and prepared as a substrate. After washing the chips in acetone and isopropanol, they were mounted to a glass slide face-down using kapton tape, and placed inside a magnetron sputtering system. A 5 nm Cr seed layer was then deposited to act as a surfactant, ensuring even layer growth, followed by 100 nm of Au. This was repeated to build up a multilayer stack of Cr and Au layers with a total thickness of ∼700 nm. At this thickness, the Au layers are sufficient to absorb almost all of the incident soft x-rays.

Using the FIB system, a circular aperture with a diameter of 3 µm was milled in the centre of each membrane window. For x-ray holography samples, a reference slit of 20 nm thickness was cut alongside this aperture at a distance of 5 µm, to allow for image reconstruction. After rotating the TEM grid holder through 90 degrees to orient it in the horizontal plane, the now-thinned lamella was once again attached to the Omniprobe, and cut free from the TEM grid via ion milling. The Omniprobe was then used to place the lamella over a circular aperture in a Si_3N_4 membrane. The lamella was fixed in place using localised Pt deposition, and the Omniprobe detached via ion milling, leaving the lamella on the surface of the substrate, as shown in 3.2**e**. In this configuration, when the x-ray beam is directed on to the sample, only scattering through the sample aperture and reference slit is observed.

3.2 Cooling Procedures

Investigation the history dependence of the magnetic states in skyrmion materials requires the use of a variety of field-temperature procedures. The measurement protocols used throughout this work are illustrated in Fig. 3.3, with reference to a generic bulk skyrmion material magnetic phase diagram. For the determination of such magnetic phase diagrams, the most widely-used measurement procedure is zero field-cooling (ZFC). Here, the sample is cooled from above T_C down to the final temperature in zero applied magnetic field, as depicted in Fig. 3.3**a**. To investigate history dependent behaviour, the high field-cooled (HFC) procedure can be utilised and contrasted to ZFC measurements, as illustrated in Fig. 3.3**b**. Here, the sample is cooled from above T_C to the target temperature under an applied field of 200 mT or more.

The formation of metastable skyrmions requires the sample to be field-cooled (FC) through the equilibrium skyrmion state, under an applied field of ∼22 mT from above T_C, as shown in Fig. 3.3**c**. An alternative FC* measurement procedure is shown in Fig. 3.3**d**. In this procedure, the sample is cooled at 0 mT from 70 K to just below the lowest temperature extent of the equilibrium skyrmion phase (∼50 K in Cu_2OSeO_3). A field of 22 mT was then applied, and the sample is finally cooled down to the target temperature. By avoiding the equilibrium skyrmion phase, a magnetic state can be prepared without any population of metastable skyrmions. Thus, measurements performed following the FC* procedure can be compared to those following the FC procedure, allowing behaviour and features specific to the presence of metastable skyrmion to be identified. After initialising the magnetic configuration of the sample with these procedures, measurements were performed with decreasing or increasing isothermal field-sweeps. For the FC and FC* measurements, measurements were taken at fields above and below the FC field by performing two separate cooling procedures and field sweeps.

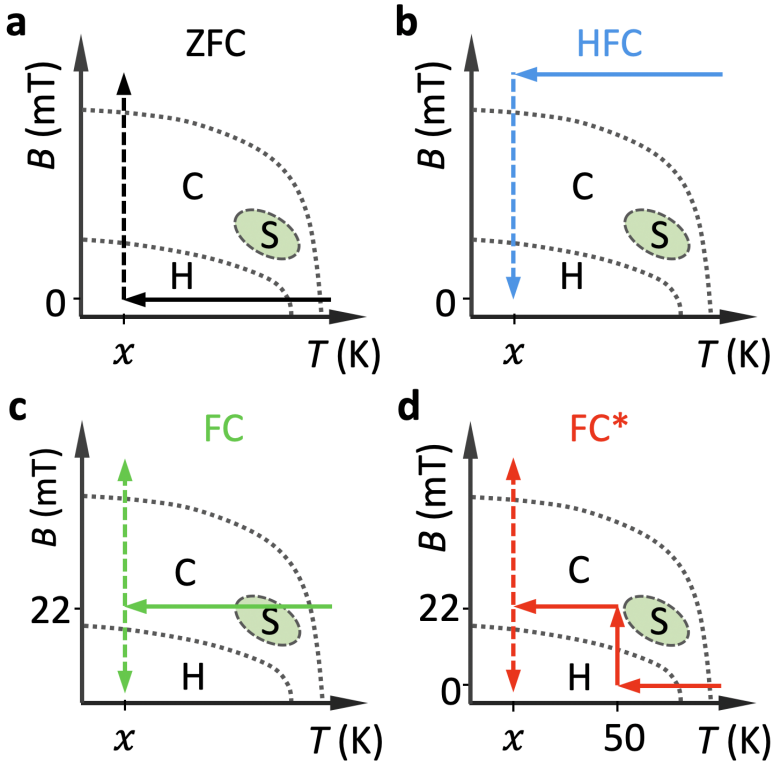

Figure 3.3: Schematic diagrams of the zero field-cooling (ZFC) (**a**), high-field cooling (**b**) and field-cooling (FC, FC*) (**c**, **d**) measurement procedures. Solid lines indicate the cooling procedure, while dashed lines indicate the measurement path. Dotted lines illustrate the boundaries between the helical (H), conical (C), and skyrmion (S) phases.

3.3 Magnetometry

Magnetometry measurements were performed using a commercial SQUID vibrating sample magnetometer: a Quantum Design MPMS3. Such devices allow the DC magnetisation of a sample to be measured as a function of temperature and applied magnetic field. The SQUID can only measure the magnetic flux $\Phi = \int \mathbf{B} \cdot dA$, or the magnetic flux density multiplied by the cross sectional area of the SQUID. To measure the magnetisation, the voltage through the SQUID, V_{SQUID}, is measured as the sample is moved through the superconducting pickup coils, as shown in Fig. 3.4. This voltage signal is then fitted automatically by the SQUID software to extract the magnetisation of the sample. In this way, the magnetisation of the sample can be measured as a function of temperature and the applied magnetic field [259].

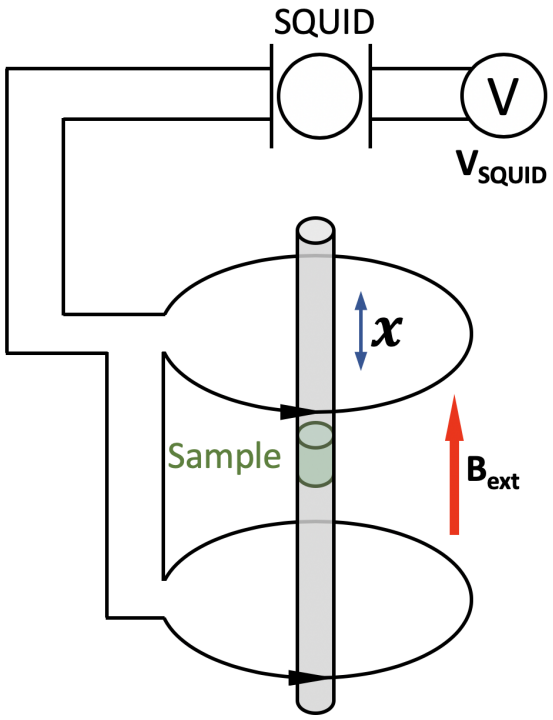

Figure 3.4: Schematic illustration of a SQUID magnetometer.

Alternating Current (AC) susceptibility measurements determine the magnetic moment of the sample in response to an oscillation of the applied magnetic field [260]. In this operation mode, the sample is not moved through the coils, and instead the time dependent sample moment induces the measured current. Such measurements are suitable for investigating the dynamics of the magnetic system. First, consider the effect of a low frequency field oscillation. Here, the magnetic moment of the sample simply follows the expected $M(H)$ curve that would be measured from DC magnetometry. For a small field, H_{AC}, oscillating at a frequency of ω, the time dependent magnetisation would be $M_{\mathrm{AC}} = (dM/dH) \cdot H_{\mathrm{AC}}\sin(\omega t)$. Thus, the amplitude of the observed M_{AC} signal is the magnetic susceptibility, $(dM/dH) = \chi$, or the slope of the $M(H)$ curve.

At higher frequencies, the magnetisation of the sample may lag behind the drive field. In this case, the AC magnetometry measurement provides both the magnitude of the susceptibility χ and the phase shift ϕ measured relative to the driving frequency. This is commonly provided as the real and imaginary components: $\chi' = \chi\cos(\phi)$ and $\chi'' = \chi\sin(\phi)$ respectively. At lower frequencies, the real compo-

nent is equivalent to the susceptibility, while the imaginary component indicates dissipative dynamic processes such as magnetic relaxation or domain wall motion [261]. There is also the opportunity to investigate the frequency and field amplitude dependence, which can be particularly useful when studying magnetic phase transition dynamics [262]. However, in this thesis, all AC susceptibility measurements were performed with a field amplitude of 1 Oe at a frequency of 10 Hz. Such measurements are suitable for determining the extent of magnetic phase boundaries in skyrmion materials, in addition to investigating their dynamic properties [263].

3.4 Small Angle Neutron Scattering

Small angle neutron scattering (SANS) is a powerful technique capable of probing material and magnetic structures on a scale of 1 to 1000 nm [264]. The neutrons for these experiments are typically produced in either continuous source nuclear reactors [265], such as the Institut Laue-Langevin (ILL), or in pulsed beam spallation sources [266]. In reactor sources, neutrons are produced as a result of fission processes in the reactor's core. In contrast, at spallation sources, neutrons are produced when intense accelerated proton pulses collide with a tungsten target. In both cases, the energy of the neutrons is reduced to desirable levels using a series of moderators. While the neutron flux of a spallation source is typically lower than a reactor, due to its pulsed nature, the time-of-flight (TOF) between the start of each pulse and detection of each individual neutron can be measured [267]. From this measurement, the energy, or wavelength, of each neutron is determined by it speed, and therefore neutrons of all energies may be utilised in scattering experiments.

SANS measurements were performed on the D33 instrument at the reactor source at ILL [268], and the ZOOM instrument at the ISIS spallation source. The samples were fixed with adhesive between two cadmium strips, and attached to a 200 µm thick aluminium plate using aluminium foil and tape, as shown in 3.5**a**. This assembly was then mounted on the end of a cryo-stick, and placed inside a helium cryostat equipped with a superconducting magnet. Cooling procedures were formed at a rate of 7 K/min and 0.5 K/min at ILL and ISIS respectively. A schematic of

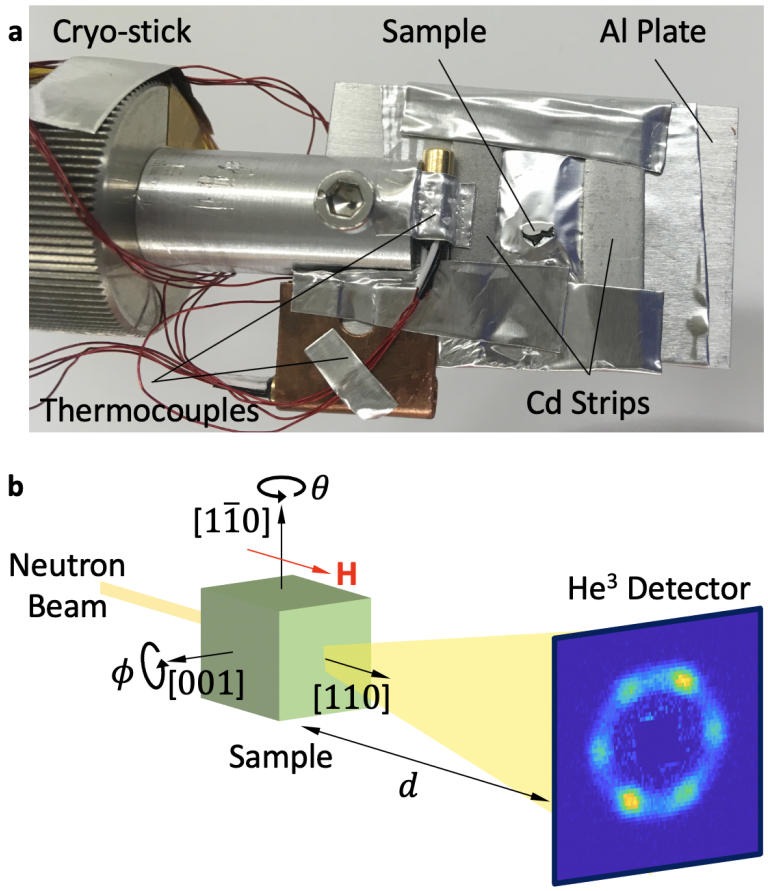

Figure 3.5: **a**, Photograph of the Cu_2OSeO_3 sample assembly for SANS measurements. **b**, Schematic illustration of the SANS diffraction experiment.

the experimental setup is shown in Fig. 3.5**b**.

During diffraction measurements, coherent scattering is observed when the orientation of the magnetic structures fulfils the Bragg condition. For SANS, this occurs when the direction of periodicity of the magnetic structure is close to perpendicular to the incident neutron beam, resulting in detection of a diffraction peak, or magnetic satellite. In both instruments, the neutrons are detected by a bank of He^3 cells.

For each Cu_2OSeO_3 crystal the $[1\bar{1}0]$ direction was aligned with the vertical rotation axis, as shown in Fig. 3.5. By rotating the sample around this axis, the magnetic field may be applied along the [100], [110] or [111] axes. A rotation around the vertical axis through θ rotates both the sample and applied magnetic field simultaneously. All SANS patterns shown are the result of summing scans

measured as a function of this rocking angle θ, between $\pm$ 10 degrees.

3.5 Synchrotron X-Ray Techniques

Synchrotrons are a type of cyclic particle accelerator, which can be engineered towards the production of x-rays. Diamond Light Source, the UK-based synchrotron, has a storage ring with a 561m circumference, and can accelerate electrons to 3 GeV. Electrons travel close to the speed of light around the synchrotron ring, emitting high energy Bremsstrahlung radiation as they are accelerated [269]. This phenomenon is exploited to produce high intensity x-ray beams as the electrons pass through the bending and undulator magnets positioned around the synchrotron ring. At each beamline, these x-rays are directed towards a series of slits, focusing mirrors and monochromator crystals, producing a highly focused and intense x-ray beam. These optics are specific to each beamline, allowing the properties of the x-ray beam, such as the energy, intensity, polarisation and coherency, to be tuned to each technique. This synchrotron radiation can be utilised by a large range of x-ray techniques, as evidenced by the variety of beamlines present around a typical synchrotron, serving a range of disciplines in the biological and physical sciences.

In this thesis, a number of synchrotron-based x-ray techniques were utilised: high resolution powder x-ray diffraction (PXRD), small angle x-ray scattering (SAXS), x-ray holography and scanning transmission x-ray microscopy (STXM). Due to the focus on magnetic skyrmions, the majority of these methods made use of low energy soft x-rays. This necessitated the use of a synchrotron, since there are currently no high-intensity, tunable, laboratory-based soft x-ray sources. The various methods will be detailed in this section.

3.5.1 Powder X-Ray Diffraction

Powder x-ray diffraction (PXRD) is an essential technique for investigating and characterising the crystal structure of polycrystalline samples [270]. In monochromatic single crystal diffraction, each (hkl) reflection is a distinct spot in the observed pattern. On the other hand, in PXRD, these spots form concentric rings due to the

random orientation of each crystallite in the sample. This introduces a multiplicity effect; for example in a cubic system, for the $\langle 100 \rangle$ family of planes, the (100), (010), (001), $(\bar{1}00)$, $(0\bar{1}0)$, and $(00\bar{1})$ spots are superimposed in the powder diffraction pattern. By measuring the scattering intensity of these peaks as a function of the scattering angle, 2θ, a powder diffraction pattern is acquired.

Although a full structure solution determination is often not possible from such data, an accurate starting model of the structure may be refined to fit the data in a process known as Rietveld refinement [271]. Using the starting model, the predicted powder pattern is calculated, and compared to the experimental data. An iterative method of least squares is then utilised to adjust the model parameters until the weighted residuals of this comparison are minimised. A variety of model parameters may be included in the refinement, including the lattice parameters, atomic positions, thermal UISO values, background polynomials, strain, preferred orientation and peak-shape profiles [272].

X-ray powder diffraction measurements were performed at the I11 beamline at the Diamond Light Source synchrotron. Polycrystalline samples of $(Cu_{1-x}Zn_x)_2OSeO_3$ with a range of Zn-doping levels were ground to fine powders. This is a crucial step: if the crystallites are too large, and the measured intensity peaks will posses non-systematic inaccuracies; if they are too small, the peaks will broaden due to finite size effects, [272]. The samples were then mounted either inside a quartz capillary tube, as shown in Fig. 3.6**a**, or fixed to the outside of the tube using a small amount of hand cream as an adhesive. Through testing, this has been shown to produce the smallest background and absorption signal in comparison to conventional glues.

The loaded capillary tubes were then positioned on the sample carousel next to the powder diffractometer instrument, as shown in Fig. 3.6**b**. The beamline is equipped with a robotic arm which can be scripted to mount the samples onto the diffractometer remotely. Powder diffraction measurements were taken with a duration of 3 hours for each sample. During this time, the sample was rotated at high speed to increase orientation randomness. The instrument's large 2θ-circle provides high resolution powder diffraction patterns by combining data from a set of five crystal analyser detectors, positioned around the 2θ circle, as seen in Fig. 3.6**b**. The

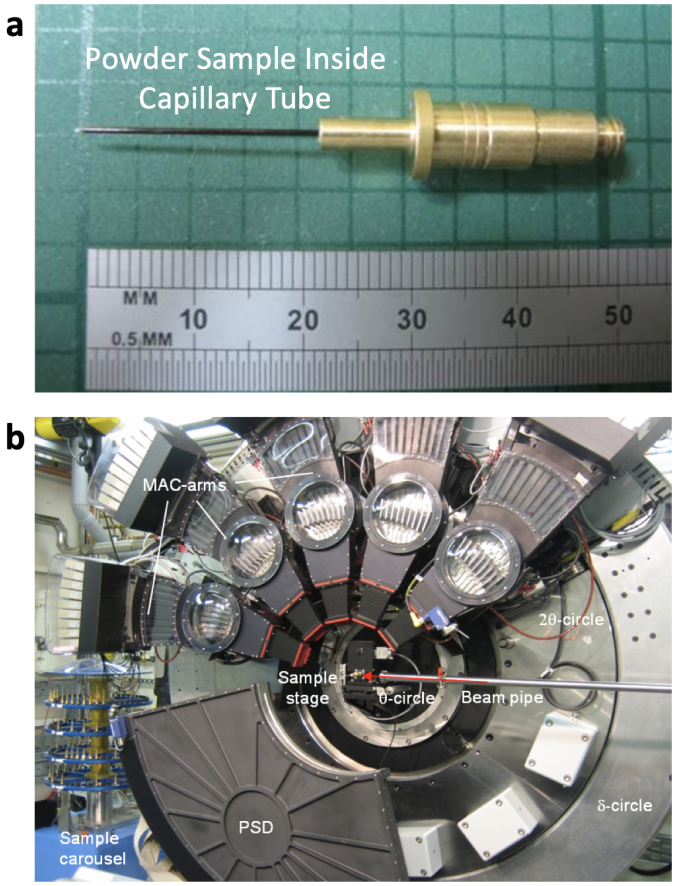

Figure 3.6: **a**, A powder sample prepared inside a capillary tube for PXRD measurements. **b**, The x-ray diffractometer at the I11 beamline, Diamond Light Source.

instrument contains a total of 45 individual Si crystals and photomultiplier-based detectors with fast pulse shaping electronics [273]. Data from this instrument measured for the $(Cu_{1-x}Zn_x)_2OSeO_3$ polycrystalline samples is presented and analysed using Rietveld refinement in Ch. 4.

3.5.2 Small Angle X-Ray Scattering

Similar to SANS, Small Angle X-Ray Scattering (SAXS), is a useful technique for investigating long range periodic magnetic structures such as skyrmion lattices [274]. The SAXS sample, prepared as described in Sec. 3.1.3, was mounted on the end of the cryostat cold finger, inside the RASOR diffractometer at the I10 beamline, at Diamond Light Source. This two-circle x-ray diffractometer operates under vacuum conditions to allow soft x-rays to be utilised, which would otherwise be absorbed

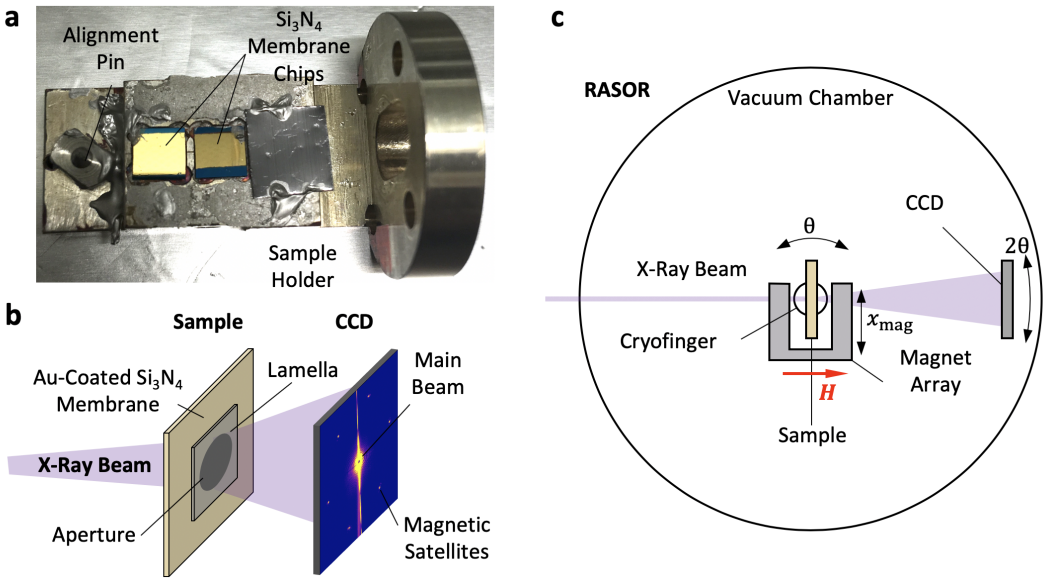

Figure 3.7: **a**, Photograph of the sample assembly for the SAXS measurements. **b**, Illustration of the SAXS diffraction experiment. **c**, Schematic diagram of the internal setup of the RASOR soft x-ray diffractometer, Diamond Light Source.

after a few cm of air. Cooling was achieved via a helium cryostat, capable of reaching a base temperature of 20 K. A variable magnetic field was applied by adjusting the height of an array of permanent magnets, allowing a field between 0 and 180 mT to be applied at the sample position.

The sample was positioned with the x-ray beam incident on the sample aperture, transmitted through the lamella sample. The scattered beam was detected by a charge coupled device (CCD) camera with 2048 × 2048 13.5 µm pixels mounted 138 mm from the sample, giving an effective q resolution of 1×10^{-3} nm^{-1}. A horizontal bar was placed in front of the CCD to act as a beamstop, preventing the direct beam from damaging the detector. A photograph of the Si_3N_4 sample mounted on the holder is shown in 3.7**a**, while an illustration of the sample setup is shown in Fig. 3.7**b** and a schematic of the diffractometer configuration is shown in Fig. 3.7**c**. With the sample, beam and CCD aligned, the transmitted beam intensity was measured as a function of the x-ray energy, allowing the L_3 absorption edge to be located. With the energy of the x-rays tuned to this edge, the magnetic scattering is enhanced by several orders of magnitude, as explained in Ch. 2. SAXS

patterns were then collected as a function of temperature and applied magnetic field, to investigate the chiral magnetic states.

3.5.3 X-Ray Holography

Holography is an imaging technique originally developed by Dennis Gabor in the 1940s, as a method to acquire both the amplitude and phase information of scattered waves, for which he was awarded the Nobel Prize in 1971 [275, 276]. By placing a coherent point source, or reference, an appropriate distance away from the object of interest, a complex-valued real-space image may be reconstructed from the resulting interference pattern.

In our experiments, we utilised an extended slit, rather than a typical pinhole, as a reference, using a technique known as Holography with Extended Reference by Autocorrelation Linear Differential Operation (HERALDO) [277]. The limiting factor of the image resolution in x-ray holography is typically the shape and size of the reference object. As such, it is often easier to create a narrow reference slit in comparison to the typical pin hole reference, resulting in a higher resolution image [278]. As we shall see, the use of an extended reference object leads to the formation of a convolved sample image in the reconstruction, which obscures the real-space details. However, by applying a linear differential filter to the measured hologram, the object image can be separated from the surrounding image convolutions [279].

HERALDO

This theoretical description of the HERALDO technique is largely based on the derivations by Guizar-Sicairos and Fienup [279], but at each stage it is related to an example reconstruction of a skyrmion lattice in FeGe. First, we assume that the field in the sample plane, $f(x, y)$ can be represented by the sum of the sample $s(x, y)$ and reference $r(x, y)$ objects, $f(x, y) = s(x, y) + r(x, y)$, as shown in the sample image in Fig. 3.8**a**. Assuming the paraxial approximation, the far field, $F(u, v)$, can be defined as the Fourier transform of the original field,

$$F(u, v) = \mathscr{F}[f(x, y)] = \int\int f(x, y)\exp[-i2\pi(ux + vy)]\mathrm{d}x\mathrm{d}y, \tag{3.5.1}$$

where x and y are the Cartesian coordinates in real-space, and u and v are the corresponding inverse coordinates in Fourier space.

When performing lensless imaging, the resulting interference pattern intensity is measured by a plane detector giving the Fourier intensity, or the square of the far field, $|F(u,v)|^2$. In our measurements, we want to reconstruct the magnetisation of the sample. By subtracting diffraction patterns measured with both left- and right-circularly polarised x-rays, exploiting the effects of XMCD (see Sec. 2.4.2), the structural components of the image are eliminated, leaving only the magnetic information. An example of the diffraction measured for one polarisation is shown in Fig. 3.8**b**, while the subtraction of both polarisations is shown in Fig. 3.8**c**. We take this subtracted data as our $|F(u,v)|^2$. This expression reveals the inherent obstacle that must be overcome in diffraction imaging: because we measure the square of the field, the phase information is lost in the measurement, and must be recovered.

This term can be expressed in terms of the inverse Fourier transform of the autocorrelation of the object field,

$$\mathscr{F}^{-1}[|F(u,v)|^2] = f \otimes f = s \otimes s + r \otimes r + s \otimes r + r \otimes s, \tag{3.5.2}$$

where

$$s \otimes r = \int\int s(x',y')r^*(x'-x,y'-y)\mathrm{d}x\mathrm{d}y \tag{3.5.3}$$

is the convolution of $s(x,y)$ and $r(x,y)$, and $(^*)$ indicates the complex conjugation. The expression in Eq. 3.5.2 reveals the problem which must be solved in typical holography methods: with knowledge of the reference object shape, we must separate either $s \otimes r$ or $r \otimes s$ from the other terms in order to deconvolve the original object field, and reconstruct the sample image [279]. For a pinhole reference, this is trivial, since it can be approximated to a Dirac delta function, and thus by applying an inverse Fourier transform to the measured $|F(u,v)|^2$, an image of the sample is seen in the $s \otimes r$ and $r \otimes s$ terms.

Turning now to HERALDO, we look at the case when we utilise an extended reference slit. If we follow the procedure used for a pinhole reference, and simply apply the inverse Fourier transform to the subtracted intensity patterns, we arrive

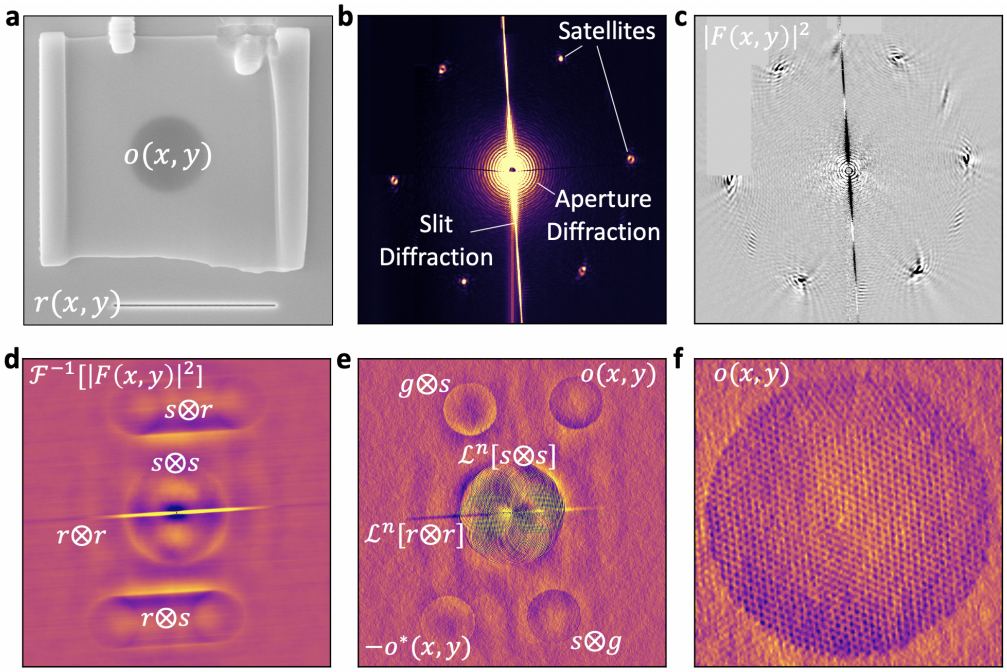

Figure 3.8: **a** SEM image of the FeGe holography lamella sample. **b**, Scattering pattern measured for a single polarisation. **c**, Subtraction of scattering patterns acquired for left and right circularly polarised x-rays. **d**, Fourier transform of **c** without linear differential filter. **e**, Fourier transform of **c** after applying a linear differential filter. **f**, Close up of the reconstructed magnetic sample image.

at the reconstruction in Fig. 3.8**d**. Here, we can see that the reconstructed images, $s \otimes r$ and $r \otimes s$, are obscured due to the convolution with the extended slit. However, HERALDO gives us a method to account for this effect and obtain an unobscured image of the sample. We select a linear differential operator $\mathscr{L}^{(n)}[...]$, such that then it is applied to the reference object $r(x, y)$, we are left with the sum of a Dirac delta function at (x_0, y_0), and another function $g(x, y)$,

$$\mathscr{L}^{(n)}[r(x,y)] = A\delta(x - x_0)\delta(y - y_0) + g(x,y), \tag{3.5.4}$$

where A is a complex-valued constant, and the n-th order differential operator is defined,

$$\mathscr{L}^{(n)}[...] = \sum_{k=0}^{n} a_k \frac{\partial^n}{\partial x^{n-k} \partial y^k}. \tag{3.5.5}$$

Applying this operator to the field autocorrelation, we come to the expression

$$\begin{aligned}\mathscr{L}^{(n)}[f \otimes f] =& \mathscr{L}^{(n)}[s \otimes s] + \mathscr{L}^{(n)}[r \otimes r] \\ &+ (-1)^n \left(s \otimes \mathscr{L}^{(n)}[r]\right) + \left(\mathscr{L}^{(n)}[r] \otimes s\right),\end{aligned} \tag{3.5.6}$$

using a common identity [279]. By utilising our imposed relation between the operator and the reference object in Eq. 3.5.4, we find

$$\begin{aligned}\mathscr{L}^{(n)}[f \otimes f] =& \mathscr{L}^{(n)}[s \otimes s] + \mathscr{L}^{(n)}[r \otimes r] + (-1)^n s \otimes g + g \otimes s \\ &+ (-1)^n A^* s(x + x_0, y + y_0) + A s^*(x_0 - x, y_0 - y).\end{aligned} \tag{3.5.7}$$

This equation reveals the result achieved by the application of the linear operator: the final two terms of Eq. 3.5.7 show that the image of the sample $s(x + x_0, y + y_0)$ and its complex conjugated twin, $s^*(x_0 - x, y_0 - y)$ are reconstructed either side of the origin. Successful deconvolution of this term requires that there is no overlap of the sample image with other images in the reconstruction. Such overlap can be prevented by milling the reference slit in a suitable position relative to the sample aperture [279].

The result of performing such an operation to our example reconstruction is shown in Fig. 3.8**e**, illustrating the deconvolution of the sample images surrounding the autocorrelation. The image labelled $o(x, y)$ is plotted in 3.8**d**, revealing the successful image reconstruction. Beyond this Fourier transform reconstruction, images may also be reconstructed from the diffraction patterns using a phase retrieval algorithm [280].

X-Ray Holography Sample Setup

X-Ray holography measurements were performed using the COMET endstation at the SEXTANTS beamline at Synchrotron Soleil. The sample configuration and instrument setup of technique are largely similar to the SAXS method described in Sec. 3.5.2 above. The primary difference in sample preparation is the addition of the 20 nm wide reference slit milled close to the main circular sample aperture, as described in Sec. 3.1.3. When the x-ray beam is incident on the sample assembly,

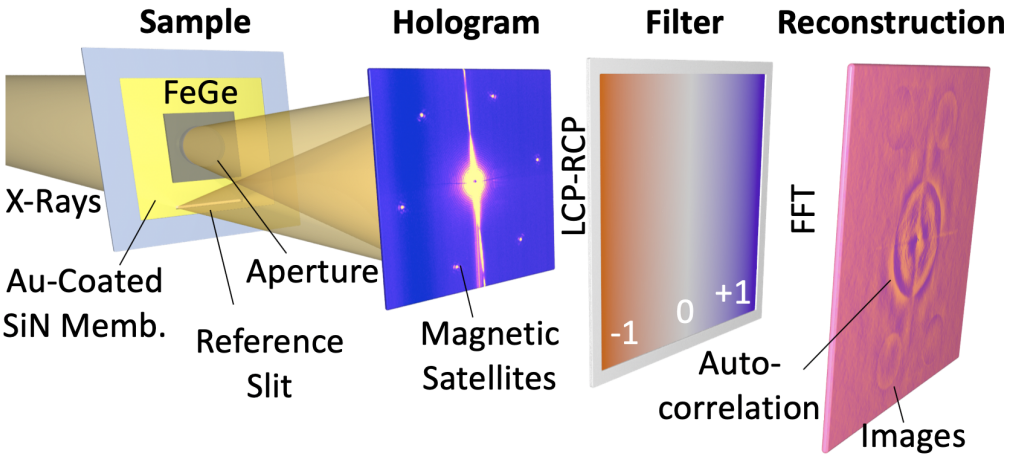

Figure 3.9: Schematic illustration of the x-ray holography experiment and reconstruction procedure.

light passes through both the sample, via the circular aperture, and the reference slit, as shown in Fig. 3.9. We estimated that the flux incident on the sample aperture was 10^9 photons per second. The scattering from these two objects is subject to wave interference, and the resulting scattering pattern was collected on a CCD placed downstream of the sample, as in the SAXS experiments. To successfully recover this phase information, holography requires a coherent x-ray source. The transverse coherence length of the x-ray beam was estimated to be 25 µm in both vertical and horizontal directions.

Two diffraction patterns were acquired with opposite circular polarisation of the incident x-ray beam. For a high quality image, we set the detector distance to 24 cm, and recorded over 100 exposures in each polarisation, for a total measurement time of 3 hours. This was primarily limited by the long CCD readout time of a few seconds in comparison to each 200 ms exposure time. Holographic reconstruction of the magnetic sample image was then performed using the HERALDO technique [277]. We estimated the spatial resolution of the presented x-ray holography images to be 25 nm, which was primarily limited by the pixel size on the CCD detector.

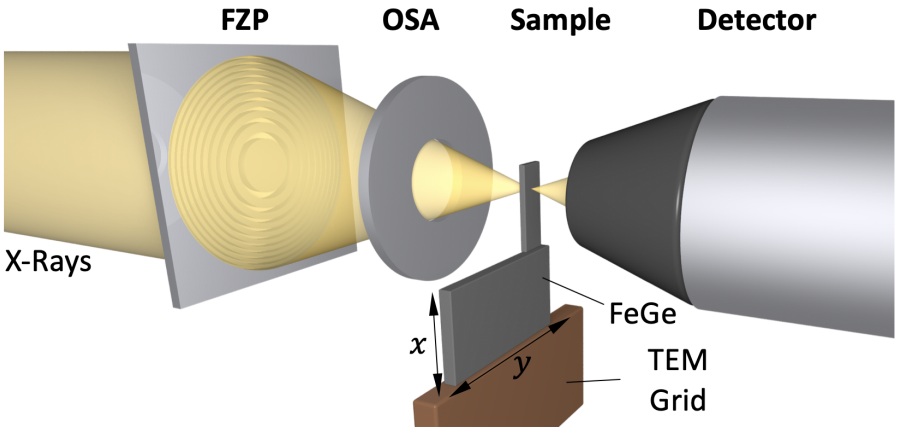

Figure 3.10: Schematic illustration of the STXM experiment setup and measurement.

3.5.4 Scanning Transmission X-Ray Microscopy

Scanning transmission microscopy measurements were performed at the MAXYMUS instrument at BESSY II synchrotron. This technique utilises a highly focused x-ray beam to image a sample pixel by pixel. By exploiting the effects of XMCD at the resonant x-ray energy, the measured transmission through the sample at each point forms an image of the magnetic contrast [281]. Because the refractive index of x-rays is near unity, conventional lens optics cannot be used to focus the x-ray beam. Instead, Fresnel zone plates, consisting of concentric rings with radially increasing line density which form a circular grating, can be used to focus the x-ray beam, in conjunction with an order separation aperture [282], as seen in Fig. 3.10. At MAXYMUS, the focused beam has a spot size of 22 nm.

With the sample mounted inside the microscope, cooling was achieved by a helium cryostat and the applied magnetic field was controlled by varying the arrangement of four permanent magnets. The vibrations from the cryostat were reduced by setting the gas flow to the lowest level feasible to ensure successful low temperature imaging of the sample. The images presented in this thesis were measured using a single x-ray polarisation. The x-ray beam was rastered across the sample by translating the sample via piezoelectric motors, as shown in Fig. 3.10. Transmission of the beam through the sample was measured by an avalanche photodiode with a 2 GHz signal bandwidth. A gated detection with a 20 ps long measurement window

was utilised such that the measurement was only active at the expected arrival time of the photons, effectively realising a 500 MHz lock-in on the synchrotron beam pulses. This signal was then compared to a reference voltage to achieve fast single photon counting. A typical STXM image required an acquisition time of 15 mins. We estimated that the spatial resolution of the presented STXM images to be 18 nm, which was primarily determined by the width of the focused x-ray beam [283].

3.6 Magnetic Resonance Spectroscopy

Magnetic systems exhibit fundamental excitations known as magnons, which represent quanta of propagation of spin procession [284]. These spin dynamics, known as magnetic resonances, can be described by the Landau-Lifshitz-Gilbert equation. They typically have a resonant frequency, or Larmor frequency, on the order of 0.5 to 50 GHz, and therefore can be excited by microwaves [285]. These effects have potential application in the emerging field of magnonics, which aims to perform information processing using spin waves [286].

Ferromagnetic resonance measurements are also a sensitive tool which can be used to study the basic properties of magnetic systems, such as the magnetic anisotropy energy, or magnetic relaxation and damping [287]. Typically, the magnetic sample is placed close to a conductive stripline which acts as a waveguide for the microwave probe signal. At the resonance frequency of the system, the microwaves couple with the magnetisation of the system, resulting in a reduction of the measured signal as the microwaves are absorbed. The absorption of the microwave signal can then measured as a function of frequency, temperature, and applied magnetic field [288].

The dynamic excitations of skyrmions were first theoretically studied by Mochizuki [289], who proposed three fundamental skyrmion resonance modes: two rotational modes, clockwise and counter-clockwise, excited by an in-plane alternating magnetic field; and a breathing mode, driven by an out-of-plane magnetic field oscillation [290]. These resonance modes were experimentally measured in Cu_2OSeO_3, and found to be on the order of 1 GHz [291, 292]. Sketches of the skyrmion modes are displayed in Fig. 3.11**a**. A range of eigenmodes has since been predicted and ob-

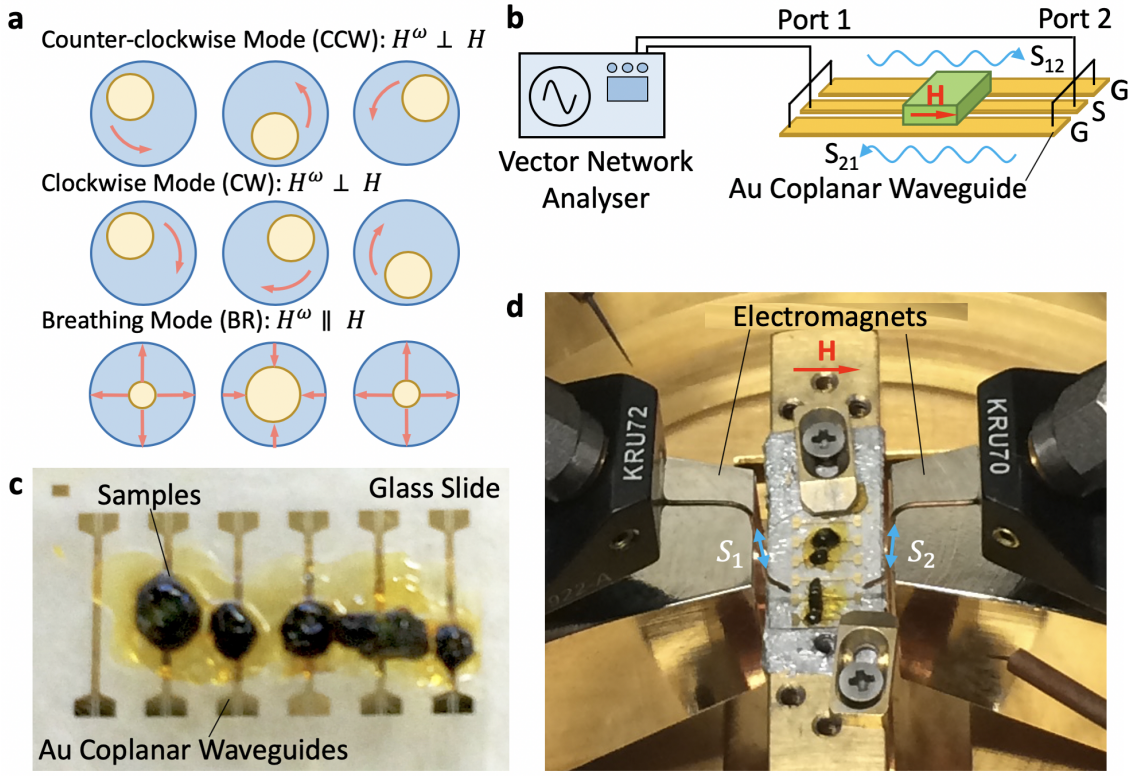

Figure 3.11: **a** Illustrations of the skyrmion resonance modes. **b**, Schematic diagram of the magnetic resonance measurement setup, **c**, Photograph of samples mounted on the Au coplanar waveguides. **d**, Photograph of the magnetic resonance measurement setup.

served for isolated skyrmions [293, 294]. Microwave resonance techniques have since been utilised to study a range of magnetoelectric and dichroism effects exhibited by the skyrmion state in the multiferroic Cu_2OSeO_3 [105, 106, 284, 292]

In this thesis, broadband microwave absorption spectroscopy was carried out on Cu_2OSeO_3 to detect the presence of metastable skyrmions. A schematic illustration of the experimental setup is shown in Fig. 3.11**b**. Coplanar Au waveguides, consisting of a signal wire in the middle of two ground wires, were prepared on a glass slide using lithography. The single crystal samples were fixed on the waveguides using GE varnish, as seen in Fig. 3.11**c**. The glass slide was then fixed at the end of a cryostat cold finger inside a vacuum chamber, between two variable electromagnets, as shown in Fig. 3.11**d**.

A vector network analyser was then connected by positioning conductive probes

at the end of each waveguide, as shown in Fig. 3.11**d**. At each temperature, the spectrum of microwave absorption caused by magnetic resonance, $\Delta S_{12}(\nu)$, was determined by subtraction of the common background $S_{12}^{\mathrm{ref}}(\nu)$ from the raw transmittance spectrum $S_{12}(\nu)$: $\Delta S_{12}(\nu) = S_{12}(\nu) - S_{12}^{\mathrm{ref}}(\nu)$. Here, a spectrum measured at an applied field of 250 mT was adopted as the reference background $S_{12}^{\mathrm{ref}}(\nu)$ – at this high field, the magnetic resonance was absent within our target frequency range from 1 GHz to 6 GHz.

Chapter 4

Characterisation of Zinc Doped Cu_2OSeO_3

Previous work on polycrystalline Zn-doped samples observed an unexpected splitting of the skyrmion region in the magnetic phase diagram into two thermally separated pockets [295]. Furthermore, in Ni-doped Cu_2OSeO_3, increasing Ni-doping led to a widening of the skyrmion phase in temperature [217]. In both works, it was argued that the disorder created by the substitution of Zn or Ni onto the Cu(I) and Cu(II) sites distorts the local trigonal bipyramidal structures, which might locally alter the strength of the DMI, leading to splitting, or enhancement, of the skyrmion phase.

In this chapter, polycrystalline and single crystal $(Cu_{1-x}Zn_x)_2OSeO_3$ samples are characterised. The following measurements and analysis were performed with masters student Sam Moody, and are featured in a publication [218]. We reveal that the polycrystalline samples show a skyrmion phase splitting, with the Zn-doped samples exhibiting two or three distinct skyrmion regions. On the other hand, the single crystal samples do not exhibit such a splitting. through careful analysis of the magnetometry data, and by making comparisons to high resolution powder x-ray diffraction (PXRD) measurements, we demonstrate that such a splitting is caused by the presence of multiple structural polymorphs of $(Cu_{1-x}Zn_x)_2OSeO_3$ in each polycrystalline sample. These distinct structural phases possess different values of T_C, and therefore exhibit the skyrmion pocket at different temperatures.

4.1 Zinc Doping Levels

The level of Zn-doping in each of the synthesised polycrystalline and single crystal samples of $(Cu_{1-x}Zn_x)_2OSeO_3$ was investigated using energy-dispersive x-ray spectroscopy (EDX) and inductively-coupled plasma mass spectroscopy (IC-PMS). Polycrystalline samples with nominal Zn levels of 2%, 8% and 12% were determined to have Zn-doping quantities of 2.0%, 6.4% and 10.5% respectively. This demonstrates that during the solid state reaction from the precursor powders, some Zn content was lost. In contrast, the single crystals grown by chemical vapour transport from these same polycrystalline powders were found to have Zn-doping levels of 0.5%, 1.8% and 2.4% respectively. This illustrates that even more Zn was lost during the chemical vapour transport crystal growth process, and it was found to be difficult to synthesis single crystals with Zn-doping levels higher than 2.5% [218]. Similar measurements were undertaken for further samples, giving polycrystalline samples with doping levels of between 0.0% and 13.4%.

4.2 Magnetic Phase Diagrams

AC susceptibility measurements were performed on four polycrystalline samples selected with a range of Zn-dopings. The real-component, χ', measured as a function of temperature and the applied magnetic field for each polycrystalline sample, are shown in Fig. 4.1**a-d**, forming a magnetic phase diagram for each sample. In Fig. 4.1**a**, data for a pristine polycrystalline sample is displayed. Typical features in the data can be utilised to determine the boundaries between each magnetic phase. The lower value of χ' around 0 mT is indicative of the helical state, while the small pocket close to T_C is characteristic of the skyrmion phase [263]. Finally, the dramatic drop of χ' at higher field indicates the boundary between the conical and field polarised states.

Considering the data measured for the 2% Zn-doped sample in 4.1**b**, the primary difference is the reduction of T_C. This is to be expected, as a non-magnetic Zn^{2+} ion substituted onto a magnetic Cu^{2+} site would reduce the average strength of the exchange energy, leading to the observed reduction of T_C. However, turning now

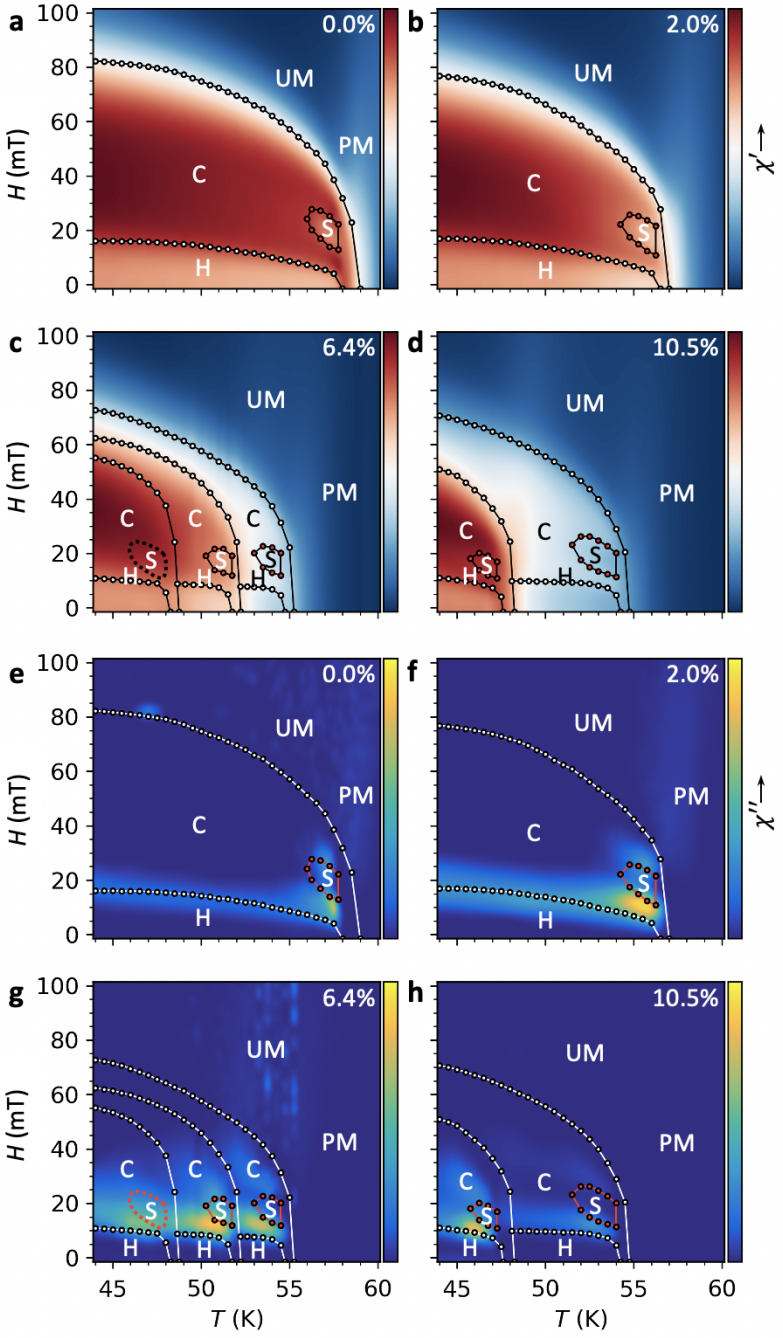

Figure 4.1: **a-h**, AC susceptibility phase diagrams of the polycrystalline samples, formed by plotting the real component (**a-d**) and imaginary component (**e-h**) as a function of temperature and applied magnetic field. The helical (H), conical (C), skyrmion (S), uniform magnetisation (UM) and paramagnetic (PM) states are labelled.

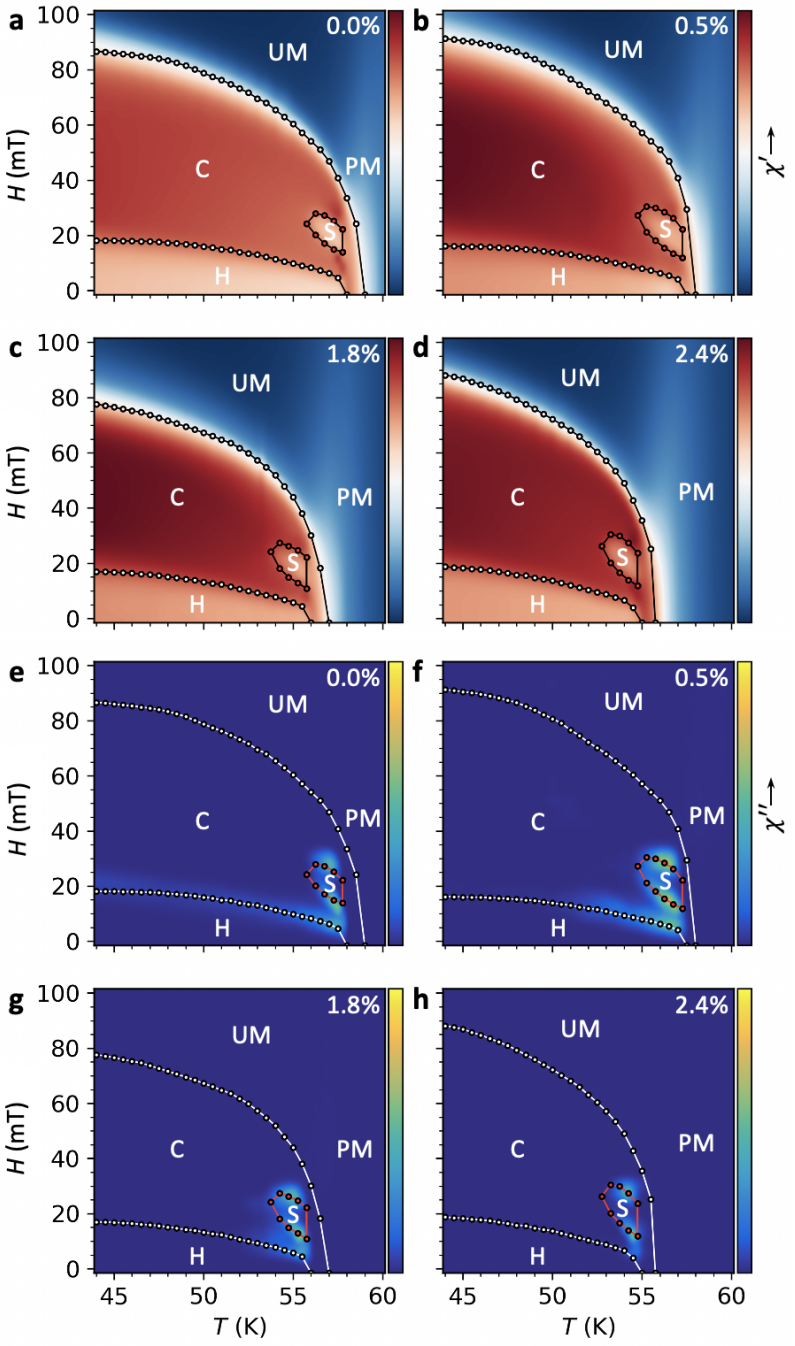

Figure 4.2: **a-h**, AC susceptibility phase diagrams of the single crystal samples, formed by plotting the real component (**a-d**) and imaginary component (**e-h**) as a function of temperature and applied magnetic field. The helical (H), conical (C), skyrmion (S), uniform magnetisation (UM) and paramagnetic (PM) states are labelled.

to the 6.4% and 10.5% polycrystals, multiple regions of lower χ' value are observed at a field of ∼20 mT, indicating that these samples exhibit three and two distinct skyrmion pockets respectively. Moreover, some of these skyrmion regions appear to have a larger temperature extent in comparison to the pristine sample. This strongly agrees with the result obtained by [295], where a similar splitting of the skyrmion pocket was observed by AC susceptibility measurements.

This splitting is more clearly observed when looking at the imaginary component of the AC susceptibility, χ''. As discussed in Sec. 3.3, the presence of χ'' indicates energy dissipation associated with magnetic phase transitions. Looking at 4.1**e** and **f**, we can see that a broad χ'' signal is seen at the boundary of the helical and conical phase, and at the border of the skyrmion and conical states, close to T_C. Looking at the higher doped samples, in 4.1**g** and **h** the additional χ'' signals at ∼20 mT provide strong evidence for multiple pockets of the skyrmion state, separated by temperature.

Fig. 4.2 displays AC susceptibility measurements for four single crystal samples with a range of Zn-doping levels. These measurements were performed with the [111] crystal axis aligned with the applied magnetic field. Looking at the real component data in Fig. 4.2**a-d**, one can see the decrease in T_C with Zn-doping, as seen in the polycrystalline samples. However, while the polycrystals displayed a splitting of the skyrmion phase, such a splitting is not seen in any of the single crystal samples. This is particularly clear when looking at the imaginary component measured for each sample in 4.2**e-h**. Furthermore, no increase in the temperature extent of the skyrmion phase is seen. This result strongly suggests that the polycrystalline samples may be exhibiting some structural effects which result in the splitting of the skyrmion phase, rather than it being due to modification of the DMI due to the substitution of the Zn onto distinct Cu sites, as was suggested by the previous work [295].

4.3 Determination of Curie Temperature

The magnetisation M of each polycrystal sample, and each single crystal sample, was measured as a function of decreasing temperature under an applied magnetic field of 25 mT, and are plotted in Fig. 4.3**a** and **b** respectively. The single crystal data sets in Fig. 4.3**b** display a single-step increase in the magnetisation as the temperature passes below T_C, as expected as the sample transitions from a paramagnetic to an ordered magnetic state. Looking at the polycrystalline sample data in 4.3**a**, it is clear that the pristine sample exhibits a similar single-step in the magnetisation. However, the Zn-doped samples exhibit two or three steps in the magnetisation.

These magnetisation curves can be utilised to determine T_C, which is often defined as the temperature with the greatest slope in the magnetisation. In Fig. 4.3**c** and **d**, the gradient of the magnetisation with temperature, dM/dT, is plotted as a function of temperature for the polycrystal and single crystal samples. This was numerically calculated from the measured data in Fig. 4.3**a** and **b**. The single crystal samples each exhibit a single minimum, which was fitted using asymmetric Lorentzian functions. From these fits, the T_C of the 0.0%, 0.5%, 1.8% and 2.4% samples was determined to be 58.5, 58.2, 57.1 and 56.2 K respectively, demonstrating the decrease of T_C with increasing Zn-doping.

Considering the polycrystalline sample data in Fig. 4.3**c**, it is clear that the doped samples exhibit two or three minima, suggesting that the sample exhibits multiple ordering transitions. Multiple superimposed split asymmetric Lorentzian functions were fitted to each dataset, allowing multiple T_C values to be defined for each sample. These results indicate that the polycrystalline sample may be composed of multiple distinct structural phases, or polymorphs, each of which exhibits a different T_C. We also determined the integrated intensity of these fitted peaks, which gives a measure of the fraction of the sample which becomes magnetised at each T_C value. These quantities will be made use of in Sec. 4.6.

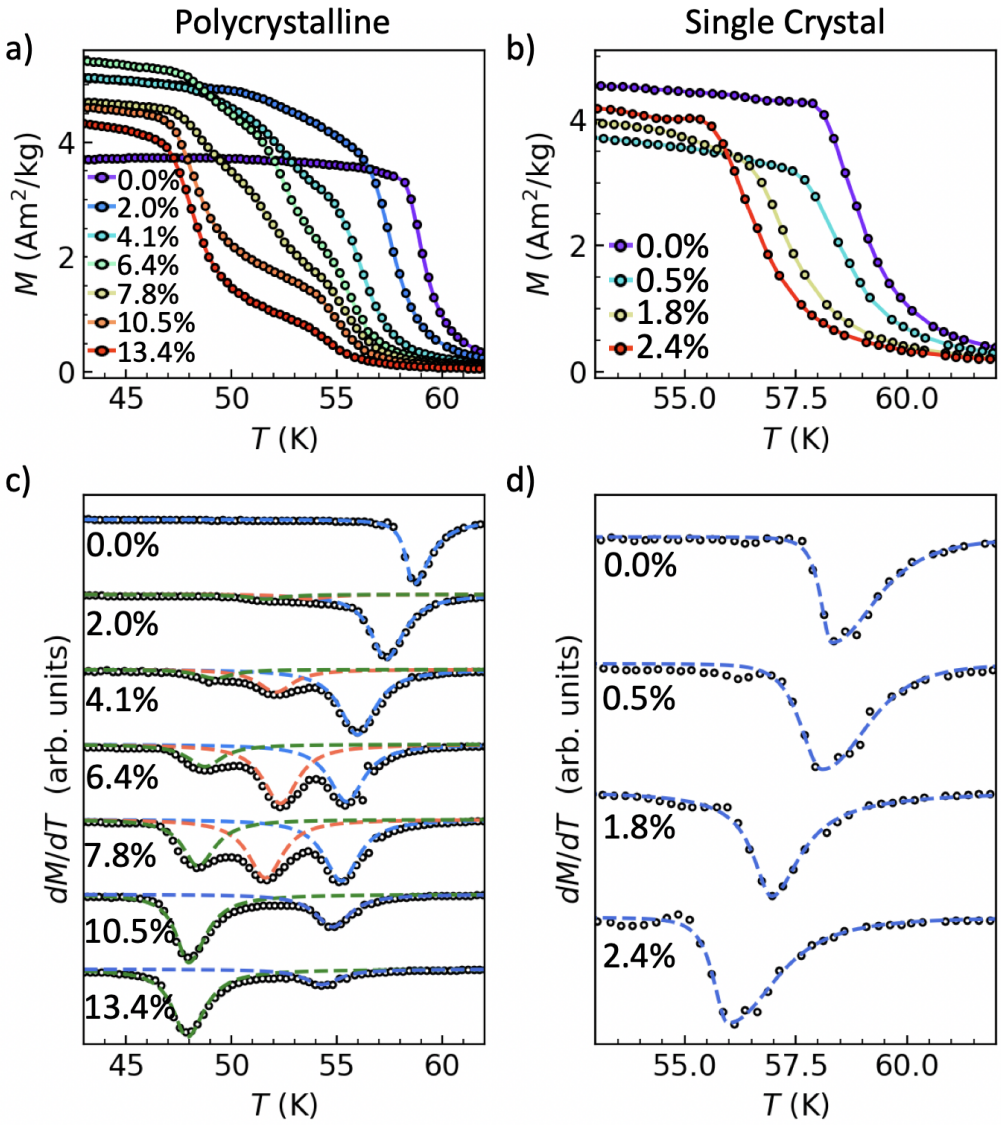

Figure 4.3: **a**,**b**, Magnetisation measured as a function of decreasing temperature for polycrystalline and single crystal samples respectively. **c**,**d**, The numerically calculated gradient of the magnetisation as a function of temperature for polycrystalline and single crystal samples respectively.

4.4 Powder X-Ray Diffraction

In order to investigate the potential for multiple distinct structural phases in the polycrystalline $(Cu_{1-x}Zn_x)_2OSeO_3$ samples, high resolution powder x-ray diffraction (PXRD) measurements were performed at the I11 beamline, Diamond Light Source, as explained in Sec. 3.5.1. Due to the instrument's high angular resolution, it is able to resolve features in the diffraction peaks which may not be observable with powder neutron diffraction or lab-based PXRD setups. For example, peak splitting was seen in powder samples of the solar cell material $CuZnSnS_4$, which was concluded to exhibit multiple polymorphic phases displaying the same basic crystal structure, but different lattice site defects [296, 297].

A 3 hour PXRD measurement was performed for each of the polycrystalline samples, and a 640c NIST Si standard, at an x-ray energy of 15 keV. Using the TOPAS-Academic software, an initial structural refinement of the Si standard was performed to calibrate the precise wavelength of the beamline and zero-point error of the diffractometer, which were then fixed for subsequent refinements.

An example powder diffraction pattern, measured for the pristine polycrystalline sample, is plotted in Fig. 4.4**a**. A Rietveld refinement was performed to fit the observed scattering data. For all refinements of the $(Cu_{1-x}Zn_x)_2OSeO_3$ samples, a basic Cu_2OSeO_3 crystal structure was used as the starting model. Due to the adjacency of Cu and Zn in the period table, meaning they differ in electron number by only one, their scattering factors are almost equivalent, and therefore including Zn in the structural model was not necessary. For high resolution data such as this, the peak broadening is dominated by the sample, and instrumental effects are negligible. Pseudo-Voigt functions were employed to describe the peak profiles. The residuals below the diffraction pattern indicate that the refined model is a good fit to the data. Fig. 4.4(b) displays a zoomed in view of a peak at $\sim$96.6 degrees, showing that in the pristine sample, a single phase model is sufficient to properly fit the experimental data. However, additional structural peaks not associated with Cu_2OSeO_3 were observed, which were determined to be due to CuO impurities, which were present in all samples.

However, looking now at the doped samples, we found that all of the diffraction

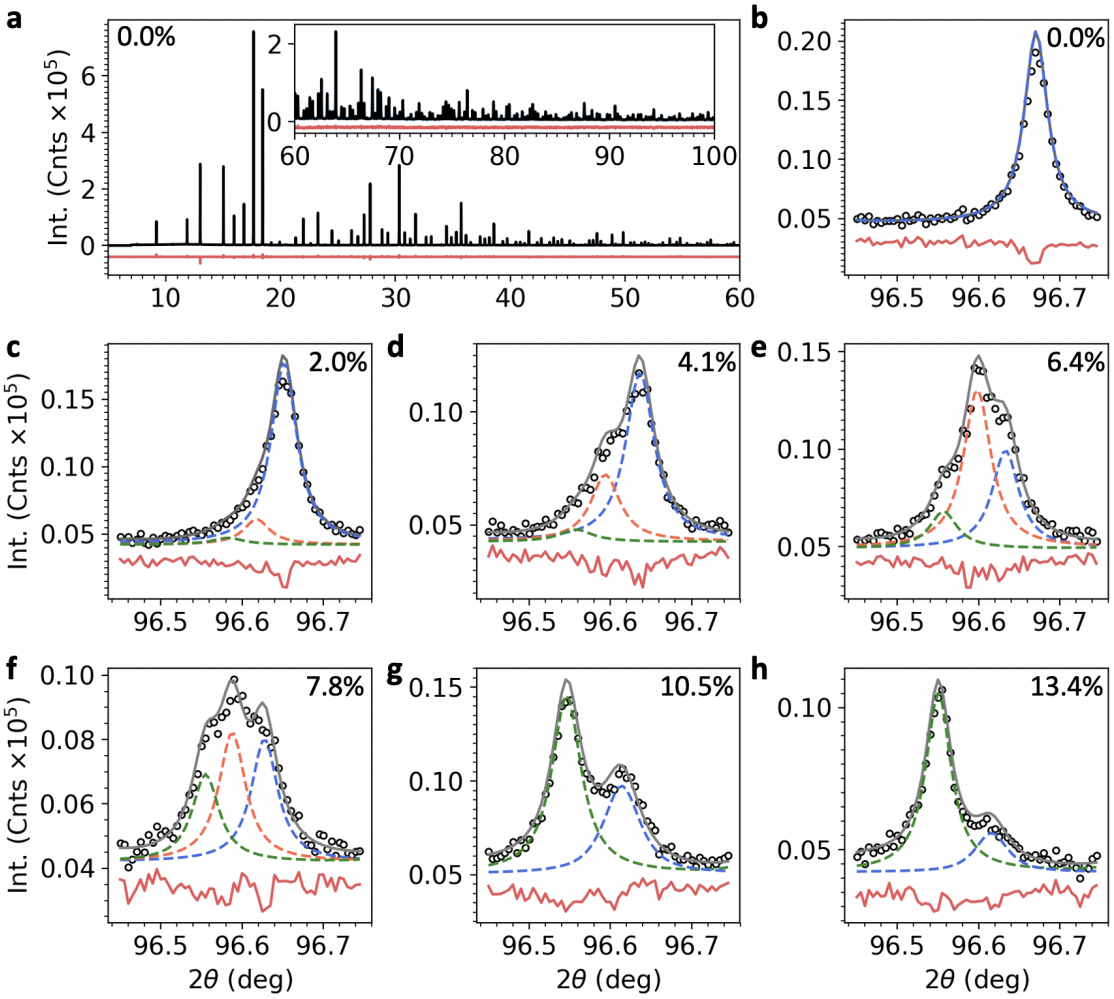

Figure 4.4: **a**, Powder diffraction pattern measured for the pristine polycrystalline sample. The inset shows scattering at higher angles. **b-h**, A single diffraction peak highlights the splitting observed at higher Zn-doping levels. Dashed lines indicate the contribution from each Cu_2OSeO_3 structural phase. The red line plots the residuals of the Rietveld refinement.

peaks in the powder pattern were split. This is illustrated by the plots in Fig. 4.4**c-h**, which display the same peak as in **b** at ∼96.6 degrees. In order to fit the data, it was necessary to include two (10.5% and 13.4% samples) or three (2.0%, 4.1%, 6.4%, 7.8% samples) distinct Cu_2OSeO_3 phases with varying lattice parameters. The peaks associated with each structural phase are shown by the dashed lines. Care was taken to utilise the same parameters for the Pseudo-Voigt peak profile function for each phase. A further impurity phase of Zn_2SiO_4 was found in the higher Zn-doping level samples, as a result of a reaction with the silica tube. These results demonstrate that the synthesised Zn-doped polycrystalline samples contain multiple structural phases of Cu_2OSeO_3.

4.5 Saturation Magnetisation

Information on the site occupancy of the Zn ion substitution in the doped polycrystalline samples can be investigated by using magnetisation measurements. A similar approach was adopted by Wu *et al* [295]. As discussion in Sec. 1.3.3, Cu_2OSeO_3 exhibits ferrimagnetism, where each Cu spin on the Cu(I) lattice sites align anti-parallel to three spins on the Cu(II) sites. This gives each bipyramidal arrangement of four Cu atoms a spin configuration of (↑↑↑↓), with a net magnetic moment of 0.5 μ_B/Cu^{2+} [139, 154]. When a non-magnetic Zn^{2+} ion is substituted onto the Cu(I) site, it will increase the net magnetic moment to 0.75 μ_B/Cu^{2+} (↑↑↑), whereas if it substitutes onto one of the three Cu(II) sites, the net moment will decrease to 0.25 μ_B/Cu^{2+} (↑↑↓).

The saturation magnetisation of each polycrystalline sample was measured as a function of an applied magnetic field between ±2 T at a temperature of 25 K. Using the mass of each polycrystalline sample, the resulting magnetisation datasets were normalised to show the magnetisation per Cu^{2+} ion site (ie, not factoring in Zn substitution), and are plotted in Fig. 4.5**a**. The magnetisation was also scaled to factor in the volume fraction of the non-magnetic impurity phases, as determined in the PXRD measurements. Immediately, it is clear that the saturation magnetisation, M_s, decreases with increasing Zn-doping.

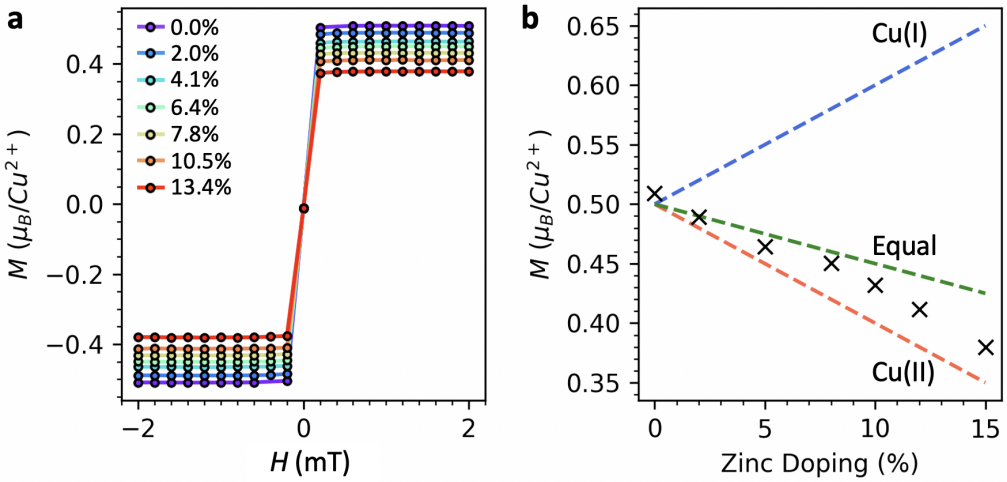

Figure 4.5: **a**, The magnetisation measured as a function of applied magnetic field at 25 K for the polycrystalline Zn-doped samples. **b**, The saturation magnetisation, M_s, of each sample plotted as a function of Zn-doping level. Dashed lines indicate the expected M_s for Cu(I) (blue), Cu(II) (orange) and equal (green) lattice site substitution.

The obtained value of M_s is plotted as a function of Zn-doping in Fig. 4.5**b**. On this plot, the dashed lines represent different Zn-substitution scenarios. The top and bottom lines illustrate the expected M_s value as a function of Zn-doping if all Zn ions substituted on the Cu(I) and Cu(II) sites respectively. The middle dashed line demonstrates the expected M_s if the Zn substituted onto all 4 Cu sites equally: a 25% chance to go onto the sole Cu(I) site, and a 75% chance to go onto one of the three Cu(II) sites. Comparing the data to these possible outcomes, it is clear that Zn has a slight preference to occupy the Cu(II) lattice sites, leading to a decrease in the observed magnetisation of the doped polycrystalline samples.

4.6 Discussion and Conclusions

The values of T_C extracted from the magnetisation data and, and the lattice parameters of each structural phase in the Rietveld refinements, are plotted in Fig. 4.6**a** as a function of Zn-doping level. This panel demonstrates that the number of steps in the magnetisation seen in each sample, or the number of T_C values, is the same

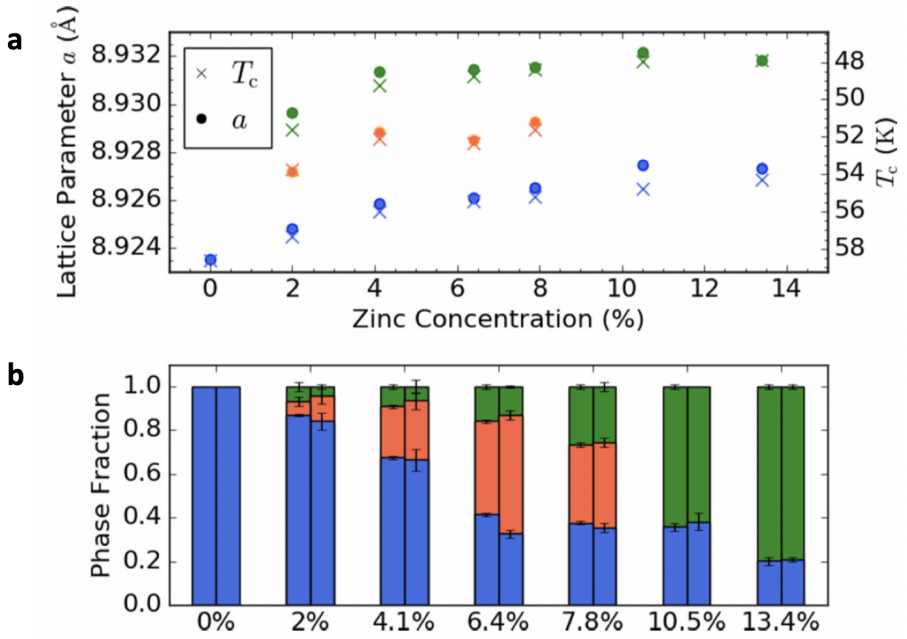

Figure 4.6: **a**, The lattice parameter and T_C of the identified Cu_2OSeO_3 structural phases is plotted as a function of Zn-doping. **b**, The volume fraction of each structural phase is plotted for each polycrystalline sample, as determined by the PXRD (left) and magnetometry (right) measurements.

as the number of structural phases required to fit the powder diffraction data. The panel also highlights the strong agreement between the two quantities: polymorphs with a larger lattice parameter also have a lower T_C. Since the substitution of Zn for Cu in the crystal structure is expected to both increase the lattice parameter [298], and decrease the value of T_C, this implies that the primary distinction between the structural phases in each sample is the level of Zn-doping they contain. Finally, Fig. 4.6**b** plots the phase volume fraction of the polymorphs in each polycrystalline sample as determined by the PXRD and magnetometry data, showing a remarkable agreement.

In summary, it was observed that an increase of Zn-doping decreased the value of T_C, while also increasing the lattice parameter. Measurements of the saturation magnetisation indicate that the Zn ions have a small preference to occupy the Cu(II) lattice sites. A combination of detailed magnetometry and PXRD measurements demonstrated that the observed splitting of the equilibrium skyrmion region in

polycrystalline $(Cu_{1-x}Zn_x)_2OSeO_3$ samples is due the presence of multiple structural phases. In each sample, these phases exhibit different values of T_C, and therefore enter the skyrmion state at different temperatures. The data suggests that the primary distinction between each structural phase is the level of Zn-doping. Because they only contain one structural phase, the single crystal samples do not exhibit the splitting of the skyrmion pocket. Therefore, it is not necessary to invoke more complex arguments about altered DMI values around each crystal lattice defect to explain the observed phenomenon [295]. It is likely that similar multiphase effects explain the enlarged skyrmion region seen in polycrystalline Ni-doped Cu_2OSeO_3 samples [217].

In further work performed by our collaborators at Warwick, it was demonstrated that by increasing the solid state reaction time for several weeks, one structural phase became dominant [218]. Therefore, if the reaction were to be continued for a prolonged period, it may be possible to achieve a single thermodynamically stable phase of polycrystalline $(Cu_{1-x}Zn_x)_2OSeO_3$.

Chapter 5

Increased Lifetime of Metastable Skyrmions by Doping

Metastable skyrmions have been observed in a range of skyrmion systems, formed by rapid field-cooling of the sample through the equilibrium skyrmion phase down to low temperatures [191]. It was noted in previous works that the inherent cation disorder present in $Fe_{0.5}Co_{0.5}Si$ [123] and the CoZnMn alloys [192, 193] may be responsible for the larger metastable skyrmion populations seen in these systems. The proposed nanoscale mechanisms of skyrmion decay, and the associated Bloch points thought to be responsible for topological unwinding [187, 199], were introduced in Sec. 1.4 and Sec. 1.5. One might expect that the doping-induced disorder would create defects or pinning sites, which may hinder the motion of the magnetic Bloch points as the metastable skyrmion decay, therefore increasing the metastable skyrmion lifetimes.

The Zn-doped Cu_2OSeO_3 single crystals, with their varying Zn-doping levels that were characterised in Ch. 4 are ideal for systematically exploring and quantifying the effect of doping on metastable skyrmions. This chapter will detail magnetometry, SANS and microwave absorption measurements observing the presence of metastable skyrmions in Zn-doped Cu_2OSeO_3, largely following a publication by the author on the topic [219]. Furthermore, it is shown that time dependent AC susceptibility measurements can be utilised to measure the metastable skyrmion lifetimes. By performing such measurements as a function of temperature across samples with a range of Zn-doping levels, it is revealed that even a small quantity

of Zn both dramatically increases the lifetime and substantially reduces the cooling rate required for the formation of the metastable SkL state. Detailed lifetime measurements demonstrate that pinning effects are responsible for the greatly increased metastable lifetimes.

5.1 Observation of Metastable Skyrmions

In order to investigate the behaviour and dynamics of metastable skyrmions, it was necessary to develop measurement techniques capable of discerning their presence. Magnetometry measurement provide an indirect, but nevertheless valuable, lab-based method of metastable skyrmion detection. However, as will be shown, magnetic resonance absorption spectroscopy and small angle neutron scattering measurements are able to directly identify signatures associated with metastable skyrmions.

5.1.1 Magnetometry

Magnetometry measurements performed for single crystal Zn-doped Cu_2OSeO_3 samples, with doping levels of 0%, 1.0%, 2.5% and 2.8% Zn, are shown in Fig. 5.1. For all measurements, the field was applied along the [111] crystal axis. The T_C of each crystal was determined from measurements of the magnetisation M as a function of decreasing temperature, and its numerically calculated derivative, shown in Fig. 5.1**a** and **b** respectively, as was done for the samples in Ch. 4. Measurements of M as a function of the applied magnetic field, shown in Fig. 5.1**c**, demonstrated that the saturation magnetisation decreases with Zn-doping level, as was seen for the polycrystalline samples in Sec. 4.5. Images of the single crystals studied in this chapter are shown in Fig. 5.1**d**.

As was discussed in Sec. 1.5, metastable skyrmions may be observed existing beyond the equilibrium skyrmion phase when FC the sample. It was demonstrated in Sec. 4.2 that AC susceptibility measurements are a powerful tool for determining magnetic phase boundaries in skyrmion systems. We performed AC susceptibility measurements on the 2.5% sample at a range of temperatures for both ZFC and FC

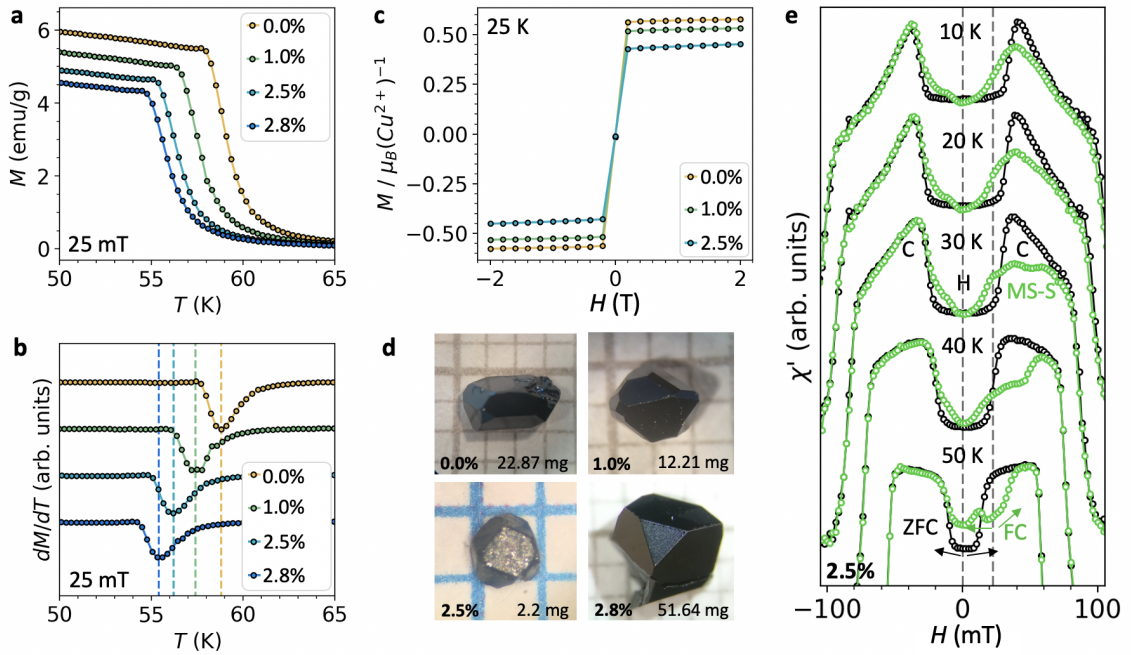

Figure 5.1: **a**, Magnetisation measured as a function of decreasing temperature for the single crystal samples. **b**, The numerically calculated gradient of the magnetisation as a function of temperature. **c**, The magnetisation measured as a function of applied magnetic field at 25 K for each sample. **d**, Photographs of the four Zn-doped samples. **e**, AC susceptibility measurements performed on the 2.5% sample after FC (green) and ZFC (black) processes at a range of temperatures.

procedures, as shown in Fig. 5.1**e**. Across all temperatures, there is a clear depression in the measured value of χ' around 22 mT after the FC process, which is consistent with the χ' signal observed for the equilibrium skyrmion state [144,205,263], and therefore indicates the presence of a metastable skyrmion population. However, this data does not provide definitive evidence for the formation of metastable skyrmions, and possess some disadvantages. Firstly, the observed χ' signal may be due to some other history-dependent effect of the FC procedure. Secondly, at lower temperatures it is challenging to determine the field extent of the supposed metastable skyrmion phase from features in the data. Therefore, other methods are required to conclusively attribute the observed χ' features to a metastable skyrmion state.

5.1.2 Microwave Absorption Spectroscopy

As discussed in 3.6, magnetic resonance spectroscopy measurements are able to probe the excitations of magnetic states. In addition to the two rotational and the breathing modes of the skyrmion lattice, the helical and conical state exhibit resonance modes associated with the procession of the spins either clockwise (H/C+) or counter clockwise (H/C-), relative to the chirality, or winding direction, of the magnetic state. Example magnetic resonance spectra measured as a function of the applied magnetic field after ZFC to 54 K in the 2.5% doped sample are shown in Fig. 5.2**a**. The colour map was created by fitting Lorentzian peaks to the raw absorption spectra at each field, as illustrated for selected fields in the right panel. As the field increases from 0 mT, the absorption associated with the helical and conical state is seen. In addition, at ∼20 mT, a further resonance is observed at 1 GHz with positive B slope, which can be attributed to the counter clockwise skyrmion mode [289]. Additional resonance modes exhibited by the skyrmion lattice, such as the clockwise and breathing modes, show weaker absorption, and are not visible in this data. At higher applied magnetic fields, the conical state signal gives way to a peak behaving similarly to a typical ferromagnetic state, where the sample exhibits a uniform magnetisation.

Measurements performed after FC with a rate of 1 K/min at 22 mT to 30 K in the 2.5% doped sample are shown in Fig. 5.2**b**. While at the higher temperature of 54 K the two helical and two conical modes could not be distinguished, at this lower temperature both states clearly exhibit two absorption branches associated with the clockwise and counter clockwise spin modes. A further resonance is detected between 20 and 80 mT with positive B slope, aesthetically similar to the skyrmion resonance seen at 54 K. This signal was not observed when performing ZFC measurements at the same temperature of 30 K, and it is therefore reasonable to attribute it to the presence of metastable skyrmions. At each field, this CCW metastable skyrmion resonance is exhibited simultaneously with the conical resonances, indicating the phase coexistence of both states. Spectra measured under the same conditions are shown in 5.2**c** and **d** for the 1.0% and 0.0% samples respectively. The resonance associated with the metastable skyrmion state is still visible in the 1.0% sample

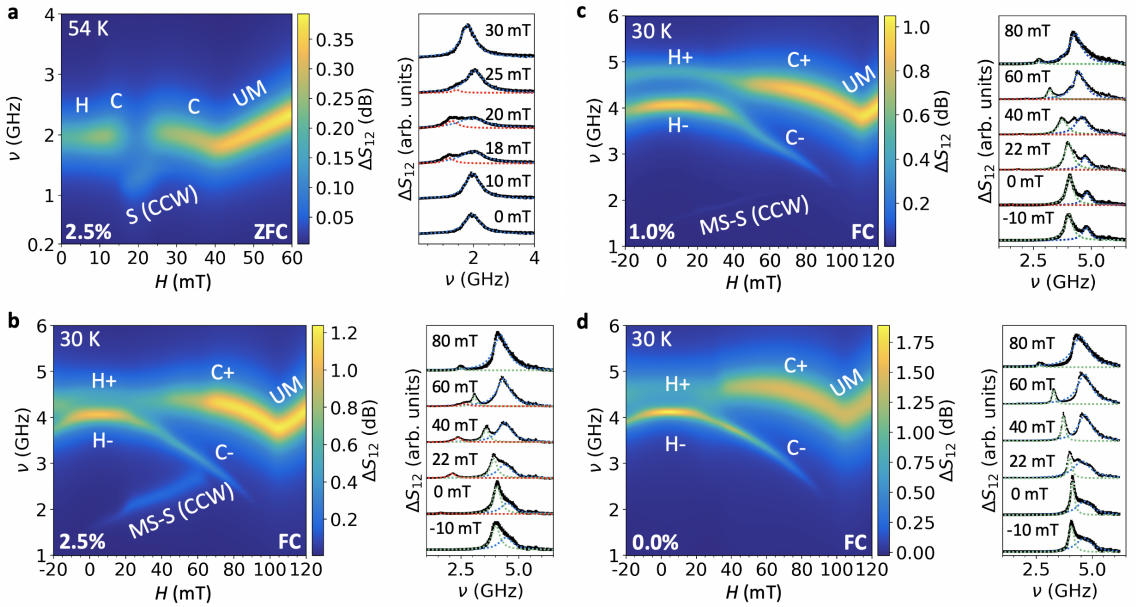

Figure 5.2: **a**, Magnetic resonance absorption spectra measured as a function of applied magnetic field after ZFC at 54 K in the 2.5% Zn-doped sample. Resonances attributed to the helical (H), conical (C), skyrmion (S) and uniform magnetisation (UM) states are labelled. **b-d**, Absorption spectra measured after FC to 30 K at 22 mT for the 2.5%, 1.0% and 0.0% Zn-doped samples respectively.

data, but at a much reduced intensity, while no such signal is observed in the pristine sample. This indicates that a smaller metastable skyrmion population has survived in the lower Zn-doped sample, and almost no population in the pristine sample. Since the cooling rate was fixed at 1 K/min for all three sets of measurements, this provides initial evidence that the presence of Zn-doping increases the lifetime of the metastable skyrmions, allowing more to survive the FC process at a specific cooling rate.

5.1.3 Metastable Skyrmion Phase Diagram

Phase diagrams for the 2.5%, 1.0% and 0.0% Zn-doped Cu_2OSeO_3 samples measured following the ZFC procedure are shown in 5.3**a-c**. The colour map plots the fitted intensity of the CCW skyrmion mode signal as a function of temperature and applied field, while the coloured points indicate the phase boundaries as determined by AC susceptibility measurements, demonstrating that the observation of the CCW

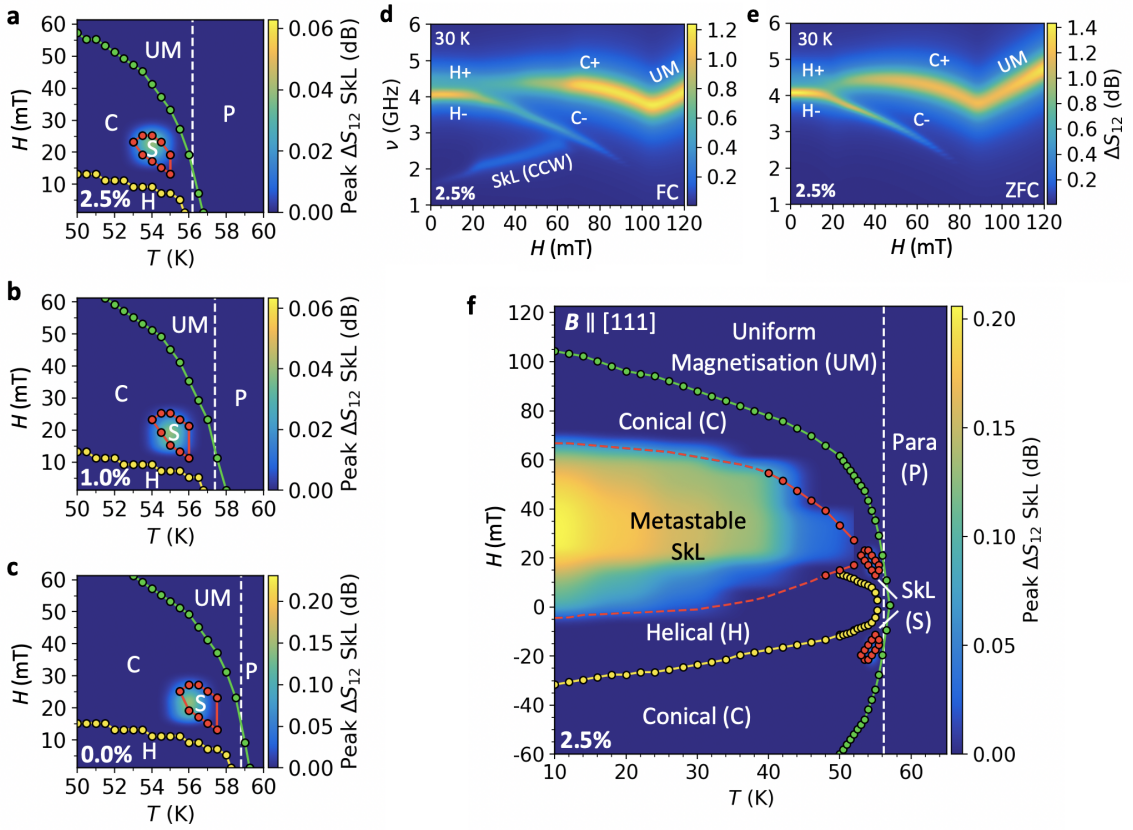

Figure 5.3: **a**-**c**, Magnetic phase diagrams determined after ZFC for the 2.5%, 1.0% and 0.0% Zn-doped samples respectively. **f**, Magnetic phase diagram measured after FC for the 2.5% sample. The dots indicate boundaries between the helical (H), conical (C), equilibrium skyrmion (S), metastable skyrmion, uniform magnetisation (UM), and paramagnetic (P) states as determined by AC susceptibility measurements. The colour map plots the intensity of the skyrmion breathing mode absorption peak.

skyrmion mode corresponds with the reduction in χ' signal associated with the skyrmion state.

Further FC measurements were performed on the 2.5% sample across a range of temperatures to determine the extent of the metastable skyrmion phase. A comparison between absorption spectra measured after FC and ZFC at 30 K are shown in 5.3**d** and **e**. The results of further FC measurements are summarised by the extended phase diagram in Fig. 5.3**f**, which demonstrates the large extent of the metastable skyrmion phase in comparison to the small equilibrium region, extending down to 0 mT at lower temperatures. Assuming that the intensity of the CCW skyrmion resonance is proportional to the metastable skyrmion population at low temperatures, it is clear that after FC, the metastable skyrmion state is stable and long-lived for increasing fields up to ∼60 mT. However, the intensity rapidly decreases when decreasing the field from 22 mT. In this low-field region of the phase diagram, the equilibrium state is the helical state, and therefore this rapid loss of skyrmion population at low field indicates that the metastable skyrmion state may more readily decay into helical domains than into to the conical state.

5.1.4 Small Angle Neutron Scattering

Small angle neutron scattering (SANS) measurements were employed to confirm our identification of the metastable skyrmion state. These measurements were performed on the larger 2.8% Zn-doped sample. The experimental set up is displayed in Fig. 5.4**a**. The sample and field can be rotated either parallel of perpendicular to the incoming neutron beam. Fig. 5.4**b** illustrates the location of the skyrmion lattice and conical magnetic peaks in reciprocal space, demonstrating that the wavevectors of the skyrmion and the conical states respectively point perpendicular and parallel to the applied magnetic field [175]. With the magnetic field applied along the [111] crystal axis and parallel to the neutron beam, Fig. 5.4**c** displays the sixfold-symmetric pattern characteristic of the hexagonal equilibrium skyrmion state at 54 K, as indicated by the blue circle in Fig. 5.4(b), with a skyrmion spacing of 63 ± 4 nm. The error indicates the distribution of spacings present in the sample, calculated from the width of the skyrmion lattice peak in the q direction.

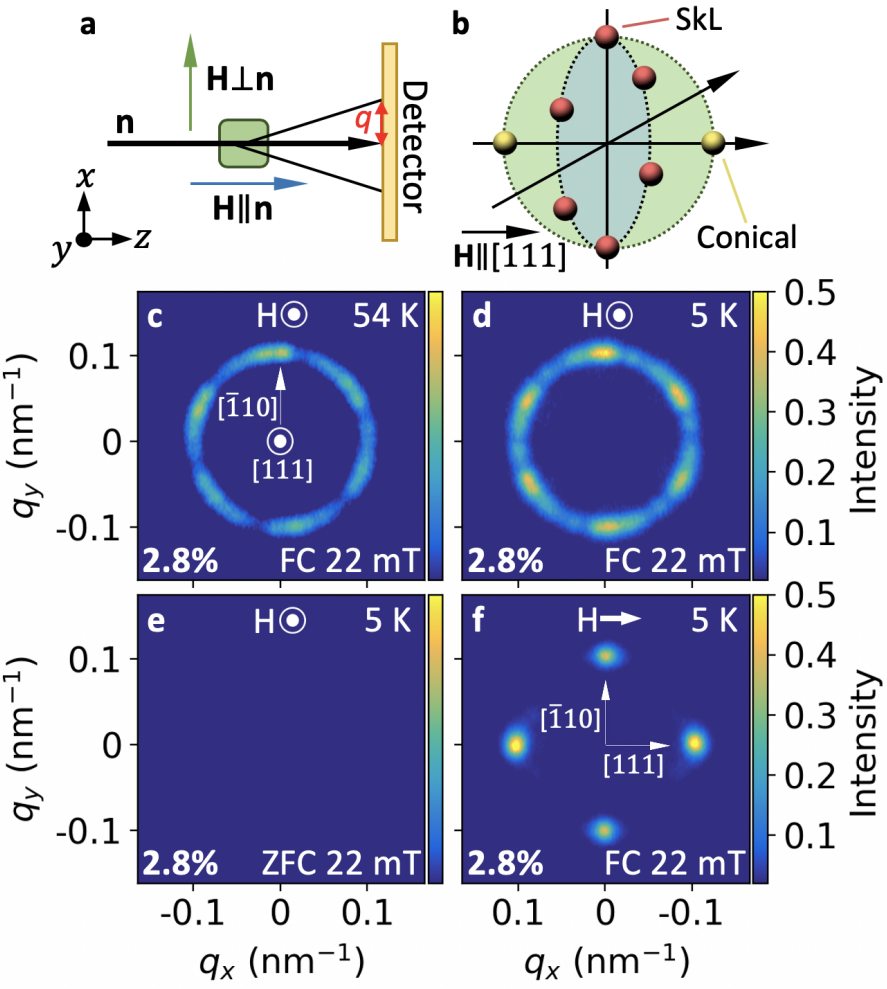

Figure 5.4: **a**, Schematic diagram of the experimental setup of the small angle neutron scattering (SANS) measurements, indicating the orientations of the magnetic field with the neutron beam (**n**). **b**, Illustration of the locations of the skyrmion (red) and conical (yellow) peaks in reciprocal space. The blue and green circles indicate the peaks observed when the field is parallel and perpendicular to the neutron beam. **cf**, SANS diffraction patterns recorded at selected temperatures, after both field cooling (**a**,**b**,**d**) and zero field cooling (**c**) procedures, with the applied magnetic field parallel (**a**,**b**,**c**) and perpendicular (**d**) to the incident neutron beam.

Fig. 5.4**d** shows the SANS pattern recorded after FC down to 5 K at 22 mT. The resulting sixfold pattern confirms the survival of the metastable skyrmion state at low temperatures, with a spacing of 63±4 nm. Fig. 5.4**e** demonstrates the absence of a sixfold pattern at 22 mT after the ZFC procedure to 5 K, indicating no skyrmions are present. Here, the magnetic state is expected to consist of helices aligned to the [100] crystalline axes. However, as no [100] directions are perpendicular to the neutron beam, we observe no diffraction intensity. Finally, Fig. 5.4**f** displays the SANS pattern measured after FC to 5 K with the magnetic field applied perpendicular to the neutron beam. Here, the vertical diffraction peaks demonstrate the presence of domains of the metastable skyrmion state, while the horizontal peaks indicate the coexistence of competing conical domains, as indicated by the green circle in Fig. 5.4**b**.

5.2 Lifetime Measurements

Now that various methods have been demonstrated for identifying the presence of metastable skyrmions, their associated annihilation dynamics can be investigated. Metastable skyrmions have been observed to decay to the conical state following a temperature dependent lifetime, τ [190, 193]. Investigating these mechanics requires a method to determine this lifetime using time-resolved measurements. Due to the long measurement times required for these measurements, AC susceptibility measurements proved to be a suitable lab-based technique, allowing for many lifetimes to be measured at a range of temperatures across different samples.

AC susceptibility data measured after ZFC and FC procedures at 50 K in the 2.5% doped sample are plotted in Fig. 5.5**a**. We previously demonstrated that the decreased value of χ' around 22 mT indicates the presence of metastable skyrmions. During the metastable decay process, the real part of the AC susceptibility, χ', relaxes from its reduced value in the skyrmion state to the higher value in the conical state, as illustrated by red arrow and the AC susceptibility data in Fig. 5.5**a**. The population of metastable skyrmions $S(t)$ has been observed to follow a decay modelled by a stretched exponential [193], with a temperature dependent

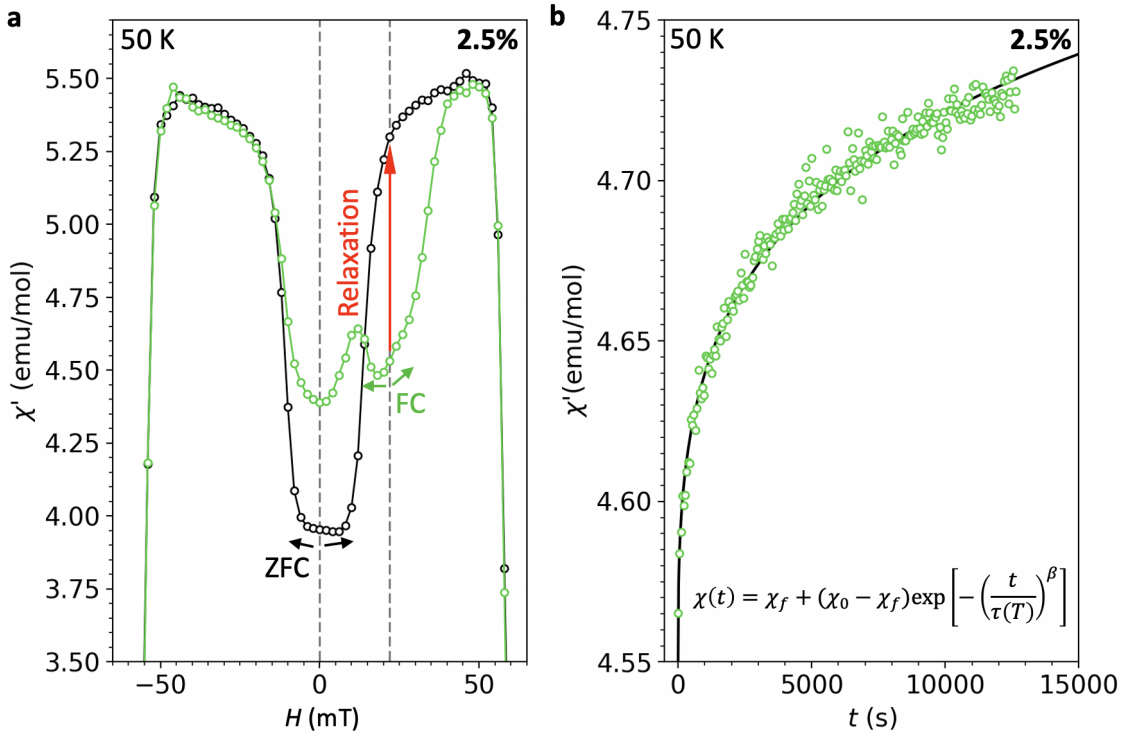

Figure 5.5: **a**, AC susceptibility measurements performed after ZFC (black) and FC (green) at 50 K in the 2.5% Zn-doped sample. The relaxation of χ' as the metastable skyrmions decay is indicated. **b**, Time-resolved AC susceptibility measurements performed after FC to 50 K in the 2.5% sample. The data is fitted with a stretched exponential.

lifetime, $\tau(T)$,

$$S(t) = S_0 \text{exp}\left[-\left(\frac{t}{\tau(T)}\right)^{\beta}\right], \tag{5.2.1}$$

where S_0 is the metastable population after cooling. Assuming that changes in $\chi'(t)$ are proportional to changes in $S(t)$, we can model the evolution of the AC susceptibility data with,

$$\chi'_N(t) = -\text{exp}\left[-\left(\frac{t}{\tau(T)}\right)^{\beta}\right]. \tag{5.2.2}$$

Here, the AC susceptibility is normalised, $\chi'_N = (\chi'_f - \chi'(t))/(\chi'_f - \chi'_0)$, where χ_0 is the initial value of χ' at $t = 0$, and χ_f is the value the system is tending to as $t \to \infty$.

An example lifetime measurement, performed by measuring χ' as a function of time at a fixed temperature and magnetic field, is shown in Fig. 5.5**b**. A fit to the equation in 5.2.2 reveals that the data is well described by the stretched exponential, allowing the values of τ and β to be extracted. The inclusion of the stretching parameter β is necessary to fit the data, and gives an indication of the spread of lifetimes present in the sample. There are a number of possible explanations as to why the samples may display a distribution of lifetimes. For example, the effects of demagnetisation would cause the magnetic field to be inhomogeneous throughout the sample [299], and it has previously been demonstrated that metastable skyrmion lifetime varies with field [202]. Another possibility is an inhomogeneous distribution of Zn within each crystal, which might alter the distribution of lifetimes throughout the spatial extent of the sample. However, studies of skyrmion formation and annihilation dynamics in Cu_2OSeO_3 around the equilibrium skyrmion phase using frequency-dependent AC susceptibility also point towards a distribution of relaxation times [262].

Lifetime measurements were then performed at a range of temperatures after FC at 22 mT in the 2.5%, 1.0% and 0.0% samples. At each temperature, an additional measurement was made by performing the FC* procedure to the same field and temperature point, giving an estimate for the value of χ'_f - the value of χ' expected

after all metastable skyrmions have decayed to the conical state. Using this value, $\chi'_N(t)$ was calculated and the data sets were fitted to Eq. 5.2.2. The resulting data and fits for each sample are shown in Fig. 5.6**a**-**c**.

Fig. 5.6**e** displays the measured values of $\tau(T)$ for each crystal, plotted as a function of $(T - T_s)/T$, where T_s is the lowest temperature extent of the equilibrium skyrmion state, taken as 4 K below T_c for all crystals. This is the point at which the metastable skyrmion lifetime should reach a minimum, just on the edge of the equilibrium region. It is evident that for a given $T - T_s$, the 2.5% crystal has a lifetime longer by a factor of ∼50 when compared to the 0% crystal.

5.3 Arrhenius' Law

The relationship between the lifetime of the metastable skyrmion state and the temperature of the sample allows us to model the measured lifetimes using Arrhenius' Law [190],

$$\tau(T) = \tau_0 \exp\left[\frac{-E_b}{k_B T}\right] = \tau_0 \exp\left[a\frac{(T_s - T)}{T}\right]. \tag{5.3.3}$$

Here, the typical activation energy term has been replaced with the energy barrier E_b protecting the metastable skyrmion state. As the sample approaches T_s, the height of E_b, and therefore the lifetime, are reduced. For the skyrmion lattice to conical transition, the temperature dependence of the energy barrier can be approximated as $E_b/k_B = a(T - T_s)$, with a as the linear proportional constant [190]. In typical chemical reactions, the energy barrier is taken as constant at all temperatures. However, previous studies support the suggestion that the energy barrier protecting the skyrmion state from the conical state varies with temperatures [262].

Using this framework, and the model of skrymion strings unwinding via Bloch point formation and motion, we present two possible ways in which the lifetime of the metastable skyrmion state can be increased with doping, as depicted in Fig. 5.6**d**. In Scenario 1, the value of a is increased, corresponding to an increase in the energy barrier which must be overcome to unwind the skyrmion state. In Scenario 2, the value of τ_0 is increased. An important component of this prefactor, which can be thought of as an attempt frequency, is an entropic correction, which concerns

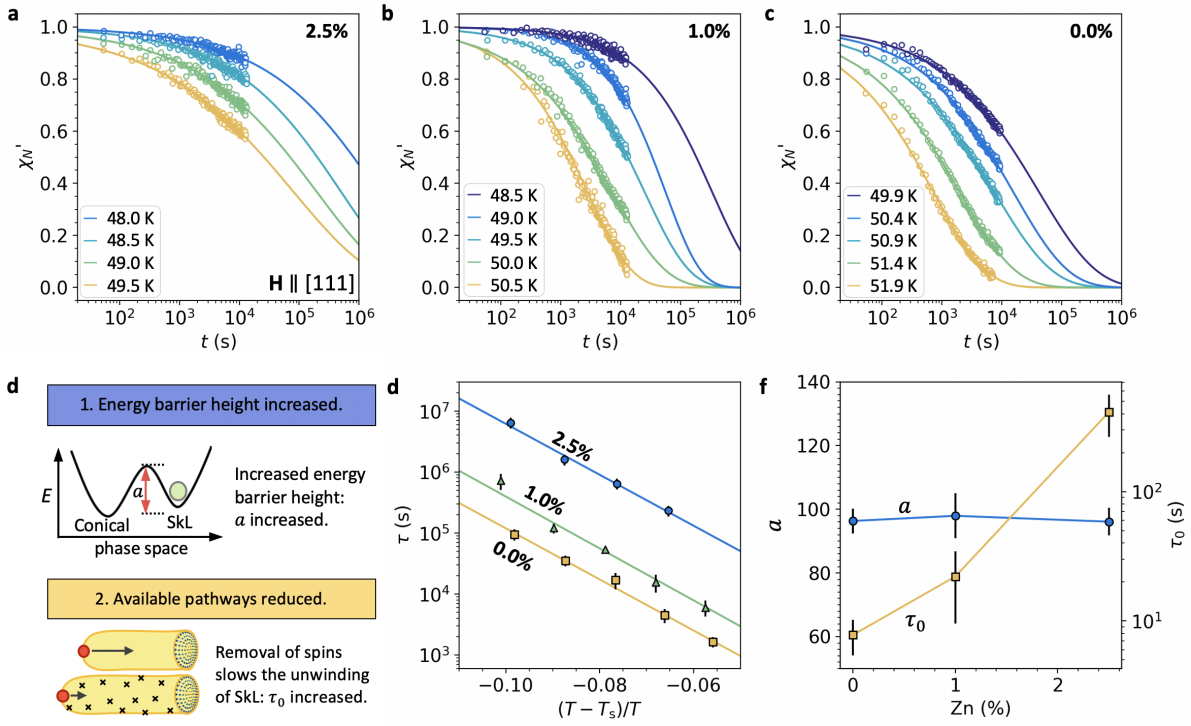

Figure 5.6: **a-c**, Normalised, time-resolved AC susceptibility measurements at a range of temperatures for the 2.5%, 1.0% and 0.0% crystals respectively. The datasets are fitted with stretched exponential functions. **d**, Schematic representations of the two possible scenarios for increasing the lifetime of metastable skyrmions, based on arguments from Arrhenius' Law. **e**, The extracted lifetimes from **a-c** plotted as a function of $T - T_s$, and fitted with Arrhenius' Law, determining values for τ_0 and a. **f**, The fitted a and τ_0 parameters are plotted as a function of the Zn-doping level.

the available pathways across an activation barrier [202,300]. Therefore, if there are fewer available pathways, the lifetime of the metastable state would be increased.

We utilise equation (5.3.3) to fit the datasets in Fig. 5.6(e) and extract the gradient, a, and the intercept, τ_0, for each crystal. Fig. 5.6f displays these fitted parameters, plotted as a function of Zn-doping level. It is clear that a is constant across all the crystals within experimental uncertainty, with an average value of 95 ± 3 which corresponds to an E_b/k_B of $\sim 5 \times 10^3$ K at 0 K. The energy barrier height is therefore not substantially altered by the introduction of non-magnetic zinc ions. In contrast, τ_0, plotted on the secondary, logarithmic axis of Fig. 5.6(f),

exhibits a non-linear increase with Zn-doping, with values of 150 ± 50, 14 ± 4 and 3 ± 1 seconds for the 2.5%, 1.0% and 0.0% crystals respectively. The magnetic structure of Cu_2OSeO_3 is composed of tetrahedra formed of four ferrimagnetically ordered Cu spins, which act as a single spin [152, 153]. If one of the Cu atoms were replaced by a non-magnetic Zn ion, then the number of accessible spin states of each tetrahedra would be greatly reduced, lowering the entropy of the system. This would be expected to limit the number of available pathways by which the Bloch points can overcome the energy barrier to unwind the skyrmion strings. Another interpretation of this result is that τ_0 would also be increased by the introduction of more pinning sites, but with the same pinning energy, as might be expected from an increase in Zn-doping.

5.4 Cooling Rate Dependent Population

The fraction of metastable skyrmions which survives after FC, S_0, is related to the cooling rate, k: because the lifetime of the metastable skyrmion state is shortest just below T_s, cooling through this region slowly results in a considerable loss of skyrmion population. We investigated this relationship by measuring χ' as a function of field after FC at a range of k between 0.5 and 40 K/min. The results for the 2.5% and 0.0% crystals, measured 10 K below T_s, are plotted in Fig. 5.7**a** and **b** respectively (blue-yellow points). These measurements are contrasted with data measured after the ZFC (black) and FC* (red) procedures. We assume that the difference in χ' between the FC and FC* processes, $\Delta\chi' = \chi'_{FC^*} - \chi'_{FC}$, is proportional to the population of metastable skyrmions. In Fig 5.7**c**, the measured value of $\Delta\chi'$ at 22 mT is plotted as a function of cooling rate for all three crystals. For all cooling rates, the value of $\Delta\chi'$ in the 2.5% crystal is far greater than that of the 0.0% crystal, and we therefore infer that the population of metastable skyrmions is substantially higher.

In order to estimate the metastable skyrmion population in each sample from this experimental data, we calculated the expected metastable skyrmion population loss during FC. Our derivation (see Appendix A Sec. A.1) yields an expression for

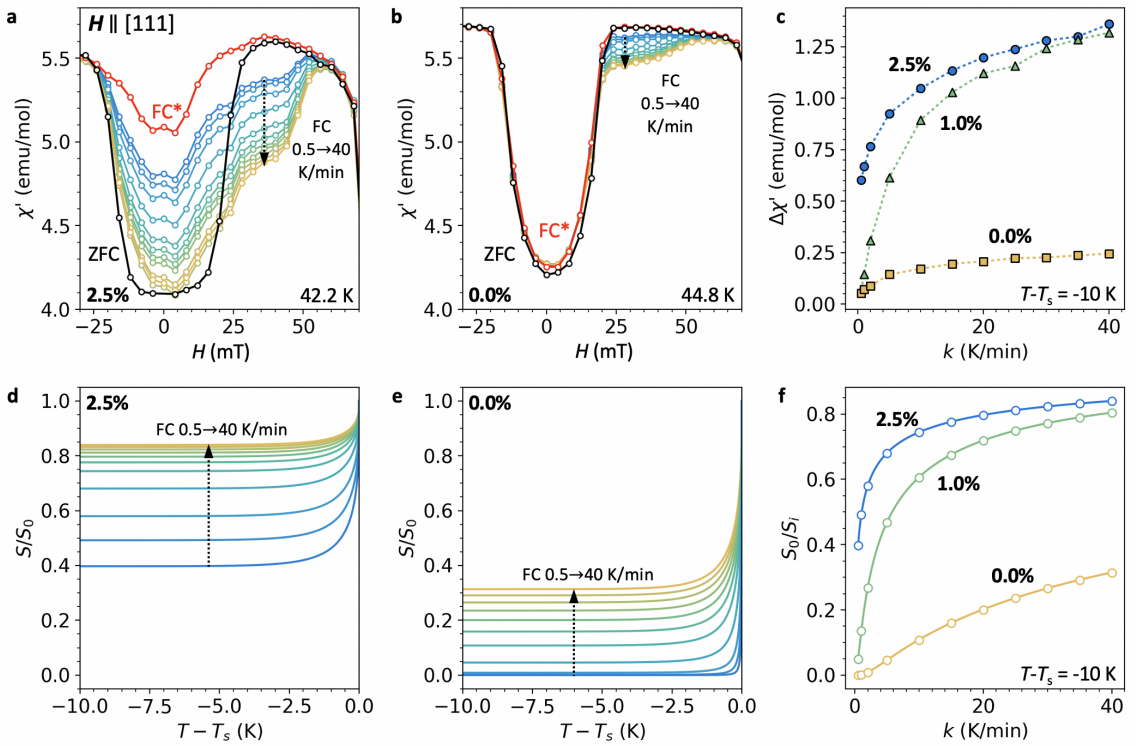

Figure 5.7: **a**,**b**, AC susceptibility, χ', plotted as a function of applied magnetic field for the 2.5% and 0.0% Zn-doped samples respectively, measured after ZFC (black) and FC* (red) procedures at 10 K below T_s. Multiple FC datasets are also shown, measured after different cooling rates between 0.5 (blue) and 40 (yellow) K/min. **c**, The difference between the FC and FC* χ' data, $\Delta\chi'$, measured at 22 mT in all samples, plotted as a function of cooling rate. **d**,**e**, The simulated evolution of the metastable skyrmion population for the 2.5% and 0.0% crystals, plotted as a function of temperature below T_s at different cooling rates, calculated using values for a and τ_0 from Fig. 5.6. **f**, The final simulated population of metastable skyrmions at 10 K below T_s, plotted as a function of cooling rate for all three samples. The circles show the simulated values at the same cooling rates measured in **c**.

the metastable population after cooling from T_s to the final temperature T_f at a rate of k,

$$S_0 = S_i \exp\left[\int_{T_\mathrm{s}}^{T_f} \frac{-\beta}{T - T_\mathrm{s}} \left(\frac{T - T_\mathrm{s}}{k\tau_0 \exp\left[a\frac{T_\mathrm{s}-T}{T}\right]}\right)^{\beta} dT\right], \tag{5.4.4}$$

where S_i is the initial skyrmion population before cooling. We use this model, and the values for β, a and τ_0 fitted for each crystal in Fig. 5.6, to simulate the evolution of the skyrmion population as a function of temperature for cooling rates between 0.5 and 40 K/min. The results for the 2.5% and 0.0% crystals are displayed in Fig. 5.7**d** and **e**. It is clear that largest population loss occurs in the first ∼2 K below T_s, after which the long lifetime effectively locks in the metastable skyrmion population. The final calculated metastable skyrmion population S_0/S_i for each crystal at $T - T_\mathrm{s} = 10$ K is plotted as a function of k in Fig. 5.7**f**.

The strong qualitative agreement between the experimental data in Fig. 5.7**c** and the simulated model in Fig. 5.7**f**, which relies upon our derivation, suggests that the Arrhenius model for $\tau(T)$ is valid, and that $E_b/k_\mathrm{B} = a(T_\mathrm{s} - T)$ is a reasonable assumption for the relationship between energy barrier and temperature. Together, these plots indicate that although a cooling rate as high as 40 K/min cannot achieve a metastable population of ∼50% in the 0.0% crystal, this is achieved at cooling rate of just 1 K/min in the 2.5% crystal.

5.5 Conclusions

The results of the detailed AC susceptibility measurements have shown that doping Zn ions onto the Cu sites in Cu_2OSeO_3 crystals increases the lifetime of the metastable skyrmion state. As a result, the cooling rate required to achieve a substantial metastable population when field-cooling is greatly reduced. The analysis of lifetimes measured as a function of temperature suggests that the removal of spins caused by the substitution of the magnetic Cu ions with non-magnetic Zn ions is responsible for this increased lifetime, limiting the number of available pathways by which the metastable skyrmion strings can unwind. The introduction of pinning sites using doping can therefore dramatically extend the lifetime of metastable

skyrmions. It is expected that this effect can be exploited to engineer the metastable skyrmion lifetime in other doped skyrmion-hosting systems.

Chapter 6

Pinning of Helimagnetic Phase Transitions by Doping

While chemical substitution can be utilised to alter the balance of magnetic energies in skyrmion systems, we have seen that it can also introduce pinning effects: as we saw in Ch. 5, Zn-doping Cu_2OSeO_3 increased the lifetime of the metastable skyrmions. Such pinning can affect other dynamic behaviour. For example, it might inhibit current-induced skyrmion motion - a phenomenon crucial to proposed skyrmion racetrack devices [55, 84]. Extrinsic defects and impurities can attract or repel skyrmions [301], or act as nucleation or annihilation sites [302], which might be exploited for technological implementation. In combination with alterations to the energy balance mentioned above, these dynamical pinning effects must be considered when engineering the properties of skyrmion materials for future applications.

In this chapter, detailed AC magnetometry and small angle neutron scattering (SANS) is utilised to investigate the effect of doping, and the role of cubic anisotropy, on helimagnetic phase transition dynamics in $(Cu_{1-x}Zn_x)_2OSeO_3$. We detail the spin textures exhibited by Cu_2OSeO_3 in Sec. 6.1. Typical phase diagrams are considered in Sec. 6.2, revealing the AC susceptibility signals exhibited by each magnetic state. This is followed by Sec. 6.3, where the detailed features of the real and imaginary components of the AC susceptibility measurements are examined and interpreted. Comparison of the helical-conical phase boundary in both samples reveal significant history-dependent pinning behaviour in the doped sample. Further investigation

of the dissipative effects indicated by peaks in the imaginary component reveals unexpected low temperature behaviour in both samples.

6.1 Chiral Magnetic States

Illustrations of the spin textures exhibited by Cu_2OSeO_3, and their corresponding SANS patterns in the two experimental configurations, are displayed in Fig. 6.1. At zero magnetic field, the helical structure is the equilibrium state, consisting of a continuous rotation of spins orthogonal to a propagation vector. In a bulk single crystal, this vector aligns along the $\langle 100 \rangle$ crystal axes due to the cubic anisotropy present in the system, giving rise to three distinct helical domains, labelled H1, H2 and H3 in Fig. 6.1**c**. Scattering from these domains can be observed in the field-parallel configuration (H1 domains), or in the field-perpendicular configuration (H2,3 domains), as shown in Fig. 6.1**d** and **e**.

Upon increasing the applied magnetic field, the helical state degeneracy is lifted, and the structure transforms to the conical state, illustrated in Fig. 6.1**f**, consisting of a continuous rotation of spins at an acute angle to the propagation vector, which is aligned to the applied field. In the field-parallel configuration, no magnetic scattering is observed, as displayed in Fig. 6.1**g**. In the field-perpendicular orientation, a single pair of conical magnetic satellites are observed, labelled C in Fig. 6.1**h**. At higher applied magnetic field, the angle of the spins to the propagation vector is reduced, resulting in a lower intensity of the magnetic diffraction peaks, before a uniform magnetisation texture is reached.

Close to 55 K and 22 mT, the skyrmion state is formed in a plane perpendicular to the applied magnetic field, as illustrated in Fig. 6.1**i**. This image highlights the elongated tube-like structure exhibited by magnetic skyrmions in bulk materials [179]. In the field-parallel configuration, three pairs of magnetic scattering peaks are observed, a characteristic signature of the hexagonal skyrmion lattice, labelled S in Fig. 6.1**j**. Due to rotational disorder of the skyrmion lattice, weak scattering can be observed in the field-perpendicular configuration, as shown in Fig. 6.1**k**. This corresponds to the intensity at the top of the ring of scattering in **j**. For further

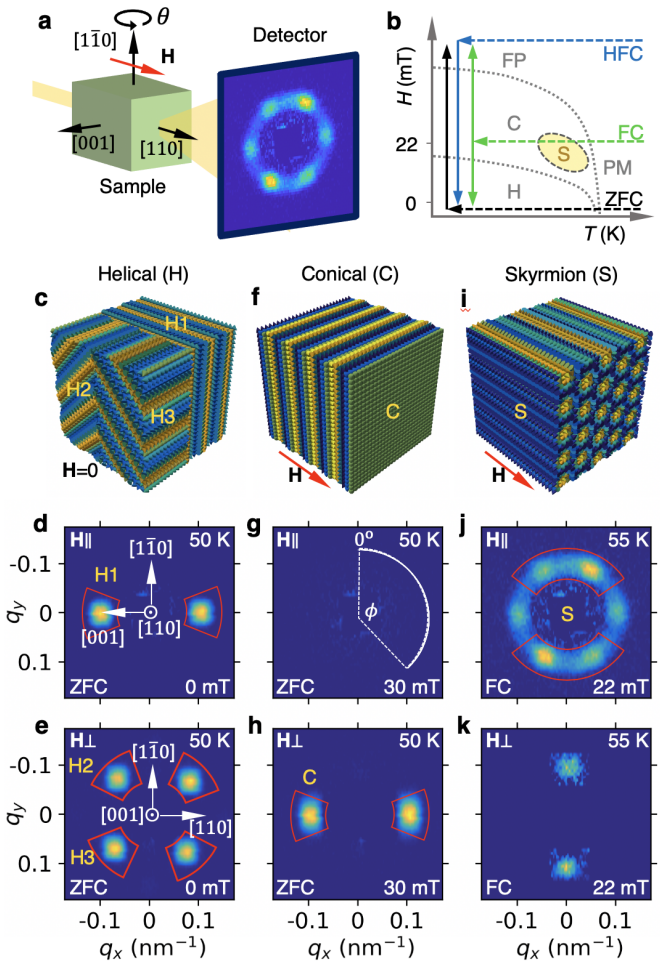

Figure 6.1: **a**, Schematic illustration of the small angle neutron scattering experiment setup. The sample and applied field can be rotated together through θ to observe the magnetic state with magnetic field directed both parallel and perpendicular to the neutron beam. The relative orientation of the Cu_2OSeO_3 samples is shown. **b**, An example, generic skyrmion material phase diagram, showing the helical (H), conical (C) and skyrmion (S) states. Representations of the measurement paths for the zero-field cooled (ZFC), high-field cooled (HFC) and field cooled (FC) procedures are shown. Three-dimensional visualisations of the spin textures and characteristic SANS patterns measured for the helical **c**-**e**, conical (**f**-**h**) and skyrmion states (**i**-**k**) states, with the field both parallel (**d**, **g**, **j**) and perpendicular (**e**, **h**, **k**) to the neutron beam. Sector boxes indicate regions of scattering summed to report intensities in subsequent figures. The azimuthal angle around each SANS pattern, ϕ, is illustrated in panel **g**.

analysis in this chapter, the intensities of the H1, H2, H3, C and S magnetic peaks as a function of applied field are reported. These intensities were calculated by summing the total counts measured inside the red sector boxes as specified in Fig. 6.1**d-k**.

6.2 AC Susceptibility Phase Diagrams

Magnetic phase diagrams are shown in Fig. 6.2 for the pristine and 2% Zn-doped samples measured using AC susceptibility magnetometry. In Fig. 6.2**a** and **b**, the colormap directly plots the real component of the AC susceptibility, χ', measured as a function of applied magnetic field after ZFC to temperatures between 50 and 60 K. At the low frequency limit, this quantity measures the local gradient of the magnetisation with the applied field, and is useful for distinguishing the temperature and field extent of the magnetic phases.

The boundaries between these magnetic phases are denoted by critical fields, H_{x}. The helical state can be identified by the reduced value of χ' close to 0 mT, and extending for increasing field up to H_{c1}, at the boundary with the conical state. In turn, the conical state exists up to H_{c2}, before transitioning to the uniform magnetisation state, characterised by a reduction in χ'. Close to T_{C}, the skyrmion state can be identified by the characteristic dip in AC susceptibility at $\sim$20 mT, a well-established signature common to skyrmion hosting bulk chiral magnets [30]. The lower and upper field boundaries of this phase are denoted H_{s1} and H_{s2} respectively. Looking at this real component, the phase diagrams for both the pristine and doped sample show no dramatic differences besides the reduction of T_{C} with increased Zn content.

At specific probe frequencies, dynamic processes may be excited, causing a phase difference between the oscillating magnetisation and the drive field. This manifests in the imaginary component of the AC susceptibility, χ'', indicating relaxation-induced energy losses, [303]. This dissipation is associated with thermodynamically irreversible dynamic processes such as domain wall motion, or, at a phase boundary, excitation between two competing magnetic phases [261]. The χ'' component of the

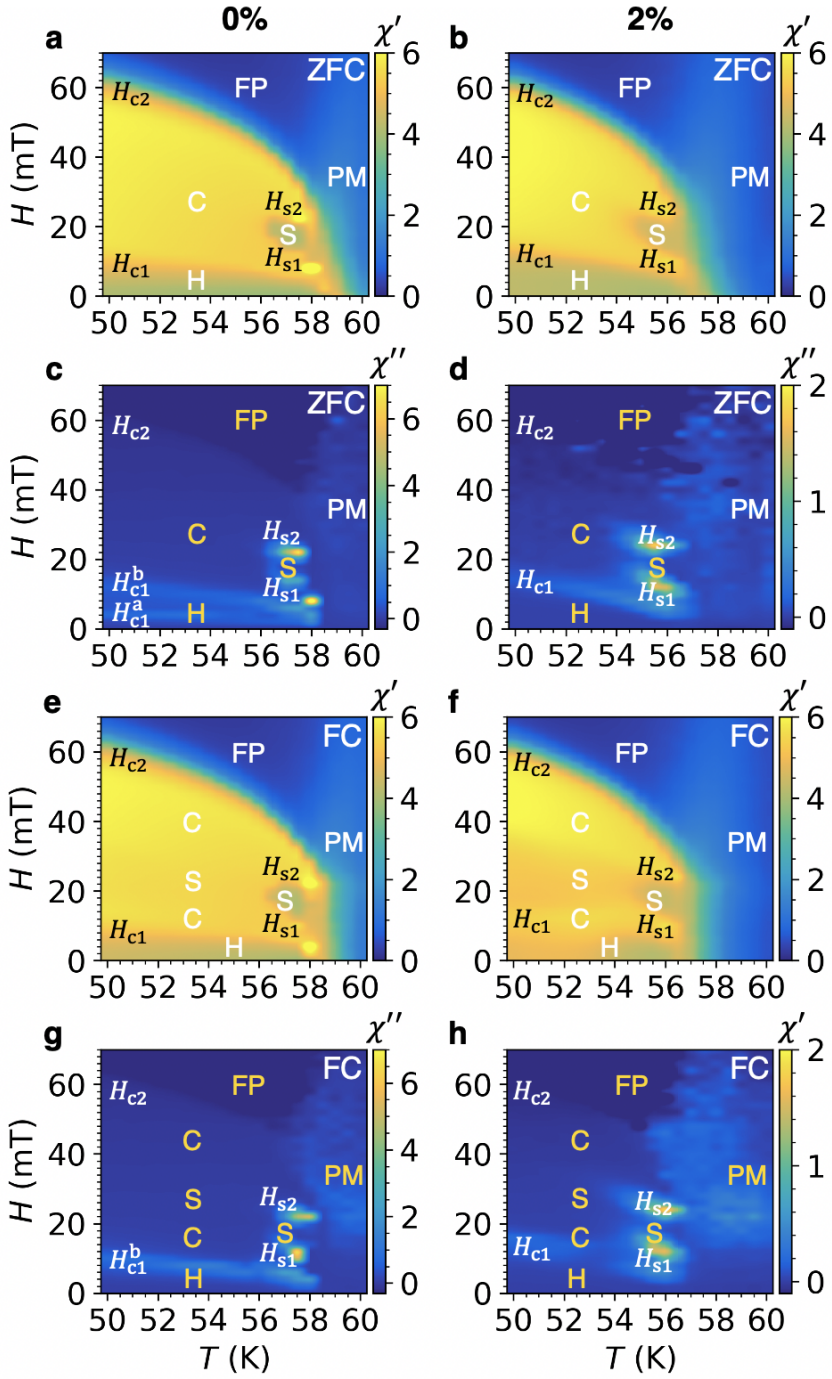

Figure 6.2: **a**-**d**, Magnetic phase diagrams, as determined by AC susceptibility measurements following the ZFC procedure, for the 0% and 2% Zn-doped samples respectively. **e**-**h** The same, but following the FC procedure. The helical (H), conical (C), skyrmion (S), uniform magnetisation (UM), and paramagnetic (PM) states are labelled. The real component χ' is plotted in **a**, **b**, **e**, **f** and the imaginary component χ'' in **c**, **d**, **g**, **h**. Critical fields marking the phase boundaries between the H and C (H_{c1}), C and UM (H_{c2}), S and C ($H_{s1,2}$) states are labelled.

AC susceptibility for both samples is plotted in Fig. 6.2**c** and **d**.

Second order phase transitions, characterised by the continuous transformation of one state into another, are not expected to exhibit a χ'' signal [225]. This can be seen by the lack of χ'' peak at H_{c2} in both Fig. 6.2**c** and **d**, as the conical state continuously deforms to the uniform magnetisation state. On the other hand, for first order phase transitions, characterised by coexistence of the two phases in the vicinity of the transition, a χ'' signal can be expected: there is significant energy loss occurring as the oscillating magnetic field drives the boundaries between the two coexisting phase volumes [225]. Such an effect is observed at the edges of the skyrmion phase in Fig. 6.2**c** and **d**, H_{s1} and H_{s2}, where a large χ'' signal is exhibited, indicating the annihilation and formation of skyrmions to and from the conical state [203]. Further χ'' peaks seen at H_{c1} indicate the helical to conical first order phase transition.

The magnitude of χ'' peaks associated with first order magnetic phase transitions can be modified by several factors [261]. Firstly, χ'' exhibits a frequency dependence, with the maximum indicating the resonant frequency of the excited dynamic processes [205, 304]. Therefore, as we only measure at 10 Hz, a change in the size of the χ'' peaks could be associated with a shift of this resonant frequency, or a broadening of the resonance due to the introduction of a range of relaxation timescales [262]. Secondly, the peak can be reduced when phase coexistence in the first order transition is suppressed, as there can be no excitation between the two magnetic states, and therefore no energy losses [225]. Finally, when considering the decay of a metastable state, transitions to the ground state are energetically preferred despite the coexistence of the magnetic states. Thus, the oscillating field may only drive the transition in one direction, and no dissipative signal is expected [225]. Distinguishing between these scenarios is challenging, but by combining the AC susceptibility data with SANS measurements, a level of understanding may be established.

Additional phase diagrams, measured following the FC measurement procedure are shown in Fig. 6.2**e-h**. The primary difference between these phase diagrams is the clear reduction in χ' signal at temperatures lower than the equilibrium skyrmion

phase, between ∼18-35 mT, particularly in the 2% Zn-doped sample, which is indicative of the formation of metastable skyrmions. A more thorough investigation of the differences between each cooling procedure, and between each sample, is detailed in the following section.

6.3 Temperature-Dependent AC Susceptibility

AC susceptibility data sets measured at a range of temperatures for both the pristine and doped samples, and following the ZFC, HFC and FC measurements procedures, are shown in Fig. 6.3. Critical field points at each phase boundary are indicated by the coloured vertical lines, and were determined by features in the data. The H_{c2} points were estimated to be at the inflection point in the χ'' data at high fields, most easily seen in Fig. 6.3**a3**. Below the equilibrium skyrmion region, no obvious feature exists for the upper skyrmion phase boundaries, H_{s2}, and the majority of the lower boundaries, H_{s1}. Therefore, these values were estimated by comparing features in the χ' data following the FC and ZFC/HFC procedures. For all the H_{c1} points, and for H_{s1} points below 40 K in the doped sample, the field value was obtained by fitting a Gaussian distribution with a linear background to the associated peak in the χ'' data.

A summary of the fitted/estimate values of the critical fields, H_x, following each measurement procedure, are plotted as a function of temperature in Fig. 6.4**a** and **b**, forming an extended magnetic phase diagram for the pristine and doped samples. In Fig. 6.4**c** and **d**, the fitted intensity of the χ'' peaks (taken as the area under each peak) at H_{c1} and H_{s1} are plotted as a function of temperature for each sample. In the following analysis, we shall explore the detailed features of the AC susceptibility data at each temperature in Fig. 6.3, while discussing the implications of these behaviours with reference to the summary panels in Fig. 6.4.

6.3.1 Equilibrium Skyrmion Phase

We first consider the data in Fig. 6.3**a**, recorded at 57 K and 56 K for the pristine and doped samples respectively. At these temperatures, the samples exhibit the

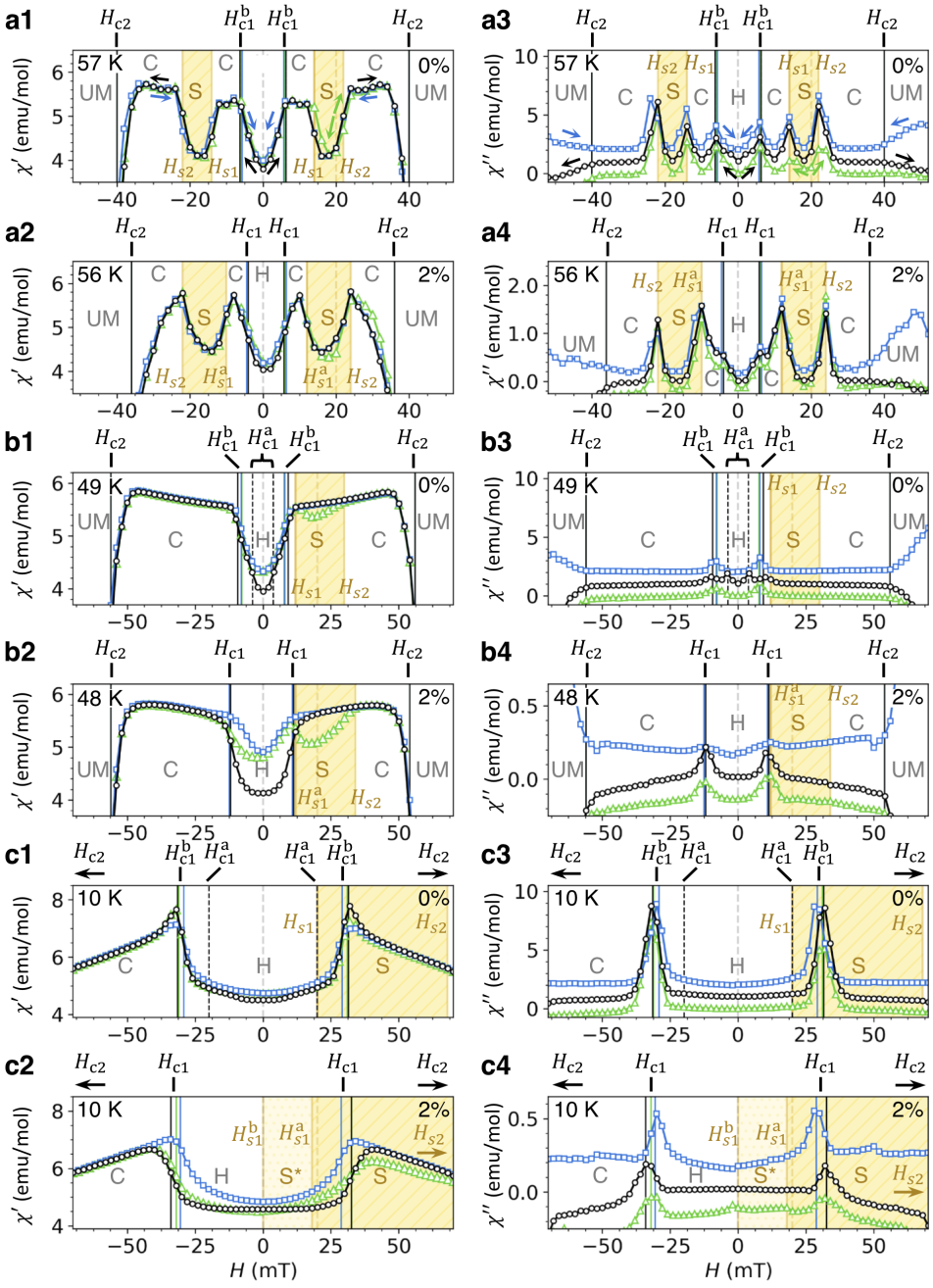

Figure 6.3: **a-c**, The real (1 and 2), and imaginary (3 and 4), components of the AC susceptibility data measured as a function of magnetic field at selected temperatures for the pristine (1 and 3) and doped (2 and 4) samples. Data acquired following the ZFC (black circles), HFC (blue squares) and FC (green triangles) measurement procedures is shown. Coloured vertical lines indicate the critical field values for phase transitions following each measurement procedure. The yellow regions indicate the extent of the skyrmion state after FC. The location of the helical (H), conical (C), skyrmion (S) and uniform magnetisation (UM) states are labelled.

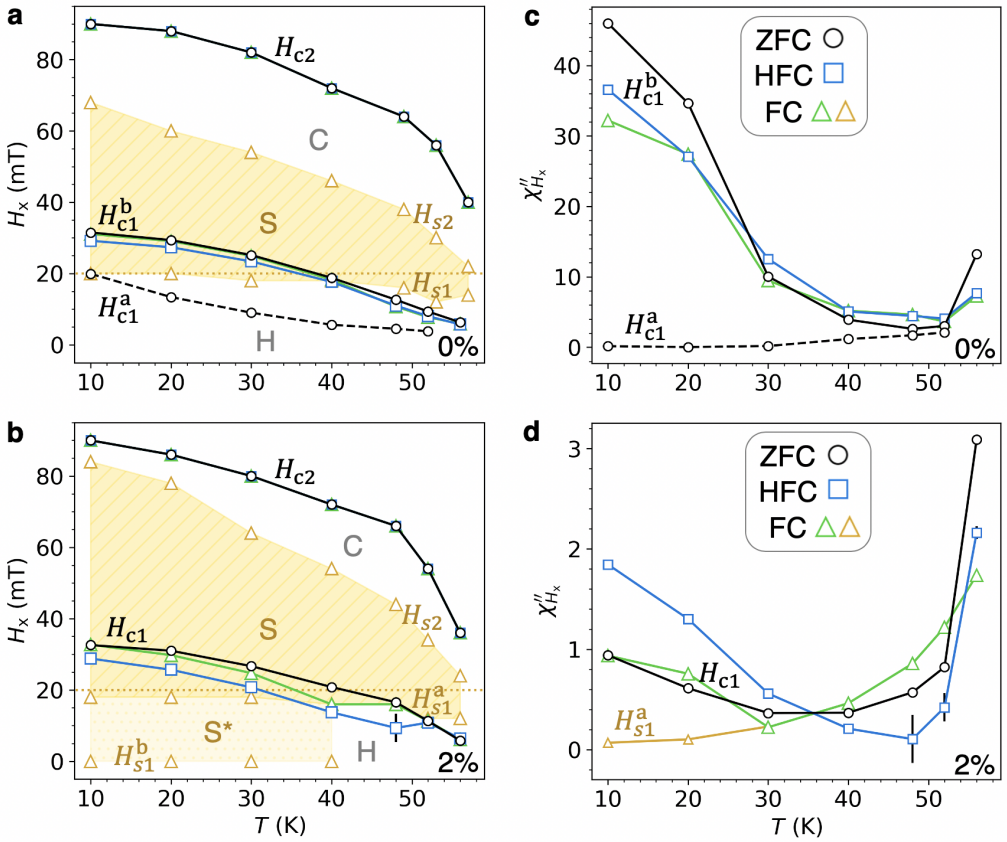

Figure 6.4: **a**, **b**, Low temperature magnetic phase diagrams for the pristine and doped samples, formed by plotting the critical field values determined for each measurement procedure versus temperature, as labelled. Filled yellow regions designate the existence of the skyrmion state after FC. The location of the helical (H), conical (C), skyrmion (S) and uniform magnetisation (UM) states are labelled. **c**, **d**, The fitted intensity of the peak in the χ'' data for the H_{c1} and H_{s1} critical fields after each measurement procedure for the pristine and doped samples respectively.

equilibrium skyrmion phase, indicated by the yellow filled regions at positive and negative applied magnetic fields. The difference in the overall shape of the χ' data between the samples, shown in Fig. 6.3**a1** and **a2**, can be attributed to the fact the measurements were not taken at the exact same temperature relative to T_C ($T_C - T = 1.8$ and 1.3 K for the pristine and doped samples respectively). For each sample at this high temperature, there are no obvious differences in the data between the ZFC, HFC and FC measurement procedures: the fitted value of all critical fields are consistent with each other.

However, comparing Fig. 6.3**a3** and **a4**, there is a significant difference in the magnitude of the χ'' peaks in the doped sample relative to the pristine sample. Such a compositional effect has been observed in $Mn_{1-x}Fe_xSi$, where the χ'' signal around the skyrmion phase was reduced for $x > 0.03$ [208], and it was argued that this indicated a decrease in the resonant frequency of the transition due to a slowing down of the dynamics by pinning effects. Therefore, following the arguments in Sec. 6.2, the reduction of the χ'' signals in our doped sample could either be caused by a broadening of the frequency dependence, or the introduction of metastable effects due to the additional pinning dynamics. The SANS data explored in later sections sheds some light on this issue, but thoroughly distinguishing between these scenarios requires future measurement of frequency dependent data.

6.3.2 Helical-Conical Phase Transition

Next, we shall consider the behaviour of the helical-conical phase transition as a function of temperature. Turning first to the χ' data at 49 K in Fig. 6.3**b1**, there is a difference in the measured value of χ' around 0 mT following the ZFC and HFC procedures: the value of χ' is larger at 0 mT after HFC than it is after ZFC. This behaviour indicates that, when following the HFC procedure, the conical to helical phase transition results in a helical state different to the one formed upon ZFC – perhaps with altered relative volumes of the H1 and H2,3 helical domains. This effect is more pronounced in the doped sample, as can be seen in Fig. 6.3**b2**, suggesting that the Zn- is hindering the conical to helical phase transition in some manner. However, for both samples, this low field divergence between the HFC and

ZFC data is reduced at the lower temperature of 10 K, as shown in Fig. 6.3**c1** and **c2**. This is surprising, as one might expect the effects of pinning in the doped sample to be more prevalent at lower temperatures, as there is less thermal energy available to enable depinning.

In the χ'' data, we see that at temperatures lower than the equilibrium skyrmion pocket, only peaks associated with helical-conical phase transition are seen. Unlike at high temperatures in Fig. 6.3**a**, at 49 K and below, we can see that there is a field offset in the peak position of each measurement procedure, indicating history-dependent behaviour in the H_{c1} phase transition point. The fitted H_{c1} values for both samples are summarised in Fig. 6.4**a** and **b** respectively, highlighting that this hysteretic field offset becomes significant below 50 K, and is more pronounced in the doped sample.

At 49 K and 48 K, it is evident that, in both samples, the magnitude of the χ'' peaks are greatly reduced relative to the data measured at 57 K and 56 K. However, remarkably, looking at the data in Fig. 6.3**c3** and **c4**, we can see that the χ'' peaks are actually larger in size at the lower temperature 10 K. This temperature dependence is made clear in the plot of the fitted H_{c1} intensities in Fig. 6.4**c** and **d**. Comparing the data for the two samples, it is clear that this low temperature increase is far greater in the pristine sample, where the intensities of the H_{c1} peaks surpass the measured intensities at 57 K. However, the doped sample still displays a marked increase below 30 K in comparison to the values at 48 K.

Once again, this could be due to a shift in the frequency dependence, suppression of phase coexistence, or metastable effects. However, considering frequency dependence, it is not possible for the χ'' peak height to first reduce and then increase if the resonant frequency varies monotonically with temperature. Furthermore, one would expect that metastable effects would suppress the peak height more at lower temperatures, due to the reduction of available thermal energy. In comparison to other skyrmion materials, the different low temperature behaviour observed in the χ'' data here in Cu_2OSeO_3 is significant, and will be explored and explained in the context of the SANS data in later sections.

6.3.3 Metastable Skyrmions

Finally, the features associated with metastable skyrmions in the FC data will be examined. In Fig. 6.3**b1** and **b2**, both samples exhibit a drop in χ' around 20 mT after FC. This is indicative of the formation of metastable skyrmions at 48 K and 49 K, as displayed by the yellow hashed regions. The signal is far greater in the doped sample, suggesting that the volume of metastable skyrmions which survived the cooling process was far greater in comparison to the pristine sample, as observed previously [219]. When considering the extent of this metastable skyrmion region, we can see that there is a lack of corresponding χ'' signals in Fig. 6.3**b3** and **b4**. Following the argument mentioned previously, this can be expected for a first order phase transitions from a metastable state, where the oscillating probe field only drives the transition in one direction.

Nevertheless, we can estimate the skyrmion phase boundary using the χ' data. It is expected that as the skyrmions annihilate at higher fields, the value of χ' in the FC data will increase until it follows the ZFC values, as shown in Fig. 6.3**b1**, **b2** and **c1**, **c2**, indicating all skyrmions have decayed to the conical state. We use this assumption to estimate the H_{s2} point for both samples at all temperatures, as summarised by the filled yellow region in Fig. 6.4**a** and **b**.

For decreasing field, determining the value of H_{s1} using the χ' data is more complicated. If the skyrmions decay into the conical state before the helical state becomes energetically favoured at the H_{c1} point, then we can expect the FC data to follow the HFC data to 0 mT. This is the scenario observed at higher temperatures in both samples, for example in Fig. 6.3**b1** and **b2**, suggesting that metastable skyrmions are annihilated before, or at, the helical-conical boundary.

At lower temperatures, the FC data in the pristine sample follows the HFC data below 20 mT, suggesting that few, or possibly no, metastable skyrmions survived the cooling process down to 10 K. A previous work looking at a pristine Cu_2OSeO_3 sample also noted a lack of metastable skyrmions surviving in this region with the field applied parallel to [110] [227]. In contrast, for the doped sample, below 20 mT the FC data follows closer to the ZFC data, as seen in Fig. 6.3**c1** and **c2**. This suggests that Zn-doping prevents the metastable skyrmions from decaying into the

helical state during the FC process. Future SANS studies will be useful to clarify this behaviour.

Examination of the FC χ'' data at 10 K in 6.3**c3** and **c4** further supports this interpretation. In the doped sample, at 30 K and below, two additional small peaks are exhibited. Since they appear only in the FC data, and only in the doped sample, it is reasonable to assume that these are associated with the presence of metastable skyrmions. The first feature, labelled H_{s1}^{a}, appears just below the cooling field of 20 mT. The second feature, labelled H_{s1}^{b}, is a small peak just below 0 mT. We have distinguished this possible low field skyrmion region, S*, by the second filled yellow area in Fig.6.3**c4** and Fig.6.4**d**. However, we argued previously that the annihilation of metastable skyrmions should exhibit no χ'' signal, due to the lack of dissipation in metastable phase transitions. Therefore, further study will be required to fully understand the origin of these dynamic features, and whether they are truly associated with the presence of metastable skyrmions.

6.4 Small Angle Neutron Scattering

While the AC susceptibility measurements provide useful information, their interpretation is only able to provide a higher-level indication of the underlying associated phenomena. However, SANS measurements provide a more detailed picture of the microscopic behaviour, allowing the relative volumes and behaviour of each magnetic structure to be compared and contrasted when following each measurement procedure. We performed SANS measurements at both ∼50 K (Fig. 6.5, 6.6, 6.7) and 5 K, (Fig. 6.8, 6.9, 6.10), with the samples in both the field parallel and field perpendicular configurations. At both temperatures, and for both samples, the intensity of the H1, H2,3, C and S magnetic peaks are plotted as a function of applied magnetic field in Fig. 6.5 and Fig. 6.8. These intensities were determined by summing the scattering in the sector boxes defined in Fig. 6.1**d-k** at each field point. The vertical lines in each figure show the critical fields determined by AC susceptibility measurements at the same temperatures, following the ZFC, HFC and FC procedures.

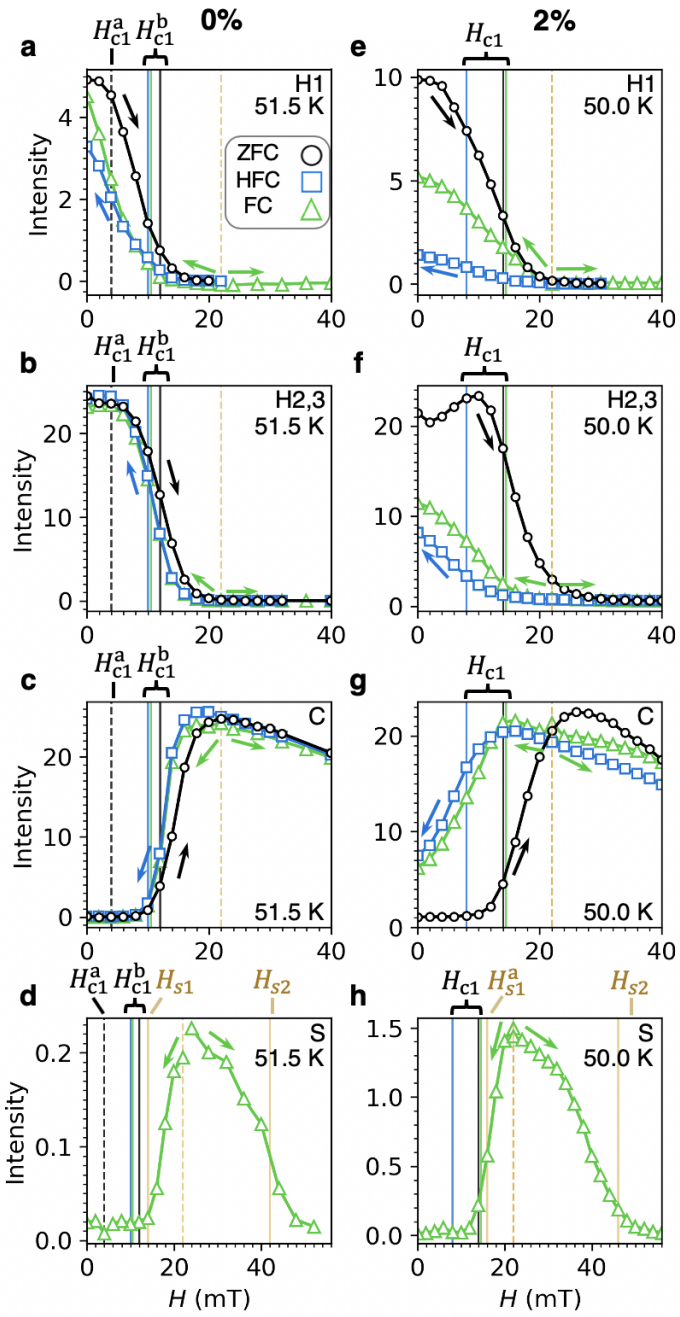

Figure 6.5: The neutron scattering intensity of the H1, H2,3, C and S peaks measured in the pristine sample at 51.5 K (**a-d**) and the doped sample at 50.0 K (**e-h**)) a function of applied magnetic field for the ZFC (black circles), HFC (blue squares) and FC (green triangles) measurement procedures. The intensities shown were determined by summing the total counts in the sector boxes as defined in 6.1 Error bars are too small to be seen.

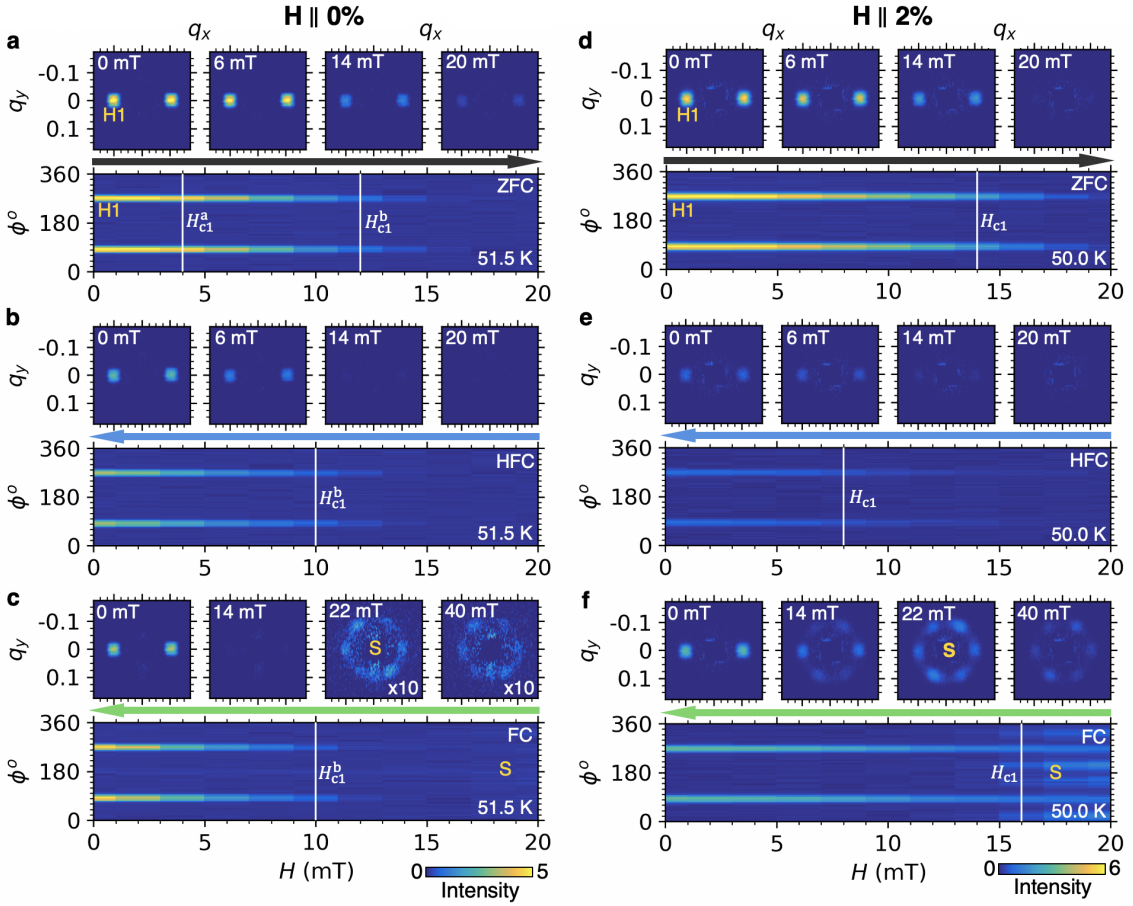

Figure 6.6: SANS patterns measured following the ZFC, HFC and FC procedures in the field parallel configuration with the pristine sample at 51.5 K (**a**-**c**), and the doped sample at 50.0 K (**d**-**f**). The upper panels display SANS patterns at selected fields, while the lower panels display the radially integrated intensity as a function of field and azimuthal angle, ϕ, around the ring of scattering. Vertical lines indicate critical fields determined by AC susceptibility measurements. For the data presented in each sample configuration, the colorscale has been fixed to enable direct comparison between images.

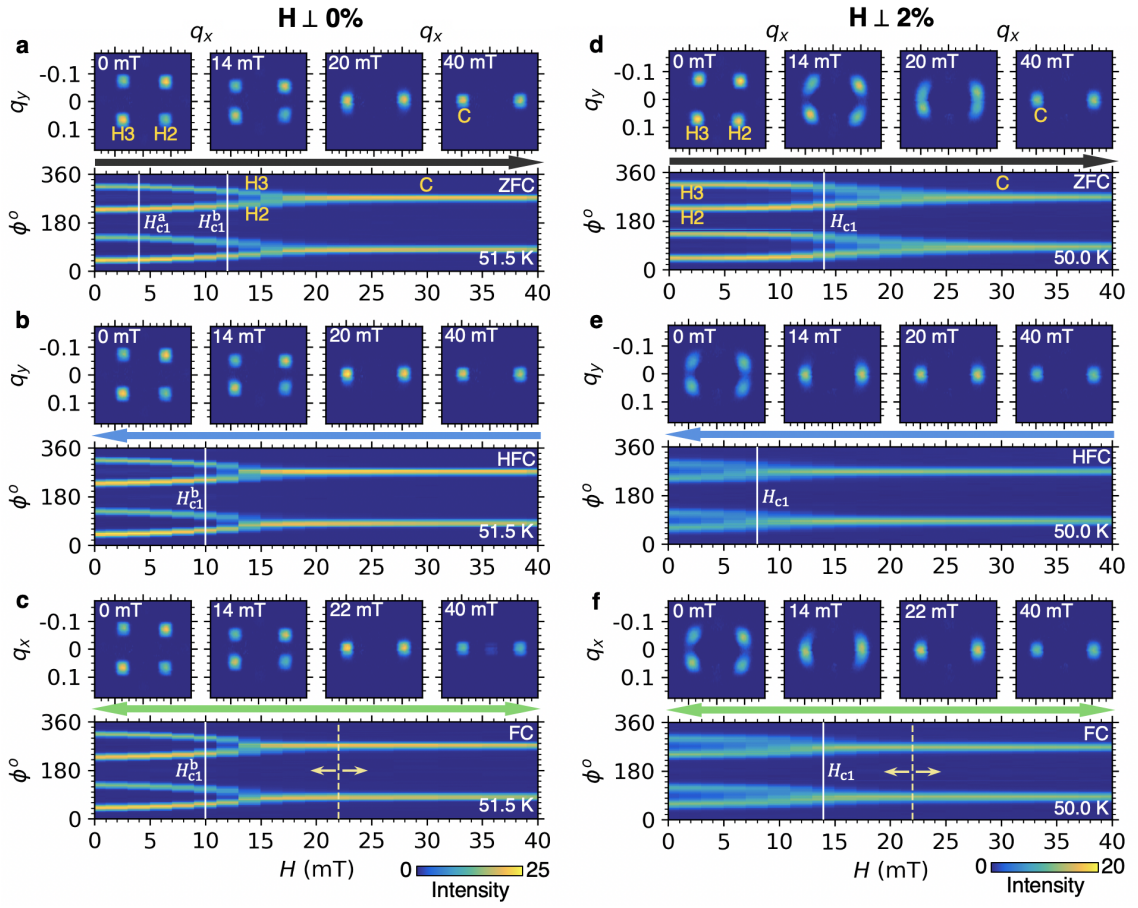

Figure 6.7: SANS patterns measured following the ZFC, HFC and FC procedures in the field perpendicular configuration with the pristine sample at 51.5 K (**a-c**), and the doped sample at 50.0 K (**d-f**). The upper panels display SANS patterns at selected fields, while the lower panels display the radially integrated intensity as a function of field and azimuthal angle, ϕ, around the ring of scattering. Vertical lines indicate critical fields determined by AC susceptibility measurements. For the data presented in each sample configuration, the colorscale has been fixed to enable direct comparison between images.

Representative SANS patterns for these field scans are displayed in the upper panels of each subplot in Fig. 6.6 and 6.7, and Fig. 6.9, 6.10. For each scattering pattern, the intensity over a q range of 0.07 and 0.13 nm^{-1} was summed radially at each azimthual angle ϕ around the centre of diffraction, as illustrated in Fig. 6.1**g**. By reducing the dimensionality of the data in this way, the behaviour and evolution of the magnetic scattering peaks at each temperature can be examined as a function of the applied magnetic field in a single colour plot, as shown in the bottom panel of each subplot in Fig. 6.6, 6.7 ($\sim$50 K), and Fig. 6.9, 6.10 (5 K). In the following sections, we shall examine and interpret this SANS data while making reference to the features of the corresponding AC susceptibility data in Fig. 6.3 and Fig. 6.4.

6.4.1 High Temperature SANS

We first consider the SANS data measured at $\sim$ 50 K. The intensity of H1 in the pristine sample, plotted in Fig 6.5**a**, exhibits a different low field behaviour for the ZFC, and HFC measurements. This can be seen clearly in the SANS patterns in Fig. 6.6**a** and **b**, where the intensity of the H1 magnetic satellites at 0 mT is comparatively lower after HFC. This effect is enhanced in the doped sample, showing an even greater difference between the ZFC and HFC measurements in Fig. 6.5**e**, as illustrated by the SANS data in Fig. 6.6**d** and **e**. This suggests that during the transition from the conical state to the helical state with decreasing magnetic field, the H1 helical domains are formed at a lower volume fraction, with the Zn-doping accentuating this effect. This fits with the observations gleaned from the χ' data around 0 mT in Fig. 6.3**b**, where the HFC value is greater compared to the ZFC value, which hinted at altered helical domain populations. This phenomena might be expected when considering the orientation of the conical and helical domains in Fig. 6.1**c** and **f**: the conical domains must rotate by 45 degrees to reorient to the H2,3 helical domains, which might require less energy than the 90 degree rotation required to reorient to the H1 helical domain, and it appears that pinning in the doped sample accentuates this effect.

In both Fig. 6.5**d** and **h** the skyrmion scattering intensity for each sample is displayed, exhibiting the broad range of field over which metastable skyrmions exist.

The H_{s1} and H_{s2} values estimated from the features seen in the χ'' data in Fig. 6.3, align well with the field extent of the skyrmion scattering in both Fig. 6.5**d** and **h**, and illustrate that, at this temperature, the metastable skyrmions decay before the conical-helical phase boundary. The skyrmion peaks can be seen clearly in Fig. 6.6**c** and **f**. The greater relative intensity of the S satellites in the doped sample confirms the formation of a larger population of metastable skyrmions, as was indicated by the AC susceptibility measurements.

In both samples, the H1 intensity at 0 mT is higher after FC in comparison to HFC. Given that the primary difference between these two measurement procedures is the formation and subsequent annihilation of metastable skyrmions, this suggests that the skyrmion state preferentially annihilates to H1 helical domains upon decreasing magnetic fields. This finding fits with the previously proposed skyrmion lattice to helical state decay process, whereby skyrmion tubes are zipped together through the motion of Bloch points [179], forming helical domains. In this process, formation of H1 domains would likely be preferred over the H2,3 domains, because they are oriented in the same plane as the skyrmion lattice, as can be seen by comparing Fig. 6.1**c** and **f**.

The intensities of H2,3 and C for the pristine sample, plotted in Fig. 6.5**b** and **c**, shows only minor differences between the three procedures, with a slight field offset in the observed behaviour. The SANS patterns for the ZFC procedure in Fig. 6.7**a** demonstrate that, at this temperature, the helical satellites rotate to their position in the conical state as a function of applied magnetic field. This indicates that the propagation vectors of the H2 and H3 helical domains themselves continuously rotate during the phase transition, maintaining long-range magnetic order throughout, with no coexistence of helical and conical states. This behaviour is replicated for the reverse conical to helical phase transition, as shown in Fig. 6.7**b** and **c**. These processes, occurring as a continuous rotation of the magnetic structure, appear more like a second order, rather than first order, phase transition. The observed suppression of helical and conical phase coexistence provides an explanation of the reduction of the H_{c1} χ'' peak at these temperatures in the AC susceptibility data in Fig. 6.4, as argued in Sec. 6.2.

On the other hand in the doped sample, the intensity of the H2,3 peaks and C peaks, plotted in 6.5**f** and **g**, show significant differences between the ZFC, HFC and FC measurements. The ZFC SANS patterns in Fig. 6.5**d** depict a gradual rotation of the helical domains to the conical state, similar to that of the pristine sample, but occurring at a higher applied magnetic field. However, at 0 mT in the HFC and FC measurements, in Fig. 6.5**e** and **f**, we see that the rotation of the conical state back to the helical state is incomplete: the magnetic structures remain partially pinned along the applied field direction. These observations strongly agree with the features seen in the AC susceptibility data at these temperatures in Fig 6.3**b**: the doped sample displayed a larger discrepancy in the value of χ' between the ZFC and HFC data around 0 mT, which hinted at an altered helical state after HFC. The AC data also showed an even greater suppression of the χ'' signal at H_{s1}, and this is explained by the observed metastable effects in the HFC SANS data. In comparison to the pristine sample, this hysteretic behaviour indicates that the presence of Zn in the doped sample introduces a pinning effect which hinders the reorientation of the helical and conical states.

6.4.2 Low Temperature SANS

We turn now to the SANS measurements performed at 5 K, shown in Fig. 6.8, 6.9 and 6.10. Looking at the ZFC data for the pristine sample in Fig. 6.8**a**, the H1 peak gradually decreases in intensity at higher fields. Simultaneously, the intensity of the H2,3 peaks initially increases, before decreasing after the critical field of H^b_{c1}, where the conical state becomes favoured, as shown in Fig. 6.8**b**. In contrast, in the ZFC data of the doped sample, shown in Fig. 6.8**d** and **e**, the H1 and H2,3 peak intensities are almost constant until just before H_{c1} at ~ 30 mT. Here H1 begins to decrease, while the H2,3 intensity shows a small increase approaching H_{c1}, before decreasing.

This could indicate that, in the pristine sample, the population of H1 helical domains steadily transforms to H2,3 helical domains as a function of field, as the degeneracy of the helical domains is lifted under an increasing applied magnetic field, and the H2,3 helical domains are energetically favoured before H^b_{c1}. On the

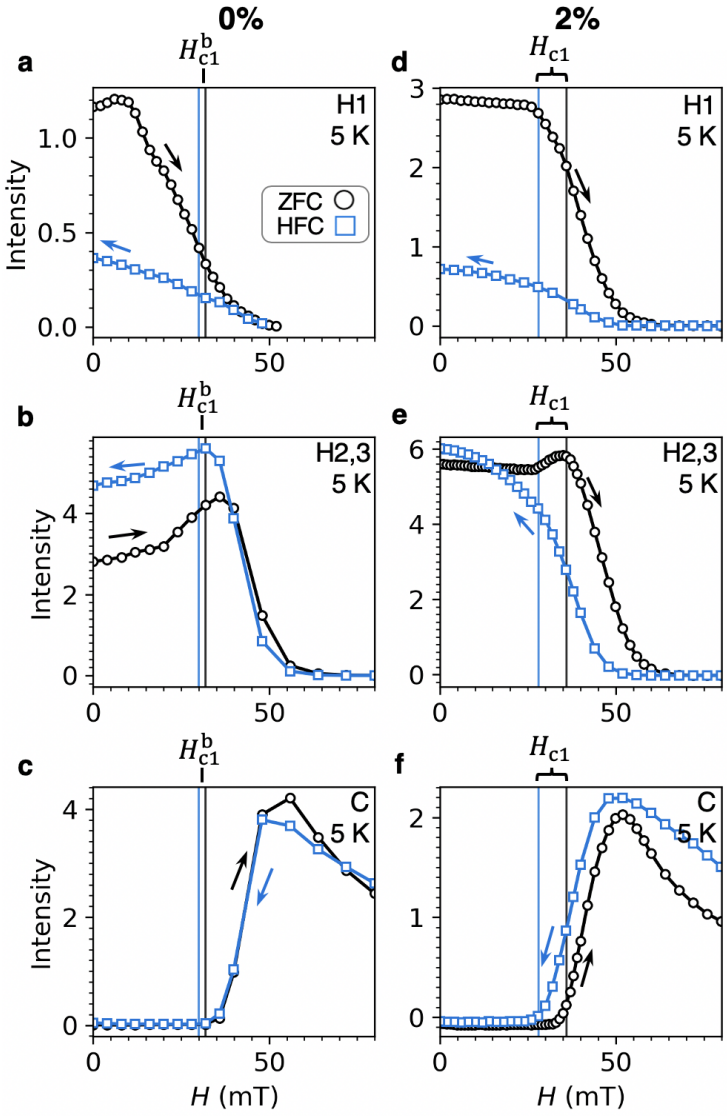

Figure 6.8: The neutron scattering intensity of the H1, H2,3 and C peaks measured in the pristine sample (**a-c**) and the doped sample (**d-f**) at 5 K as a function of applied magnetic field for the ZFC (black circles), HFC (blue squares) and FC (green triangles) measurement procedures. The intensities shown were determined by summing the total counts in the sector boxes as defined in 6.1. Error bars are too small to be seen.

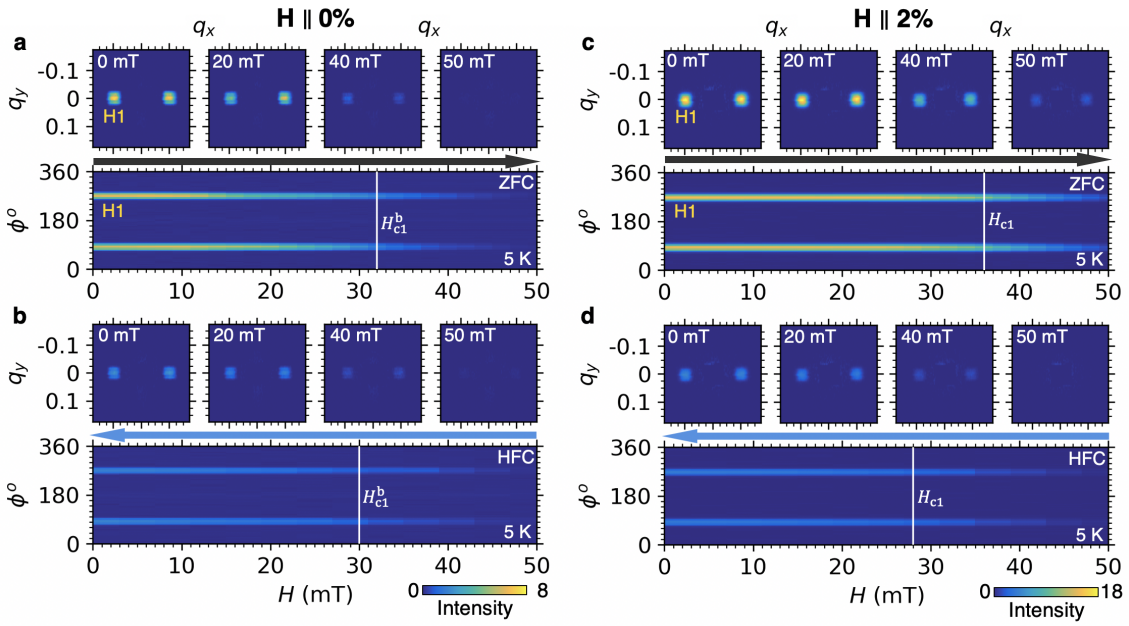

Figure 6.9: SANS patterns measured following the ZFC and HFC procedures in the field parallel configuration with the pristine sample (**a**, **b**), and the doped sample (**c**, **d**) at 5 K. The upper panels display SANS patterns at selected fields, while the lower panels display the radially integrated intensity as a function of field and azimuthal angle, ϕ, around the ring of scattering. Vertical lines indicate critical fields determined by AC susceptibility measurements. For the data presented in each sample configuration, the colorscale has been fixed to enable direct comparison between images.

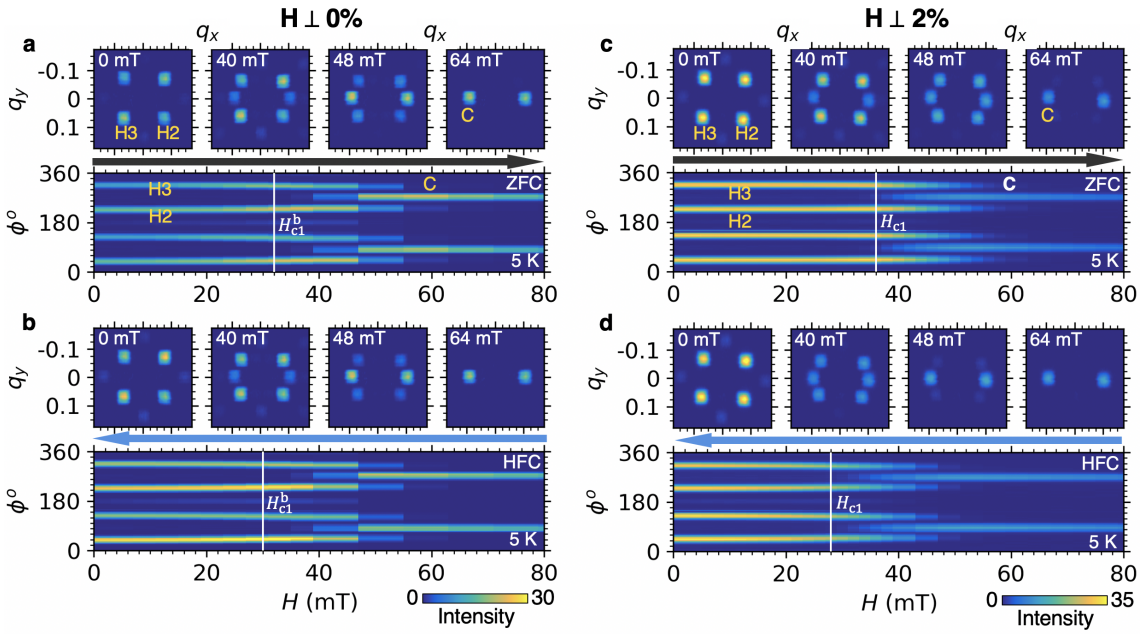

Figure 6.10: SANS patterns measured following the ZFC and HFC procedures in the field perpendicular configuration with the pristine sample (**a**, **b**), and the doped sample (**c**, **d**) at 5 K. The upper panels display SANS patterns at selected fields, while the lower panels display the radially integrated intensity as a function of field and azimuthal angle, ϕ, around the ring of scattering. Vertical lines indicate critical fields determined by AC susceptibility measurements. For the data presented in each sample configuration, the colorscale has been fixed to enable direct comparison between images.

other hand, in the doped sample, this process is largely suppressed. The observed behaviour may explain the presence of the additional H_{c1}^{a} χ'' peaks observed during ZFC in the pristine sample in Fig. 6.3, but not in the doped sample. Another explanation of this behaviour could be a distortion of the helical state with increasing field [305], which would explain the drop in H1 intensity, but not the increase in H2,3 intensity.

Turning now to the HFC measurements for the pristine sample, in comparison to the 51.5 K data, we see an further reduction in the H1 intensity at 0 mT relative to the ZFC data, as seen in Fig. 6.8**a** and Fig. 6.9**b**. Considering Fig. 6.8**d** and Fig. 6.9**d**, we can see that the difference in HFC behaviour between the pristine and doped samples is less pronounced than it was at ∼50 K. This suggests that at lower temperatures, the reduction in H1 domain population after HFC is largely due to energetic considerations, and pinning from the chemical substitution has less effect.

The intensity of the H2,3 helical domain peaks measured in both the pristine and doped samples are shown in Fig. 6.8**b** and **e**. Looking at both the H2,3 and C peak intensities, there is a dramatic field offset in the observed trends for the doped sample, agreeing with the significant hysteresis displayed by the χ'' peak position in AC data relative to the pristine sample in Fig 6.3. In the pristine sample, the H2,3 intensity at 0 mT is higher after HFC than in the ZFC process, again suggesting that H2,3 helical domains are favoured when the conical state transforms to the helical state with decreasing field.

In the 50 K measurements of the doped sample, the H2,3 satellites showed a large reduction in intensity at 0 mT for the HFC measurements, caused by pinning of the magnetic domains as they rotated from the conical to the helical state. However, notably, at this lower temperature, H2,3 intensity is higher at 0 mT after HFC in comparison to the ZFC data, exhibiting similar low temperature behaviour to the pristine sample. This is surprising, as one might expect the effects of pinning to be greater at lower temperatures.

Fig. 6.10 reveals the details of the altered low temperature behaviour. In Fig. 6.10**a** and **b**, we see the helical to conical phase transition in the field-perpendicular configuration. At 51.5 K, the phase transition was characterised by a continuous

rotation of the magnetic structures as a function of applied field, and phase coexistence was suppressed. In contrast, at 5 K, the simultaneous detection of both helical and conical peaks in one SANS pattern indicates phase coexistence, as expected for a first order phase transition.

The altered low temperature behaviour is more clearly evident in the 2% sample, as shown in Fig. 6.10**c** and **d**. After HFC at 50 K, the Zn-doping hindered the continuous rotation of the conical structure to the helical state. However, at 5 K we see that at 0 mT the helical domains fully reorient to the [100] and [010] directions after HFC. As in the pristine sample, there is phase coexistence of the helical and conical states for both ZFC and HFC processes. This implies that the pinning which hindered the domain reorientation at higher temperature does not affect the phase transition in the same manner at low temperature.

6.5 The Role of Cubic Anisotropy

To investigate and understand this behaviour further, we performed a set of temperature dependent SANS measurements on the doped sample in the field perpendicular orientation. For the first measurement, the sample was HFC at 200 mT to 50 K and then the magnetic field was decreased to 0 mT, forming the pinned helical state, as seen previously in Fig. 6.7**e**. From this point, SANS measurements were performed as the sample was cooled down to 5 K, and, after resetting the magnetic state upon a subsequent cooling procedure, as the sample was heated from 50 K to 58 K. The resulting SANS data is shown in Fig. 6.11**a**. For increasing temperature data, the partially pinned helical state gradually rotates and orients along the $\langle 100 \rangle$ axes at higher temperatures, before disappearing at T_{C}. This can be expected, as at higher temperatures there is more energy available to overcome the pinning energy. However, we can see that upon decreasing the temperature from 50 K to 5 K, the helices start to reorient to the $\langle 100 \rangle$ axes below 40 K, despite the reduction in available thermal energy. This suggests that another contribution must be providing the energy to overcome the pinning at low temperatures.

In these skyrmion-hosting helimagnets, the orientation of the helical domains is

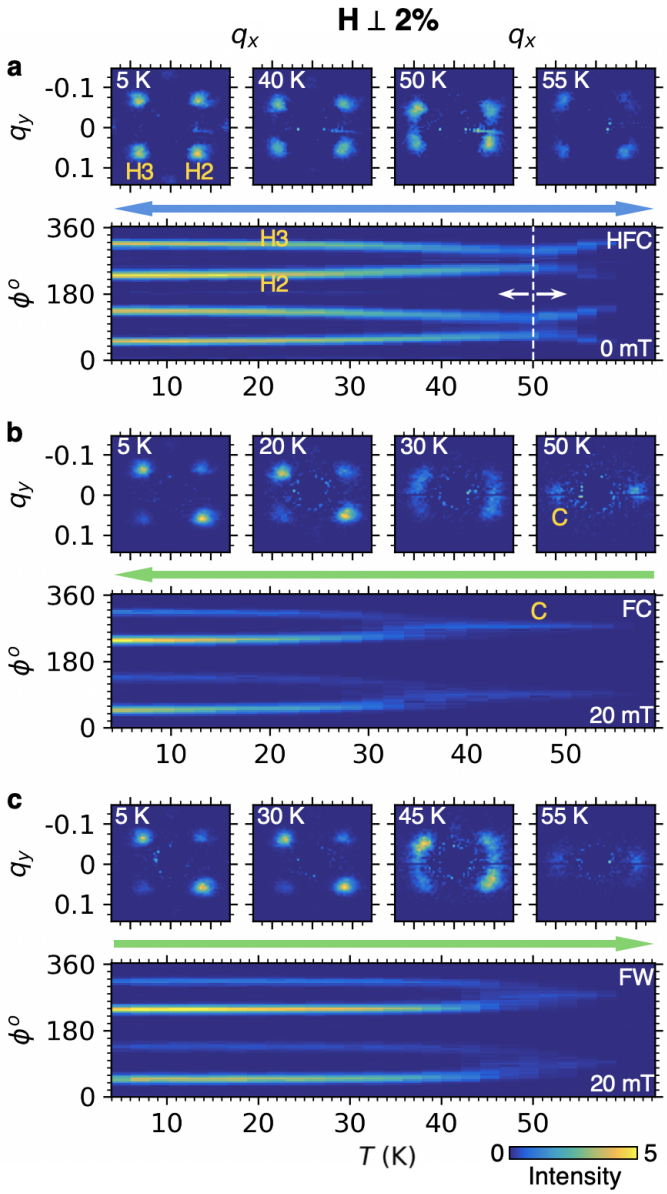

Figure 6.11: SANS data measured as a function of temperature after: high-field cooling (HFC) to 0 mT **a**, while field cooling (FC) at 20 mT to 5 K **b**, and field warming at 20 mT to 58 K **c**. The upper panels display SANS patterns at selected temperatures, while the lower panels display the radially integrated intensity as a function of temperature and azimuthal angle, ϕ, around the ring of scattering.

determined by the cubic anisotropy. As discussed in the introduction, recent studies have shown that the anisotropy constant in Cu_2OSeO_3 greatly increases in magnitude below 40 K [225]. This provides an explanation for the observed behaviour in this study: the cubic anisotropy becomes strong enough at low temperature to overcome the pinning of the conical-helical reorientation in both the pristine and doped sample. From the previously reported AC susceptibility measurements we have surveyed and referenced, it appears that the larger low temperature χ'' signal at the helical-conical phase boundary is unique to Cu_2OSeO_3, suggesting the cubic anisotropy term is responsible for the emergence of helical-conical phase coexistence at low temperatures.

There are other noticeable effects of the increased cubic anisotropy strength in Cu_2OSeO_3. In the archetypal skyrmion material MnSi, it has been observed that the H_{c1} value does not change dramatically as a function of temperature [208]. Since the value of H_{c1} is an indicator of the strength of the cubic anisotropy, this illustrates that the anisotropy does not significantly change as function of temperature. In comparable chemically doped materials such as $Fe_{1-x}Co_xSi$ and $Mn_{1-x}Fe_xSi$, the measured value of H_{c1} greatly increases with decreasing temperature, however this is suggested to be due to the pinning of the helical-conical phase transition [123, 204, 205, 208]. This is concluded by noting that, upon decreasing the field from the conical state, such as after HFC or FC, the pinning effects are strong enough to fully prevent reorientation to the helical state, even close to T_C [203]. This is similar to the behaviour we saw at 50 K in the Zn-doped sample in this study.

In contrast, the behaviour of H_{c1} as a function of temperature in both the pristine and doped Cu_2OSeO_3 samples in this study are remarkably similar. This is highlighted in Fig 6.4**a** and **b**: both samples display an increase in H_{c1} at lower temperatures. Although the doped sample does exhibit an offset in H_{c1} between ZFC and HFC measurements, these are small compared to the effect seen in other chemically substituted materials. This limited history-dependent behaviour in both samples indicates that the dominant determinant of H_{c1} value in Cu_2OSeO_3 is the strong, temperature dependent cubic anisotropy, which, at low temperature, is able to largely overcome the effects of pinning introduced by the non-magnetic Zn dopant.

A final consideration in the context of the role of cubic anisotropy is the behaviour of metastable skyrmions. In previous studies, when FC through the skyrmion pocket in the materials such as MnSi, $Fe_{1-x}Co_xSi$ and $Mn_{1-x}Fe_xSi$, the skyrmion state coexists with the conical state down to base temperature, and the helical state is not observed [203,205]. On the other hand, in Cu_2OSeO_3, due to the increase of H_{c1} at low temperatures, the helical phase manifests below 35 K when FC the sample through the skyrmion region at 20 mT, as seen by the transition of the C to H2,3 magnetic satellites in Fig. 6.8**b**. A similar transition is seen upon field warming (FW) in Fig. 6.11**b**, but at a higher temperature. As speculated when considering the FC χ' data in Fig. 6.3, it is likely that the emergence of the helical state while FC results in the loss of metastable skyrmion population. Such losses might be limited by avoiding the helical phase during the FC process: by cooling at 20 mT to 40 K, increasing the field to 40 mT, and then continuing the cooling process.

6.6 Conclusions

A combination of detailed AC susceptibility magnetometry and small angle neutron scattering was utilised to study the phase transitions between, and relative volumes of, the helical, conical and skyrmion states in both pristine and Zn-doped Cu_2OSeO_3. Comparison of the data between the samples, and three distinct measurement protocols, resulting in a number of observations and conclusions.

Measurements in both samples have demonstrated that upon HFC, the H1 helical domain volume fraction at 0mT is reduced after HFC in comparison to ZFC at both high and low temperature, with the effect greater in the Zn-doped sample. This can be understood when considering the 90 degree rotation required to transform the conical state to the H1 helical orientation, which likely imposes a larger energy barrier in comparison to the 45 degree rotation required to form the H2,3 helical domains. In contrast, the larger H1 intensity at 0 mT after the FC protocol indicates that the metastable skyrmion state preferentially decays to H1 helical domains, lending support to the previously proposed skyrmion-to-helical decay mechanism: the zipping together of skyrmion tubes via the motion of magnetic Bloch points.

In the pristine sample, an additional low field peak in the ZFC χ'' data suggested a further phase transition, which was identified to be H1 helical domains transforming to H2,3 domains as the helical domain degeneracy is lifted by the applied field before the helical-to-conical phase boundary at H_{c1}. The lack of this peak in the doped sample suggests that this reorientation is effectively prevented by the introduction of pinning.

At 51.5 K, the pristine sample SANS data revealed that the helical-conical phase transition, for both ZFC and HFC procedures, is characterised by a continuous rotation of the H2,3 helical domains towards the conical state as a function of the applied field, and suppression of phase coexistence. This was accompanied by a dramatic reduction in the corresponding χ'' dissipation peak, indicative of suppression of phase coexistence in a first order phase transition. In the doped sample at 50.0 K, the magnetic texture did not fully reorient to the $\langle 100 \rangle$ helical domain axes upon decreasing field to 0 mT after HFC, suggesting they were partially pinned along the magnetic field direction. This behaviour appears to be consistent with that seen in other doped helimagnets, where the disorder introduces a similar pinning effect.

In contrast, at 5 K, the SANS data illustrated that the same phase transition displayed coexistence of the helical and conical phases. The corresponding peaks in the χ'' data greatly increasing in magnitude at lower temperature, as expected for a first order transition exhibiting phase coexistence. Remarkably, the pinning effects which dominated the magnetic reorientations in the doped sample at 50 K, appear to be overcome at this lower temperature, despite the reduction of available thermal energy. In comparison to other archetypal helimagnets, this behaviour appears to be unique to Cu_2OSeO_3. We attribute this low temperature behaviour to the large, temperature dependent cubic anisotropy energy present in Cu_2OSeO_3: at low temperature, the anisotropy becomes strong enough to overcome the pinning energy in the absence of thermal activation. The relatively moderate history-dependence of the helical-conical phase boundary in both the pristine and doped samples demonstrates the dominance of this anisotropic energy contribution.

Overall, these results highlight further unique behaviour exhibited by the magnetic phase transitions in Cu_2OSeO_3 due to its comparatively large, temperature

dependent cubic anisotropy. Comparisons between pristine and doped samples reveal the role of disorder in the slowing down and pinning of the helimagnetic phase transition dynamics, highlighting that these may be effectively overcome by other energy contributions. Consideration and further study of these effects will be crucial when utilizing chemical substitution, or doping, to manipulate the delicate energy balance for exploitation in future applications of skyrmion materials.

Chapter 7

Real Space Imaging of Metastable Skyrmion Tubes

While they are commonly portrayed as two dimensional objects, in reality magnetic skyrmions are thought to exist as elongated, tube-like objects extending through the thickness of the host material, as illustrated in Fig. 7.1. The study of this skyrmion tube (SkT) state is vital for furthering the understanding of skyrmion formation and dynamics for future applications. Furthermore, skyrmion tubes have potential applications in magnonics-based computing [230, 306].

In previous chapters, the lifetime of metastable skyrmions, and other dynamic phase transition effects, were investigated via bulk property measurements, such as AC susceptibility magnetometry and SANS. However, true understanding of topological phase transition dynamics relies upon observation of local features and phenomenon, which necessitates the use of real-space imaging techniques. A prime example of this is the theorised presence of magnetic Bloch points at the ends of broken skyrmion tubes, which are thought to be responsible for the unwinding of the skyrmion state into topologically trivial states [190, 192]. When transitioning to the helical state, such Bloch points are thought to zip together neighbouring skyrmion tubes [179]. On the other hand, when transitioning to the conical state, it has been suggested that skyrmion tubes unwind via the motion of Bloch points formed at the end of each individual tube [187, 188]. However, direct experimental imaging of skyrmion tubes, and such associated dynamic phenomena, has yet to be reported.

In this chapter, the first x-ray microscopy measurements of skyrmions in bulk chiral magnets are shown, made possible by the adaptation of the MAXYMUS instrument for cryogenic capabilities. Futhermore, the real-space observation of skyrmion tubes in a lamella of FeGe is demonstrated with x-ray imaging and comparative micromagnetic simulations, confirming their extended 3D structure. The work is primarily based on a published article [307]. Accompanying micromagnetic simulations were performed by David Cortés-Ortuño. The formation of these structures at the edge of the sample highlights the importance of confinement and edge effects in the stabilisation of the SkT state, opening the door to further investigations into this unexplored dimension of the skyrmion spin texture.

7.1 Suitability of Skyrmion Imaging Techniques

Real-space observation of the vertical dimension of the SkT state and their associated dynamics requires an in-plane magnetic field applied perpendicular to the imaging axis. In addition, typically imaging techniques require a sample thin enough for transmission measurements. In this section, the suitability of typical magnetic imaging techniques is discussed with the goal of imaging skyrmion tubes in such a sample and field configuration.

Electron imaging techniques, in the form of Fresnel mode Lorentz Transmission Electron Microscopy (LTEM) [124], and electron holography [102, 308], have been widely applied to image magnetic skyrmions. However, due to the deflection of electrons travelling through magnetic fields, these methods do not easily allow for the application of an in-plane magnetic field [309]. LTEM also has the disadvantage of not being able to observe Néel-type skyrmions unless the sample is tilted from the imaging axis [310]. There is also a defocus requirement to achieve magnetic contrast, limiting the effective spatial resolution. Furthermore, electron techniques image the stray in-plane magnetic flux density generated by the spin texture, rather than the direct magnetisation of the sample. This is also true of Magnetic Force Microscopy, which has the additional disadvantage of being solely surface sensitive, and as a result, interpretation of the true magnetisation is challenging [186, 311].

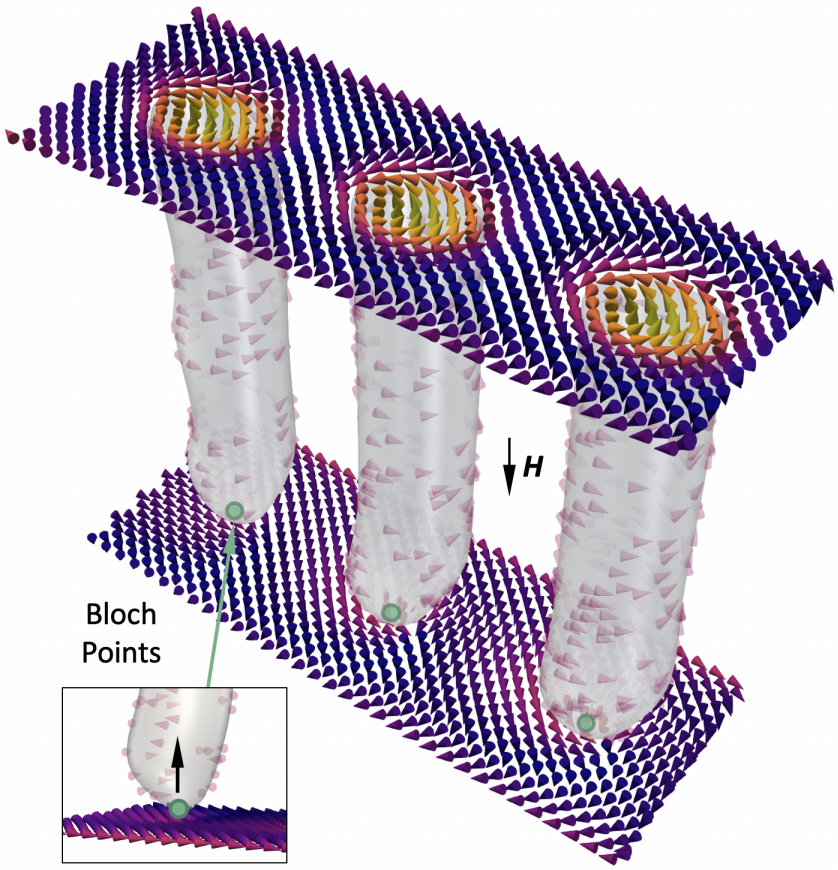

Figure 7.1: Three dimensional visualisation of three magnetic skyrmion tubes from the micromagnetic simulations presented in this chapter, illustrating their extended spin structure. The inset highlights the location of the magnetic Bloch point at the end of each skyrmion tube.

In photon-based techniques, the probe particles are unaffected by the direction of the applied magnetic field, and have the advantage of imaging the direct magnetisation of the sample. However, optical techniques utilising the visible spectrum, such as Kerr Effect microscopy, lack the spatial resolution to image all but the largest of skyrmions in multilayer thin films [73, 83].

On the other hand, magnetically sensitive x-ray imaging techniques, in the form of x-ray holography and Scanning Transmission X-ray Microscopy (STXM), achieve the required spatial resolution while allowing a fully variable applied magnetic field axis. Further benefits include the possibility to reconstruct three dimensional magnetic structures using vector field tomography [312], and a picosecond time-resolution capable of probing skyrmion dynamics [294, 313, 314]. Despite clear advantages, these techniques have only seen limited use for the study of bulk DMI skyrmions [315]. While STXM instruments have been employed to observe skyrmions in multilayer thin films [62, 115], such microscopes have not previously been fitted with the cryogenic temperature capabilities required for the observation of skyrmions in bulk chiral magnets.

7.2 Sample Characterisation

We performed initial magnetometry measurements to characterise a bulk single crystal FeGe sample, displayed in Fig. 7.2**a** and **b**. The T_C of the sample, defined as the point of greatest slope in M, was found to be 280.5 K, as determined by the magnetisation vs temperature data in Fig. 7.2**a**. A magnetic phase diagram of the crystal is shown in Fig. 7.2**b**, highlighting the limited extent of the SkL state in the bulk material. The colourmap plots the real component of the AC susceptibility measured during field sweeps after zero field-cooling at each temperature. A region with a characteristic dip in the AC signal is a well known indicator of the SkL state [263].

Thin lamella samples were prepared from single crystals of FeGe, as described in Sec. 3.1.3. Microscopy images of the thin lamella samples of FeGe are shown in Fig. 7.2**c** and **d**. Sample 1, shown in Fig. 7.2**c**, consists of a ∼120 nm thick lamella

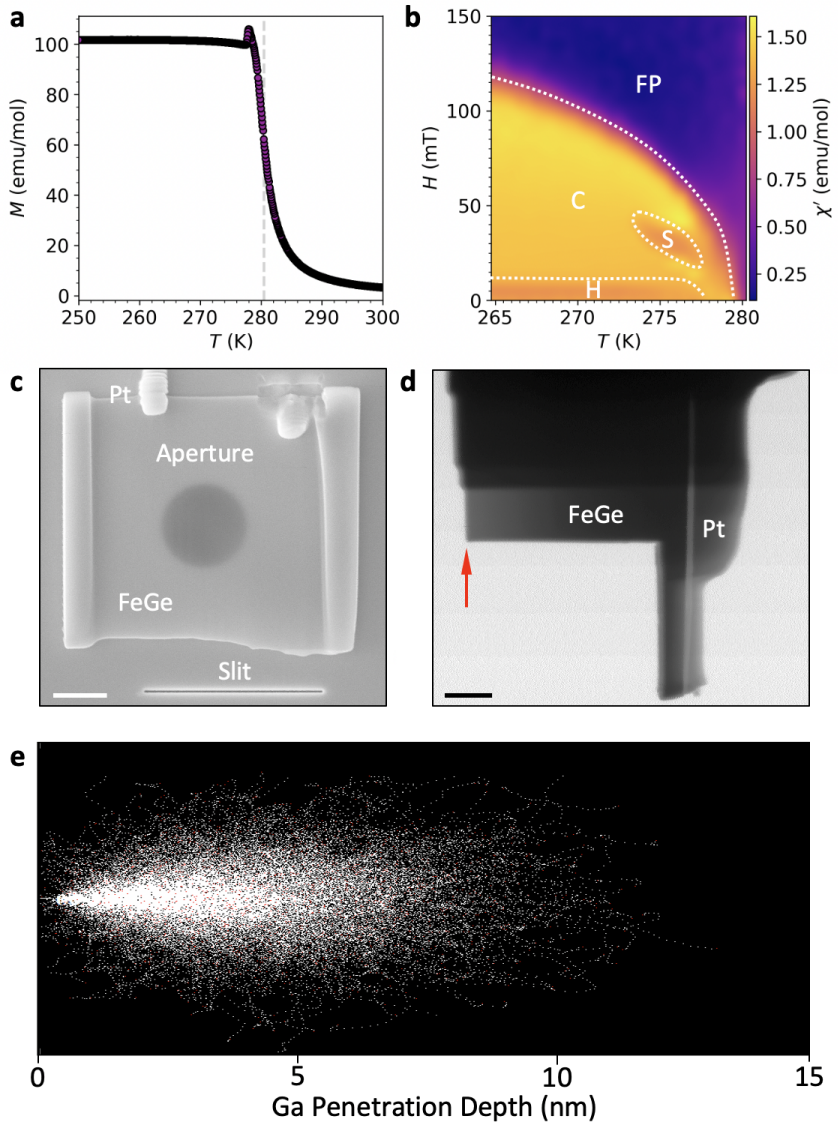

Figure 7.2: **a**, A plot of magnetisation against temperature as measured for the bulk FeGe single crystal. The grey dotted line marks the determined T_C of $\sim$ 280.5 K. **b**, The magnetic phase diagram of the bulk FeGe sample, as determined by AC susceptibility measurements. The extent of the helical (H), conical (C), skyrmion lattice (S) and field polarised (FP) states are labelled. **c**, Scanning electron micrograph of sample 1. **d**, Scanning transmission x-ray micrograph of sample 2. The red arrow indicates the location of the observed magnetic skyrmion tubes. Scale bars, 2 µm.

fabricated by focused ion beam. This lamella was placed over a 3 µm aperture in a Si_4N_3 membrane, which was sputter coated on the reverse side with ∼600 nm of Au, and fixed in position by a single Pt deposition weld. A 20 nm thick reference slit was milled 3.5 µm from the sample aperture. The Au layer serves to block the majority of the incoming x-ray beam, leaving only scattering from the sample aperture and the reference slit incident on the CCD. Sample 2, shown in Fig. 7.2**d**, consists of a ∼120 nm thick lamella again fabricated by focused ion beam. The lamella was further ion milled into the L-shape shown in the sample image. The contrast in the image demonstrates that the bottom left corner of the sample, highlighted by the red arrow, is the thinnest part of the sample. As we shall see, the observed SkT spin texture was located in this corner.

Utilising the widely available TRIM software, the Ga implantation in the resulting lamella samples was estimated to extent less than ∼10 nm into the surface, as shown in Fig. 7.2**e**. Thus, the majority of the lamella's volume was unaltered from the bulk crystal, and the effects of pinning and disorder caused by ion implantation were minimal.

7.3 Chiral Spin Textures in Lamellae

Small angle x-ray scattering measurements were performed to determine the magnetic phase diagram of the thin lamella sample 1. Example magnetic x-ray diffraction patterns obtained from the sample are shown in Fig. 7.3**a-c**. The two broad magnetic satellites in the Fig. 7.3**a** are characteristic of a helical state with weak alignment along a preferred crystalline axis, as determined by the present cubic anisotropy [316]. In FeGe, the helices align along ⟨100⟩ directions at high temperature, and ⟨111⟩ directions at lower temperatures [174]. However, in a thin lamella, the helical propagation direction is fixed in the plane of the sample. Upon application of an out-of-plane magnetic field, six magnetic peaks are observed, indicating the presence of the SkL state, as shown in Fig. 7.3**b**. When an in-plane magnetic field is applied, the helical state propagation vector rotates as it transitions to the conical structure, as shown by the magnetic peaks aligned to the applied in-plane

field direction in Fig. 7.3**c**.

For each diffraction pattern, the total scattering intensity at each azimuthal angle ϕ, as shown in Fig. 7.3**a**, was summed over a q range from 0.01 to 0.015 nm^{-1} and fitted with a Gaussian distribution. Figure 7.3**d** displays the fitted intensity and angular position of one of each pair of magnetic peaks as a function of applied out-of-plane magnetic field at 250 K. The broad magnetic peak of the helical state transforms to three narrow magnetic peaks in the SkL state, indicating a transition from multiple helical domains with differing orientations to a highly ordered, single SkL domain state. A similar data set for an in-plane magnetic field at 100 K is shown in Fig 7.3**e**, illustrating the transition of the broad helical magnetic peak through a rotation of the spin texture, to the conical state.

By acquiring such CCD images as a function of applied magnetic field after ZFC, such diffraction patterns were used to plot the phase diagrams in Fig. 7.4**a** and **b**, determined with magnetic fields applied out-of-plane and in-plane respectively. At low applied magnetic fields the helical state is at equilibrium, illustrated in Fig. 7.4**c**. Under an out-of-plane magnetic field, the equilibrium SkL state, illustrated in Fig. 7.4**c**, exists across a large range of field and temperature in comparison to the bulk single crystal state. This phenomenon has previously been attributed to shape anisotropy and confinement effects due to the reduced dimensionality of the sample [56,57,98,317,318]. At higher out-of-plane magnetic fields, the magnetisation is expected to form the out-of-plane conical and field polarised states. However, these are indistinguishable for diffraction measurements in this field configuration.

Under an in-plane magnetic field the helical state rotates as it transitions to the conical structure across all temperatures, as shown in Fig. 7.4**b**. As discussed in the previous section, the application of an in-plane magnetic field is also expected to stabilise the in-plane SkT state. However, we found that in this field configuration the extent of the equilibrium skyrmion region was greatly suppressed in our lamella samples, possibly entirely, as evidenced by the lack of an identifiable SkT state in Fig. 7.3**b**. This behaviour can be expected when considering that the effects of shape anisotropy and confinement, which enhance the stability of the SkL in the out-of-plane field configuration, may work to reduce the stability of the SkT state

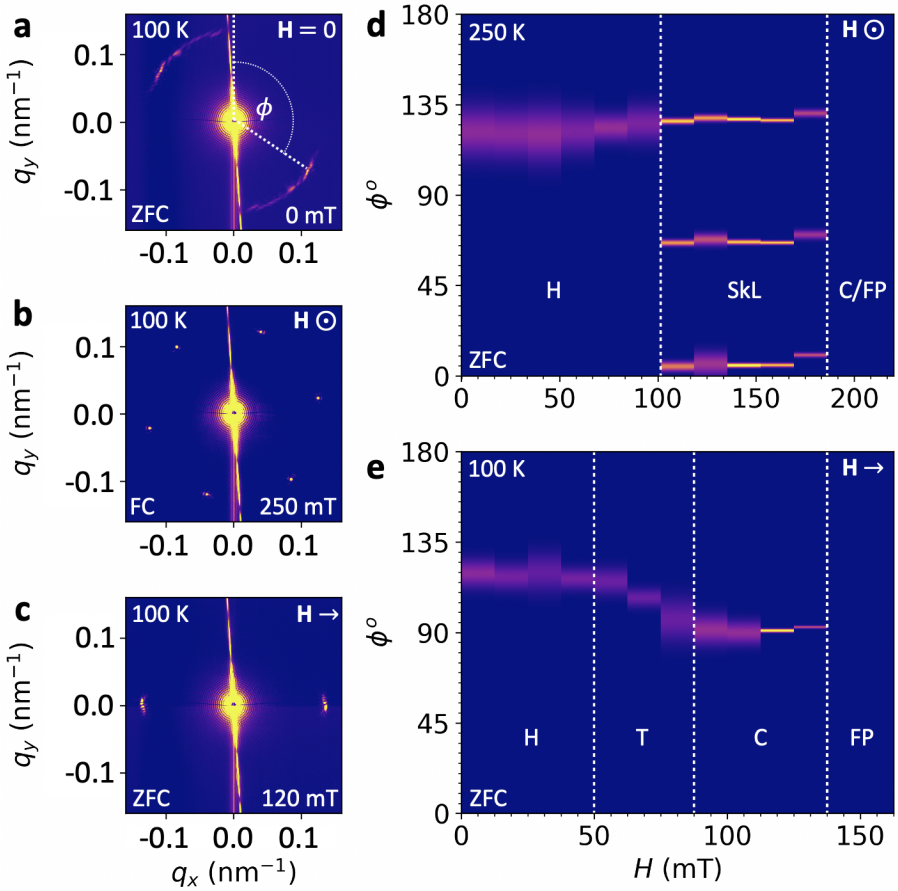

Figure 7.3: **a**-**c**, CCD images of the magnetic x-ray diffraction patterns obtained for the helical (H), skyrmion lattice (SkL) and conical (C) states respectively. The central yellow spot is the main x-ray beam, blocked by a beamstop, while the smaller outer peaks are the magnetic diffraction satellites. **d**,**e**, Fitted angular profiles of the magnetic diffraction patterns plotted as a function of applied out-of-plane and in-plane magnetic field respectively. Determined boundaries between the magnetic states are labelled and shown by the dashed white lines.

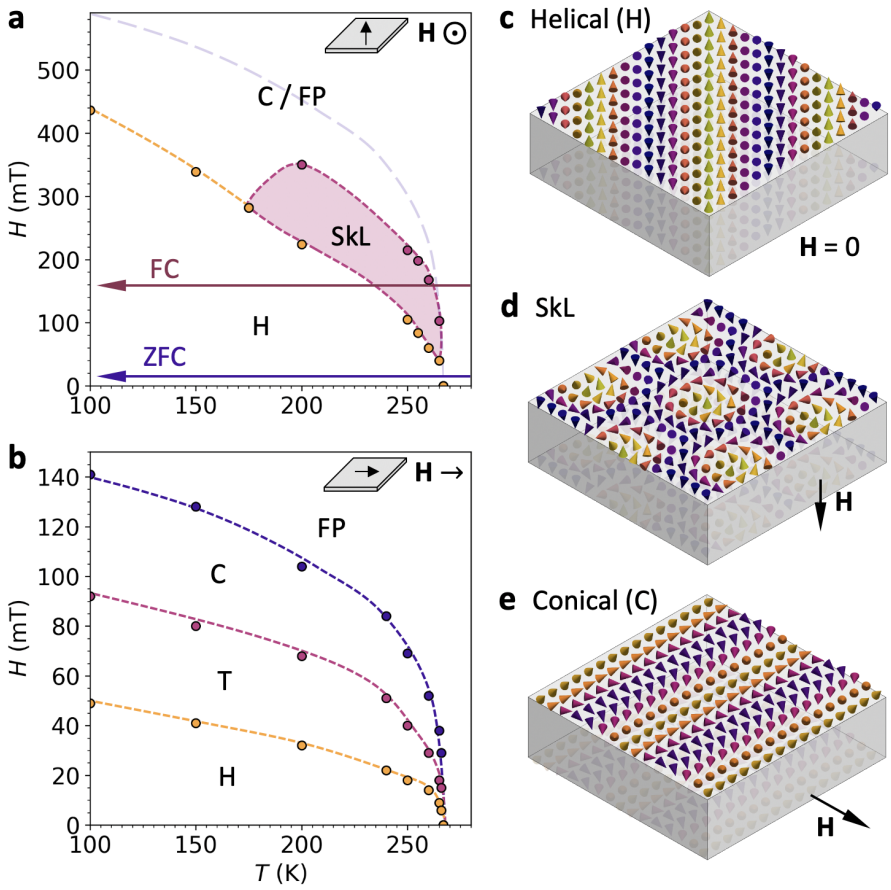

Figure 7.4: **a**,**b**, Phase diagrams of the ∼120 nm FeGe lamella for out-of-plane and in-plane applied magnetic field respectively, as determined magnetic x-ray diffraction. Schematics of each field configuration are shown as insets. In **a**, boundaries between the helical (H) and skyrmion lattice (SkL) states are displayed by yellow and magenta dots. The expected boundary between the indistinguishable conical (C) and field polarised (FP) states is estimated by the purple dashed line. In **b**, yellow, magenta and purple dots boundaries indicate the boundaries between the helical (H), helical rotation transition (T), conical (C) and field polarised (FP) states. **c**-**e**, Schematic illustrations of the spin textures as they are expected to appear in a thin lamella.

for the in-plane field arrangement. However, due to the sample construction required for these diffraction measurements, the field of view was limited to the centre of the lamella, and therefore it was not possible to detect potential formation of a SkT state at the edges of the sample.

7.4 Real Space Imaging of Chiral Spin Textures

Magnetic contrast images acquired by the x-ray holography, STXM and LTEM techniques are presented in Fig. 7.5. Both x-ray imaging techniques achieve magnetic contrast by exploiting the resonant enhancement of the magnetic scattering and absorption of x-rays close to the L_3 absorption edge of the magnetic Fe atoms. The magnetic signal was maximised by tuning the x-ray energy ∼708 eV after measuring an x-ray magnetic circular dichroism (XMCD) spectrum, as described in Sec. 2.4.2. In the STXM measurements, in order to achieve magnetic contrast at these energies without suffering from spectral compression due to the increased absorption at the resonant edge, we found that the thickness of the FeGe sample was required to be less than 150 nm. The observed magnetic contrast in the images is proportional to m_z, the out-of-plane component of the sample magnetisation [241].

In contrast, LTEM provides the in-plane components of the magnetic flux generated by the underlying magnetisation, highlighting the complementary nature of these two techniques. Simulated x-ray images were created from comparative micromagnetic simulations by averaging the simulated out-of-plane magnetisation m_z through the thickness of the simulated spin texture, and are in excellent agreement with the experimental images. The simulations were performed with a discretisation of 4 nm. To facilitate realistic comparison of the simulated images to the experimental data, we limited their resolution to 20 nm. We achieved this by averaging each 5×5 array of the 4 nm pixels in the simulated image into a 20 nm pixel. The micromagnetic simulation methods and detailed results are explored in the Appendix Sec. B.1.

To achieve sufficient magnetic contrast in both the x-ray holography and STXM measurements, we found that it was necessary to maximise the ordered magnetic

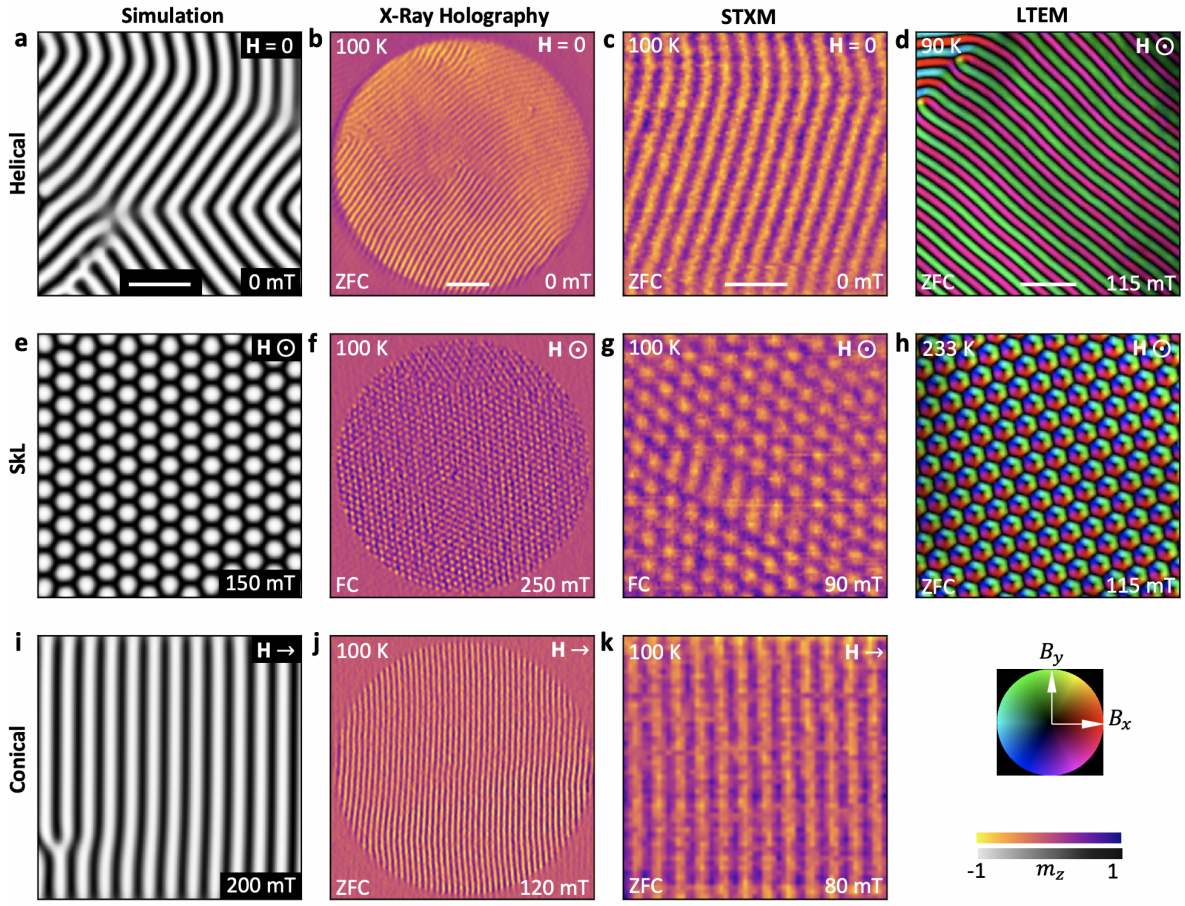

Figure 7.5: Micromagnetic simulations, experimental x-ray holography images, STXM images and LTEM images of the (**a-d**) helical, (**e-h**) SkL and (**i-k**) conical magnetic spin textures. The simulation, x-ray holography and STXM images plot the normalised out-of-plane magnetisation, m_z, as the colour map, while the LTEM images plot the in-plane magnetic flux density as the colour map, with the direction indicated by the colour wheel at the bottom right. Scale bar in **b**, 500 nm. All other scale bars, 200 nm.

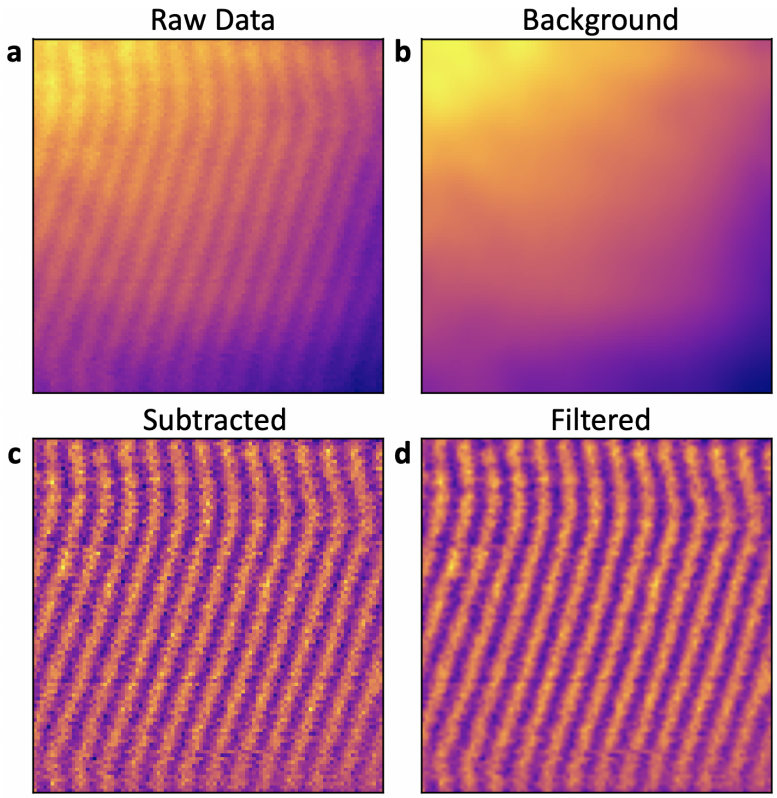

Figure 7.6: **a**, The raw STXM data recorded with a single x-ray polarisation. **b**, The background image produced by performing a wide Gaussian filter to the raw data. **c**, The image formed by subtracting the background image from the raw data. **d**, The image formed after applying a Gaussian filter to the subtracted data. **e**, The image after applying a hamming interpolation. Scale bar, 100 nm.

moment by acquiring images below 150 K. The helical state is featured in Fig. 7.5**a**-**d**, demonstrating the formation of stripe-like structures in diagonal orientations with a measured period of $\sim$ 70 nm. Figures 7.5**e**-**h** display images of the SkL state for an out-of-plane applied magnetic field, with a measured period of $\sim$ 83 nm. As no equilibrium SkL state is present at 150 K and below, we utilised field cooling to generate a metastable SkL state for the x-ray images presented in Fig. 7.5**f** and **g**. Images of the conical state under an in-plane magnetic field are displayed Figs. 7.5**i**-**k**, with a period of $\sim$ 70 nm.

Due to the slight variation in sample thickness across the second lamella sample, the intensity of transmitted x-rays varied across each STXM image, as shown by the example raw image shown in Fig. 7.6**a**. Therefore, a background smoothing

process was performed in order to allow the magnetic contrast in the images to be displayed clearly. In order to achieve this, a Gaussian filter was applied with a width of 3 pixels to each STXM image, producing a blurred image which effectively acts as a background, mapping the transmitted x-ray intensity variation due to sample thickness, Fig. 7.6**b**.

By subtracting this background image from the original image, an image with uniform background contrast is acquired, revealing the magnetic contrast as seen in Fig. 7.6**c**. We then applied a Gaussian filter with a width of 0.5 pixels and some minor interpolation, producing the final image in Fig. 7.6**d**. In principle, all structural contrast could be eliminated by subtracting a true background image, collected under the same imaging conditions but at a temperature above T_C. Alternatively, a subtraction of magnetic contrast images measured with opposite x-ray polarisation would leave only magnetic contrast. In practice, it was found that alignment of the corresponding images challenging due to sample and beam drift, as well as the large size of the imaging pixels relative to the magnetic structures.

7.5 Observation of Magnetic Skyrmion Tubes

After demonstrating successful x-ray imaging of chiral magnetic structures for both out-of-plane and in-plane applied magnetic fields, we investigated the possibility of observing the in-plane magnetic SkT state. When observed perpendicular to its central axis, an individual Bloch skyrmion tube is expected to exhibit both light and dark contrast, as the spins point in opposing directions either side of the central skyrmion core. We performed a variety of magnetic and temperature procedures in search of stabilising such an in-plane SkT state.

Comparative STXM images of the corner region of the second FeGe lamella sample are shown after ZFC, revealing the local orientation of the helical state in Fig. 7.7**a**, and after the application of an in-plane field of 35 mT, showing formation of the conical state along the magnetic field direction in Fig. 7.7**b**. Fig. 7.7**c** displays a STXM image acquired after FC the sample under an applied in-plane magnetic field of 35 mT. The three pairs of light and dark horizontal stripes at the corner of

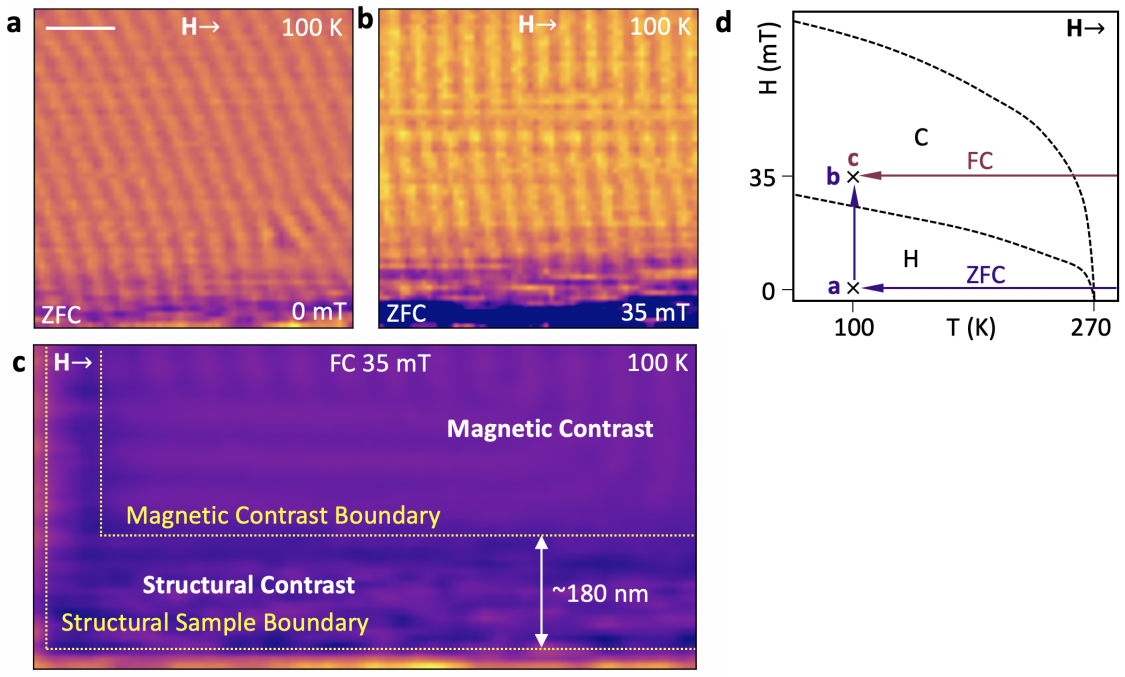

Figure 7.7: **a**-**c**, Scanning transmission x-ray microscopy images of the same corner area of the sample recorded after ZFC (**a**,**b**) and FC (**c**) procedures. The limit of the magnetic contrast region and the structural edge of the sample are depicted by yellow dashed lines in **c**. **d**, Illustrative phase diagram depicting the field-temperature paths taken for each measurement. Scale bar, 200 nm.

the sample are aligned along the applied magnetic field direction, and thus have the expected appearance of the SkT spin texture embedded in the vertical stripes of the conical state. A schematic illustration of temperature-field path taken during these measurements is shown in Fig. 7.7**d**. A region which exhibited no magnetic contrast before the structural edge of the sample is highlighted by the dashed yellow lines in 7.7**c**. This edge region can be composed of redeposited or damaged FeGe which builds up at the edge of the sample during ion milling, leading to observed structural contrast between the limit of the ordered magnetic contrast and the structural edge of the sample.

Fig. 7.8**a** displays a clearer micrograph of the potential SkT spin texture, showing the three skyrmion tubes in the corner of the lamella sample. While the uppermost skyrmion tube bends directly into the conical stripes, the two lower tubes appear to bulge outward at their ends before terminating in the conical state. Upon increasing the applied magnetic field, the skyrmion tubes decrease in length, before being annihilated by the conical state at 130 mT, as shown in Figs. 7.8**b-d**.

To validate the identification of these structures as the SkT state, we performed supporting micromagnetic simulations. These simulations were based on an idealised model which does not consider surface roughness, sample defects or temperature, but nevertheless provide an invaluable comparison to the experimental data. The simulation was initialised by relaxing a state consisting of three paraboloid-shaped skyrmion tube precursors at a range of in-plane magnetic fields, with the state at 150 mT showing the closest agreement to experiment (see Appendix Sec. B.3 for more details). The magnetic field was then varied to explore the field-dependent behaviour of the simulated SkT state. The average m_z through the thickness of the simulated sample was calculated to produce a simulated x-ray image of the magnetic state. Selected simulated images are displayed in Figs. 7.8**e-h**, showing remarkable agreement to the corresponding experimental micrographs. In Fig. 7.8**e**, at 80 mT, the end of the uppermost skyrmion tube curves into the conical state, while the two lower tubes appear to bulge at the end, replicating the behaviour observed in the experimental image in Fig. 7.8**a**.

Selected three dimensional visualisations of the simulations are displayed in Figs.

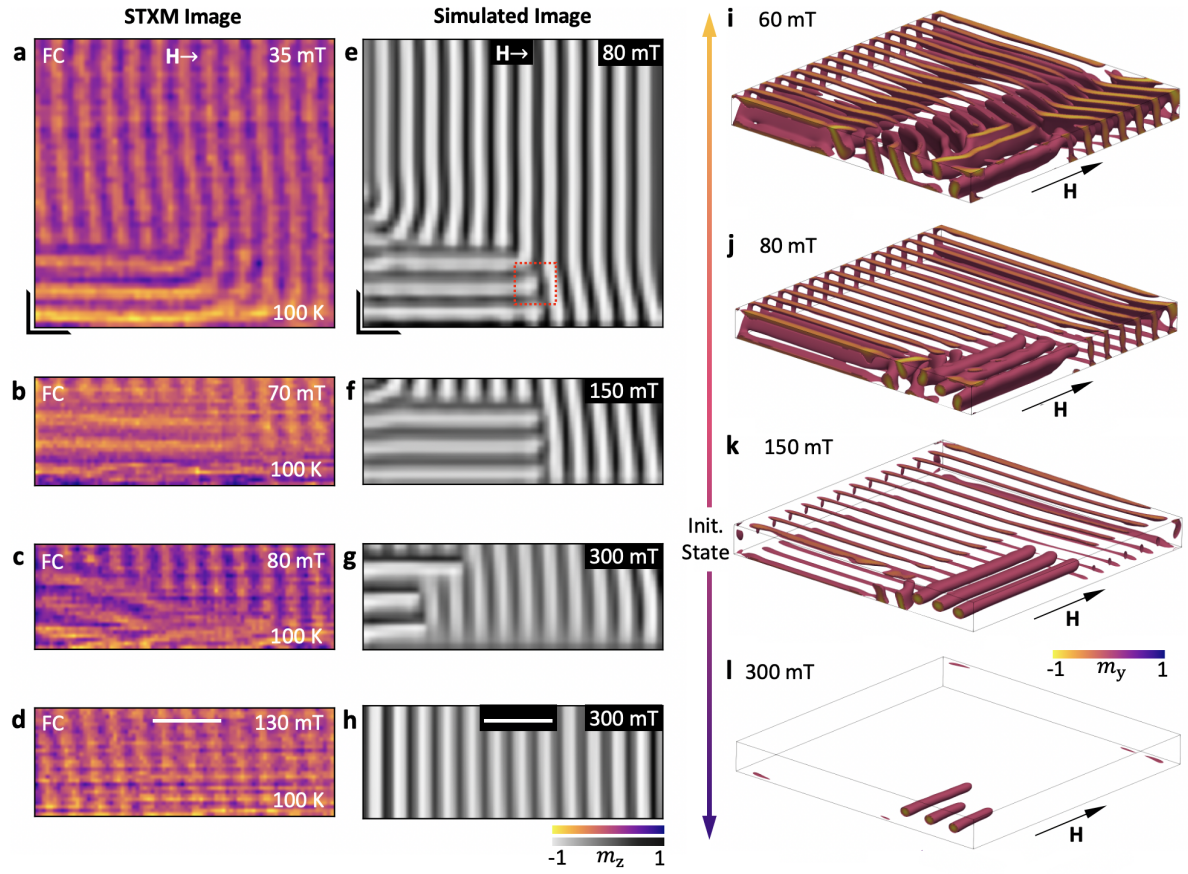

Figure 7.8: **a-d**, Scanning transmission x-ray micrographs of the skyrmion tube spin texture embedded in the conical state observed as a function of applied in-plane magnetic field. The colourmap plots the normalised out-of-plane magnetisation averaged through the thickness of the sample, m_z. The black L-shape in **a** indicates the location of the corner of the sample. **e-h**, Simulated images of the skyrmion tube spin texture embedded in the conical state, as determined from micromagnetic simulations calculated as a function of applied in-plane magnetic field, where the colourmap plots the normalised out-of-plane magnetisation averaged through the thickness. **i-l**, Three dimensional visualisations of the micromagentic simulations for selected magnetic fields, obtained by plotting cells with normalised m_y between -1 and 0.

7.8**i-l**. The additional surface structures which disappear with increasing field in Fig. 7.8**i-k** are chiral edge twists in the conical state at the sample boundary [319]. At decreasing magnetic fields, the skyrmion tubes branch into the helical state and expand to touch the surfaces of the simulated sample, establishing partial skyrmion tube edge states shown in Fig. 7.8**i**. Upon increasing the magnetic field, the skyrmion tubes decrease in length, as seen in the experimental images. Despite the qualitative agreement of the experimental and simulated images exhibited in Fig. 7.8, it is worth noting that in the simulation the SkT state exists over a higher magnetic field range in comparison to the experimental observations. This has the secondary effect of altering the relative magnetic contrast of the SkT and conical structures, due to the reduction of the spin canting angle in the cone state with changing applied field. However, this can be attributed to two factors. Firstly, micromagnetic simulations are not able to incorporate thermal effects, and are effectively performed at 0 K, whereas the experimental images were acquired at 100 K. Secondly, the lateral extent of the simulated sample is smaller than the measured lamella, exaggerating the effects of the demagnetising field.

A cross section through the end of one of the simulated skyrmion tubes is shown in Fig. 7.9**a**, highlighting the presence of a magnetic Bloch point. The discretisation of the magnetic spin texture in the simulations means that the estimated energy of large scale objects, such as the skyrmion tube itself, is robust, but small scale objects where the magnetisation rapidly changes, such as the Bloch points, may be inaccurate. Additionally, the 4 nm cell size in the simulation limited the size of the Bloch points to a nanometer scale, while in reality a Bloch point can be expected to exist on the scale of individual spins – beyond the limits of our current imaging resolution. Nevertheless, the image in Fig. 7.8**a** may represent the experimental observation of the magnetic configuration around the Bloch point at the end of a skyrmion tube, and is a crucial first step towards direct experimental comparison to theoretical work on Bloch points [179, 320].

We performed additional simulations commencing from a randomly initialised helical state at 0 mT, and found that the SkT state was also stabilised during an in-plane magnetic field sweep, as depicted by the visualisation in Fig. 7.9**b** (see

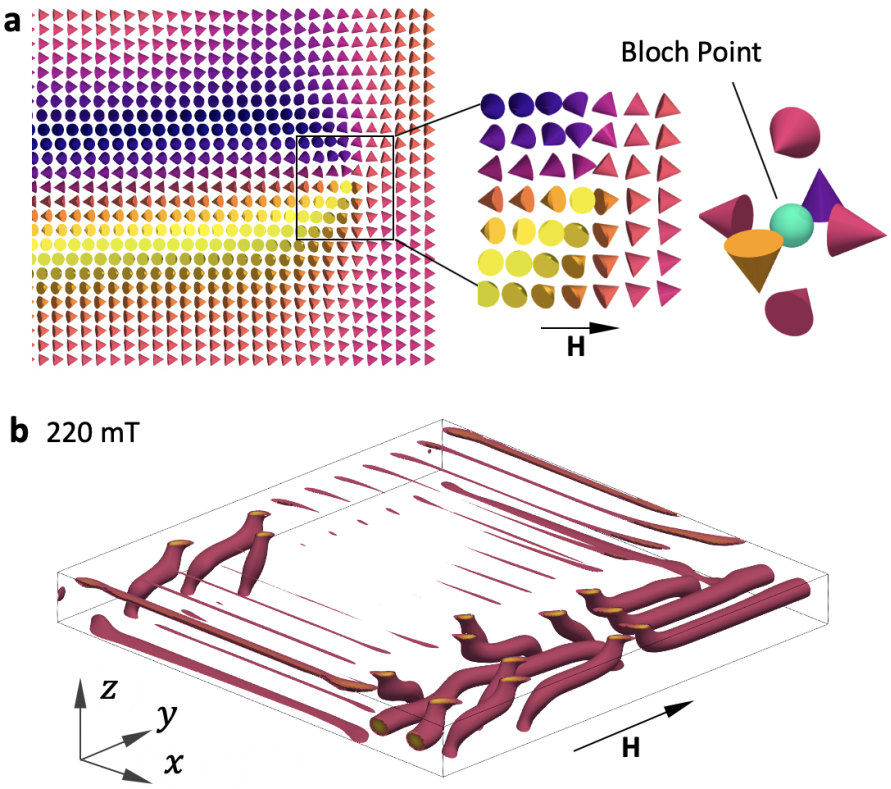

Figure 7.9: **a**, A cross section of spins from the simulation in Fig. 7.8**e**, location shown by the red box, highlighting the presence of a magnetic Bloch point at the end of each skyrmion tube. **b**, Three dimensional visualisation of the skyrmion tube state achieved after a field sweep from an initially randomised state. Scale bars, 200 nm.

Appendix Sec. B.4 for more details and visualisations). In contrast to the previous simulations, the ends of the tubes curve to touch the upper and lower faces of the sample. Such edge states may be energetically favourable in comparison to the formation of a magnetic Bloch point. Previous studies have demonstrated that the SkL state has improved stability at the sample boundaries for out-of-plane magnetic fields [58]. Our results suggest that the stability of the SkT state is similarly enhanced at the sample edge for in-plane magnetic fields. This may also explain why no SkT state was observed in the in-plane magnetic phase diagram in Fig. 7.4**b**, where the field of view was restricted to the centre of the FeGe lamella.

7.6 Discussion

The helical/conical period, $d_{\mathrm{h,c}}$, and the distance between each skyrmion tube, d_{ss}, were extracted from the experimental and simulated data, and are plotted as a function of applied magnetic field in Fig. 7.10**a** and **b** respectively. The skyrmion-edge distance d_{se} for the simulated data is also plotted. In both the simulation and experiment, $d_{\mathrm{h,c}}$ was found to remain approximately constant across the full range of applied magnetic field. In contrast, the simulated d_{ss} and d_{se} increase with applied magnetic field, exhibiting skyrmion-skyrmion and skyrmion-edge interactions which are attractive at low fields, and repulsive at higher fields, in agreement with studies of such interactions for the out-of-plane SkL state [85, 321].

At low and high fields, d_{ss} becomes respectively smaller and larger than the skyrmion radius. In both instances, the magnetisation of the SkT spin texture necessarily distorts from a sinusoidal function. This can be seen in Fig. 7.10**d** and **e**, where the out-of-plane component of the magnetisation across the width of the SkT exhibits an asymmetrical distortion that varies as a function of applied magnetic field and is not observed in the conical state. This distortion is functionally similar to the distortion of the helical state into a chiral soliton lattice [322], and is parameterised by ν in 7.10**c**, where $\nu = 0$ corresponds to an undistorted sinusoidal magnetisation (see Appendix A Sec. A.2).

While the experimental behaviour of d_{ss} is not exactly replicated by the simu-

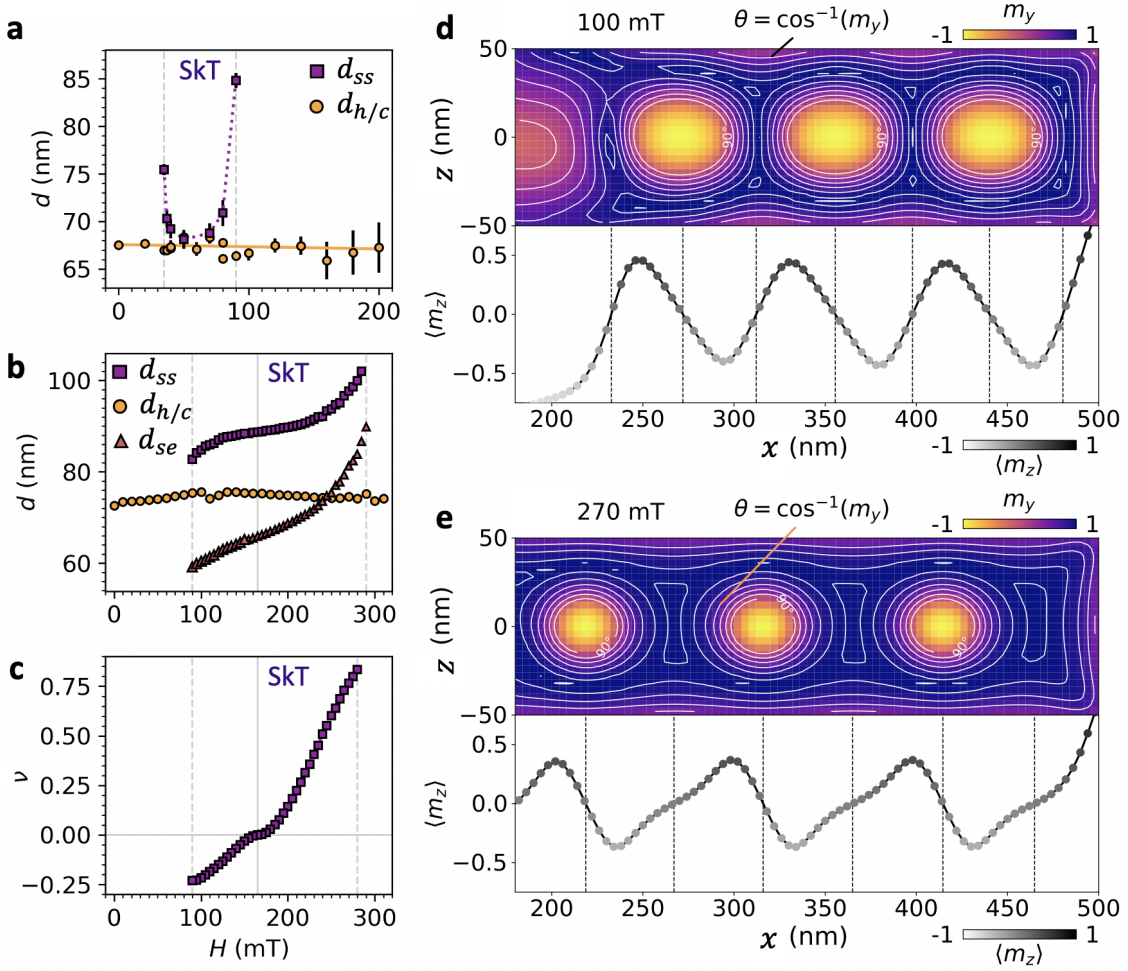

Figure 7.10: **a**,**b**, The skyrmion-skyrmion tube spacing, d_{ss}, the skyrmion-edge distance d_{se}, and helical/conical state period, $d_{\mathrm{h/c}}$, plotted as a function of applied magnetic field for the experimental and simulated images respectively. Error bars on the experimental data indicate the standard deviation obtained when fitting line profiles of the magnetic contrast from the STXM images with a sine function. **c**, The parameterised distortion, ν, of the out-of-plane magnetisation profile of the skyrmion tube state as a function of applied magnetic field. **d**,**e**, The m_{y} component of cross sections through the simulated skyrmion tube states at 100 and 270 mT are plotted in the top panels. Isocontours highlight the lines of constant m_{y}. The calculated average out-of-plane component, $\langle m_{\mathrm{z}} \rangle$, is plotted in the bottom panels. Vertical dotted lines indicate positions of maximum/minimum m_{y}.

lations, its value is nevertheless highly variable, ranging from 67 nm to 86 nm, in contrast to the constant value of $d_{\mathrm{h,c}}$. This provides strong evidence that the observed SkT spin texture is distinct from these topologically trivial magnetic states. We suggest that the discrepancy may be due to the formation of the SkT structure by field cooling, producing a pinned metastable state which relaxes over the first few field increments, before displaying the expected increase in d_{ss} at higher applied fields. Such pinning effects are not considered in the simulation model. In the future, achieving a lower temperature in the STXM instrument would allow the metastable skyrmion tubes to exist over a larger range of applied field, allowing this behaviour to be examined more thoroughly.

7.7 Conclusions

The successful application of x-ray holography and STXM for bulk skyrmion systems has been demonstrated, owing to the adaptation of existing instruments for cryogenic sample environments. Furthermore, the in-plane skyrmion tube spin texture was imaged in real-space for the first time, allowing this unexplored dimension of the magnetic skyrmion to be investigated. The field-evolution of the SkT state, and its location at the sample boundary in both the experiment and simulation, highlights the importance of confinement and boundary effects in the formation of this magnetic structure and the emergent skyrmion-skyrmion and skyrmion-edge interactions. Both the development of cryogenic x-ray microscopy, and the experimental realisation of in-plane skyrmion tube structures, open the door to new measurement techniques and experiments capable of investigating the detailed mechanisms governing skyrmion formation and annihilation.

Chapter 8

Summary and Conclusions

We have seen that chemical substitution is a powerful method of altering the properties of magnetic skyrmions. Particularly, the lifetime of metastable skyrmions is greatly increased by the pinning introduced by the presence of non-magnetic zinc ions substituted into Cu_2OSeO_3. These pinning effects also hinder the phase transition between the helical and conical states, preventing the large scale rotation of helimagnetic domains. However, it was revealed that additional magnetic energy terms, specifically the large low temperature cubic anisotropy in Cu_2OSeO_3, are able to overcome such pinning effects. This illustrates the careful balance of magnetic energies responsible for the formation and dynamics of magnetic spin textures, and demonstrates that the detrimental effects of defects and disorder introduced by chemical substitution may mitigated by careful consideration of the magnetic interaction terms. Controlled manipulation of this energy balance will be crucial both for the engineering of skyrmion materials towards device applications, and for the exploration of new topological phases of matter. For future work in this area, it would be enlightening to explore the effect of chemical substitution, or doping, on more exotic skyrmion phenomena, such as the nucleation of low temperature skyrmions in Cu_2OSeO_3, or the stabilisation of square skyrmion lattices, or meron-antimeron lattices, in MnSi and the CoZnMn alloys.

Through the development of real-space x-ray imaging, the vertical dimension of the skyrmion state was directly visualised for the first time. The use of x-ray imaging was demonstrated to posses the advantage of allowing imaging with an in-

plane magnetic field, which was vital for the successful observation of the skyrmion tube state. Comparative micromagnetic simulations gave a glimpse at the potential power of such methods when investigating local topological defect dynamics, such as the motion of magnetic Bloch points located at the end of each broken skyrmion tube. Following this line of research, it would be interesting to attempt time resolved imaging of skyrmion tubes dynamics such as the current-induced topological unwinding of skyrmion tubes by Bloch points, or the resonant dynamics of skyrmion lattices. The continued development of real-space imaging techniques, particularly with the large parameter space provided by cyrogenic temperatures and a variable sample and magnetic field orientation, will allow for full nanoscale visualisation of exotic spin textures and their localised dynamic mechanisms. It is anticipated that this will open new avenues of investigation for both skyrmions, and beyond into further condensed matter systems.

References

[1] Skyrme, T. H. R. A unified field theory of mesons and baryons. *Nuclear Physics* **31**, 556–569 (1962).

[2] Marciano, W. & Pagels, H. Quantum chromodynamics. *Nature* **279**, 479–483 (1979).

[3] Nagaosa, N. & Tokura, Y. Topological properties and dynamics of magnetic skyrmions. *Nature Nanotechnology* **8**, 899–911 (2013).

[4] Lancaster, T. Skyrmions in magnetic materials. *Contemporary Physics* **60**, 246–261 (2019).

[5] Rößler, U. K., Bogdanov, A. N. & Pfleiderer, C. Spontaneous skyrmion ground states in magnetic metals. *Nature* **442**, 797–801 (2006).

[6] Mühlbauer, S. *et al.* Skyrmion Lattice in a Chiral Magnet. *Science* **323**, 915–919 (2009).

[7] Asorey, M. Space, matter and topology. *Nature Physics* **12**, 616–618 (2016).

[8] Lindner, N. H., Refael, G. & Galitski, V. Floquet topological insulator in semiconductor quantum wells. *Nature Physics* **7**, 490–495 (2011).

[9] Moore, J. E. The birth of topological insulators. *Nature* **464**, 194–198 (2010).

[10] Trang, C. X. *et al.* Conversion of a conventional superconductor into a topological superconductor by topological proximity effect. *Nature Communications* **11**, 159 (2020).

[11] Sato, M. & Ando, Y. Topological superconductors: a review. *Reports on Progress in Physics* **80**, 076501 (2017).

[12] Lan, H.-S., Chang, S. T. & Liu, C. W. Semiconductor, topological semimetal, indirect semimetal, and topological Dirac semimetal phases of $Ge_{1-x}Sn_x$ alloys. *Physical Review B* **95**, 201201 (2017).

[13] Burkov, A. A. Topological semimetals. *Nature Materials* **15**, 1145–1148 (2016).

[14] Rößler, U. K., Leonov, A. A. & Bogdanov, A. N. Chiral Skyrmionic matter in non-centrosymmetric magnets. *Journal of Physics: Conference Series* **303**, 012105 (2011).

[15] Fert, A., Reyren, N. & Cros, V. Magnetic skyrmions: advances in physics and potential applications. *Nature Reviews Materials* **2**, 1–15 (2017).

[16] Bogdanov, A. N. & Rößler, U. K. Chiral Symmetry Breaking in Magnetic Thin Films and Multilayers. *Physical Review Letters* **87**, 037203 (2001).

[17] Al Khawaja, U. & Stoof, H. Skyrmions in a ferromagnetic Bose–Einstein condensate. *Nature* **411**, 918–920 (2001).

[18] Choi, J.-y., Kwon, W. J. & Shin, Y.-i. Observation of Topologically Stable 2D Skyrmions in an Antiferromagnetic Spinor Bose-Einstein Condensate. *Physical Review Letters* **108**, 035301 (2012).

[19] Nych, A., Fukuda, J.-i., Ognysta, U., Žumer, S. & Muševič, I. Spontaneous formation and dynamics of half-skyrmions in a chiral liquid-crystal film. *Nature Physics* **13**, 1215–1220 (2017).

[20] Matteis, G. D., Martina, L. & Turco, V. Skyrmion States in Chiral Liquid Crystals. *Theoretical and Mathematical Physics* **196**, 1150–1163 (2018).

[21] Sohn, H. R. O. *et al.* Light-controlled skyrmions and torons as reconfigurable particles. *Optics Express* **27**, 29055–29068 (2019).

[22] Back, C. H. *et al.* The 2020 Skyrmionics Roadmap. *Journal of Physics D: Applied Physics* (2020).

[23] Leeuw, F. H. D., Doel, R. V. D. & Enz, U. Dynamic properties of magnetic domain walls and magnetic bubbles. *Reports on Progress in Physics* **43**, 689–783 (1980).

[24] Leonov, A. O., Rößler, U. K. & Mostovoy, M. Target-skyrmions and skyrmion clusters in nanowires of chiral magnets. *EPJ Web of Conferences* **75**, 05002 (2014).

[25] Zhang, S., Kronast, F., van der Laan, G. & Hesjedal, T. Real-Space Observation of Skyrmionium in a Ferromagnet-Magnetic Topological Insulator Heterostructure. *Nano Letters* **18**, 1057–1063 (2018).

[26] Yu, X. Z. *et al.* Biskyrmion states and their current-driven motion in a layered manganite. *Nature Communications* **5**, 1–7 (2014).

[27] Peng, L. *et al.* Generation of high-density biskyrmions by electric current. *npj Quantum Materials* **2**, 1–7 (2017).

[28] Loudon, J. C. *et al.* Do Images of Biskyrmions Show Type-II Bubbles? *Advanced Materials* **31**, 1806598 (2019).

[29] Ezawa, M. Compact merons and skyrmions in thin chiral magnetic films. *Physical Review B* **83**, 100408 (2011).

[30] Wilhelm, H. *et al.* Precursor Phenomena at the Magnetic Ordering of the Cubic Helimagnet FeGe. *Physical Review Letters* **107**, 127203 (2011).

[31] Yi, S. D., Onoda, S., Nagaosa, N. & Han, J. H. Skyrmions and anomalous Hall effect in a Dzyaloshinskii-Moriya spiral magnet. *Physical Review B* **80**, 054416 (2009).

[32] Lin, S.-Z., Saxena, A. & Batista, C. D. Skyrmion fractionalization and merons in chiral magnets with easy-plane anisotropy. *Physical Review B* **91**, 224407 (2015).

[33] Yu, X. Z. *et al.* Transformation between meron and skyrmion topological spin textures in a chiral magnet. *Nature* **564**, 95–98 (2018).

[34] Takagi, R. *et al.* Low-Field Bi-Skyrmion Formation in a Noncentrosymmetric Chimney Ladder Ferromagnet. *Physical Review Letters* **120**, 037203 (2018).

[35] Phatak, C., Heinonen, O., De Graef, M. & Petford-Long, A. Nanoscale Skyrmions in a Nonchiral Metallic Multiferroic: Ni_2MnGa. *Nano Letters* **16**, 4141–4148 (2016).

[36] Yu, X. *et al.* Magnetic stripes and skyrmions with helicity reversals. *Proceedings of the National Academy of Sciences* **109**, 8856–8860 (2012).

[37] Wang, W. *et al.* A Centrosymmetric Hexagonal Magnet with Superstable Biskyrmion Magnetic Nanodomains in a Wide Temperature Range of 100–340 K. *Advanced Materials* **28**, 6887–6893 (2016).

[38] Peng, L. *et al.* Real-Space Observation of Nonvolatile Zero-Field Biskyrmion Lattice Generation in MnNiGa Magnet. *Nano Letters* **17**, 7075–7079 (2017).

[39] Zuo, S. L. *et al.* Direct observation of the topological spin configurations mediated by the substitution of rare-earth element Y in MnNiGa alloy. *Nanoscale* **10**, 2260–2266 (2018).

[40] Kiselev, N. S., Bogdanov, A. N., Schäfer, R. & Rößler, U. K. Chiral skyrmions in thin magnetic films: new objects for magnetic storage technologies? *Journal of Physics D: Applied Physics* **44**, 392001 (2011).

[41] Sampaio, J., Cros, V., Rohart, S., Thiaville, A. & Fert, A. Nucleation, stability and current-induced motion of isolated magnetic skyrmions in nanostructures. *Nature Nanotechnology* **8**, 839–844 (2013).

[42] Koshibae, W. *et al.* Memory functions of magnetic skyrmions. *Japanese Journal of Applied Physics* **54**, 053001 (2015).

[43] Finocchio, G., Büttner, F., Tomasello, R., Carpentieri, M. & Kläui, M. Magnetic skyrmions: from fundamental to applications. *Journal of Physics D: Applied Physics* **49**, 423001 (2016).

[44] Jonietz, F. *et al.* Spin Transfer Torques in MnSi at Ultralow Current Densities. *Science* **330**, 1648–1651 (2010).

[45] Everschor, K., Garst, M., Duine, R. A. & Rosch, A. Current-induced rotational torques in the skyrmion lattice phase of chiral magnets. *Physical Review B* **84**, 064401 (2011).

[46] Schulz, T. *et al.* Emergent electrodynamics of skyrmions in a chiral magnet. *Nature Physics* **8**, 301 (2012).

[47] Koshibae, W. & Nagaosa, N. Theory of current-driven skyrmions in disordered magnets. *Scientific Reports* **8**, 1–13 (2018).

[48] Shibata, K. *et al.* Current-Driven Motion of Domain Boundaries between Skyrmion Lattice and Helical Magnetic Structure. *Nano Letters* **18**, 929–933 (2018).

[49] Yu, X. *et al.* Current-Induced Nucleation and Annihilation of Magnetic Skyrmions at Room Temperature in a Chiral Magnet. *Advanced Materials* **29**, 1606178 (2017).

[50] Parkin, S. S. P., Hayashi, M. & Thomas, L. Magnetic Domain-Wall Racetrack Memory. *Science* **320**, 190–194 (2008).

[51] Slonczewski, J. C. Current-driven excitation of magnetic multilayers. *Journal of Magnetism and Magnetic Materials* **159**, L1–L7 (1996).

[52] Hayashi, M. *et al.* Dependence of Current and Field Driven Depinning of Domain Walls on Their Structure and Chirality in Permalloy Nanowires. *Physical Review Letters* **97**, 207205 (2006).

[53] Koyama, T. *et al.* Observation of the intrinsic pinning of a magnetic domain wall in a ferromagnetic nanowire. *Nature Materials* **10**, 194–197 (2011).

[54] Fert, A., Cros, V. & Sampaio, J. Skyrmions on the track. *Nature Nanotechnology* **8**, 152–156 (2013).

[55] Tomasello, R. *et al.* A strategy for the design of skyrmion racetrack memories. *Scientific Reports* **4**, 1–7 (2014).

[56] Yu, X. *et al.* Observation of the Magnetic Skyrmion Lattice in a MnSi Nanowire by Lorentz TEM. *Nano Letters* **13**, 3755–3759 (2013).

[57] Du, H. *et al.* Highly Stable Skyrmion State in Helimagnetic MnSi Nanowires. *Nano Letters* **14**, 2026–2032 (2014).

[58] Du, H. *et al.* Edge-mediated skyrmion chain and its collective dynamics in a confined geometry. *Nature Communications* **6**, 1–7 (2015).

[59] Stolt, M. J. *et al.* Selective Chemical Vapor Deposition Growth of Cubic FeGe Nanowires That Support Stabilized Magnetic Skyrmions. *Nano Letters* **17**, 508–514 (2017).

[60] Romming, N. *et al.* Writing and Deleting Single Magnetic Skyrmions. *Science* **341**, 636–639 (2013).

[61] Tchoe, Y. & Han, J. H. Skyrmion generation by current. *Physical Review B* **85**, 174416 (2012).

[62] Woo, S. *et al.* Observation of room-temperature magnetic skyrmions and their current-driven dynamics in ultrathin metallic ferromagnets. *Nature Materials* **15**, 501–506 (2016).

[63] Hrabec, A. *et al.* Current-induced skyrmion generation and dynamics in symmetric bilayers. *Nature Communications* **8**, 1–6 (2017).

[64] Garanin, D. A., Capic, D., Zhang, S., Zhang, X. & Chudnovsky, E. M. Writing skyrmions with a magnetic dipole. *Journal of Applied Physics* **124**, 113901 (2018).

[65] Zhang, S. *et al.* Direct writing of room temperature and zero field skyrmion lattices by a scanning local magnetic field. *Applied Physics Letters* **112**, 132405 (2018).

[66] Mochizuki, M. & Watanabe, Y. Writing a skyrmion on multiferroic materials. *Applied Physics Letters* **107**, 082409 (2015).

[67] Schott, M. *et al.* The Skyrmion Switch: Turning Magnetic Skyrmion Bubbles on and off with an Electric Field. *Nano Letters* **17**, 3006–3012 (2017).

[68] Hsu, P.-J. *et al.* Electric-field-driven switching of individual magnetic skyrmions. *Nature Nanotechnology* **12**, 123–126 (2017).

[69] Koshibae, W. & Nagaosa, N. Creation of skyrmions and antiskyrmions by local heating. *Nature Communications* **5**, 5148 (2014).

[70] Je, S.-G. *et al.* Creation of Magnetic Skyrmion Bubble Lattices by Ultrafast Laser in Ultrathin Films. *Nano Letters* **18**, 7362–7371 (2018).

[71] Zhou, Y. & Ezawa, M. A reversible conversion between a skyrmion and a domain-wall pair in a junction geometry. *Nature Communications* **5**, 4652 (2014).

[72] Lin, S.-Z. Edge instability in a chiral stripe domain under an electric current and skyrmion generation. *Physical Review B* **94**, 020402 (2016).

[73] Jiang, W. *et al.* Blowing magnetic skyrmion bubbles. *Science* **349**, 283–286 (2015).

[74] Iwasaki, J., Mochizuki, M. & Nagaosa, N. Current-induced skyrmion dynamics in constricted geometries. *Nature Nanotechnology* **8**, 742–747 (2013).

[75] Mochizuki, M. Controlled creation of nanometric skyrmions using external magnetic fields. *Applied Physics Letters* **111**, 092403 (2017).

[76] Fraerman, A. A. *et al.* Skyrmion states in multilayer exchange coupled ferromagnetic nanostructures with distinct anisotropy directions. *Journal of Magnetism and Magnetic Materials* **393**, 452–456 (2015).

[77] Müller, J., Rosch, A. & Garst, M. Edge instabilities and skyrmion creation in magnetic layers. *New Journal of Physics* **18**, 065006 (2016).

[78] Hanneken, C. *et al.* Electrical detection of magnetic skyrmions by tunnelling non-collinear magnetoresistance. *Nature Nanotechnology* **10**, 1039–1042 (2015).

[79] Du, H. *et al.* Electrical probing of field-driven cascading quantized transitions of skyrmion cluster states in MnSi nanowires. *Nature Communications* **6**, 7637 (2015).

[80] Neubauer, A. Topological Hall Effect in the *a*-phase of MnSi. *Physical Review Letters* **102** (2009).

[81] Lee, M., Kang, W., Onose, Y., Tokura, Y. & Ong, N. P. Unusual Hall effect anomaly in MnSi under pressure. *Physical Review Letters* **102**, 186601 (2009).

[82] Kanazawa, N. *et al.* Large topological Hall effect in a short-period helimagnet MnGe. *Physical Review Letters* **106**, 156603 (2011).

[83] Jiang, W. *et al.* Direct observation of the skyrmion Hall effect. *Nature Physics* **13**, 162–169 (2017).

[84] Zhang, X. *et al.* Skyrmion-skyrmion and skyrmion-edge repulsions in skyrmion-based racetrack memory. *Scientific Reports* **5**, 1–6 (2015).

[85] Du, H. *et al.* Interaction of Individual Skyrmions in a Nanostructured Cubic Chiral Magnet. *Physical Review Letters* **120**, 197203 (2018).

[86] Leonov, A. O. & Mostovoy, M. Edge states and skyrmion dynamics in nanostripes of frustrated magnets. *Nature Communications* **8**, 1–7 (2017).

[87] Zhang, X., Zhou, Y. & Ezawa, M. Antiferromagnetic Skyrmion: Stability, Creation and Manipulation. *Scientific Reports* **6**, 1–8 (2016).

[88] Yu, G. *et al.* Room-Temperature Creation and Spin–Orbit Torque Manipulation of Skyrmions in Thin Films with Engineered Asymmetry. *Nano Letters* **16**, 1981–1988 (2016).

[89] Kim, S. K., Lee, K.-J. & Tserkovnyak, Y. Self-focusing skyrmion racetracks in ferrimagnets. *Physical Review B* **95**, 140404 (2017).

[90] Zhang, S. L. *et al.* Manipulation of skyrmion motion by magnetic field gradients. *Nature Communications* **9**, 2115 (2018).

[91] Rohart, S. & Thiaville, A. Skyrmion confinement in ultrathin film nanostructures in the presence of Dzyaloshinskii-Moriya interaction. *Physical Review B* **88**, 184422 (2013).

[92] Du, H., Ning, W., Tian, M. & Zhang, Y. Field-driven evolution of chiral spin textures in a thin helimagnet nanodisk. *Physical Review B* **87**, 014401 (2013).

[93] Du, H., Ning, W., Tian, M. & Zhang, Y. Magnetic vortex with skyrmionic core in a thin nanodisk of chiral magnets. *EPL (Europhysics Letters)* **101**, 37001 (2013).

[94] Beg, M. *et al.* Ground state search, hysteretic behaviour, and reversal mechanism of skyrmionic textures in confined helimagnetic nanostructures. *Scientific Reports* **5**, 17137 (2015).

[95] Guslienko, K. Y. Skyrmion State Stability in Magnetic Nanodots With Perpendicular Anisotropy. *IEEE Magnetics Letters* **6**, 1–4 (2015).

[96] Gilbert, D. A. *et al.* Realization of ground-state artificial skyrmion lattices at room temperature. *Nature Communications* **6**, 8462 (2015).

[97] Carey, R. *et al.* Hysteresis of nanocylinders with Dzyaloshinskii-Moriya interaction. *Applied Physics Letters* **109**, 122401 (2016).

[98] Zhao, X. *et al.* Direct imaging of magnetic field-driven transitions of skyrmion cluster states in FeGe nanodisks. *Proceedings of the National Academy of Sciences* (2016).

[99] Zhang, X., Ezawa, M. & Zhou, Y. Magnetic skyrmion logic gates: conversion, duplication and merging of skyrmions. *Scientific Reports* **5**, 9400 (2015).

[100] Zhang, S., Baker, A. A., Komineas, S. & Hesjedal, T. Topological computation based on direct magnetic logic communication. *Scientific Reports* **5**, 1–11 (2015).

[101] Upadhyaya, P., Yu, G., Amiri, P. K. & Wang, K. L. Electric-field guiding of magnetic skyrmions. *Physical Review B* **92**, 134411 (2015).

[102] Li, Z.-A. *et al.* Magnetic Skyrmion Formation at Lattice Defects and Grain Boundaries Studied by Quantitative Off-Axis Electron Holography. *Nano Letters* **17**, 1395–1401 (2017).

[103] Song, K. M. *et al.* Skyrmion-based artificial synapses for neuromorphic computing. *Nature Electronics* **3**, 148–155 (2020).

[104] Zázvorka, J. *et al.* Thermal skyrmion diffusion used in a reshuffler device. *Nature Nanotechnology* **14**, 658–661 (2019).

[105] Mochizuki, M. & Seki, S. Magnetoelectric resonances and predicted microwave diode effect of the skyrmion crystal in a multiferroic chiral-lattice magnet. *Physical Review B* **87**, 134403 (2013).

[106] Okamura, Y. *et al.* Microwave magnetoelectric effect via skyrmion resonance modes in a helimagnetic multiferroic. *Nature Communications* **4**, 1–6 (2013).

[107] Finocchio, G. *et al.* Skyrmion based microwave detectors and harvesting. *Applied Physics Letters* **107**, 262401 (2015).

[108] Navau, C., Del-Valle, N. & Sanchez, A. Analytical trajectories of skyrmions in confined geometries: Skyrmionic racetracks and nano-oscillators. *Physical Review B* **94**, 184104 (2016).

[109] Moutafis, C. *et al.* Magnetic bubbles in FePt nanodots with perpendicular anisotropy. *Physical Review B* **76**, 104426 (2007).

[110] Beausoleil, W. F., Brown, D. T. & Phelps, B. E. Magnetic Bubble Memory Organization. *IBM Journal of Research and Development* **16**, 587–591 (1972).

[111] Zhang, X. *et al.* Skyrmion-electronics: writing, deleting, reading and processing magnetic skyrmions toward spintronic applications. *Journal of Physics: Condensed Matter* **32**, 143001 (2020).

[112] Thiaville, A., Rohart, S., Jué, E., Cros, V. & Fert, A. Dynamics of Dzyaloshinskii domain walls in ultrathin magnetic films. *EPL (Europhysics Letters)* **100**, 57002 (2012).

[113] Boulle, O. *et al.* Room-temperature chiral magnetic skyrmions in ultrathin magnetic nanostructures. *Nature Nanotechnology* **11**, 449–454 (2016).

[114] Dovzhenko, Y. *et al.* Magnetostatic twists in room-temperature skyrmions explored by nitrogen-vacancy center spin texture reconstruction. *Nature Communications* **9**, 1–7 (2018).

[115] Moreau-Luchaire, C. *et al.* Additive interfacial chiral interaction in multilayers for stabilization of small individual skyrmions at room temperature. *Nature Nanotechnology* **11**, 444–448 (2016).

[116] Chen, G., Mascaraque, A., N'Diaye, A. T. & Schmid, A. K. Room temperature skyrmion ground state stabilized through interlayer exchange coupling. *Applied Physics Letters* **106**, 242404 (2015).

[117] Baltz, V., Marty, A., Rodmacq, B. & Dieny, B. Magnetic domain replication in interacting bilayers with out-of-plane anisotropy: Application to Co/Pt multilayers. *Physical Review B* **75**, 014406 (2007).

[118] Dupé, B., Kruse, C. N., Dornheim, T. & Heinze, S. How to reveal metastable skyrmionic spin structures by spin-polarized scanning tunneling microscopy. *New Journal of Physics* **18**, 055015 (2016).

[119] Heinze, S. *et al.* Spontaneous atomic-scale magnetic skyrmion lattice in two dimensions. *Nature Physics* **7**, 713–718 (2011).

[120] von Bergmann, K., Menzel, M., Kubetzka, A. & Wiesendanger, R. Influence of the Local Atom Configuration on a Hexagonal Skyrmion Lattice. *Nano Letters* **15**, 3280–3285 (2015).

[121] Pappas, C. *et al.* Chiral Paramagnetic Skyrmion-like Phase in MnSi. *Physical Review Letters* **102**, 197202 (2009).

[122] Janoschek, M. *et al.* Fluctuation-induced first-order phase transition in Dzyaloshinskii-Moriya helimagnets. *Physical Review B* **87**, 134407 (2013).

[123] Münzer, W. *et al.* Skyrmion lattice in the doped semiconductor FeGe. *Physical Review B* **81**, 041203 (2010).

[124] Yu, X. Z. *et al.* Real-space observation of a two-dimensional skyrmion crystal. *Nature* **465**, 901–904 (2010).

[125] Bannenberg, L. J. *et al.* Universality of the helimagnetic transition in cubic chiral magnets: Small angle neutron scattering and neutron spin echo spectroscopy studies of $Fe_{1-x}Co_xSi$. *Physical Review B* **95**, 144433 (2017).

[126] Yu, X. Z. *et al.* Near room-temperature formation of a skyrmion crystal in thin-films of the helimagnet FeGe. *Nature Materials* **10**, 106–109 (2011).

[127] Moskvin, E. *et al.* Complex Chiral Modulations in FeGe Close to Magnetic Ordering. *Physical Review Letters* **110**, 077207 (2013).

[128] Kanazawa, N. *et al.* Possible skyrmion-lattice ground state in the B20 chiral-lattice magnet MnGe as seen via small-angle neutron scattering. *Physical Review B* **86**, 134425 (2012).

[129] Tanigaki, T. *et al.* Real-Space Observation of Short-Period Cubic Lattice of Skyrmions in MnGe. *Nano Letters* **15**, 5438–5442 (2015).

[130] Tokunaga, Y. *et al.* A new class of chiral materials hosting magnetic skyrmions beyond room temperature. *Nature Communications* **6**, 7638 (2015).

[131] Takagi, R. *et al.* Spin-wave spectroscopy of the Dzyaloshinskii-Moriya interaction in room-temperature chiral magnets hosting skyrmions. *Physical Review B* **95**, 220406 (2017).

[132] Lancaster, T. Transverse field muon-spin rotation measurement of the topological anomaly in a thin film of MnSi. *Physical Review B* **93** (2016).

[133] Meynell, S. A. *et al.* Hall effect and transmission electron microscopy of epitaxial MnSi thin films. *Physical Review B* **90**, 224419 (2014).

[134] Zhang, S. L. *et al.* Engineering helimagnetism in MnSi thin films. *AIP Advances* **6**, 015217 (2016).

[135] Kanazawa, N. *et al.* Direct observation of anisotropic magnetic field response of the spin helix in FeGe thin films. *Physical Review B* **94**, 184432 (2016).

[136] Wilson, M. N., Butenko, A. B., Bogdanov, A. N. & Monchesky, T. L. Chiral skyrmions in cubic helimagnet films: The role of uniaxial anisotropy. *Physical Review B* **89**, 094411 (2014).

[137] Figueroa, A. I. *et al.* Strain in epitaxial MnSi films on Si(111) in the thick film limit studied by polarization-dependent extended x-ray absorption fine structure. *Physical Review B* **94**, 174107 (2016).

[138] Zhang, S. L. *et al.* Room-temperature helimagnetism in FeGe thin films. *Scientific Reports* **7**, 1–10 (2017).

[139] Seki, S., Yu, X. Z., Ishiwata, S. & Tokura, Y. Observation of Skyrmions in a Multiferroic Material. *Science* **336**, 198–201 (2012).

[140] Makino, K. *et al.* Thermal stability and irreversibility of skyrmion-lattice phases in Cu_2OSeO_3. *Physical Review B* **95**, 134412 (2017).

[141] Sidorov, V. A., Petrova, A. E., Berdonosov, P. S., Dolgikh, V. A. & Stishov, S. M. Comparative study of helimagnets MnSi and Cu_2OSeO_3 at high pressures. *Physical Review B* **89**, 100403 (2014).

[142] Seki, S. *et al.* Formation and rotation of skyrmion crystal in the chiral-lattice insulator Cu_2OSeO_3. *Physical Review B* **85**, 220406 (2012).

[143] Yang, J. H. *et al.* Strong Dzyaloshinskii-Moriya Interaction and Origin of Ferroelectricity in Cu_2OSeO_3. *Physical Review Letters* **109**, 107203 (2012).

[144] Omrani, A. A. *et al.* Exploration of the helimagnetic and skyrmion lattice phase diagram in Cu_2OSeO_3 using magnetoelectric susceptibility. *Physical Review B* **89**, 064406 (2014).

[145] Zhang, S. L. *et al.* Resonant elastic x-ray scattering from the skyrmion lattice in Cu_2OSeO_3. *Physical Review B* **93**, 214420 (2016).

[146] White, J. S. *et al.* Electric field control of the skyrmion lattice in Cu_2OSeO_3. *Journal of Physics: Condensed Matter* **24**, 432201 (2012).

[147] White, J. *et al.* Electric-Field-Induced Skyrmion Distortion and Giant Lattice Rotation in the Magnetoelectric Insulator Cu_2OSeO_3. *Physical Review Letters* **113**, 107203 (2014).

[148] Okamura, Y., Kagawa, F., Seki, S. & Tokura, Y. Transition to and from the skyrmion lattice phase by electric fields in a magnetoelectric compound. *Nature Communications* **7**, 1–6 (2016).

[149] Okamura, Y. *et al.* Directional electric-field induced transformation from skyrmion lattice to distinct helices in multiferroic Cu_2OSeO_3. *Physical Review B* **95**, 184411 (2017).

[150] Wilson, M. N. *et al.* Measuring the formation energy barrier of skyrmions in zinc-substituted Cu_2OSeO_3. *Physical Review B* **99**, 174421 (2019).

[151] Zhang, S. L. *et al.* Multidomain Skyrmion Lattice State in Cu_2OSeO_3. *Nano Letters* **16**, 3285–3291 (2016).

[152] Romhányi, J., van den Brink, J. & Rousochatzakis, I. Entangled tetrahedron ground state and excitations of the magnetoelectric skyrmion material Cu_2OSeO_3. *Physical Review B* **90**, 140404 (2014).

[153] Janson, O. *et al.* The quantum nature of skyrmions and half-skyrmions in Cu_2OSeO_3. *Nature Communications* **5**, 1–11 (2014).

[154] Kohn, K. A New Ferrimagnet Cu_2SeO_4. *Journal of the Physical Society of Japan* **42**, 2065–2066 (1977).

[155] Nayak, A. K. *et al.* Magnetic antiskyrmions above room temperature in tetragonal Heusler materials. *Nature* **548**, 561–566 (2017).

[156] Kézsmárki, I. *et al.* Néel-type skyrmion lattice with confined orientation in the polar magnetic semiconductor GaV_4S_8. *Nature Materials* **14**, 1116–1122 (2015).

[157] Bordács, S. *et al.* Equilibrium Skyrmion Lattice Ground State in a Polar Easy-plane Magnet. *Scientific Reports* **7**, 1–11 (2017).

[158] Franke, K. J. A. *et al.* Magnetic phases of skyrmion-hosting $GaV_4S_{8-y}Se_y$ ($y = 0, 2, 4, 8$) probed with muon spectroscopy. *Physical Review B* **98**, 054428 (2018).

[159] Hicken, T. J. *et al.* Magnetism and Néel skyrmion dynamics in $GaV_4S_{8-y}Se_y$. *Physical Review Research* **2**, 032001 (2020).

[160] Leonov, A. O. & Mostovoy, M. Multiply periodic states and isolated skyrmions in an anisotropic frustrated magnet. *Nature Communications* **6**, 1–8 (2015).

[161] Karube, K. *et al.* Disordered skyrmion phase stabilized by magnetic frustration in a chiral magnet. *Science Advances* **4**, eaar7043 (2018).

[162] Kurumaji, T. *et al.* Skyrmion lattice with a giant topological Hall effect in a frustrated triangular-lattice magnet. *Science* **365**, 914–918 (2019).

[163] Hirschberger, M. *et al.* Skyrmion phase and competing magnetic orders on a breathing kagomé lattice. *Nature Communications* **10**, 5831 (2019).

[164] Khanh, N. D. *et al.* Nanometric square skyrmion lattice in a centrosymmetric tetragonal magnet. *Nature Nanotechnology* **15**, 444–449 (2020).

[165] Bak, P. & Jensen, M. H. Theory of helical magnetic structures and phase transitions in MnSi and FeGe. *Journal of Physics C: Solid State Physics* **13**, L881–L885 (1980).

[166] Diep, H. T. Critical Properties of Helimagnets. *Europhysics Letters (EPL)* **7**, 725–730 (1988).

[167] Stishov, S. M. *et al.* Heat capacity and thermal expansion of the itinerant helimagnet MnSi. *Journal of Physics: Condensed Matter* **20**, 235222 (2008).

[168] Uchida, M. *et al.* Topological spin textures in the helimagnet FeGe. *Physical Review B* **77**, 184402 (2008).

[169] Stishov, S. M. *et al.* Magnetic phase transition in the itinerant helimagnet MnSi: Thermodynamic and transport properties. *Physical Review B* **76**, 052405 (2007).

[170] Pfleiderer, C., McMullan, G. J. & Lonzarich, G. G. Pressure induced crossover of the magnetic transition from second to first order near the quantum critical point in MnSi. *Physica B: Condensed Matter* **206-207**, 847–849 (1995).

[171] Pfleiderer, C., McMullan, G. J., Julian, S. R. & Lonzarich, G. G. Magnetic quantum phase transition in MnSi under hydrostatic pressure. *Physical Review B* **55**, 8330–8338 (1997).

[172] Pappas, C. *et al.* Magnetic fluctuations and correlations in MnSi: Evidence for a chiral skyrmion spin liquid phase. *Physical Review B* **83**, 224405 (2011).

[173] Mühlbauer, S. *et al.* Kinetic small angle neutron scattering of the skyrmion lattice in MnSi. *New Journal of Physics* **18**, 075017 (2016).

[174] Lebech, B., Bernhard, J. & Freltoft, T. Magnetic structures of cubic FeGe studied by small-angle neutron scattering. *Journal of Physics: Condensed Matter* **1**, 6105–6122 (1989).

[175] Adams, T. *et al.* Long-Wavelength Helimagnetic Order and Skyrmion Lattice Phase in Cu_2OSeO_3. *Physical Review Letters* **108**, 237204 (2012).

[176] Pappas, C. *et al.* Magnetic Fluctuations, Precursor Phenomena, and Phase Transition in MnSi under a Magnetic Field. *Physical Review Letters* **119**, 047203 (2017).

[177] Buhrandt, S. & Fritz, L. Skyrmion lattice phase in three-dimensional chiral magnets from Monte Carlo simulations. *Physical Review B* **88**, 195137 (2013).

[178] Schütte, C. & Rosch, A. Dynamics and energetics of emergent magnetic monopoles in chiral magnets. *Physical Review B* **90**, 174432 (2014).

[179] Milde, P. *et al.* Unwinding of a Skyrmion Lattice by Magnetic Monopoles. *Science* **340**, 1076–1080 (2013).

[180] Leonov, A. O., Bogdanov, A. N. & Inoue, K. Toggle-switch-like crossover between two types of isolated skyrmions within the conical phase of cubic helimagnets. *Physical Review B* **98**, 060411 (2018).

[181] Rybakov, F. N., Borisov, A. B., Blügel, S. & Kiselev, N. S. New Type of Stable Particlelike States in Chiral Magnets. *Physical Review Letters* **115**, 117201 (2015).

[182] Kanazawa, N. *et al.* Critical phenomena of emergent magnetic monopoles in a chiral magnet. *Nature Communications* **7**, 11622 (2016).

[183] Charilaou, M., Braun, H.-B. & Löffler, J. F. Monopole-Induced Emergent Electric Fields in Ferromagnetic Nanowires. *Physical Review Letters* **121**, 097202 (2018).

[184] Leonov, A. O. & Inoue, K. Homogeneous and heterogeneous nucleation of skyrmions in thin layers of cubic helimagnets. *Physical Review B* **98**, 054404 (2018).

[185] Elías, R. G. & Verga, A. Magnetization structure of a Bloch point singularity. *The European Physical Journal B* **82**, 159 (2011).

[186] Milde, P. *et al.* Heuristic Description of Magnetoelectricity of Cu_2OSeO_3. *Nano Letters* **16**, 5612–5618 (2016).

[187] Kagawa, F. *et al.* Current-induced viscoelastic topological unwinding of metastable skyrmion strings. *Nature Communications* **8**, 1–8 (2017).

[188] Zheng, F. *et al.* Experimental observation of chiral magnetic bobbers in B20-type FeGe. *Nature Nanotechnology* **13**, 451–455 (2018).

[189] Pfleiderer, C. *et al.* Skyrmion lattices in metallic and semiconducting B20 transition metal compounds. *Journal of Physics: Condensed Matter* **22**, 164207 (2010).

[190] Oike, H. *et al.* Interplay between topological and thermodynamic stability in a metastable magnetic skyrmion lattice. *Nature Physics* **12**, 62–66 (2016).

[191] Nakajima, T. *et al.* Skyrmion lattice structural transition in MnSi. *Science Advances* **3**, e1602562 (2017).

[192] Karube, K. *et al.* Robust metastable skyrmions and their triangular–square lattice structural transition in a high-temperature chiral magnet. *Nature Materials* **15**, 1237–1242 (2016).

[193] Karube, K. *et al.* Skyrmion formation in a bulk chiral magnet at zero magnetic field and above room temperature. *Physical Review Materials* **1**, 074405 (2017).

[194] Morikawa, D. *et al.* Deformation of Topologically-Protected Supercooled Skyrmions in a Thin Plate of Chiral Magnet $Co_8Zn_8Mn_4$. *Nano Letters* **17**, 1637–1641 (2017).

[195] Chacon, A. *et al.* Observation of two independent skyrmion phases in a chiral magnetic material. *Nature Physics* **14**, 936–941 (2018).

[196] Uzdin, V. M., Potkina, M. N., Lobanov, I. S., Bessarab, P. F. & Jónsson, H. Energy surface and lifetime of magnetic skyrmions. *Journal of Magnetism and Magnetic Materials* **459**, 236–240 (2018).

[197] Lin, C. *et al.* A metastable liquid melted from a crystalline solid under decompression. *Nature Communications* **8**, 1–6 (2017).

[198] Tavella, F. *et al.* Soft x-ray induced femtosecond solid-to-solid phase transition. *High Energy Density Physics* **24**, 22–27 (2017).

[199] Milde, P., Neuber, E., Bauer, A., Pfleiderer, C. & Eng, L. M. Surface pinning and triggered unwinding of skyrmions in a cubic chiral magnet. *Physical Review B* **100**, 024408 (2019).

[200] Peng, L. *et al.* Relaxation Dynamics of Zero-Field Skyrmions over a Wide Temperature Range. *Nano Letters* **18**, 7777–7783 (2018).

[201] Müller, J. *et al.* Magnetic Skyrmions and Skyrmion Clusters in the Helical Phase of Cu_2OSeO_3. *Physical Review Letters* **119**, 137201 (2017).

[202] Wild, J. *et al.* Entropy-limited topological protection of skyrmions. *Science Advances* **3**, e1701704 (2017).

[203] Bauer, A., Garst, M. & Pfleiderer, C. History dependence of the magnetic properties of single-crystal $Fe_{1-x}Co_xSi$. *Physical Review B* **93**, 235144 (2016).

[204] Bannenberg, L. J. *et al.* Extended skyrmion lattice scattering and long-time memory in the chiral magnet $Fe_{1-x}Co_xSi$. *Physical Review B* **94**, 104406 (2016).

[205] Bannenberg, L. J. *et al.* Magnetic relaxation phenomena in the chiral magnet $Fe_{1-x}Co_xSi$: An ac susceptibility study. *Physical Review B* **94**, 134433 (2016).

[206] Grigoriev, S. V. *et al.* Helical spin structure of $Mn_{1-y}Fe_ySi$ under a magnetic field: Small angle neutron diffraction study. *Physical Review B* **79**, 144417 (2009).

[207] Franz, C. *et al.* Real-Space and Reciprocal-Space Berry Phases in the Hall Effect of $Mn_{1-x}Fe_xSi$. *Physical Review Letters* **112**, 186601 (2014).

[208] Bannenberg, L. J., Weber, F., Lefering, A. J. E., Wolf, T. & Pappas, C. Magnetization and ac susceptibility study of the cubic chiral magnet $Mn_{1-x}Fe_xSi$. *Physical Review B* **98**, 184430 (2018).

[209] Bannenberg, L. J., Dalgliesh, R. M., Wolf, T., Weber, F. & Pappas, C. Evolution of helimagnetic correlations in $Mn_{1-x}Fe_xSi$ with doping: A small-angle neutron scattering study. *Physical Review B* **98**, 184431 (2018).

[210] Grigoriev, S. V. *et al.* Chiral Properties of Structure and Magnetism in $Mn_{1-x}Fe_xGe$ Compounds: When the Left and the Right are Fighting, Who Wins? *Physical Review Letters* **110**, 207201 (2013).

[211] Shibata, K. *et al.* Towards control of the size and helicity of skyrmions in helimagnetic alloys by spin–orbit coupling. *Nature Nanotechnology* **8**, 723–728 (2013).

[212] Koretsune, T., Nagaosa, N. & Arita, R. Control of Dzyaloshinskii-Moriya interaction in $Mn_{1-x}Fe_xGe$: a first-principles study. *Scientific Reports* **5**, 1–10 (2015).

[213] Grigoriev, S. V. *et al.* Spin-wave dynamics in Mn-doped FeGe helimagnet: Small-angle neutron scattering study. *Journal of Magnetism and Magnetic Materials* **459**, 159–164 (2018).

[214] Fujishiro, Y. *et al.* Topological transitions among skyrmion- and hedgehog-lattice states in cubic chiral magnets. *Nature Communications* **10**, 1059 (2019).

[215] Karube, K. *et al.* Controlling the helicity of magnetic skyrmions in a β-Mn-type high-temperature chiral magnet. *Physical Review B* **98**, 155120 (2018).

[216] Wu, H. C. *et al.* Physical pressure and chemical expansion effects on the skyrmion phase in Cu_2OSeO_3. *Journal of Physics D: Applied Physics* **48**, 475001 (2015).

[217] Chandrasekhar, K. D., Wu, H. C., Huang, C. L. & Yang, H. D. Effects of Jahn-Teller distortion on the skyrmion stability of $(Cu_{1-x}Ni_x)_2OSeO_3$. *Journal of Materials Chemistry C* **4**, 5270–5274 (2016).

[218] Štefančič, A. *et al.* Origin of skyrmion lattice phase splitting in Zn-substituted Cu_2OSeO_3. *Physical Review Materials* **2**, 111402 (2018).

[219] Birch, M. T. *et al.* Increased lifetime of metastable skyrmions by controlled doping. *Physical Review B* **100**, 014425 (2019).

[220] Sukhanov, A. S. *et al.* Increasing skyrmion stability in Cu_2OSeO_3 by chemical substitution. *Physical Review B* **100**, 184408 (2019).

[221] Han, M.-G. *et al.* Scaling, rotation, and channeling behavior of helical and skyrmion spin textures in thin films of Te-doped Cu_2OSeO_3. *Science Advances* **6**, eaax2138 (2020).

[222] Blundell, S. *Magnetism in Condensed Matter* (OUP Oxford, 2001).

[223] Cullity, B. D. & Graham, C. D. *Introduction to Magnetic Materials* (John Wiley & Sons, Ltd, 2008).

[224] Wang, J. *et al.* Temperature dependence of magnetic anisotropy constant in iron chalcogenide Fe_3Se_4: Excellent agreement with theories. *Journal of Applied Physics* **112** (2012).

[225] Halder, M. *et al.* Thermodynamic evidence of a second skyrmion lattice phase and tilted conical phase in Cu_2OSeO_3. *Physical Review B* **98**, 144429 (2018).

[226] Qian, F. *et al.* New magnetic phase of the chiral skyrmion material Cu_2OSeO_3. *Science Advances* **4**, eaat7323 (2018).

[227] Bannenberg, L. J. *et al.* Multiple low-temperature skyrmionic states in a bulk chiral magnet. *npj Quantum Materials* **4**, 1–8 (2019).

[228] Zhang, S. L., Laan, G. v. d. & Hesjedal, T. Direct experimental determination of the topological winding number of skyrmions in Cu_2OSeO_3. *Nature Communications* **8**, 1–7 (2017).

[229] Chauleau, J.-Y. *et al.* Chirality in Magnetic Multilayers Probed by the Symmetry and the Amplitude of Dichroism in X-Ray Resonant Magnetic Scattering. *Physical Review Letters* **120**, 037202 (2018).

[230] Seki, S. *et al.* Propagation dynamics of spin excitations along skyrmion strings. *Nature Communications* **11**, 1–7 (2020).

[231] Paolasini, L. Resonant and magnetic X-ray diffraction by polarized synchrotron radiation. *École thématique de la Société Française de la Neutronique* **13**, 03002 (2014).

[232] Hill, J. P. & McMorrow, D. F. Resonant Exchange Scattering: Polarization Dependence and Correlation Function. *Acta Crystallographica Section A: Foundations of Crystallography* **52**, 236–244 (1996).

[233] Paolasini, L. & de Bergevin, F. Magnetic and resonant X-ray scattering investigations of strongly correlated electron systems. *Comptes Rendus Physique* **9**, 550–569 (2008).

[234] Brito, J. A. & Archer, M. Chapter 10 - Structural biology techniques: X-ray crystallography, cryo-electron microscopy, and small-angle X-ray scattering. In Crichton, R. R. & Louro, R. O. (eds.) *Practical Approaches to Biological Inorganic Chemistry (Second Edition)*, 375–416 (2020).

[235] Cromer, D. T. & Liberman, D. Relativistic Calculation of Anomalous Scattering Factors for X Rays. *The Journal of Chemical Physics* **53**, 1891–1898 (1970).

[236] Blume, M. Magnetic scattering of x rays (invited). *Journal of Applied Physics* **57**, 3615–3618 (1985).

[237] Gibbs, D., Moncton, D. E., D'Amico, K. L., Bohr, J. & Grier, B. H. Magnetic x-ray scattering studies of holmium using synchrotron radiation. *Physical Review Letters* **55**, 234–237 (1985).

[238] Detlefs, C., Sanchez del Rio, M. & Mazzoli, C. X-ray polarization: General formalism and polarization analysis. *The European Physical Journal Special Topics* **208**, 359–371 (2012).

[239] Hannon, J. P., Trammell, G. T., Blume, M. & Gibbs, D. X-Ray Resonance Exchange Scattering. *Physical Review Letters* **61**, 1245–1248 (1988).

[240] Wilson, M. N. *et al.* Stability and metastability of skyrmions in thin lamellae of Cu_2OSeO_3. *Physical Review Research* **2**, 013096 (2020).

[241] Blume, M. & Gibbs, D. Polarization dependence of magnetic x-ray scattering. *Physical Review B* **37**, 1779–1789 (1988).

[242] de Bergevin, F. & Brunel, M. Diffraction of X-rays by magnetic materials. I. General formulae and measurements on ferro- and ferrimagnetic compounds. *Acta Crystallographica Section A: Crystal Physics, Diffraction, Theoretical and General Crystallography* **37**, 314–324 (1981).

[243] Thole, B. T., Carra, P., Sette, F. & van der Laan, G. X-ray circular dichroism as a probe of orbital magnetization. *Physical Review Letters* **68**, 1943–1946 (1992).

[244] Altarelli, M. Orbital-magnetization sum rule for x-ray circular dichroism: A simple proof. *Physical Review B* **47**, 597–598 (1993).

[245] van der Laan, G. *et al.* Experimental proof of magnetic x-ray dichroism. *Physical Review B* **34**, 6529–6531 (1986).

[246] van der Laan, G. & Figueroa, A. I. X-ray magnetic circular dichroism—A versatile tool to study magnetism. *Coordination Chemistry Reviews* **277-278**, 95–129 (2014).

[247] Carra, P., Thole, B. T., Altarelli, M. & Wang, X. X-ray circular dichroism and local magnetic fields. *Physical Review Letters* **70**, 694–697 (1993).

[248] Stöhr, J. Exploring the microscopic origin of magnetic anisotropies with X-ray magnetic circular dichroism (XMCD) spectroscopy. *Journal of Magnetism and Magnetic Materials* **200**, 470–497 (1999).

[249] Marshall, W. & Lovesey, S. W. *Theory of thermal neutron scattering: the use of neutrons for the investigation of condensed matter* (Clarendon Press Oxford, 1971).

[250] Sears, V. F. Neutron scattering lengths and cross sections. *Neutron News* **3**, 26–37 (1992).

[251] Lovesey, S. W. Theory of neutron scattering by electrons in magnetic materials. *Physica Scripta* **90**, 108011 (2015).

[252] Zhu, Y. Small-angle neutron scattering. In Zhu, Y. (ed.) *Modern Techniques for Characterizing Magnetic Materials*, 65–105 (2005).

[253] Zhu, Y. Magnetic neutron scattering. In Zhu, Y. (ed.) *Modern Techniques for Characterizing Magnetic Materials*, 3–64 (2005).

[254] Binnewies, M., Glaum, R., Schmidt, M. & Schmidt, P. Chemical Vapor Transport Reactions – A Historical Review. *Zeitschrift für anorganische und allgemeine Chemie* **639**, 219–229 (2013).

[255] Volkert, C. A. & Minor, A. M. Focused Ion Beam Microscopy and Micromachining. *MRS Bulletin* **32**, 389–399 (2007).

[256] Ali, M. Y., Hung, W. & Yongqi, F. A review of focused ion beam sputtering. *International Journal of Precision Engineering and Manufacturing* **11**, 157–170 (2010).

[257] Vernon-Parry, K. D. Scanning electron microscopy: an introduction. *III-Vs Review* **13**, 40–44 (2000).

[258] Tao, T., Ro, J., Melngailis, J., Xue, Z. & Kaesz, H. D. Focused ion beam induced deposition of platinum. *Journal of Vacuum Science & Technology B: Microelectronics Processing and Phenomena* **8**, 1826–1829 (1990).

[259] Jackson, T. J., Keene, M. N. & Gough, C. E. A SQUID magnetometer for low field DC magnetization and AC susceptibility measurements. *Measurement Science and Technology* **3**, 988–991 (1992).

[260] Magnusson, J., Djurberg, C., Granberg, P. & Nordblad, P. A low field superconducting quantum interference device magnetometer for dynamic measurements. *Review of Scientific Instruments* **68**, 3761–3765 (1997).

[261] Bałanda, M. AC Susceptibility Studies of Phase Transitions and Magnetic Relaxation: Conventional, Molecular and Low-Dimensional Magnets. *Acta Physica Polonica A* **124**, 964–976 (2013).

[262] Levatić, I., Šurija, V., Berger, H. & Živković, I. Dissipation processes in the insulating skyrmion compound Cu_2OSeO_3. *Physical Review B* **90**, 224412 (2014).

[263] Bauer, A. & Pfleiderer, C. Magnetic phase diagram of MnSi inferred from magnetization and ac susceptibility. *Physical Review B* **85**, 214418 (2012).

[264] Dewhurst, C. D. *et al.* The small-angle neutron scattering instrument D33 at the Institut Laue–Langevin. *Journal of Applied Crystallography* **49**, 1–14 (2016).

[265] Carpenter, J. M. The development of compact neutron sources. *Nature Reviews Physics* **1**, 177–179 (2019).

[266] Watanabe, N. Neutronics of pulsed spallation neutron sources. *Reports on Progress in Physics* **66**, 339–381 (2003).

[267] Gutmann, M. J., Kockelmann, W., Chapon, L. C. & Radaelli, P. G. Phase imaging using time-of-flight neutron diffraction. *Journal of Applied Crystallography* **39**, 82–89 (2006).

[268] Dewhurst, C. D. D33—a third small-angle neutron scattering instrument at the Institut Laue Langevin. *Measurement Science and Technology* **19**, 034007 (2008).

[269] Elder, F. R., Gurewitsch, A. M., Langmuir, R. V. & Pollock, H. C. Radiation from Electrons in a Synchrotron. *Physical Review* **71**, 829–830 (1947).

[270] Harris, K. D. M., Tremayne, M. & Kariuki, B. M. Contemporary Advances in the Use of Powder X-Ray Diffraction for Structure Determination. *Angewandte Chemie International Edition* **40**, 1626–1651 (2001).

[271] Rietveld, H. M. A profile refinement method for nuclear and magnetic structures. *Journal of Applied Crystallography* **2**, 65–71 (1969).

[272] Young, R. A. *The Rietveld Method*. International Union of Crystallography Monographs on Crystallography (Oxford University Press, Oxford, New York, 1995).

[273] Thompson, S. P. *et al.* Beamline I11 at Diamond: A new instrument for high resolution powder diffraction. *Review of Scientific Instruments* **80**, 075107 (2009).

[274] Yamasaki, Y. *et al.* Dynamical process of skyrmion-helical magnetic transformation of the chiral-lattice magnet FeGe probed by small-angle resonant soft x-ray scattering. *Physical Review B* **92**, 220421 (2015).

[275] Garbor, D. The Nobel Prize in Physics (1971).

[276] Popescu, G. Gabor's holography at sea. *Light: Science & Applications* **8**, 19 (2019).

[277] Duckworth, T. A. *et al.* Magnetic imaging by x-ray holography using extended references. *Optics Express* **19**, 16223–16228 (2011).

[278] Duckworth, T. A. *et al.* Holographic imaging of interlayer coupling in Co/Pt/NiFe. *New Journal of Physics* **15**, 023045 (2013).

[279] Guizar-Sicairos, M. & Fienup, J. R. Holography with extended reference by autocorrelation linear differential operation. *Optics Express* **15**, 17592–17612 (2007).

[280] Yokoyama, Y., Arima, T.-h., Okada, M. & Yamasaki, Y. Sparse Phase Retrieval Algorithm for Observing Isolated Magnetic Skyrmions by Coherent Soft X-ray Diffraction Imaging. *Journal of the Physical Society of Japan* **88**, 024009 (2019).

[281] Fischer, P. *et al.* Imaging of magnetic domains by transmission x-ray microscopy. *Journal of Physics D: Applied Physics* **31**, 649–655 (1998).

[282] Fischer, P. Viewing spin structures with soft X-ray microscopy. *Materials Today* **13**, 14–22 (2010).

[283] Nolle, D. *et al.* Note: Unique characterization possibilities in the ultra high vacuum scanning transmission x-ray microscope (UHV-STXM) "MAXYMUS" using a rotatable permanent magnetic field up to 0.22 T. *Review of Scientific Instruments* **83**, 046112 (2012).

[284] Seki, S. *et al.* Magnetochiral nonreciprocity of volume spin wave propagation in chiral-lattice ferromagnets. *Physical Review B* **93**, 235131 (2016).

[285] Garst, M., Waizner, J. & Grundler, D. Collective spin excitations of helices and magnetic skyrmions: review and perspectives of magnonics in non-centrosymmetric magnets. *Journal of Physics D: Applied Physics* **50**, 293002 (2017).

[286] Yu, H. *et al.* Approaching soft X-ray wavelengths in nanomagnet-based microwave technology. *Nature Communications* **7**, 1–7 (2016).

[287] von Bardeleben, H. J., Cantin, J. L. & Gendron, F. *Electron Paramagnetic Resonance Spectroscopy: Applications* (Springer International Publishing, Cham, 2020).

[288] Kittel, C. On the Theory of Ferromagnetic Resonance Absorption. *Physical Review* **73**, 155–161 (1948).

[289] Mochizuki, M. Spin-Wave Modes and Their Intense Excitation Effects in Skyrmion Crystals. *Physical Review Letters* **108**, 017601 (2012).

[290] Schwarze, T. *et al.* Universal helimagnon and skyrmion excitations in metallic, semiconducting and insulating chiral magnets. *Nature Materials* **14**, 478 (2015).

[291] Onose, Y., Okamura, Y., Seki, S., Ishiwata, S. & Tokura, Y. Observation of Magnetic Excitations of Skyrmion Crystal in a Helimagnetic Insulator Cu_2OSeO_3. *Physical Review Letters* **109**, 037603 (2012).

[292] Mochizuki, M. & Seki, S. Dynamical magnetoelectric phenomena of multiferroic skyrmions. *Journal of Physics: Condensed Matter* **27**, 503001 (2015).

[293] Beg, M. *et al.* Dynamics of skyrmionic states in confined helimagnetic nanostructures. *Physical Review B* **95**, 014433 (2017).

[294] Büttner, F. *et al.* Dynamics and inertia of skyrmionic spin structures. *Nature Physics* **11**, 225–228 (2015).

[295] Wu, H. C. *et al.* Unexpected observation of splitting of skyrmion phase in Zn doped Cu_2OSeO_3. *Scientific Reports* **5**, 13579 (2015).

[296] Bosson, C. J. *et al.* Polymorphism in Cu_2ZnSnS_4 and New Off-Stoichiometric Crystal Structure Types. *Chemistry of Materials* **29**, 9829–9839 (2017).

[297] Bosson, C. J. *et al.* Cation disorder and phase transitions in the structurally complex solar cell material Cu_2ZnSnS_4. *Journal of Materials Chemistry A* **5**, 16672–16680 (2017).

[298] Rumble, R., J. (ed.) *CRC Handbook of Chemistry and Physics, 100th Edition* (CRC Press, 2019).

[299] Reimann, T. Neutron diffractive imaging of the skyrmion lattice nucleation in MnSi. *Physical Review B* **97** (2018).

[300] Desplat, L., Suess, D., Kim, J.-V. & Stamps, R. L. Thermal stability of metastable magnetic skyrmions: Entropic narrowing and significance of internal eigenmodes. *Physical Review B* **98**, 134407 (2018).

[301] Fernandes, I. L., Bouaziz, J., Blügel, S. & Lounis, S. Universality of defect-skyrmion interaction profiles. *Nature Communications* **9**, 1–7 (2018).

[302] Fallon, K. *et al.* Controlled Individual Skyrmion Nucleation at Artificial Defects Formed by Ion Irradiation. *Small* **16**, 1907450 (2020).

[303] Topping, C. V. & Blundell, S. J. A.C. susceptibility as a probe of low-frequency magnetic dynamics. *Journal of Physics: Condensed Matter* **31**, 013001 (2018).

[304] Qian, F. *et al.* Phase diagram and magnetic relaxation phenomena in Cu_2OSeO_3. *Physical Review B* **94**, 064418 (2016).

[305] Izyumov, Y. A. Modulated, or long-periodic, magnetic structures of crystals. *Soviet Physics Uspekhi* **27**, 845 (1984).

[306] Xing, X., Zhou, Y. & Braun, H. Magnetic Skyrmion Tubes as Nonplanar Magnonic Waveguides. *Physical Review Applied* **13**, 034051 (2020).

[307] Birch, M. T. *et al.* Real-space imaging of confined magnetic skyrmion tubes. *Nature Communications* **11**, 1726 (2020).

[308] Park, H. S. *et al.* Observation of the magnetic flux and three-dimensional structure of skyrmion lattices by electron holography. *Nature Nanotechnology* **9**, 337–342 (2014).

[309] Arita, M., Tokuda, R., Hamada, K. & Takahashi, Y. Development of TEM Holder Generating In-Plane Magnetic Field Used for *In-Situ* TEM Observation. *Materials Transactions* **55**, 403–409 (2014).

[310] McGrouther, D. *et al.* Internal structure of hexagonal skyrmion lattices in cubic helimagnets. *New Journal of Physics* **18**, 095004 (2016).

[311] Soumyanarayanan, A. *et al.* Tunable room-temperature magnetic skyrmions in Ir/Fe/Co/Pt multilayers. *Nature Materials* **16**, 898–904 (2017).

[312] Donnelly, C. *et al.* Three-dimensional magnetization structures revealed with X-ray vector nanotomography. *Nature* **547**, 328–331 (2017).

[313] Bukin, N. *et al.* Time-resolved imaging of magnetic vortex dynamics using holography with extended reference autocorrelation by linear differential operator. *Scientific Reports* **6**, 36307 (2016).

[314] Sluka, V. *et al.* Emission and propagation of 1D and 2D spin waves with nanoscale wavelengths in anisotropic spin textures. *Nature Nanotechnology* **14**, 328–333 (2019).

[315] Ukleev, V. *et al.* Element-specific soft x-ray spectroscopy, scattering, and imaging studies of the skyrmion-hosting compound $Co_8Zn_8Mn_4$. *Physical Review B* **99**, 144408 (2019).

[316] Siegfried, S.-A. *et al.* Spin-wave dynamics in the helimagnet FeGe studied by small-angle neutron scattering. *Physical Review B* **95**, 134415 (2017).

[317] Rybakov, F. N., Borisov, A. B. & Bogdanov, A. N. Three-dimensional skyrmion states in thin films of cubic helimagnets. *Physical Review B* **87**, 094424 (2013).

[318] Leonov, A. *et al.* Chiral Surface Twists and Skyrmion Stability in Nanolayers of Cubic Helimagnets. *Physical Review Letters* **117**, 087202 (2016).

[319] Meynell, S. A., Wilson, M. N., Fritzsche, H., Bogdanov, A. N. & Monchesky, T. L. Surface twist instabilities and skyrmion states in chiral ferromagnets. *Physical Review B* **90**, 014406 (2014).

[320] Hertel, R. & Schneider, C. M. Exchange Explosions: Magnetization Dynamics during Vortex-Antivortex Annihilation. *Physical Review Letters* **97**, 177202 (2006).

[321] Leonov, A. O., Monchesky, T. L., Loudon, J. C. & Bogdanov, A. N. Three-dimensional chiral skyrmions with attractive interparticle interactions. *Journal of Physics: Condensed Matter* **28**, 35LT01 (2016).

[322] Okamura, Y. *et al.* Emergence and magnetic-field variation of chiral-soliton lattice and skyrmion lattice in the strained helimagnet Cu_2OSeO_3. *Physical Review B* **96**, 174417 (2017).

Appendix A

Derivations

A.1 Metastable Skyrmion Population Loss

To simulate the loss of metastable skyrmion population as the sample is cooled, we derived the following model. We begin with the expression for a population of metastable skyrmions decaying over time t with a temperature dependent lifetime $\tau(T)$,

$$S(t) = S_0 \exp\left[-\left(\frac{t}{\tau(T)}\right)^{\beta}\right], \tag{A.1.1}$$

Unlike a standard exponential function which is self-similar, when $\beta \neq 1$ the shape of a stretched exponential function changes with time. To account for this, we consider the population decay during the cooling process as a series of time steps with duration Δt, each starting at a time $t_n = n\Delta t$. For a single time step, this gives,

$$\frac{S_{n+1}}{S_n} = \frac{\exp\left[-\left(\frac{t_n+\Delta t}{\tau(T)}\right)^{\beta}\right]}{\exp\left[-\left(\frac{t_n}{\tau(T)}\right)^{\beta}\right]}. \tag{A.1.2}$$

It follows that the final population, S_0, after N time steps is a product series,

$$S_0 = S_i \prod_{n=1}^{N} \exp\left[\left(\frac{t_n}{\tau(T)}\right)^{\beta} - \left(\frac{t_n + \Delta t}{\tau(T)}\right)^{\beta}\right], \tag{A.1.3}$$

$$S_0 = S_i \exp\left[\sum_{n=1}^{N}\left(\frac{t_n}{\tau(T)}\right)^{\beta} - \left(\frac{t_n+\Delta t}{\tau(T)}\right)^{\beta}\right], \tag{A.1.4}$$

where S_i is the initial population before cooling commences. We now define the sum inside of the exponential function to be $g(t)$, and take the limit as $\Delta t \to 0$,

$$\begin{aligned}\lim_{\Delta t\to 0} g(t) = &\lim_{\Delta t\to 0}\sum_{n=1}^{N}\left(\frac{t_n}{\tau(T)}\right)^{\beta} \\ &- \lim_{\Delta t\to 0}\sum_{n=1}^{N}\left(\frac{t_n+\Delta t}{\tau(T)}\right)^{\beta}\end{aligned} \tag{A.1.5}$$

Performing a Taylor expansion of the second term around $\Delta t = 0$ yields,

$$\begin{aligned}\lim_{\Delta t\to 0} g(t) = &\lim_{\Delta t\to 0}\sum_{n=1}^{N}\left(\frac{t_n}{\tau(T)}\right)^{\beta} \\ - \lim_{\Delta t\to 0}\sum_{n=1}^{N}&\left[\left(\frac{t_n}{\tau(T)}\right)^{\beta} + \beta\frac{\Delta t}{t_n}\left(\frac{t_n}{\tau(T)}\right)^{\beta}\right] + \mathcal{O}^2.\end{aligned} \tag{A.1.6}$$

The higher order terms of Δt^2 are infinitesimally small as $\Delta t \to 0$ leaving,

$$\lim_{\Delta t\to 0} g(t) = -\lim_{\Delta t\to 0}\sum_{n=1}^{N}\beta\frac{\Delta t}{t_n}\left(\frac{t_n}{\tau(T)}\right)^{\beta} \tag{A.1.7}$$

$$\lim_{\Delta t\to 0} g(t) = -\beta\int_0^{t_f}\frac{1}{t}\left(\frac{t}{\tau(T)}\right)^{\beta} dt, \tag{A.1.8}$$

where t_f is the time at the end of the cooling process. Finally, we substitute back into our equation for S_0, to find an expression for the population of metastable skyrmions as a function of time,

$$S_0 = S_i \exp\left[-\beta\int_0^{t_f}\frac{1}{t}\left(\frac{t}{\tau(T)}\right)^{\beta} dt\right]. \tag{A.1.9}$$

In our analysis, we assume that the lifetime depends upon the temperature of according to our modified Arrhenius' law,

$$\tau(T) = \tau_0 \exp\left[a\left(\frac{T_s - T}{T}\right)\right], \tag{A.1.10}$$

where T_s is the lowest extent of the equilibrium skyrmiom phase in temperature. With a linear cooling rate, $k < 0$, starting at $T = T_s$, we can write $T = T_s + kt$. We substitute equation A.1.10 into equation A.1.9, and perform a change of variables from t to T to reveal the dependence of S_0 on the cooling rate k,

$$S_0 = S_i \exp\left[\int_{T_s}^{T_f} \frac{-\beta}{T - T_s}\left(\frac{T - T_s}{k\tau_0 \exp\left[a\frac{T_s - T}{T}\right]}\right)^{\beta} dT\right]. \tag{A.1.11}$$

A.2 Skyrmion Tube Distortion

To characterise the distortion of the magnetisation profiles of the skyrmion tubes, we used the mathematics of the distortion of the helical state into a chiral soliton lattice with an applied field. We can write,

$$\frac{\mathrm{E}(\kappa)}{\kappa} = \sqrt{\frac{1}{h}}, \tag{A.2.12}$$

where $\mathrm{E}(\kappa)$ is the complete elliptical integral of the second kind, h is the ratio between the applied field and the critical field (H/H_C), and κ is the modulus of the elliptical function, for which we want to solve. Using the value of κ determined by minimising this equation, the magnetisation profile of the distorted helical state for the vector $\vec{Q} \parallel \hat{x}$ and $\vec{H} \parallel \hat{z}$ is,

$$\begin{aligned} \mathbf{M} &= M_s(0, M_y, M_z), \\ M_y &= \sin(2\mathrm{am}(\sqrt{H}\frac{x}{\kappa}, \kappa)), \\ M_z &= \cos(2\mathrm{am}(\sqrt{H}\frac{x}{\kappa}, \kappa)), \end{aligned} \tag{A.2.13}$$

where $\mathrm{am}(u, v)$ is the Jacobi amplitude function, and M_s is the saturation magnetisation. This can be conveniently expressed using the Jacobi Elliptic functions $\mathrm{sn}(u, v) = \sin(\mathrm{am}(u, v))$ and $\mathrm{cn}(u, v) = \cos(\mathrm{am}(u, v))$ as,

$$\begin{aligned} M_y &= 2\mathrm{cn}(\sqrt{H}\frac{x}{\kappa}, \kappa)\mathrm{sn}(\sqrt{H}\frac{x}{\kappa}, \kappa), \\ M_z &= \mathrm{cn}^2(\sqrt{H}\frac{x}{\kappa}, \kappa) - \mathrm{sn}^2(\sqrt{H}\frac{x}{\kappa}, \kappa). \end{aligned} \tag{A.2.14}$$

For the magnetisation profiles the relevant component of the magnetisation is M_{y}. This expression is then used to fit the magnetisation profiles, using the effective applied field h as a fitting parameter, and adding in an adjustable phase offset ϕ such that $x \to x + \phi$. This yields,

$$M_{\mathrm{y}} = 2\mathrm{cn}(\sqrt{H}\frac{x+\phi}{\kappa}, \kappa)\mathrm{sn}(\sqrt{H}\frac{x+\phi}{\kappa}, \kappa). \tag{A.2.15}$$

For the high field curves above 165 mT, this equation fits the simulated magnetization profiles. For the lower field curves, the distortion is seen to have the opposite directionality. This can be mathematically described by adding a negative sign and a phase offset of π, giving,

$$M_{\mathrm{y}} = -2\mathrm{cn}(\sqrt{H}\frac{x+\phi-\pi}{\kappa}, \kappa)\mathrm{sn}(\sqrt{H}\frac{x+\phi-\pi}{\kappa}, \kappa). \tag{A.2.16}$$

As shown in Fig. 7.10, the out-of-plane component of the magnetisation across the width of the SkT exhibits an asymmetrical distortion that varies as a function of applied magnetic field and is not observed in the conical state. The ratio of the applied field to the critical field, h, parameterises the magnitude of this distortion. We define $\nu = h$ for fields of 165 mT and above, and $\nu = -h$ for fields less than 165 mT, where the SkT state is essentially not distorted. This can be seen in Fig. 7.10**c**, where ν, obtained by fitting the magnetisation profiles with the chiral soliton lattice equations, is plotted as a function of applied magnetic field. The profiles of the SkT state reveal that the direction of the asymmetry is opposite at low and high magnetic fields. This is most easily visualised in Fig. 7.10**d** and **e**. At low applied fields, such as at 100 mT in Fig. 7.10**d**, the magnetisation profile varies fastest between the skyrmion tubes, due to the reduced separation of the tubes relative to their radii. Conversely, at high fields, such as at 270 mT in Fig. 7.10**e**, the magnetisation profile changes fastest within each skyrmion tube, due to the increased separation of the tubes relative to their radii. This leads to the magnetisation profile of the tubes appearing distorted, due to the varying skyrmion tube separation.

Appendix B

Micromagnetic Simulations

B.1 Micromagnetic Method

Simulations of the various magnetic configurations observed in the experiments were performed using the micromagnetic code OOMMF [1]. The data was processed using the OOMMFPy library, available online [2]. The simulations were performed by David Cortés-Ortuño, and are included here for completeness. The simulated system was specified with dimensions 1000 nm × 1000 nm × 100 nm, using finite difference cells with a volume of $4\,\mathrm{nm}^3$, and magnetic parameters of FeGe. We describe the FeGe system using the energy functional of a chiral magnet with symmetry class T, which reads

$$E = \int_V \mathrm{d}V \left\{ A \sum_{\alpha=\mathrm{x,y,z}} \left(\nabla m_\alpha\right)^2 + D\mathbf{m}\cdot(\nabla\times\mathbf{m}) - M_\mathrm{s}\mathbf{m}\cdot\mathbf{B}_\mathrm{a} - \frac{M_\mathrm{s}}{2}\mathbf{m}\cdot\mathbf{B}_\mathrm{d} \right\}, \quad \text{(B.1.1)}$$

where $\mathbf{m}$ is the normalised magnetisation, $A = 8.78\,\mathrm{pJ\ m^{-1}}$ is the exchange constant, $M_\mathrm{s} = 384\,\mathrm{kA\ m^{-1}}$ is the saturation magnetisation, $D = 1.58\,\mathrm{mJ\ m^{-2}}$ is the DMI constant, $\mathbf{B}_\mathrm{a}$ is the applied field and $\mathbf{B}_\mathrm{d}$ is the demagnetising field. The energy minimisation of a specified initial state was performed using OOMMF's conjugate gradient method. The same minimisation technique was applied to reach equilibrium states at each step of the simulated field sweeps.

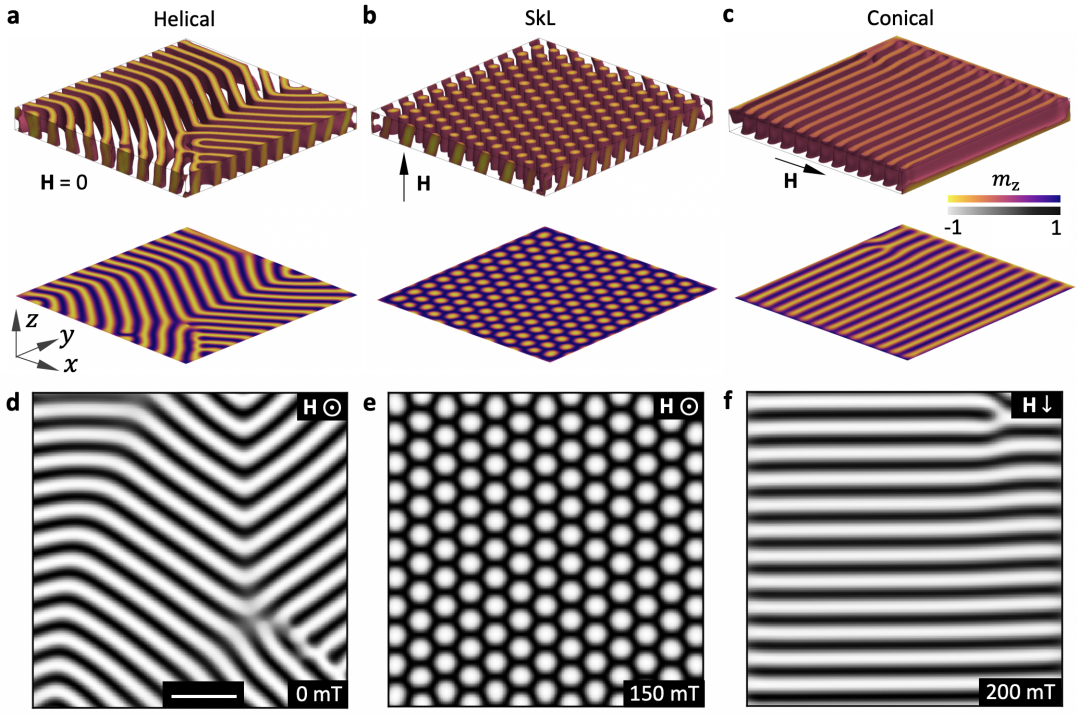

Figure B.1: **a-c**, Three dimensional visualisations of the helical, SkL and conical states presented in Fig. 2 in the main text, created by plotting cells with m_z components between -1 and 0. **e-f**, Simulated images of each simulated state, as shown in Fig. 2 of the main text. Scale bar, 200 nm.

B.2 Simulated Images

To generate the simulated states shown in Fig. 7.5, a precursor state was initiated and then relaxed using an energy minimisation algorithm at varied applied field strengths. To initialise the SkL state a triple-q model was used. In the case of the conical and helical states, the simulation was initialised with one-dimensional spirals with a periodicity 70 nm. The top three dimensional visualisations in Fig. B.1**a-c** were created by plotting cells with an out-of-plane magnetisation component $m_z < 0$. The bottom images are z-slices through the centre of the simulated sample. The black and white plots in Fig. B.1**d-f** are averages of the out-of-plane magnetisation component m_z across the thickness of the sample, as shown in Fig. 3 of the main text.

The averaging process used to create the simulated images is most clearly visualised from Fig. B.2, where magnetisation profiles of a y-slice through the thickness

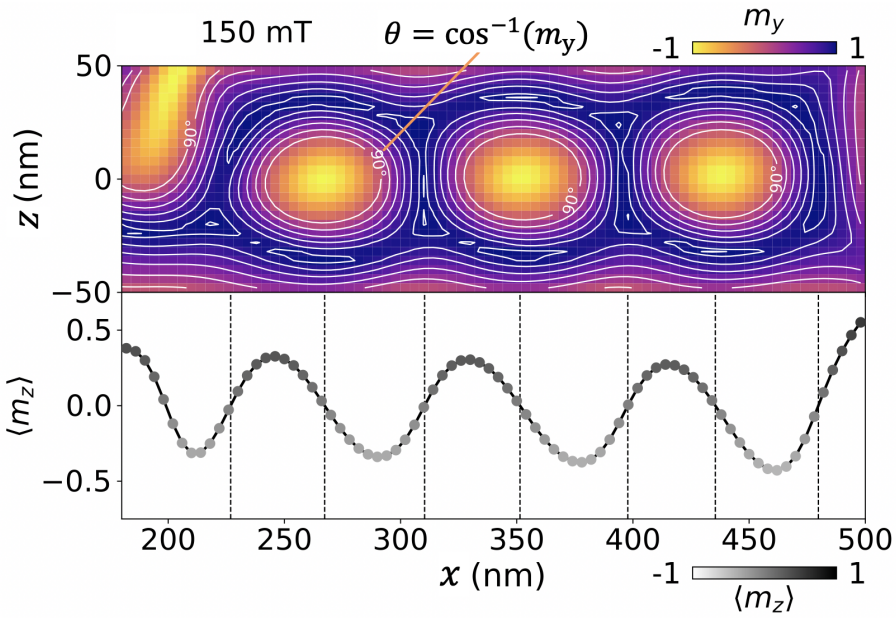

Figure B.2: The m_y component of a cross section through the simulated skyrmion tube state at 150 mT is plotted in the top panel. Isocontours highlight the lines of constant m_y. The calculated average out-of-plane component, $\langle m_\mathrm{z} \rangle$, is plotted in the bottom panel. Vertical dotted lines indicate positions of maximum/minimum m_y.

of the simulated sample are shown. The top image of Fig. B.2 illustrates the in-plane y-component of the magnetisation together with isocontour lines. The $\theta = 90°$ curve refers to the $m_\mathrm{y} = 0$ surface, which encloses a skyrmion tube or a configuration pinned at the top surface, as shown at the top left of the image. The bottom plot of Fig. B.2 shows the average m_z component across the thickness of the sample (z-direction), $\langle m_\mathrm{z} \rangle$, where the strongest contrast is the positive out-of-plane component.

Zero values of the $\langle m_\mathrm{z} \rangle$ were computed using a linear interpolation of the curve and a root finding algorithm and are displayed as the dashed vertical lines. It can be seen that these zeros coincide with both the skyrmion tube centres and the middle point between two skyrmion tubes. Accordingly, the skyrmion centre zeros can be used to compute the inter-skyrmion distance and the distance of a skyrmion from the edge of the sample. In the main text the skyrmion-skyrmion and skyrmion-edge distances were both calculated using the zero at the centre of the rightmost skyrmion

tube. In the case of skyrmion-skyrmion distance, it was computed from the zero of the adjacent skyrmion at the left.

B.3 Initialising Skyrmion Tubes

To generate the simulated three skyrmion tube states presented in the main text, a function was applied to generate three paraboloid-shaped Bloch skyrmion precursors, with the core oriented opposite to the magnetisation of the rest of the field polarised sample. By defining

$$\mathbf{m} = (\sin\Theta\cos\Psi, \sin\Theta\sin\Psi, -\cos\Theta), \tag{B.3.2}$$

the functions $\Theta = \Theta(r, z)$, $\Psi = \Psi(\varphi)$, with (r, φ, z) as cylindrical coordinates, are specified as

$$\begin{aligned} \Theta(r,z) &= \frac{\pi}{r_{\mathrm{par}}(z)} r, \quad r_{\mathrm{par}}(z) = \sqrt{\frac{r_{\mathrm{tube}}}{z_{\mathrm{tube}}} z}, \quad 0 \leq z \leq 600\,\mathrm{nm} \\ \Psi(\varphi) &= \varphi + \frac{\pi}{2}. \end{aligned} \tag{B.3.3}$$

Based on these functions, each of the three tubes was initialised with $r_{\mathrm{tube}} = 40\,\mathrm{nm}$ and $z_{\mathrm{tube}} = 600\,\mathrm{nm}$. The largest radius of the tube was specified with a value smaller than the helical length of FeGe due to the limited thickness of the 100 nm sample. The tube length was chosen according to the length of the tubes observed from the experimental images. To generate three tubes, the first tube was located with its centre at a distance of 125 nm from the edge of the sample and the second and third tubes were positioned with a 160 nm separation. The rest of the sample was initialised in a field-polarised state with magnetisation $\mathbf{m} = (0, +1, 0)$.

An overview of the initial state for the three tube system is shown in Fig. SB.3**a**. The regions within the $m_{\mathrm{y}} = 0$ isosurfaces are shown in the top image and a z-slice at the centre of the sample is shown at the middle image, together with a simulated image at the bottom. This initial state was relaxed at a range of magnetic fields by minimising the energy using a conjugate gradient algorithm implemented in the OOMMF code [1], and the resulting states are are shown in Fig. SB.3**b**-**f**. The

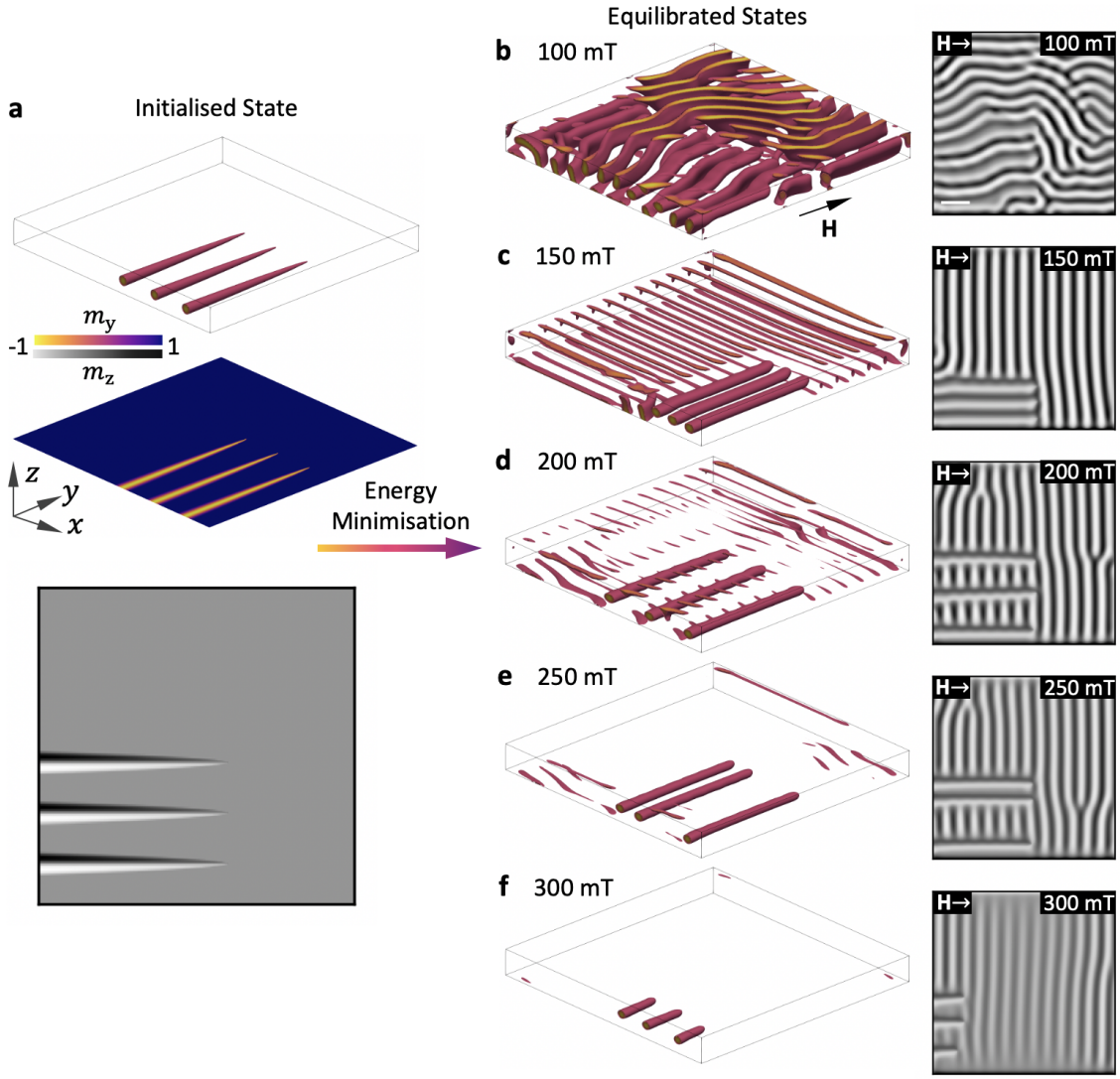

Figure B.3: **a**, Visualisation of the initial skyrmion tube state, featuring three paraboloid-shaped skyrmion tube precursors in a ferromagnetic background. The simulated x-ray image is shown below. **b-f**, Visualisations, created by plotting cells with m_y components between -1 and 0, and simulated x-ray images of the magnetic state after energy minimisation at a range of in-plane applied magnetic fields. Scale bar, 100 nm.

150 mT simulated state most resembles the three tube configuration seen in the experiments, displayed in Fig. SB.3**c**. Therefore, we chose this state to simulate the field sweep and observe the evolution of the skyrmion tubes with increasing and decreasing magnetic fields for comparison with the experimental data.

B.4 Randomly Initialised Field Sweeps

In order to examine the possibility of skyrmion tube formation from a field sweep starting at 0 mT, we initialised a helical state at 0 mT from a fully randomised precursor state, performing an energy relaxation using the conjugate gradient minimisation method. The resulting initial state is shown in Fig. SB.4**a**, with m_{y} isosurfaces in the left plot and the average out of plane magnetisation through the thickness, $\langle m_{\mathrm{z}} \rangle$, in the right plot. Two field sweep processes were simulated starting from this initial zero field helical state, applying both an in-plane and an out-of-plane magnetic field. Results of the in-plane field sweep are shown in Fig. SB.4**a-e**. Images at the left side of these figures show the region within the $m_{\mathrm{y}} = 0$ isosurface. As the magnetic field is increased skyrmion tubes form with their ends pinned at the sample surfaces, which may be energetically favoured in comparison to the formation of Bloch points. Results of the out-of-plane field sweep are shown in Fig. SB.5**a-e**, with m_{z} isosurfaces depicted in the images to the left side of every field sweep stage. In this case, skyrmions are again primarily stabilised close to the boundaries of the sample, highlighting the importance of confinement and edge effects.

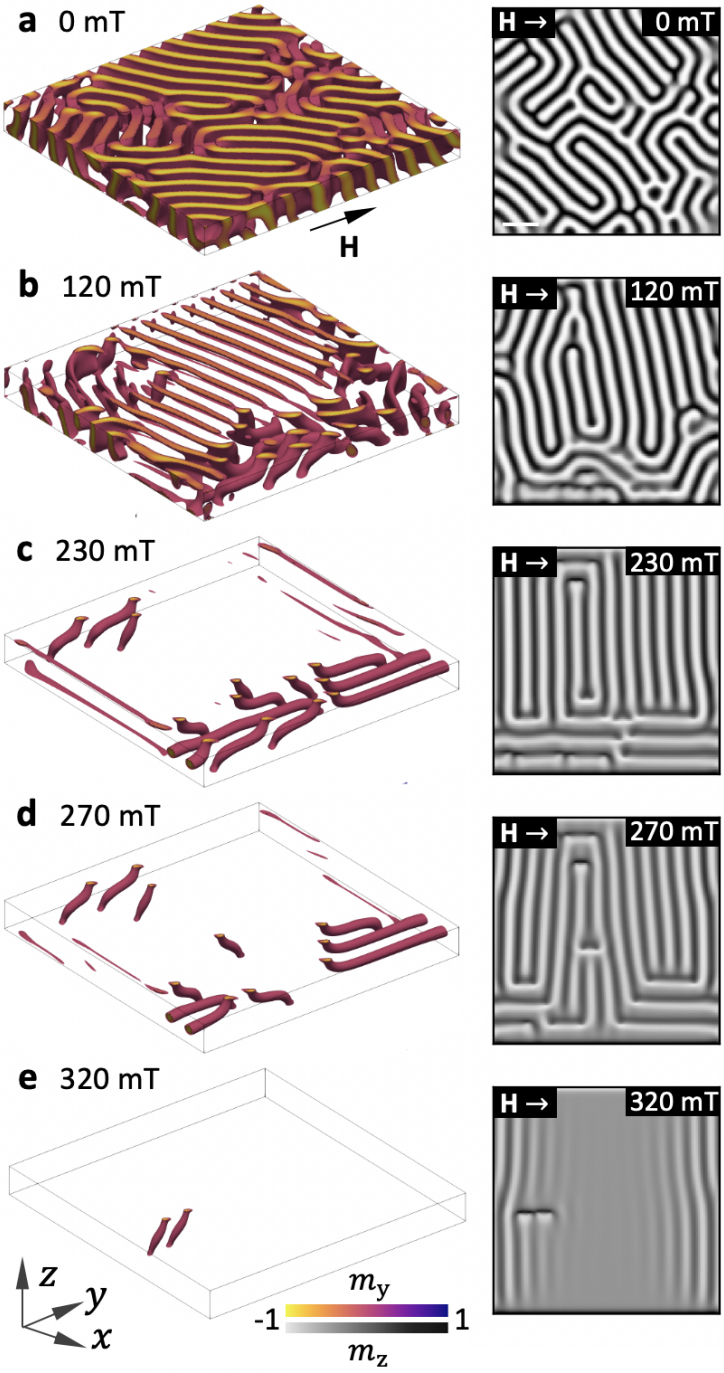

Figure B.4: **a**-**e**, Selected three dimensional visualisations, created by plotting cells with m_y components between -1 and 0, and simulated images of the magnetic state during an in-plane field sweep from an initially randomised state. Scale bar, 100 nm.

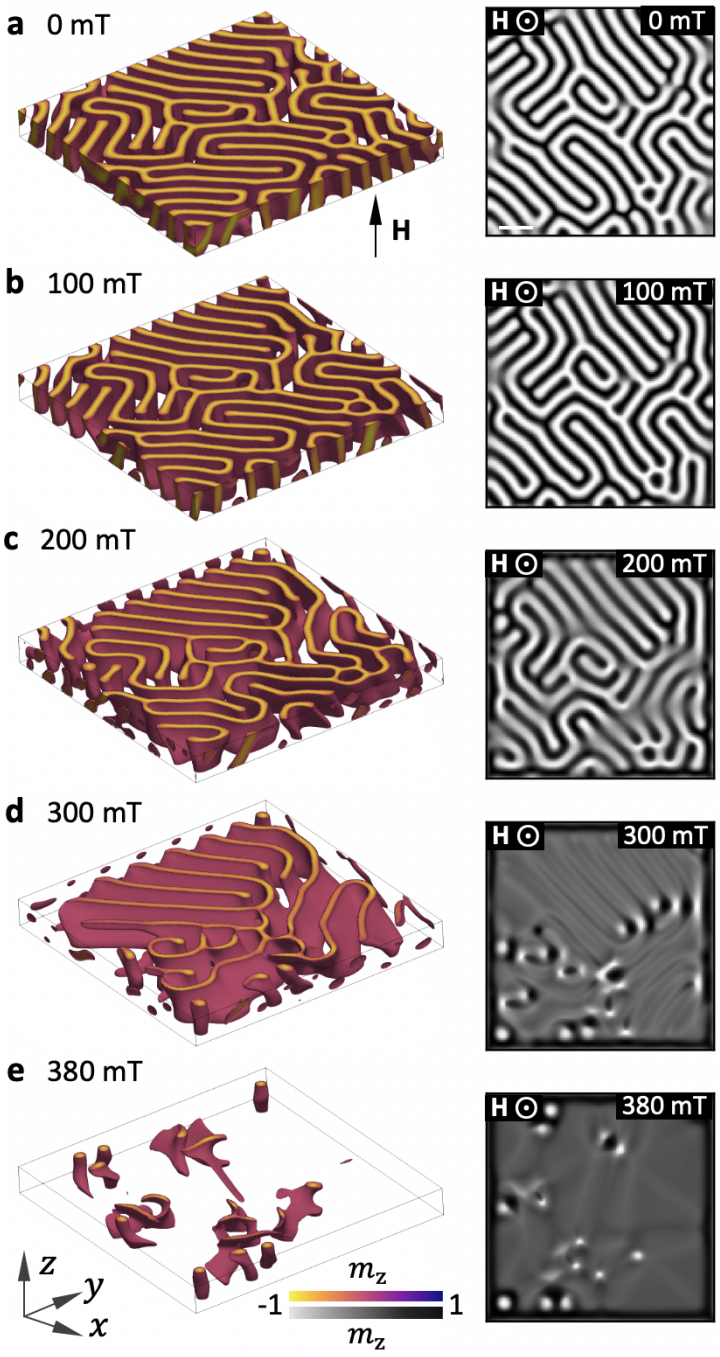

Figure B.5: textbfa-**e**, Selected three dimensional visualisations, created by plotting cells with m_z components between -1 and 0, and simulated images of the magnetic state during an out-of-plane field sweep from an initially randomised state. Scale bar, 100 nm.

References

[1] Donahue, M. J. & Porter, D. G. OOMMF User's Guide, Version 1.0, *National Institute of Standards and Technology*, Gaithersburg, MD (1999).

[2] Cortés-Ortuño, D. OOMMFpy python module. doi: 10.5281/zenodo.2611194 (2019).